technische universität dortmund

Max-Planck-Institut für molekulare Physiologie

mpi

Atomic insights into muscle contraction by transmission electron cryomicroscopy

Dissertation

zur Erlangung des akademischen
Grades eines Doktors der Naturwissenschaften
der Fakultät für Physik
der Technischen Universität Dortmund

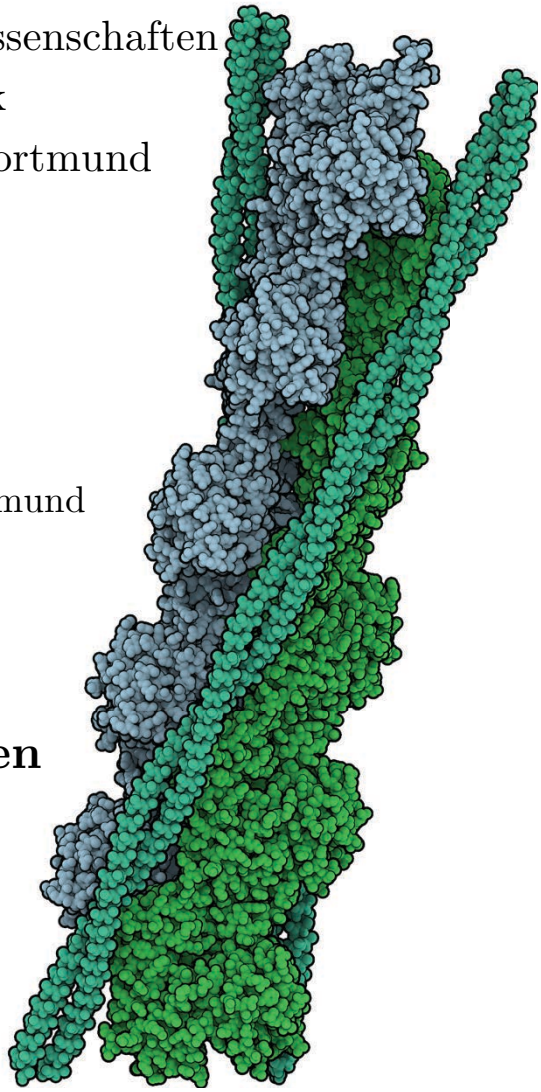

angefertigt am
Max-Planck-Institut für
Molekulare Physiologie in Dortmund

vorgelegt von

Julian von der Ecken

September 2016

Erstgutachter	**Prof. Dr. Metin Tolan** Fakultät Physik, Technische Universität Dortmund
Zweitgutachter	**Prof. Dr. Stefan Raunser** Abteilung für Strukturbiochemie, Max-Planck-Institut für molekulare Physiologie Fakultät für Chemie und Chemische Biologie, Technische Universität Dortmund

Tag der Abgabe der Dissertation: 15. September 2016

Content

Content ..... **I**
List of Figures ..... **III**
1 Abstract & Zusammenfassung **1**
1.1 Abstract 1
1.2 Zusammenfassung 2
2 Introduction **3**
2.1 Structural biology at atomic resolution 3
2.2 Cytoskeleton and motor proteins 6
2.2.1 Actin, Myosin and their interplay 7
2.2.2 Structure determination in this context 14
2.3 Electron microscopy 19
2.3.1 Transmission electron microscopy on biological samples 20
2.3.2 Single particle and helical reconstruction 24
2.3.3 Recent developments in TEM: “resolution revolution” 27
2.4 Aim of this work 32
3 Material and Methods **33**
3.1 Protein purification 33
3.1.1 Protein samples 33
3.1.2 Purification of G-actin 34
3.1.3 Final purification step of G-actin 35
3.2 Sample preparation for TEM 37
3.2.1 Negative staining 37
3.2.2 Cryo vitrification 39
3.3 Screening and data acquisition 41
3.3.1 Screening with negative staining 41
3.3.2 Screening for cryo-EM sample conditions 42
3.3.3 Data acquisition for high-resolution cryo-EM 43
3.4 Computational methods in cryo-EM 44
3.4.1 Data pre-processing 45
3.4.2 Two-dimensional (2D) classification 47
3.4.3 Three-dimensional (3D) refinement 49
3.4.4 Correcting for particle movement and beam-induced damage 50
3.4.5 Methods for sanity check of projection parameters of filamentous samples 51
3.4.6 Post-processing and resolution estimation 51
3.5 Model building and refinement 53
3.5.1 Preparation of the EM density map 53
3.5.2 Model building 53
3.5.3 Model refinement and validation 54

3.6 Tools for visualization and characterization of a protein structure 56
4 Results & Discussion 57
4.1 Reconstitution of the protein complexes 57
4.1.1 Evaluation of F-actin with negative staining EM 57
4.1.2 Reconstitution of the F-actin-tropomyosin complex 59
4.1.3 Vitrification of F-actin complexes 60
4.1.4 Decoration of F-actin with myosin in cryo-EM 62
4.2 Improved helical reconstruction: HELICON 64
4.2.1 Helixboxer and shiftali 65
4.2.2 Helicon and heliconlocal 67
4.3 Structure of a skeletal F-actin-tropomyosin complex 70
4.3.1 Abstract 70
4.3.2 Structure of F-actin-tropomyosin 71
4.3.3 Intra- and Interstrand contacts of the F-actin filament 73
4.3.4 The D-loop and its key function for the filament stability 74
4.3.5 G- to F-actin transition 75
4.3.6 Tropomyosin position on F-actin in an Apo-state 78
4.3.7 Model of tropomyosin transition by myosin binding 80
4.3.8 Applied methods 83
4.4 Structure a human cytoplasmic actomyosin complex 88
4.4.1 Abstract 88
4.4.2 Structure of the ATM complex 89
4.4.3 Helix-loop-helix motif as the key binding region 90
4.4.4 Cardiomyopathy loop completes the rigor interface 92
4.4.5 Role of loop 2 in initial binding 93
4.4.6 Loop 3 as an assistant 94
4.4.7 Supporting instead of activation loop 95
4.4.8 Myosin-induced conformational changes in F-actin 96
4.4.9 Actin-induced conformational changes in myosin 97
4.4.10 Mechanism of myosin binding to F-actin 98
4.4.11 Applied methods 101
4.5 Comprehensive discussion and outlook 107
4.5.1 Validation of the results 107
4.5.2 The results and their perspectives 110
4.5.3 General perspectives of cryo-EM 114
5 References 117
6 Appendix 139
6.1 Tables 139
6.2 Figures 144
Danksagungen 153
Publikationen und Konferenzbeiträge 155
Förderung 157

List of Figures

Figure 2.1: Resolution limits of imaging technologies. 3
Figure 2.2: Variety of F-actin-myosin interaction. 6
Figure 2.3: Actin polymerization and ATP hydrolysis. 7
Figure 2.4: F-actin subunit and subdomains. 8
Figure 2.5: The myosin family and myosin class II. 9
Figure 2.6.: Myosin architecture and cross-bridge cycle. 10
Figure 2.7: The Cross-bridge cycle in detail. 12
Figure 2.8: Tropomyosin hinders and allows myosin binding to F-actin. 13
Figure 2.9: First structures of actin 15
Figure 2.10: Atomic models of F-actin. 17
Figure 2.11: Atomic model of actomyosin. 18
Figure 2.12: Setup of a transmission electron microscope. 20
Figure 2.13: The contrast transfer function (CTF). 22
Figure 2.14: Projection image of vitrified samples. 24
Figure 2.15: Projection parameters and helical symmetry. 25
Figure 2.16: Refinement and reconstruction. 26
Figure 2.17: Cryo-EM structures at atomic resolution. 27
Figure 2.18: Layout of different types of cameras. 28
Figure 2.19: Motion correction of movie frames. 29
Figure 2.20: DQE of different detectors. 30
Figure 3.1: EM grid layout. 37
Figure 3.2: Grids and plunge freezers. 39
Figure 3.3: Used transmission electron microscopes. 42
Figure 3.4: Schematic workflow of data processing. 44
Figure 3.5: CTF parameter set and CTF estimation. 46
Figure 3.6: Filament selection and extraction. 47
Figure 3.7: Example of 2D-classifications. 48
Figure 3.8: Particle-based movie refinement. 51
Figure 3.9: Define geometry weights in model refinement. 55
Figure 4.1: Evaluation of the quality and concentration of F-actin sample. 58
Figure 4.2: Empirical adjustment of tropomyosin concentration. 59
Figure 4.3: Screening for best vitrification conditions for F-actin-tropomyosin. 61
Figure 4.4: Decoration of F-actin with myosin. 62
Figure 4.5: The *HELICON* workflow. 64
Figure 4.6: *Helixboxer* - manual boxing of filaments. 65
Figure 4.7: *Shifitali* - centering the segments. 66
Figure 4.8: *Helicon* – initial aligning of the segments. 67
Figure 4.9: Heliconlocal - allowing flexibility to the segments within a filament. 68

Figure 4.10: Cryo-EM structure of F-actin decorated with tropomyosin. 71
Figure 4.11: Micrograph and 2D-classification of the cryo-EM dataset. 72
Figure 4.12: Representative regions and resolution of the F-actin cryo-EM map. 73
Figure 4.13: Filament stability by intrastrand and interstrand interactions. 74
Figure 4.14: Destabilization of the D-loop binding. 75
Figure 4.15: G-actin to F-actin transition 76
Figure 4.16: Model of barbed end binding and G- to F-actin transition 77
Figure 4.17: Model of pointed end binding and G- to F-actin transition 78
Figure 4.18: F-actin interaction with tropomyosin. 79
Figure 4.19: Comparison of reconstructions regarding the tropomyosin position on F-actin. 80
Figure 4.20: Tropomyosin transition on F-actin induced by myosin binding. 81
Figure 4.21: Model of tropomyosin transition on F-actin during myosin binding 82
Figure 4.22: Micrographs and two-dimensional classification with negative staining EM. 84
Figure 4.23: B-factor distribution and not resolved N and C termini. 86
Figure 4.24: Structure and model of the ATM complex. 89
Figure 4.25: Resolution range of the density map. 90
Figure 4.26: Helix-loop-helix motif bound to F-actin 91
Figure 4.27: Interfaces of the ATM complex. 92
Figure 4.28: Cardiomyopathy loop 93
Figure 4.29: Stabilization of loop 2. 94
Figure 4.30: Sequence-dependent interaction of supporting loop with N terminus of F-actin. 95
Figure 4.31: Comparison of PPS and rigor state and induced changes in F-actin. 96
Figure 4.32: Comparison of rigor and rigor-like myosin structures. 98
Figure 4.33: Model of myosin binding to F-actin. 99
Figure 4.34: Strut attraction to the base of loop 2 promotes cleft closure. 100
Figure 4.35: Two-dimensional classifications and three-dimensional refinement. 102
Figure 4.36: Average and local resolution. 103
Figure 4.37: Model refinement and B-factor distribution. 105
Figure 4.38: Fitting of atomic model to EM density by the 'Dirty laundry server' 109
Figure A6.1: Inter- and intrastrand F-actin interactions. 144
Figure A6.2: Nucleotide binding site 145
Figure A6.3: Sequence alignment of the HLH motif. 146
Figure A6.4: Loop 2 and loop 3 on F-actin 147
Figure A6.5: Sequence-dependent interaction of supporting loop with the N terminus of F-actin. 148
Figure A6.6: Myosin-induced conformational changes in F-actin. 149
Figure A6.7: Different alignments of models for weak to strong binding of myosin. 150
Figure A6.8: Lever arm movement between PPS and rigor state 151

1 Abstract & Zusammenfassung

1.1 Abstract

Force generation for muscle contraction is based on the interaction of myosin filaments with actin filaments (F-actin). Interestingly, the fundamental mechanism is equivalent to a single transport process of a myosin dimer carrying a cargo on an actin microfilament of the cytoskeleton. Proteins like for example tropomyosin regulate both types of interaction. Researchers have tried to analyse the molecular structures of the involved proteins for more than fifty years. However, until recently high-resolution structures of F-actin in complex with myosin or tropomyosin were lacking, which could shed light on the mechanochemical reaction cycle during interaction from a structural point of view. Although crystal structures of monomeric actins and isolated myosins could give first insights in how conformational changes drive the transformation of chemical energy into directed mechanical force, an actomyosin complex could not be crystallized.

In my doctoral thesis I present a structure of F-actin in complex with tropomyosin and a structure of the F-actin-myosin-tropomyosin complex. I applied transmission electron cryo microscopy (cryo-EM) to obtain the structures. Furthermore, I could improve the processing of the data by using the symmetry parameters of the actin filament for determination of the projection parameters to perform the reconstruction.

With the F-actin-tropomyosin structure several proposed interaction sides of the F-actin subunits were directly visualized and confirmed. Furthermore, based on the structure a model was developed describing the mechanism of polymerization of the actin filament. The DNase-binding loop is the key mediator during polymerization. The position of tropomyosin on F-actin differs from previous structures, so that these published results should be revised or extended. A comparison of the position of tropomyosin on F-actin with and without bound myosin revealed that tropomyosin has to perform a significant shift or rotation on the actin filament to release the myosin binding site during transition.

The structure of the F-actin-myosin-tropomyosin complex is in the rigor state. In this state nucleotide-free myosin is strongly bound to F-actin. For the first time, the structure allows analysing of the interface of all three proteins at near-atomic resolution and evaluating of known mutagenesis studies. A comparison of the structure with other intermediate states of myosin made it possible to propose a mechanism on how F-actin promotes the ATPase activity of myosin. In particular, the C-terminal base of loop 2 attracts the strut in myosin while getting stabilized by the N terminus of an F-actin subunit.

The structures and derived atomic models of both complexes will lead to a better understanding of diseases like myopathies, in particular cardiomyopathies. In addition, the established methods can be further applied to actomyosin complexes, in which actin, myosin or tropomyosin are stabilized in other intermediate states of the reaction cycle.

1.2 Zusammenfassung

Jede Kontraktion eines Muskels basiert auf dem Zusammenspiel von Millionen Myosinmolekülen mit Aktinfilamenten (F-Aktin). Dabei unterscheidet sich interessanterweise der fundamentale Mechanismus der Interaktion nicht von dem, der bei Transportprozessen in der Zelle stattfindet, wenn nur ein Myosindimer eine Fracht entlang des Aktinzytoskeletts bewegt. Sowohl die Muskelkontraktion als auch die Transportprozesse werden dabei von aktinbindenden Proteinen wie zum Beispiel Tropomyosin reguliert. Die Interaktion aller beteiligten Proteine wird seit mehr als einem halben Jahrhundert studiert. Dennoch fehlen bis dato hochauflösende Strukturen dieser Proteine in einem Komplex, um den höchst komplexen Reaktionszyklus während der Interaktion strukturell im Detail zu verstehen, bei dem chemische in mechanische Energie umgewandelt wird. Obwohl Kristallstrukturen von monomerem Aktin und isoliertem Myosin bereits seit vielen Jahren erste Aufschlüsse über die Strukturänderungen während der Interaktion geben konnten, wurde eine Kristallisation eines Aktomyosin-Komplexes nicht erreicht.

Im Rahmen meiner Doktorarbeit habe ich die Struktur von F-Aktin in Komplex mit Tropomyosin und die Struktur des F-Aktin-Myosin-Tropomyosin-Komplexes gelöst. Für die Strukturbestimmung habe ich die Methode der Transmissionselektronen-Kryomikroskopie (Kryo-EM) angewendet. Darüber hinaus habe ich die Datenauswertung dahingehend verbessert, dass die vorhandenen Symmetrieinformationen während der Bestimmung der Projektionsparameter für die Erstellung der Rekonstruktion besser genutzt werden konnten.

Mit der Struktur des F-Aktin-Tropomyosin-Komplexes wurden nicht nur viele bereits bekannte Wechselwirkungen der Aktinuntereinheiten direkt visualisiert und bestätigt, sondern sie diente auch als Grundlage für ein Modell des Polymerisationsmechanismus von Aktin. Die DNase-bindende Domäne von Aktin nimmt dabei eine Schlüsselrolle ein. Die Position von Tropomyosin auf F-Aktin unterscheidet sich von vorherigen Modellen, sodass diese hinterfragt beziehungsweise erweitert werden müssen. Ein Vergleich der Position von Tropomyosin auf Aktin in An- und Abwesenheit von Myosin hat ergeben, dass Tropomyosin eine signifikante Rotation oder Verschiebung auf dem Aktinfilament vornehmen muss, um die Bindungsstelle für Myosin während der Interaktion freizugeben.

Die Struktur des F-Aktin-Myosin-Tropomyosin-Komplexes ist im Rigor-Zustand, bei dem Myosin nukleotidfrei und fest an das Aktinfilament gebunden ist. Die Struktur erlaubte zum ersten Mal die Beschreibung der Schnittstellen der drei Proteine in fast atomarer Auflösung und die Evaluierung von bekannten Mutationsstudien. Ein Vergleich mit Strukturen anderer Zwischenzustände von Myosin ermöglichte das Aufstellen eines Modells, das den Mechanismus der aktininduzierten Verstärkung der ATP-Hydrolyseaktivität über die Wechselwirkung der C-terminalen Basis von Loop 2 mit dem „Strut“ von Myosin erklärt, während der N-Terminus von Aktin stabilisierend wirkt.

Durch das Lösen der Strukturen beider Komplexe ist es nun möglich mit den erstellten molekularen Modellen krankheitsbedingte Fehlfunktionen, die zum Beispiel bei Herzmuskelerkrankungen (Kardiomyopathien) auftreten, besser zu verstehen und weiter zu analysieren. Darüberhinaus können die etablierten Methoden für weitere Analysen von Aktomyosin-Komplexen genutzt werden, in denen andere Zwischenzustände des Reaktionszyklus von Aktin, Myosin oder Tropomyosin betrachtet werden.

2 Introduction

2.1 Structural biology at atomic resolution

It is known that it is possible to decode the genomic code. But just by encrypting a four-letter code or knowing an amino acid sequence it is neither possible to understand the function nor possible to determine the three-dimensional structure of a biological molecule directly (for example of a protein). The aim of structural biology is to determine the structure of a molecule or molecular complex of interest and thereby to reveal its architecture and its functionality.

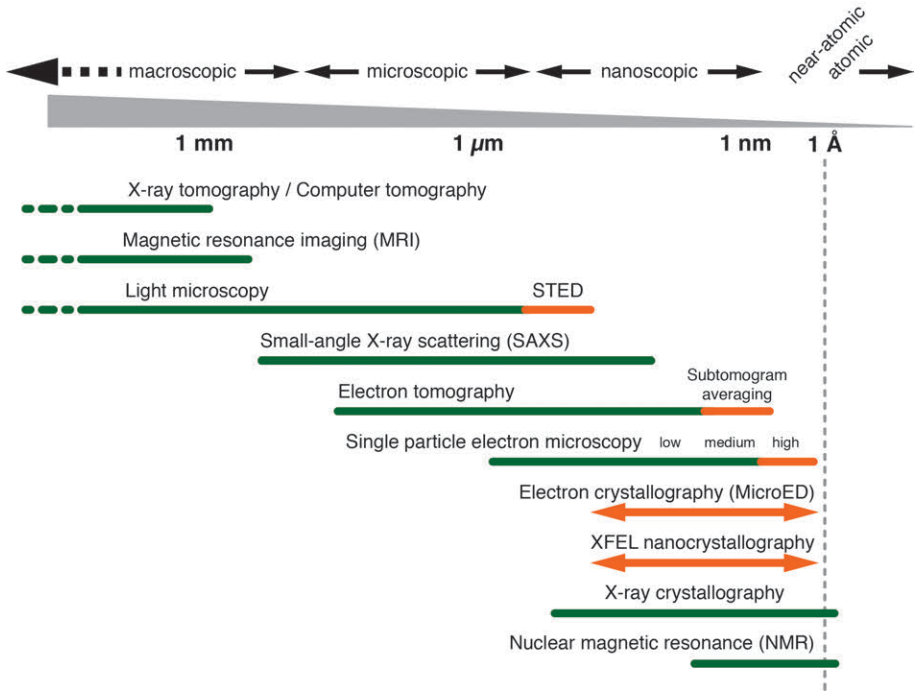

Figure 2.1: Resolution limits of imaging technologies.

General overview of different methods applied in imaging in a biological context. The techniques are ordered regarding to their resolution ranges. To obtain a near-atomic or atomic structure only the last five methods from the bottom to the top including single particle electron microscopy are suitable. Significant improvements in the resolution ranges or new methods within the last years are highlighted in orange. For example 'Stimulated Emission Depletion' (STED) pushed the resolution of florescence light microscopy (Hell and Wichmann, 1994; Klar et al., 2001). In addition, the limits have to be further defined for the very young methods of using a free-electron laser (XFEL) on nanocrystals or electron diffraction by microcrystals (MicroED) for structure determination (indicated by arrows). The upper methods can be used for larger scales as well (indicated by pointed line).

Different methods can be applied for that purpose and have been established in the last decades. Besides that, new technologies made it possible to derive new applications and perform significant improvements within the last years. The main differences of the methods are the achievable resolution

ranges and the applicable size and type of the target. In Figure 2.1 several imaging technologies are ordered with respect to their resolution limits. Only the latter five techniques are suitable to obtain structures with a resolution in the nanometre range. Especially X-ray crystallography is the most abundant and established method and has been used worldwide over the last decades to obtain atomic models of molecules including proteins. However, since for crystallography the biological sample has to be crystallized in a non-physiological environment, obtaining diffracting crystals from several protein classes is difficult. Examples for these cases can be membrane proteins, filaments or larger protein complexes. Furthermore, it has to be ensured that the sample itself is suitable (like being homogenous, not flexible and stable) to allow the actual crystallization. Young technologies like free-electron laser (XFEL) nano-crystallography (Chapman et al., 2011; Gavira, 2015; Helliwell, 2013) or electron diffraction on microcrystals (MicroED; Nannenga et al., 2014; Shi et al., 2013; 2016) made it possible to collect diffraction patterns of tiny crystals and to derive the three-dimensional structure of the molecule. Nevertheless, these methods still require the formation of crystals to determine the structure. Other methods like 'small-angle X-ray scattering' (SAXS) and 'nuclear magnetic resonance' (NMR) spectroscopy can fill some of the left gaps and can be used in a complementary manner, but have their own limitation. SAXS deals with the biological sample in solution and thereby a more native environment (Mertens and Svergun, 2010). Besides, in SAXS it is possible to expose the sample to extreme conditions (e.g. pH, pressure, salt concentrations) to study its structure or behaviour (Gao et al., 2015; Schroer et al., 2010), which is not possible in a crystallographic setup. Unfortunately, the overall resolution is in the lower nanometre range and can only describe the overall shape. In comparison to SAXS, NMR is capable of obtaining the three-dimensional structure of a protein in its more native environment in solution up to atomic resolution. Nevertheless, NMR is limited to small proteins ($\leq$ 20 - 30 kDa) and the interpretation of the data gets more difficult with an increasing molecular weight (Wüthrich, 2001). But not all biological samples are soluble. Therefore, proteins like for example membrane proteins cannot be analysed easily in theses setups of SAXS or NMR.

Transmission electron microscopy - in particular single particle electron microscopy (single particle EM, see also section 2.3) - has been used for a long time to study biological objects. Recently, it went through a great improvement in terms of resolution (see subsection 2.3.3). In comparison to crystallography, the samples in EM can be in solution similar to SAXS but furthermore structures at near-atomic and atomic resolution like it is possible in crystallography can be obtained. The method is still limited by the size of the molecule ($\geq$ 100-200 kDa), but the barrier is being moved towards higher resolution for smaller proteins continuously. The big advantage is that larger protein complexes or filamentous structures can be structurally analysed and heterogeneity (for example due to flexibility or conformational states) can be compensated by digital sorting methods during analysis of the data. Furthermore, by embedding of proteins in lipid bilayers (e.g. nanodiscs) the protein class of membrane proteins can be analysed.

Besides using only one method to obtain structural information, it is possible to apply several methods in parallel (hybrid approach). For example a full protein complex derived from single particle EM can be built by using several subcomponents, which are already solved at atomic resolution by crystallography (Gatsogiannis et al., 2014; Urnavicius et al., 2015). In addition, a pseudo-atomic model derived from single particle EM can be used to solve the diffraction pattern in crystallography (Meusch et al., 2014). Other hybrid approaches are applied to directly obtain structural, quantitative and correlative information using a combination of transmission electron microscopy and fluorescence microscopy (Bykov et al., 2016; Kukulski et al., 2012; Wolff et al., 2016). Furthermore, electron

tomography can be applied to study a greater field of view and the respective biological object, area or compartment in its native environment like in a cell, but is still limited to the mid-nanometre range (Asano et al., 2016; Mahamid et al., 2016). One method to improve the resolution in tomography is to average tomograms of the same molecule via a 'subtomogram averaging' approach (Briggs, 2013; Schur et al., 2015).

Altogether, when crystallization of the respective protein sample is possible, conventional X-ray crystallography or younger adaptions of this method (using XFELs or electron diffraction) will most likely result in a protein structure at atomic resolution. However, for several types of proteins, their dynamics or environments make structural analysis and obtaining diffracting crystals difficult and thereby deriving an atomic model is only achievable by other methods like transmission electron microscopy and single particle analysis.

2.2 Cytoskeleton and motor proteins

All eukaryotic cells have a highly dynamic protein network – the cytoskeleton – of elongated (filamentous) protein assemblies, which stabilizes the shape and architecture of the cell. The cytoskeleton is not only the backbone of a cell, but also coordinates a network for transport processes within a cell and is responsible for motility and growth of the cell itself (Fletcher and Mullins, 2010). Three kinds of filament classes form the cytoskeleton in a eukaryotic cell: microtubules, intermediate filaments and microfilaments. The microfilaments are built up out of actin, which is one of the most abundant and conserved proteins and has a variety of function in eukaryotic cells (Figure 2.2a; Lodish et al., 2008).

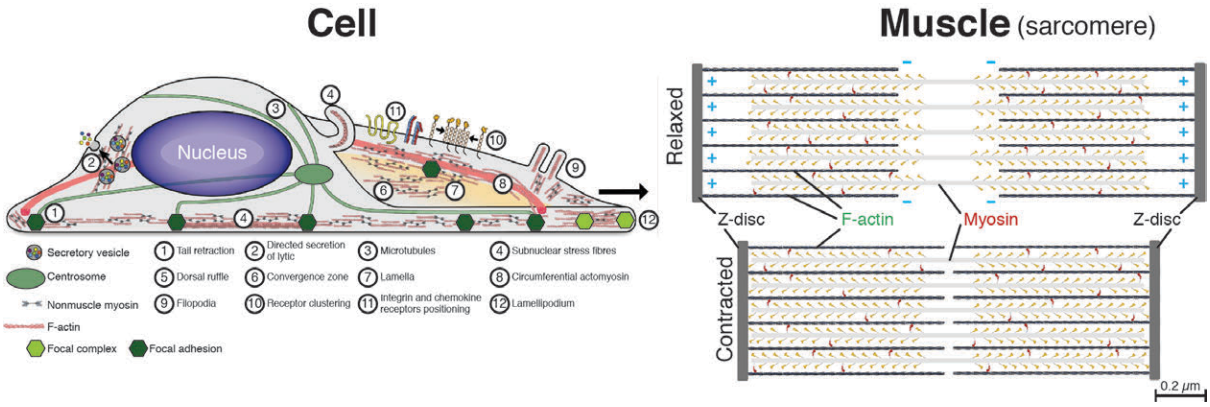

Figure 2.2: Variety of F-actin-myosin interaction.

a, The fundamental mechanism of F-actin-myosin interaction is present in several parts of a cell. For example, actomyosin interaction (of nonmuscle myosins and actins) takes part in cell migration, secretion, receptor positioning and vesicle transport. Figure taken from Heissler and Manstein (2012). **b**, Scheme of a sarcomere (basic contractile unit in a striated muscle tissue, size ~ 2 µm). The sarcomere describes the area between two Z-discs. F-actin filaments are bound to the Z-discs and are aligned to the inner sarcomere with its minus end from both sides. The bipolar myosin filaments can 'walk' on F-actin to the plus end and thereby induce a shortening of the sarcomere during muscle contraction. Figure taken from Spudich (2014).

Prokaryotes have protein families in their cytoskeleton, which share the same fundamental architecture and mechanisms with actin. MreB and ParM are the respective actin-like proteins in a prokaryotic cell in the case of actin (Erickson, 2001; Gunning et al., 2015a). Besides cell stability and motility, cytoskeletal proteins are involved in directed transport processes. For that purpose, motor proteins can 'walk' on the filament while carrying the cargo. The energy is derived by ATP-hydrolysis in a mechanochemical reaction cycle (Lymn and Taylor, 1971; Vale and Milligan, 2000). The movement of myosin, the respective motor protein for actin, represents a fundamental mechanism of force generation and interaction. Interestingly the fundamental interaction does not differ between the interplay of a single myosin molecule with a cytoplasmic actin (microfilament, Figure 2.2a) or the interplay of several myosin heads with muscular actin (thin filament) within a muscle fibre (Figure 2.2b; Spudich, 2014; Squire, 1997). This section introduces into the architecture and interplay of actin and myosin (subsection 2.2.1) and gives an overview of structure determination of the proteins on its own and in complex (subsection 2.2.2).

2.2.1 Actin, Myosin and their interplay

Actin exists in two structural forms

Monomeric actin (G-actin, globular actin) consists of 374 - 375 amino acids and has a molecular weight of ~ 42 kDa. There are six different genes that encode actin in *Homo sapiens*. Actin isoforms mainly differ in their localization (skeletal: *ACTA1*; smooth muscle: *ACTA2*, *ACTG2*; cytoskeletal: *ACTB*, *ACTG1*; cardiac: ACTC1) but show the same structural organisation (Gunning et al., 1997). Besides a high sequence identity between the human isoforms (identity ≥ 94 %), they also show a very high conservation with actins from other organisms (100 % and 84 % identity of skeletal actin (*ACTA1*) to *Oryctolagus cuniculus* (European rabbit) and *Cyanidioschyzon merolae* (Red alga), respectively), making this one of the most conserved protein families known.

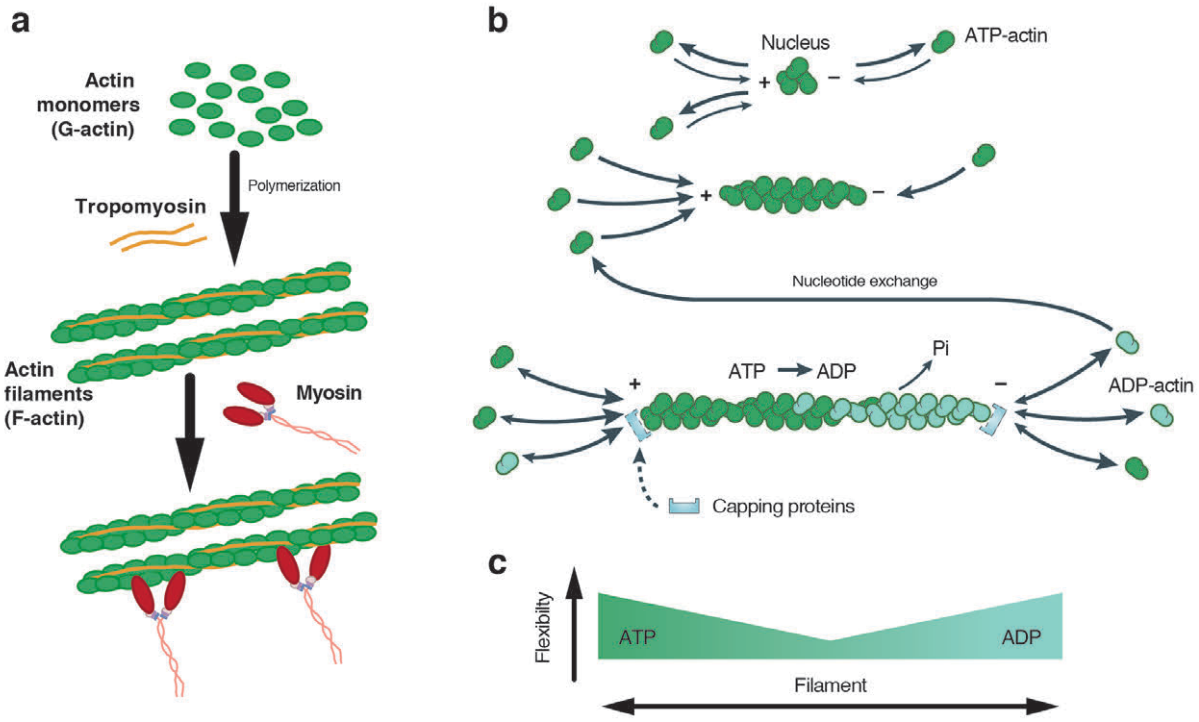

Figure 2.3: Actin polymerization and ATP hydrolysis.

a, Monomeric actin (G-actin; globular actin) can polymerize to double-stranded actin filament (F-actin; filamentous actin). Myosin can bind to F-actin and can create a force to move on F-actin in one direction (direction can differ between myosin classes). Tropomyosin is wrapped around F-actin and is part of a regulatory mechanism, which switches the F-actin-myosin interaction on and off. **b**, F-actin polymerisation (nucleation and elongation) is a highly dynamic process, in which actin can associate and dissociate to and from both sides of the filament. Furthermore, within the filament ATP is hydrolysed to ADP-P_i and P_i is released. In addition, capping proteins can specifically stop growing of the ends of F-actin. Subfigure modified and adapted by permission from Macmillan Publishers Ltd: Nature Review Cancer of Nürnberg et al. (2011). **c**, Due to the hydrolysis of ATP and induced conformational changes in the F-actin subunit (see also Figure 2.4), the filament itself has a structural inhomogeneity. Especially at the ends, the respective conformational state is unknown and shows a higher flexibility in comparison to the rest of the filament.

Actin can polymerize to actin filaments (F-actin, filamentous actin, Figure 2.3) and form the so-called microfilaments, which are part of the cytoskeleton of the cell (see introduction of this section). Actin can make up to 5 % of the weight of a single cell (Blanchoin et al., 2014; Nürnberg et al., 2011). Besides the cytoskeleton, F-actin is one of the main parts of a muscle fibre. Within a sarcomere (smallest contractile unit in a muscle fibre), F-actin is aligned in parallel and forms the thin filament with the regulatory proteins troponin and tropomyosin (Figure 2.2b). The force-generating interaction with the motor protein myosin for both cases is discussed later in this subsection (Figure 2.3a).

The polymerisation of G-actin to F-actin is a highly dynamic process (Figure 2.3b). The actin filament is a polar double-stranded helix. Both ends have different association and dissociation rates resulting in a net growing (plus) and net shrinking (minus) end of the filaments (Figure 2.3b). Polymerisation starts by forming an initial nucleus. This seed is elongated on both ends by addition of G-actin. Nucleation and polymerisation can be induced by high ionic strength (~ 50-100 mM like physiological conditions in the cell) and by different actin-binding proteins (Dominguez, 2016; Hertzog and Carlier, 2005). Furthermore, different binding proteins can control polymerization by capping the ends (e.g. CapZ, gelsolin, tropomodulin) and crosslink filaments or initiate new filaments (e.g. alpha-actinin, Arp2/3, Spire; Dominguez, 2016; Edwards et al., 2014; Fletcher and Mullins, 2010; Nürnberg et al., 2011).

F-actin has an ATPase activity. ATP-Mg^{2+} binds to the G-actin form of actin and activates it for polymerisation. Once a new monomer is bound to F-actin, it hydrolyses ATP to ADP-P_i and finally releases P_i from the filament. In addition, ADP-actin can bind to the filament at a lower rate. The ATPase activity of actin gets accelerated in the filamentous form suggesting a structural difference between the monomeric actin in its G- and F-form (see next paragraph). Due to the higher association rate at the plus end (10x higher than the minus end), the filament can be described by a gradient from ATP- over ATP-P_i- to ADP-actin (Figure 2.3b). Thereby, the two ends differ in their primarily bound nucleotide (ADP-actin at the minus end region, ATP-actin at the plus end region). Due to the binding of new ATP- and ADP-actin on both ends, the ends show a higher structural flexibility and heterogeneity (Figure 2.3c; Jégou and Romet-Lemonne, 2016; Murakami et al., 2010; Narita et al., 2011). The rate constants were firstly estimated by Pollard (Pollard, 1986) after his lab visualized the different growing speeds using electron microscopy (Woodrum et al., 1975; see also next subsection). In the final steady state between filaments and monomeric actin, the rate of polymerization and depolymerization are equal, and thus the filament length does not change. This results in a directional movement of the filament of cytoskeletal actin, while new ATP is continuously consumed. This process is called treadmilling (Kirschner, 1980).

Conformational changes of an F-actin subunit and its dimensions

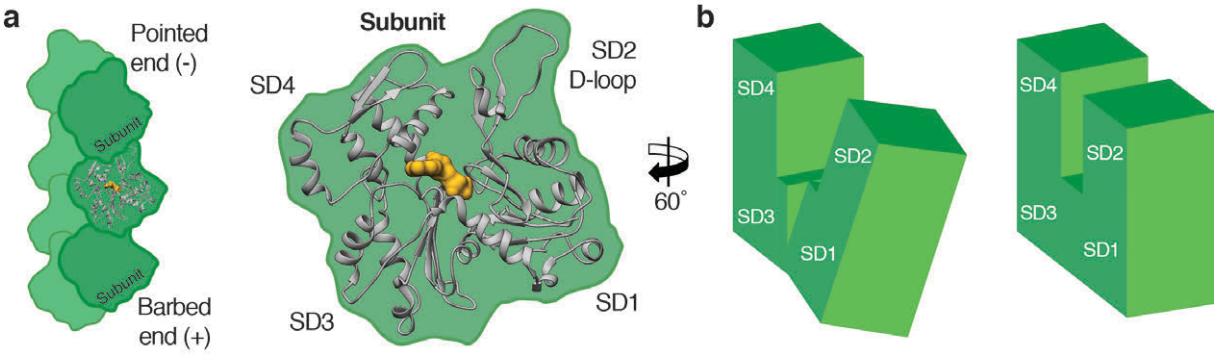

Figure 2.4: F-actin subunit and subdomains.

a, General architecture of an F-actin subunit of the double-stranded F-actin filament. An F-actin subunit consists of four subdomains (SD). The nucleotide (yellow) is bound in the centre of the subunit. The N and C terminus are located in SD1. SD2, which is composed of the so-called D-loop, is thought to play an essential role in polymerisation, as it is highly flexible in the G-actin form of actin. **b**, During filament formation the subunit undergoes a conformational change. SD1 and SD2 are rotated relative to SD3 and SD4. Thereby, the subunit is flattened. Subfigure **b** is adapted from Dominguez and Holmes (2011).

During filament formation G-actin does not only hydrolyse ATP, but also undergoes a conformational change. In Figure 2.4a an F-actin subunit is shown of the filament. The subunit can be split into four subdomains (SD). N and C terminus is located in the SD1 and SD2 is composed of the exposed DNase

binding loop (D-loop). The D-loop is sensitive to the bound nucleotide and is thought to play an essential role in polymerisation (Dominguez and Holmes, 2011; Durer et al., 2012). The nucleotide binds to a cleft between SD2 and SD4, which is oriented to the pointed end of the filament. During polymerisation, SD1 and SD2 rotated relative to SD3 and SD4 (Figure 2.4b). Therefore, the subunit seems to be flatten (Dominguez and Holmes, 2011). The size of one subunit is roughly 5.5 x 5.5 x 3.5 nm and the maximal diameter of the filament is ~ 10 nm. As F-actin is a double-stranded filament, the height of an asymmetric subunit is only half the size of a subunit parallel to the filament axis. The axial repeat is described by the rise of ~ 2.7-2.8 nm. While 28 subunits create one full repeat of the filament (~ 72 nm), the filament has already a pseudo-repeat after 14 subunits (~ 36 nm). Despite actin forms this filamentous order, it is not clear, if F-actin shows a remaining flexibility within the filament (Egelman et al., 1982; Galkin et al., 2010). Moreover, actin has the task to be flexible especially in the case of cytoskeletal actin, which can form bent filaments (Blanchoin et al., 2014; Nürnberg et al., 2011). Nevertheless, the helical architecture allows myosin to repetitively bind to the F-actin filament and using it as a trail.

The myosin family

Myosin belongs to a very large family, whose members couple ATP hydrolysis with a directional movement (Coluccio, 2007). In general, all myosins show an equivalent architecture and have the same actin-binding mechanism. The family is divided into different classes (given as Roman numerals, Figure 2.5a) depending on the localization, functionality, oligomerisation and domain organisation (Hodge and Cope, 2000; Syamaladevi et al., 2012).

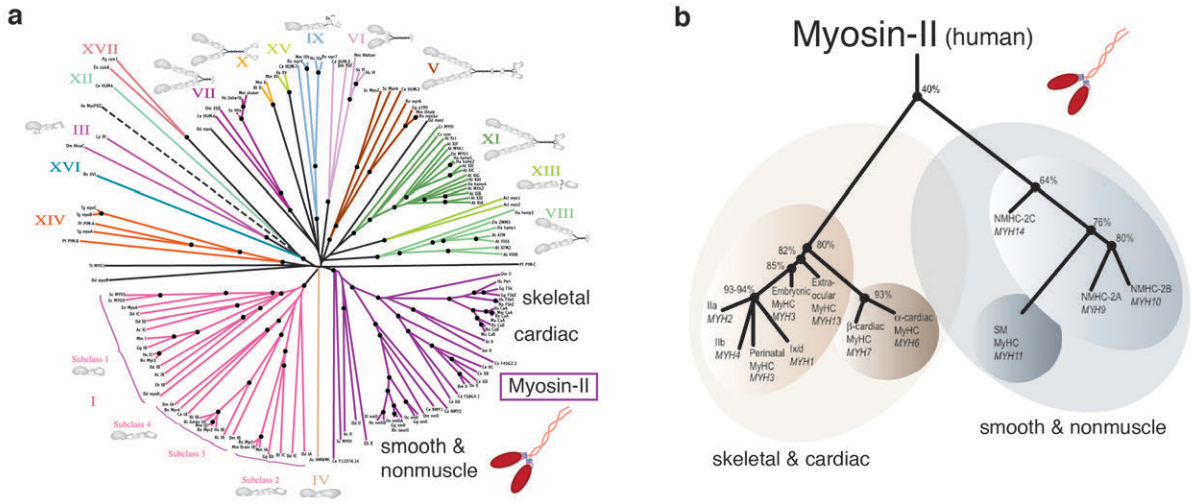

Figure 2.5: The myosin family and myosin class II.

a, An phylogenetic tree of the myosin family based on the motor region of myosin (see Figure 2.6). Example to illustrate the complexity and richness of the family. Myosin classes are always given as Roman numerals. Classes differ in function (e.g. localisation, walking direction) and overall architecture (e.g. number of assembled myosin heads and light chains). The myosin-II class describes a dimeric myosin class and is known as conventional myosin. Mainly skeletal and cardiac muscle consists of myosin-II, but also smooth and nonmuscle myosin-II isoforms exists. The tree was created by Hodge and Cope (2000). **b**, Close-up phylogenetic tree of myosin-II from *Homo sapiens* taken from Heissler and Manstein (2012). Although isoforms are assigned to either skeletal, cardiac, smooth muscle or nonmuscle myosins, they are present in the other tissues but at a much smaller fraction.

The most prominent class, abundant in skeletal muscles, is myosin-II (Figure 2.5b) and is called 'conventional' myosin, while other myosin classes are called 'unconventional' (Hartman et al., 2011). Myosin-II is mainly present in all muscle forms and in addition nonmuscle tissues. Each gene codes for a specific myosin. Although they are primarily present in a specific tissue, they can be found in other

at much smaller fractions (Heissler and Manstein, 2012). The variety of functions is already illustrated for nonmuscle myosin-II in Figure 2.2a and skeletal myosin-II in Figure 2.2b (Heissler and Manstein, 2012; Vicente-Manzanares et al., 2009). Although the actin-myosin interaction has this diverse functionality, the fundamental architecture of myosin and its binding mechanism remain the same.

All myosin share the same architecture and binding mechanism

All myosins are composed of a N-terminal motor domain, which can bind to actin filaments. An upper 50-kDa and a lower 50-kDa domain form the prominent actin-binding cleft. The motor domain is connected via the converter and neck domain to a lever arm, which finally ends in a C terminal targeting domain (for example for vesicle binding). Motor and neck domain form the so-called head region of the myosin. The main difference between myosin classes is their neck domains. Figure 2.6a illustrates the overall architecture of myosin-II. One essential and one regulatory light chain bind to myosin-II and two myosins dimerize forming a double-headed myosin dimer (Heissler and Manstein, 2012; Sweeney and Houdusse, 2010a). In addition, their lever arms assemble to a coiled-coil structure. For example, other myosin classes are only single-headed myosins or have extra light chains (Figure 2.5a; Cope et al., 1996).

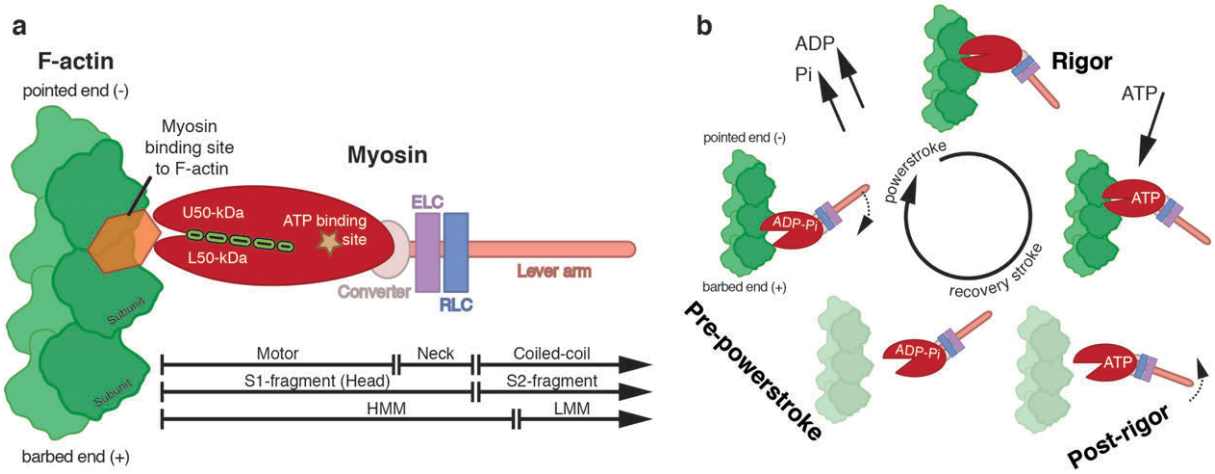

Figure 2.6.: Myosin architecture and cross-bridge cycle.

a, Overall domain organisation of myosin-II. Scheme shows the myosin heavy mero myosin (HHM) consisting of the motor, the neck region (essential light chain (ELC) and regulatory light chain (RLC)) and part of the lever arm. The converter is the connector between motor domain and neck region. The motor domain is the N-terminal part of myosin and has a prominent lower 50-kDa (L50-kDa) and an upper 50-kDa (U50-kDa) domain, which create the actin binding cleft (indicated with a green dotted line). The lever arm continues into the light mero myosin (LMM), which for example dimerize in myosin-II. Myosin only binds to F-actin between two F-actin subunits (region highlighted in orange) and can create a force to the direction of the barbed end of F-actin. **b**, Cartoon of the simplified cross-bridge cycle of myosin-F-actin interaction. Myosin is rigidly bound (rigor state) to F-actin, when no nucleotide is present in the binding pocket. Binding of ATP weakens the binding strength due to conformational changes in the head region of myosin, which leads to a detaching of myosin from F-actin (post-rigor state). Afterwards, ATP is hydrolysed to ADP-P_i and the lever arm is primed to its pre-powerstroke state position (recovery stroke). Finally, myosin reattaches to the next position on F-actin, which amplifies ADP- and P_i-release and the lever arm swings back (powerstroke). F-actin and myosin form again a strong binding interface.

The motor domain is highly conserved between myosin classes (Cope et al., 1996; Richards and Cavalier-Smith, 2005). Several surface loops of myosin, which have only regulatory function such as fine tuning of the actin affinity or the ATP hydrolysis, mainly differ between different classes (Clark et al., 2005; Gyimesi et al., 2008; Kojima et al., 2001; Yengo and Sweeney, 2004).

The head domain binds between two subunits of F-actin (Figure 2.6a), while closing the actin-binding cleft. As mentioned before, myosin can create a directed force and thus transport for example a cargo.

While only myosin-VI travels towards the pointed end of actin filaments, most myosins transport or 'walk' to the barbed end (Sweeney and Houdusse, 2010b). Cargo transporting myosins are double-headed myosins and walk in a hand-over-hand manner on the actin filaments (Yildiz et al., 2003). The most studied case is the interaction within a muscle fibre. In a sarcomere, the smallest contractile unit in muscle fibre, several myosin dimers form a bipolar myosin filament (thick filament, see Figure 2.2b). Both ends of the myosin filaments pull to the minus end of actin resulting in a reduced size of the sarcomere (defined by the distance of the Z-discs, see Figure 2.2b), which results in a shortening of the full muscle fibre and finally the contraction of the whole muscle (Squire, 1997). For both cases the fundamental mechanism of actin-myosin interaction is the same and is described with the 'cross-bridge cycle' (Figure 2.6b, see next paragraph).

Cross-bridge cycle

Myosins have different states depending on the currently bound nucleotide, major conformational changes of the lever arm region, the actin binding cleft and rearrangement of inner myosin motifs. A simplified overview of the highly dynamic cross-bridge cycle is given in Figure 2.6b. Particularly, Lymn and Taylor firstly described the ATP hydrolysis cycle during interaction with actin. Therefore, the cycle is also referred to as the Lymn-Taylor model (Lymn and Taylor, 1970; 1971). The structural mechanism of muscle contraction is named as the 'swinging lever arm hypothesis' and was introduced by Huxley and Hanson (Holmes, 1997; Huxley and Hanson, 1954; Huxley, 1969). Furthermore, myosin has a basal ATP activity and can undergo the conformational changes without binding to actin. Nevertheless, myosin shows an actin-activated ATPase activity, but it is still not known how actin structurally activates myosin in detail (Furch et al., 1998; Kojima et al., 2001; Onishi et al., 2006; Várkuti et al., 2015).

If no nucleotide is bound to the head region of myosin, myosin binds to actin in the so-called rigor state with a high affinity. The actin-binding cleft is closed and the lever arm is in a 'relaxed' position. When no ATP is available and the binding site on actin is not hindered by other molecular mechanisms (see next paragraph), a muscle keeps stiff (e.g. in the case of *rigor mortis*). As soon ATP binds to myosin, myosin opens the actin-binding cleft and detaches from actin (post-rigor state). While being detached from the actin filament ATP is hydrolysed to ADP-P_i. The gained energy primes the lever arm (recovery stroke) and the myosin is in its pre-powerstroke state. Afterwards, pre-powerstroke state myosin rebinds on a new position on actin, closes the actin-binding cleft and releases P_i and ADP. Finally, the lever arm performs the powerstroke, which transformed the released energy to a relative movement between actin and myosin. The cycle can start again.

The cycle as given above deals as an overview, while several reviews describe the mechanism in detail (Geeves and Holmes, 1999; Geeves, 2016; Sweeney and Houdusse, 2010a). Each step can be understood as an equilibrium between two states with a respective constant (Figure 2.7). Different myosins classes differ in these constants (Greenberg et al., 2016). For example, a double-headed myosin proceeding isolated on cytoskeletal actin stays as long as possible in an ADP-state strongly bound to F-actin. In this state, no new ATP can bind, which would induce a detachment from actin. Thus, the probability that both heads are detached at the same time would be significantly reduced. In this case, often a load-dependent ADP released is proposed, which is controlled by the rebinding of the leading myosin (leading head) and its applied force to the trailing myosin (trailing head) (Sweeney and Houdusse, 2004; Walklate et al., 2016). Besides the global conformational changes of the actin-binding cleft or the lever arm region, specific other motifs experience conformational changes during the cycle (for example

switch-I, switch-II, P-loop, not discussed) and have to be taken into account to differentiate between the given steps. These motifs can be found in other motor proteins or Ras GTPases and show similarities in structural arrangement and function (Müller and Goody, 2016; Sablin, 2001; Smith and Rayment, 1996). These inner changes are often labelled with addition symbols (Figure 2.7; Geeves, 2016). Finally, the whole cycle can be divided into strong and weak actin binding. Myosin states at the transition between strong and weak binding to actin have a low affinity and a short lifetime. The post-rigor and pre-powerstroke states are not stable and myosin directly detaches or performs next steps of the cycle, respectively. These intermediate states are difficult to stabilize bound to actin and only structural analyses are performed on isolated myosin (Preller and Manstein, 2013).

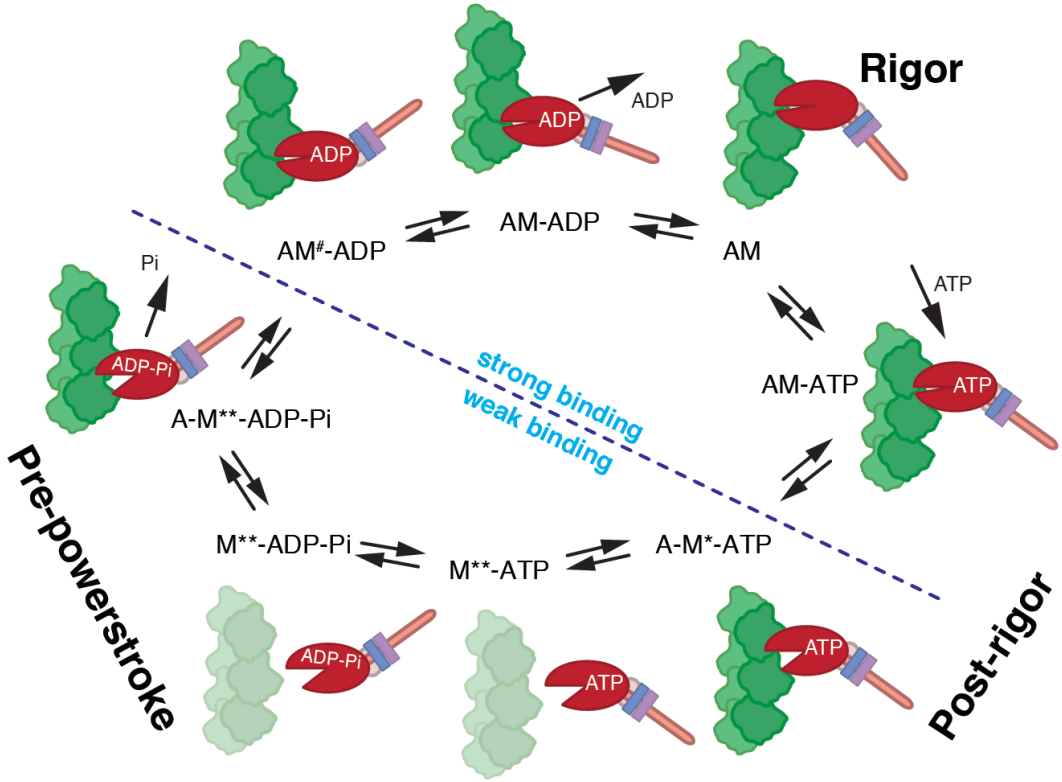

Figure 2.7: The Cross-bridge cycle in detail.

Cartoon of the cross-bridge cycle of myosin-F-actin interaction in greater detail. Each position in the cycle describes changes in either the current F-actin-myosin binding strength, the bound nucleotide or conformational changes within myosin (A=Actin; M=Myosin; *, **, # indicate different conformational changes in the head region, not discussed but reviewed in (Sweeney and Houdusse, 2010a; Geeves, 2016). Each step has an equilibrium constant, which differs between each step and myosin classes (indicated by two arrows). The cycle can be divided in strongly and weakly bound myosin to F-actin.

Although the full mechanism has been investigated since more than a half-century and the mechanochemical reaction cycle has been studied for several myosin classes in great detail, structural information of the actin-myosin complex (actomyosin) in different states is still missing (see also next subsection). In addition, the exact release point of P_i or ADP in relation to the power stroke is still under discussion (Binder et al., 2015; Llinas et al., 2015; Muretta et al., 2015). Furthermore, several other proteins are regulating actin and myosin. Thus analysis of isolated actin and myosin is a simplified complex and their mechanism has to be interpreted with respect to these regulatory proteins.

Regulation of myosin binding to actin

The most prominent proteins regulating the actin-myosin interaction are tropomyosin and troponin, which are involved in the myosin-actin interaction in striated muscle. Tropomyosin is also found in the actin filaments of smooth muscles and non-muscle cells. In this case, tropomyosin has still a regulatory function on polymerisation and stability of F-actin and myosin binding (Gunning et al., 2008; 2015b; Manstein and Mulvihill, 2016). Tropomyosin has a variety of isoforms in each tissue but always forms its prominent coiled-coil structure (Geeves et al., 2014; Phillips, 1986; Whitby and Phillips, 2000). Tropomyosin consist of two alpha-helical chains and polymerizes directly on F-actin to a long tube-like structure that wraps around the filament (Brown and Cohen, 2005; Coulton et al., 2006; Schmidt et al., 2015). Every tropomyosin molecule has several pseudo-repeats and binds over up to seven F-actin subunits (tropomyosin length depends on the isoform; Geeves et al., 2014). As F-actin is a double-stranded helix, two tropomyosin tubes bind to each side of the filament. In cardiac and skeletal muscle, tropomyosin interaction is further regulated by troponin, which can move tropomyosin on F-actin into different positions. Calcium binding induces this conformational change in troponin, which modifies the tropomyosin position (Orzechowski et al., 2014a; Resetar et al., 2002; Sun et al., 2009; Tobacman and Adelstein, 1986). If no calcium is bound to troponin, tropomyosin is held in a blocked state (B-state) and occupies the myosin-binding site on F-actin. Even when myosin is in a primed state (pre-powerstroke state, see paragraph before), it cannot bind to the actin filament (Figure 2.8a).

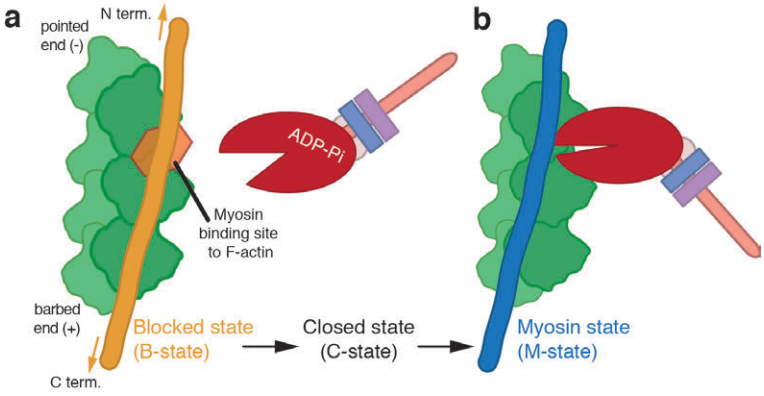

Figure 2.8: Tropomyosin hinders and allows myosin binding to F-actin.

a, Tropomyosin (yellow tube, B-state) is wrapped around F-actin (green) and occupies the myosin binding site (orange). Troponin (not shown) can induce the release of the myosin-binding site through moving of tropomyosin to a closed state and thereby allows myosin to bind to F-actin (C-state, not shown). **b**, When myosin finally is bound, tropomyosin is moved to a third position on F-actin (Myosin state; blue tube).

As soon calcium binds to troponin, tropomyosin is released to the closed state (C-state). As soon myosin binds to F-actin, tropomyosin is further moved to its myosin state (M-state) position (Figure 2.8b). The polymerization and moving of tropomyosin is highly cooperative and transmitted though the whole filament. This cooperative mechanism is described is known as 'Gestalt-binding' (Holmes and Lehman, 2008; Lehman et al., 2013b). Although the mechanism is basically understood a high-resolution structure is still missing. Thus, the interplay of tropomyosin with F-actin, myosin and troponin could be structurally elucidated. Furthermore, the structural basis for the cooperativity is not known. It is unknown which kind of movement is performed by tropomyosin (rolling and/or shifting) (Rynkiewicz et al., 2015). In particular, the structural details of the connection of two adjacent tropomyosins molecules (N and C terminus overlap) is still being discussed regarding its specific structure and its function for Gestalt-binding (Lehman et al., 2013a; Li et al., 2014; Mamidi et al., 2013).

2.2.2 Structure determination in this context

A historical overview

Structural analysis of actin and myosin basically started in the nineteen forties, when for the first time the interplay between actin and myosin was identified as being responsible for the ATP-dependent muscle contraction (Banga and Szent-Györgyi, 1940; Banga et al., 1947; Szent-Györgyi, 1948). Later in the 1950s Huxley and colleagues revealed the organisation and fundamental sliding mechanism in striated muscles using electron microscopy on muscle biopsies (Huxley and Hanson, 1954; Huxley, 1953). It took another decade until actin-myosin interaction was discovered in nonmuscle cells by detecting it in slime moulds (Adelman et al., 1968; Hatano and Oosawa, 1966). By these results the high abundance and conservation of actin in eukaryotic cells were proposed and that actin is not unique to muscle cells.

During that time experiments showed that with myosin heads decorated actin filaments have an arrow-like shape (Figure 2.9a) and by this the polarity of the filament could be directly visualized with electron microscopy (Huxley, 1963; Ishikawa et al., 1969). Furthermore, the different polymerization behaviours of both ends of the filaments were discovered and quantified by adding new monomeric actin to decorated filaments and the naming of pointed and barbed end were introduced (Hayashi and Ip, 1976; Woodrum et al., 1975). DeRosier and Klug could obtain the first reconstruction of a helical object using transmissions electron microscopy (De Rosier and Klug, 1968). This method made it possible to reveal for the first time a model of F-actin decorated with the head domain of myosin in the absence of ATP (Moore et al., 1970).

Several other low-resolution structural work and kinetic studies were performed on isolated actin and myosin or on actin and myosin as a complex (actomyosin) within the next years. The first low-resolution reconstruction of F-actin obtained by transmission electron microscopy were presented during this time giving first hints on how the filament is organized (Egelman, 1985). However, it took until 1990 when for the first time a high-resolution X-ray crystal structure of monomeric G-actin was obtained (Figure 2.9b; Kabsch et al., 1990). In the same issue of *Nature* the same group used this G-actin model to fit it into a structure determined by fibre diffraction of F-actin (Figure 2.9c; Holmes et al., 1990). They analysed the diffraction pattern of gels of oriented F-actin filaments, which were obtained by ultracentrifugation. For the first time they could propose an atomic model of F-actin, which showed how the two strands and each subunit are oriented relative to each other. In addition, they identified the relevant inter- and intrastrand contacts. Although their data showed information in the range up to 8 Å they claimed that there are only minimal changes between G-actin and an F-actin subunit and were not able to detect conformational changes (see Figure 2.4, paragraph 'Conformational changes of an F-actin subunit and its dimensions' in subsection 2.2.1 and next paragraph in this subsection). In addition, these fibre diffraction studies made it possible to define the helical rise to 27.5 Å. Although this parameter was assumed to be a constant, studies showed that F-actin has a flexibility in twist (numbers of units per turn) and the given angle should be assumed to be a median value (Egelman and DeRosier, 1991; Egelman et al., 1982; 1983). These general flexibility of actin is still being discussed and analysed with new methods at higher-resolution ranges (Galkin et al., 2012; Oda and Maéda, 2010).

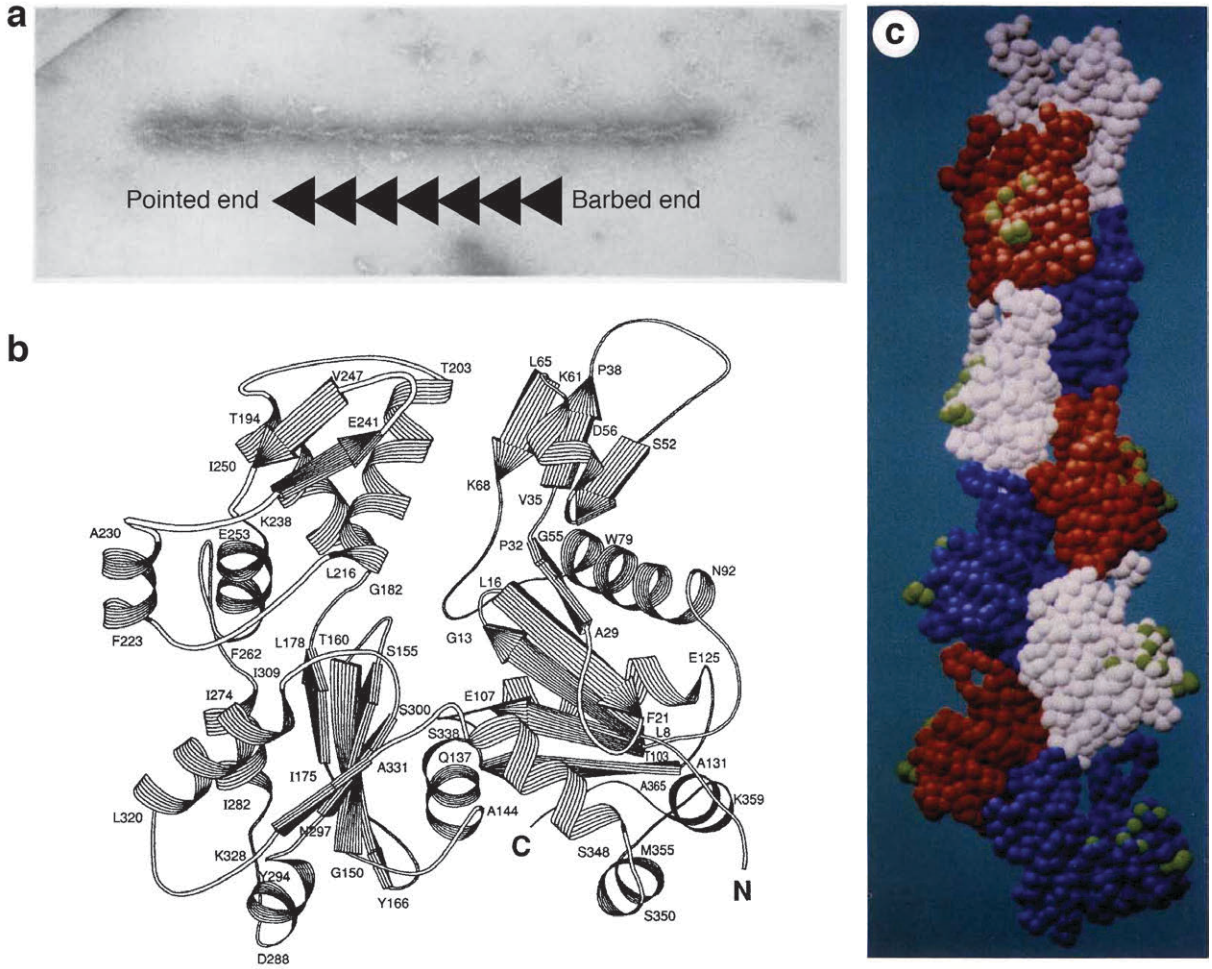

Figure 2.9: First structures of actin.

a, In 1963 Huxley analysed actin filaments decorated with myosin heads with transmission electron microscopy. The arrow-shaped structure was already visible. Reprinted from Huxley (1963) with permission from Elsevier. **b**, It took until 1990 when Kabsch and colleagues solved the crystal structure of G-actin in complex with DNase. Shown is only G-actin. Reprinted by permission from Macmillan Publishers LTD: Kabsch et al. (1990). **c**, In a back-to-back publication the F-actin filament structure could be observed on a higher resolution. But the resolution was not sufficient to observe the conformational change of an F-actin subunit with respect to its G-actin form. Reprinted by permission from Macmillan Publishers LTD: Holmes et al. (1990).

Only three years later after revealing the first structure of G-actin and the model of F-actin, the myosin head region was solved by X-ray crystallography (Rayment et al., 1993b). Myosin was in a post-rigor state with an open actin-binding cleft. Rayment et al. suggested for the first time that this unknown cleft could close when myosin binds to actin and releases its hydrolysis products (see paragraph 'Cross-bridge cycle' in subsection 2.2.1). In the same year new medium-resolution structures of the actomyosin complex were published using transmission electron cryomicroscopy (cryo-EM) on myosin-decorated actin filaments (Rayment et al., 1993a; Schröder et al., 1993). Using the newly determined structures Rayment et al. (1993a) could propose a first model of myosin binding to actin at molecular level. They described the region of prominent motifs and loops of myosin, which bind to F-actin but they could not describe the interface in great detail. A short time before, there had already been equivalently resolved reconstructions of actomyosin, but the authors lacked the information of the crystal structures to interpret their results at the same level (Milligan and Flicker, 1987; Milligan et al., 1990). Besides the myosin rigor state on F-actin, an ADP-bound state to F-actin was obtained showing a slightly different conformation of the lever arm (Jontes et al., 1995; Milligan, 1996; Whittaker et al., 1995). In addition, researchers tried to verify and visualize the proposed cleft closure

and different states of myosin with cryo-EM (Volkmann et al., 2000; 2005). However, the interface of actin and myosin could only be modelled, as these cryo-EM reconstructions were in the range of 15 - 30 Å and no secondary structure elements were visible. Only crystal structures of isolated myosin motor domains could reveal conformational changes of myosin within the reaction cycle with and without bound nucleotides or analogues (Coureux et al., 2004; 2003; Dominguez et al., 1998; Fisher et al., 1995; Gulick et al., 1997; Houdusse et al., 2000; Kollmar et al., 2002). These structures showed for example cleft closure and rearrangements in the nucleotide binding pocket as well as priming of the converter and lever arm. In addition, several G-actin crystal structures were obtained within the next years (Graceffa and Dominguez, 2003; McLaughlin et al., 1993; Morton et al., 2000; Otterbein et al., 2001; Schutt et al., 1993). The D-loop showed the highest variability, being absent in many structures or forming different secondary structural elements. Interestingly, it was assumed that the D-loop could be sensitive to the nucleotide state of actin and therefore play an essential role in filament formation (Orlova and Egelman, 1995; Oztug Durer et al., 2010). But a model of F-actin was needed to address these questions.

Obtaining atomic models of F-actin and actomyosin

As obtaining a high-resolution structure with X-ray crystallography of F-actin was not possible, fibre diffraction was still the method of choice to improve the resolution and quality of the model (Lorenz et al., 1993; Tirion et al., 1995). It took until 2009 when Oda and colleagues could solve F-actin to a reasonable resolution to interpret F-actin on atomic level (Oda et al., 2009). They optimized the gels of F-actin for fibre diffraction by applying a magnetic field to improve the alignment and order of the F-actin filaments, which are diamagnetic. The conformational changes of G- to F-actin (for example the flattening) were firstly described in this contribution and the intra- and interstrand contacts were given on a more detailed level as before. The resolution was improved from 7 – 10 Å (Holmes et al., 1990) up to 3.3 - 5.6 Å (radial and equatorial resolution differs significantly in fibre diffraction).
Cryo-EM was more and more applied on different types of larger proteins, protein complexes and filamentous samples (see section 2.3). This method made it possible to achieve a reasonable resolution (~ 6-7 Å) and to fit crystal structures into the density reliably. Fujii and colleagues presented the first cryo-EM-derived model of F-actin at ~ 7 Å shorty after the previous model of Oda et al. (Fujii et al., 2010). They defined the variable twist of F-actin to $166.6^\circ \pm 0.6^\circ$. The F-actin fibres diffracted up to 3.3 Å and 5.6 Å in radial and equatorial direction, respectively. Although the stated resolutions were different, the overall structure was the same between the fibre diffraction structure and the cryo-EM model. In addition, Fujii et al. used crystal structures of G-actin to restrain their model, which led to a more reliable model (Dominguez and Holmes, 2011). Especially the D-loop region differed, which was directly visible in the Fujii et al. density map. However, both models could only propose the interface of the F-actin subunits on the level of residues.

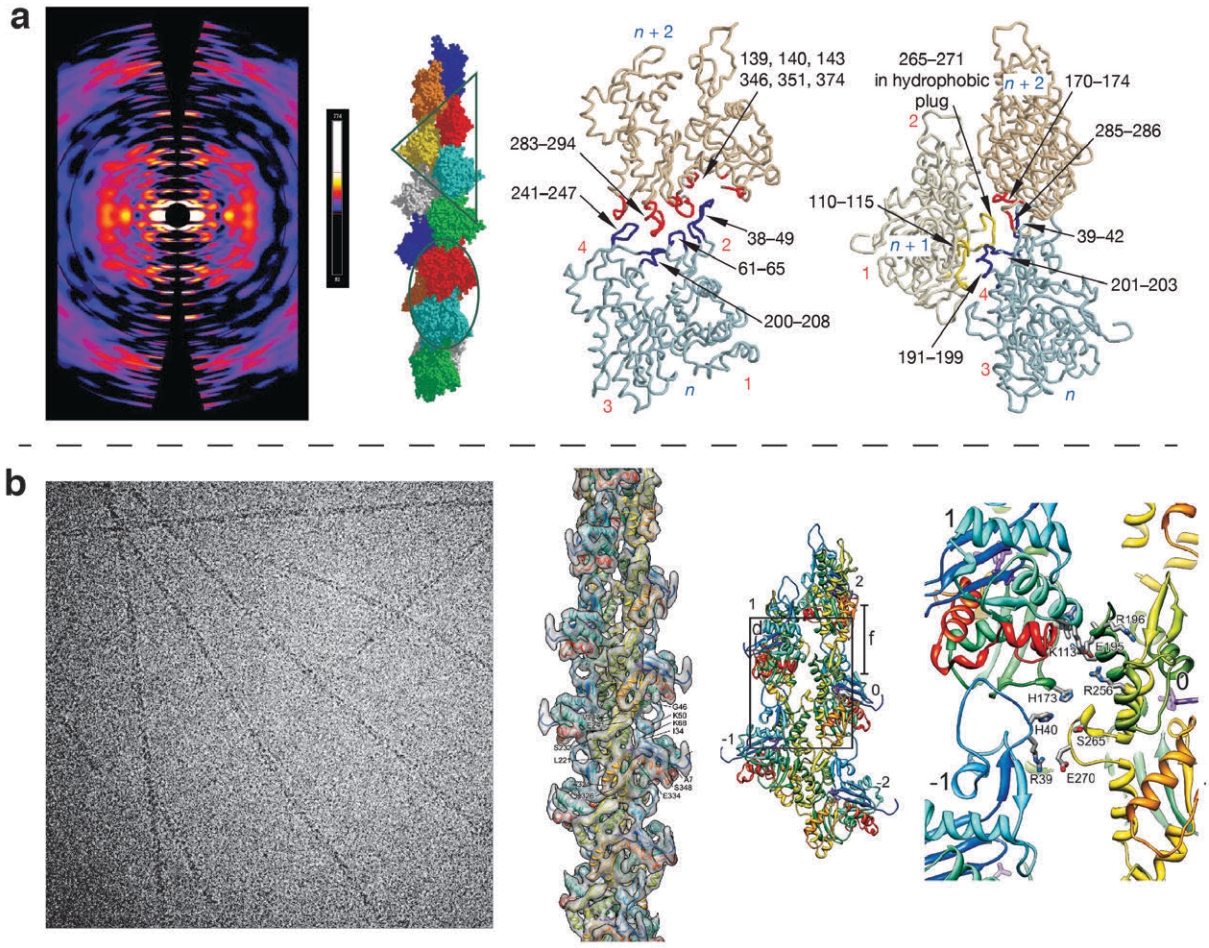

Figure 2.10: Atomic models of F-actin.

Data derived by fibre diffraction (**a**) and cryo-EM (**b**) made it possible to obtain an atomic model of F-actin and describe the interface and the conformational changes of the subunits. Given are examples of the experimental data (diffraction pattern in **a** and transmission image **b**), for the obtained model of the filaments (model surface in **a** and fitted model into the density map in **b**) and for the final interpretation of interfaces of the subunits (intra- and interstrand contacts in **a** and interstrand contacts in **b**). Reprinted by permission from Macmillan Publishers LTD: **a**, Oda et al. (2009) and **b**, Fujii et al. (2010).

The next big goal was to optimize the sample preparation and reconstitution to obtain a whole actomyosin structure by cryo-EM. Then in 2012, Behrmann et al. solved the structure of actomyosin complex by cryo-EM (Behrmann et al., 2012a). The medium resolution was sufficient to accurately fit crystal structures of actin, myosin and tropomyosin in the electron density map (Figure 2.11a). The interface could be described for the first time, while other publications at the same time could only report the models of these interfaces (Lorenz and Holmes, 2010; Volkmann et al., 2005). Behrmann et al. used an optimized sample reconstitution of actomyosin by the well-established proteins of skeletal α1-actin from *Oryctolagus cuniculus* and myosin-IE from *Dictyostelium discoideum*. In addition, the filament was decorated with tropomyosin (α1-tropomyosin from *Mus Musculus*) and thereby the M-state position of the coiled-coil tropomyosin tube was directly revealed. Crystal structures of tropomyosin could be fitted it in the density map. Several studies had already analysed tropomyosin on F-actin with low-resolution methods like negative staining EM (see next paragraph). The transition between a modelled C-state (Li et al., 2011) and the obtained M-state were described as a shift and a rotation on the F-actin filament (Figure 2.11b, c).

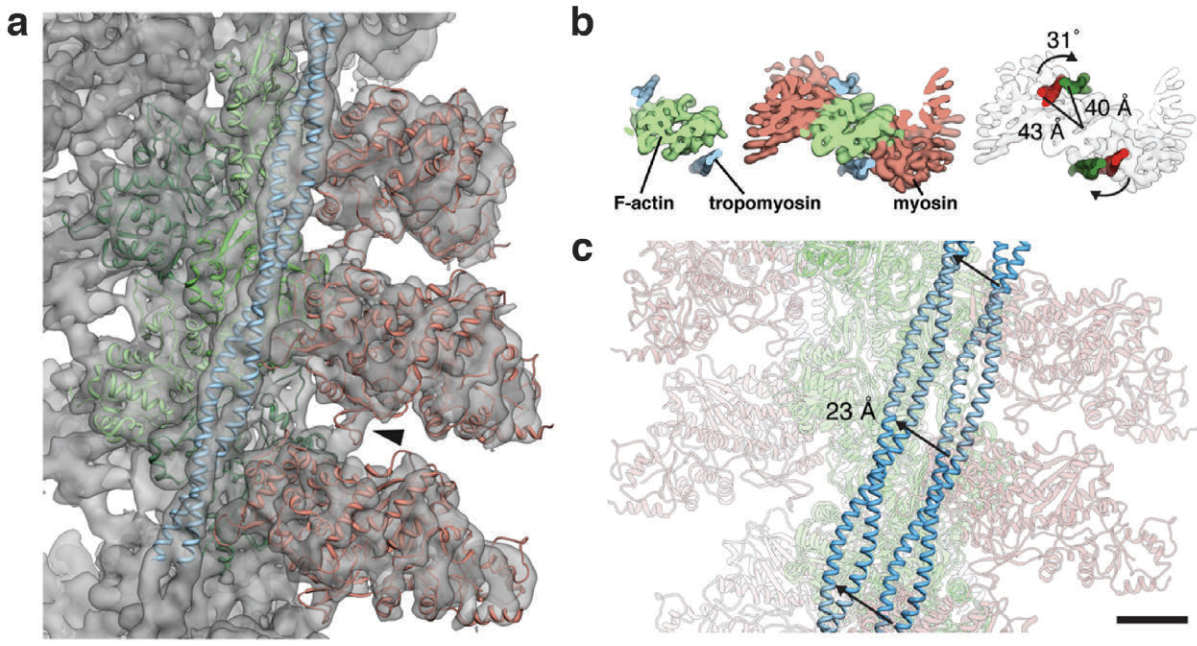

Figure 2.11: Atomic model of actomyosin.

a, Atomic model of rigor state actomyosin (green, red) with tropomyosin (blue) in its density map (grey), which was revealed with cryo-EM at a resolution of 8 Å. **b**, Tropomyosin position differs between a proposed closed state (dark green; Li et al., 2011) and the myosin state (dark red). **c**, The transition between both states is described by a shift of 23 Å and a rotation of 31 ° on the F-actin filament. Reprinted from Behrmann et al. (2012a) with permission from Elsevier.

Structural analysis of tropomyosin

As described before the actomyosin complex of Behrmann et al. (2012a) was also decorated with tropomyosin (Figure 2.11). The structure of tropomyosin alone was solved by X-ray crystallography quite early (Phillips, 1986). Subsequent structures gain insights into higher resolution features (Whitby and Phillips, 2000). Nevertheless, the long coiled-coil structure has a higher flexibility and therefore it is not totally known how much the crystal packing can modify the actual structure. The models show only parts of the tropomyosin molecule (Brown et al., 2001; Li et al., 2002; Rao et al., 2012). Besides that, several models were proposed by using molecular dynamics simulations of tropomyosin in the region of the N and C terminus junction and landscaped its binding to F-actin (Lehman et al., 2013a; Li et al., 2011; Orzechowski et al., 2014b). The tropomyosin models, in particular the tropomyosin position on F-actin, were often obtained by using low-resolution electron microscopy work of F-actin decorated with tropomyosin. Some studies used troponin or other binding-proteins to alter the position of tropomyosin (see paragraph 'Regulation of myosin binding to actin' in subsection 2.2.1; Li et al., 2011; Mun et al., 2014; Orzechowski et al., 2014b; Yang et al., 2014). Recently, a cryo-EM structure of F-actin decorated with tropomyosin described an unknown position between C- and M-state in the absence of troponin and myosin at a reported resolution of ~ 8 Å (Sousa et al., 2013). The question came up how tropomyosin lays on F-actin under physiological conditions and if tropomyosin is only shifting or rolling or if it performs a combination (Rynkiewicz et al., 2015). It is an open question how the position is altered by myosin or troponin. Therefore, high-resolution structures of the different states are needed, which could reveal the mechanism on atomic level.

2.3 Electron microscopy

Electron microscopy is a widely used term for different types of microscopy and it has to be distinguished between 'scanning electron microscopy' (SEM) and 'transmissions electron microscopy' (TEM). As the name suggests in first case, only the surface is scanned, while in the latter one the transmitted electrons are detected which carry information of the entire specimen at higher resolution. In addition, there are applications, which combine both methods in 'scanning transmission electron microscopy' (STEM). The development of electron microscopes goes back to the beginning of the twentieth century, when the first prototype of an EM was invented by Ernst Ruska and Max Knoll in 1931 (Knoll and Ruska, 1932b; 1932a). It was originally termed as 'Elektronen-Übermikroskopie', because it was superior ('Über') in resolution to conventional light microscopy. Finally, Ruska was awarded the Nobel Prize in Physics for the invention of the EM and his achievements in electron optics in 1986 (Robinson, 1986; Ruska, 1987a; 1987b). It was and is primary applied in material science and physics but has its application in structural biology since the nineteen-forties, when Porter and colleagues started to visualize the first biological samples (Geuze, 1999; Harris, 2000; Porter et al., 1945).

Nowadays, TEM is capable to obtain high-resolution three-dimensional (3D) structures of biological samples and has the advantage that the sample is visualized in its physiological environment instead being part of artificial packing as in crystallography. However, X-ray crystallography is the frontier when obtaining molecular models of small proteins at atomic resolution as described in section 2.1. This section deals as an overview of the general setup of a TEM, how the information of the image is derived and how the 3D-structure is reconstructed (subsection 2.3.1 and 2.3.2). Furthermore, it describes how recent developments – especially in the detector system – made it possible to obtain structures at atomic resolution using cryo-EM (subsection 2.3.3).

2.3.1 Transmission electron microscopy on biological samples

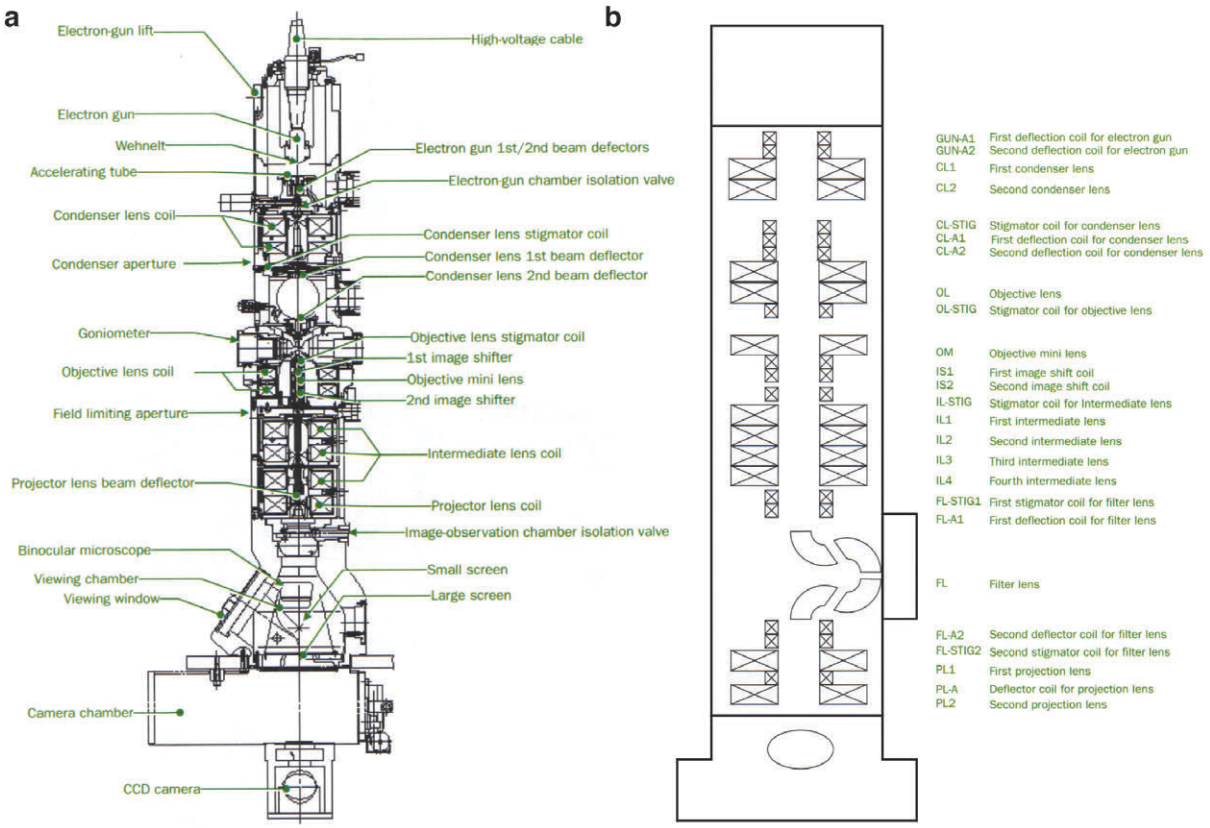

Figure 2.12: Setup of a transmission electron microscope.

Drawing (**a**) and scheme (**b**) of a typical TEM. The electron gun on the top emits electrons, which are accelerated with a high voltage. The (magnetic) lenses and apertures can be divided into the gun, condenser, object and projection system (top to bottom). The sample is inserted between condenser and object system. Microscopes of the new generation have an additional third condenser lens for optimal parallel illumination of the sample (see subsection 2.3.3). The transmission image is finally visualized on a fluorescence screen and recorded on film or on a camera. The images are extracted from the user manual of the JEOL JEM1400 and JEM-3200FSC.

The basic setup of a transmission electron microscope (TEM) is given in Figure 2.12. In principle, the setup is equivalent to a light microscope, while in TEM accelerated electrons are used instead of light. The electron has a charge and a velocity. Thereby, the electron beam can be manipulated either with electrostatic fields (Coulomb force) or magnetic fields (Lorentz force) instead of conventional lenses present in light microscopy (e.g. polished glass lens). However, the lenses do not change the absolute electron energy, as the applied force is always perpendicular to the beam direction.

In electron microscopy different 'electron guns' ('filaments') can be used as an emission source. Examples are tungsten filaments, lanthanum hexaboride (LaB_6) filaments or field emission guns (FEG). They primary differ in their mechanism of electron release and thereby their quality and brightness. The quality can be defined as the coherence of the emitted electrons (ΔE = 1.5-3 eV for LaB_6 down to $\Delta E = \sim 0.2$ eV for a high-brightness XFEG) and the brightness as the quantity of emitted electrons. A high voltage is applied for acceleration of the electrons. In high-resolution TEM for structural biology, the electrons are accelerated with a high voltage of 200 kV or 300 kV. The lens system can be divided into different sections (for example from top to bottom into the gun, the condenser, the objective, the intermediate and the projection lens system) (Reimer and Kohl, 2008; Reimer, 2013). In addition, apertures are present in the condenser and object system. The lenses are coils and the current and thereby the intensity of the magnetic field is tuneable. Furthermore,

different types of coils apply different modification to the electron beam. For examples gun and condenser system have coils for only moving of the electron beam (shifting and tilting). In addition, there are coils for correction of astigmatism (stigmators). The electron beam runs through the central axis of the microscope, which works under high vacuum conditions to prevent any scattering of the beam before and after interacting with the sample. The objective lens defines the central axis by definition and the other lenses have to be aligned relative to it (see section 3.3 in Material and Methods chapter). The actual overall magnification is finally applied in the intermediate and projection lens systems before the projection is detected on a fluorescence screen, on film or on a camera.

Image formation and contrast transfer function

The recorded image is a transmission image (projection) of a three-dimensional object. In comparison to crystallography, where a diffraction pattern (Fourier-space image) is recorded, the projection in EM is a real-space image and carries full amplitude and phase information. Thereby, the image can be taken directly as it is to reconstruct the structure. In crystallography, the unknown phases of the diffraction pattern have to be determined prior to structure determination (Rhodes, 2010).

The grey scale of the image can be understood classically as the intensity of the transmitted electrons through the sample at the respective position. But it has to be considered that when the electron beam hits the sample, the interaction can be either elastic or inelastic. The elastic scattered electrons carry the evaluable information, the inelastic interaction deposits energy and rather contributes to noise. With higher electron energy, the ratio between the probability of inelastic and elastic scattered electrons changes. At 300 kV the probability (to be more precise the cross section) of the event of an elastic scattered event is 10^6 higher than for X-rays. However, the ratio of inelastic to elastic scattering events is in the range of three, which means that with one elastic scattering event three inelastic scattered events come along (numbers are given for carbon; Henderson, 1995). In addition, the ratio of the cross section is worse for light atoms, which are important for biological samples consisting mainly of carbon, oxygen and nitrogen (cross section of inelastic and elastic scattering is proportional to $Z^{4/3}$ and $Z^{1/3}$, respectively (Robenek et al., 1995)). These light atoms suffer mostly from radiation damage and the overall electron dose has to be kept at a minimum. Furthermore, the bending angle is very small and the scattered electrons cannot easily be filtered with an aperture. Therefore, the contrast of an image is not sufficient when only the amplitude contrast derived from filtering scattered electrons is used. The contrast is too weak and a phase contrast is needed in addition.

To describe the phase contrast, the electron has to be considered as a wave transmitting an object, which applies a phase shift to the scattered electrons. Again, only the elastic scattered electrons carry the evaluable information. On the level of the image, the elastic scattered electrons interfere with the not scattered electron beam creating the phase contrast. The phase shift induces amplification, reduction or a shift of the wave, which are dependent on the frequency. A biological sample is a weak phase object with a phase shift of 90° ($\pi/2$) and this results in a minimal change of the amplitude of the superimposed wave. Therefore, in TEM a defocus in the range of micrometres is being usually applied during acquisition, in order to create an additional phase shift (optimal another 90°) by applying a defocus in the range of micrometres during acquisition. The additional phase shift $\chi(q,\Delta z)$ introduces a resulting phase contrast which is described by the 'contrast transfer function' (CTF):

$$CTF = -2\sin\chi(q,\Delta z) = -2\sin\pi(\Delta z\lambda q^2 - \frac{1}{2}C_s\lambda^3 q^4)$$

The CTF depends on the spatial frequency q and the defocus Δz. The microscope specific spherical aberration C_s and the wavelength λ, which only depends on the respective acceleration voltage, are constants. Thus, the contrast of an image at a defined defocus is only frequency-dependent. The image has a frequency-dependent positive or a negative phase contrast and can range from full contrast, over reduced contrast to the total extinction of the contrast at a single frequency. The described pattern is illustrated in Figure 2.13 and is observable in the Fourier-transformation ('power-spectrum', Figure 2.13c) of a real-space image (Figure 2.13b). In TEM the image is recorded with a negative defocus ($\Delta z < 0$). Thereby, the first peak of the CTF is negative and the overall image seems to be black-white inverted. A correction for the CTF has to be applied to compensation for the inverted contrast ('phase flipping') and the reduced amplitude of the contrast ('amplitude correction') of the respective frequencies (Penczek, 2010a). Furthermore, a series of different defocus values has to be recorded to reconstruct the structure with the full information over all frequencies as some frequencies are completely suppressed in a single image (zero-crossings in Figure 2.13c, 'Thon rings'; Thon, 1971).

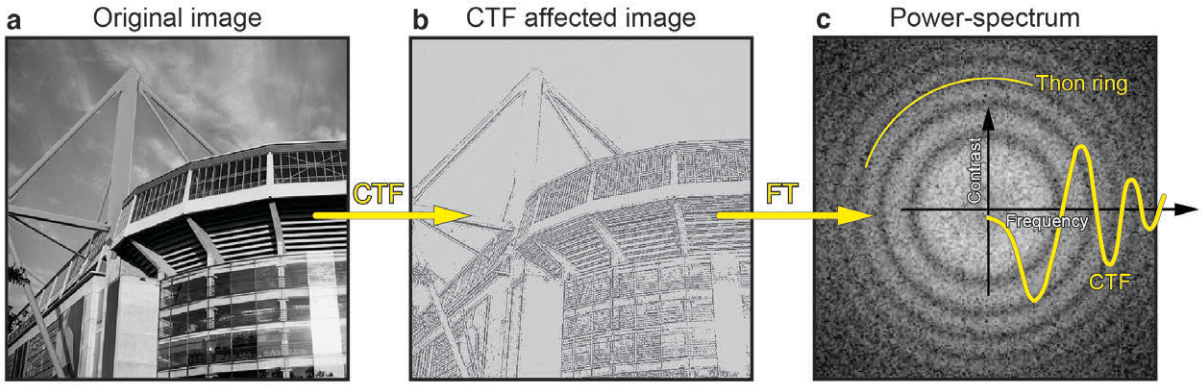

Figure 2.13: The contrast transfer function (CTF).

a, Example for an unmodified image (photo; Bigge, 2002). **b**, In TEM the recorded image is affected by the CTF. However, the image is a real-space image (photo CTF-modified). **c**, The modulation of the frequency spectrum by the CTF can be identified by a Fourier-transformation (FT) of the image to its power-spectrum. The CTF is rotational symmetric. A rotational average of the two-dimensional power-spectrum is a sinusoidal oscillation and can be used to estimate the CTF from the experimental data. No information is present at the respective frequency of a zero-crossing ('Thon ring'; Thon, 1971). Therefore, a series of different defocus values has to be recorded to compensate for the missing information. The image in **c** is an example of a typical power-spectrum from a real TEM image and is not derived from the CTF-modified photo of **b**.

Since the lens systems of a microscope are not working perfectly (aberrations; fluctuation of the lens current) and the electrons have a limited coherence (quality of the electron gun; microscope alignment and nonparallel illumination), the frequencies are damped at higher frequencies. This characteristic is added to the CTF by a Gaussian envelope function. The function decreases faster for higher defocus values. In conclusion, an image at stronger defocus has a higher contrast but suffers from decreased high-resolution information. Thereby, the maximal achievable resolution depends on the imaging conditions and the applied defocus. Furthermore, a significant level of noise is present, which arises at the sample (inelastic scattered electrons) and at the detector (false pixel signals; back-scattered electrons; see also subsection 2.3.3). In addition, the detector system itself has a frequency-dependent sensibility, which later can be corrected ('modulation transfer function (MTF)' correction) by increasing the respective frequencies. A more comprehensive description of the image formation and the CTF is given in several specialised literatures (Frank, 1973; 1996; Penczek, 2010b; 2010a; Reimer and Kohl, 2008).

Sample preparation of a protein sample

In comparison to crystallography, the prepared sample is in its physiological environment (dissolved in a buffer solution) and does not have to be arranged in a higher order like a crystal lattice. Furthermore, it is possible to directly visualize conformational changes induced by for example different buffer conditions (pH, ionic strength, nucleotide) for which diffracting crystals cannot be obtained. In particular, larger and more flexible proteins (or protein complexes and filaments) are difficult to crystallize or it is technically not possible to obtain a crystal of them. The EM experiment can be understood as a measurement of a single object (particle). Only in the further computational analysis, the information of thousands of particles is merged and averaged to recover the fully structural information. However, the sample has to be either dried or frozen, as the specimen is transferred into the microscope under vacuum. Otherwise it would directly vaporise the liquid.
As described before in this subsection, the light atoms of a biological sample hamper the observed contrast. Therefore, it is possible to embed the protein in heavy metal-containing solution before the actual drying process (see subsection 3.2.1 in Material and Methods chapter). Heavy atoms induce a much higher amplitude contrast because of the higher probability for elastic scattering (Henderson, 1995). Therefore, in this case the protein itself is not directly visualized and it is an indirect measurement of its shape, instead. The result is a negative image of the structure ('negative staining'), in which the protein appears white, while the heavy metal shell is dark (Booth et al., 2011; Ohi et al., 2004). Moreover, the staining solution can prevent distortions of the object and falling apart during drying. This preparation method can only obtain a low-resolution reconstruction, because the grain size and the flattening, especially for larger or hollow structures, limit the contrast. Furthermore, the heavy metal solution cannot permeate the sample and the recorded projection represents only the overall shape of the surface.
As the preparation with negative staining does not allow a high-resolution projection of the biological sample, a more technically demanding method is required (see also subsection 3.2.2 in Material and Methods chapter). For the first time Dubochet and colleagues used rapid freezing to vitrify the sample and to fix the sample in low-density amorphous ice some decades ago (Dubochet and McDowall, 1981; Dubochet et al., 1988; Nogales and Scheres, 2015). The freezing process requires a very cold medium (e.g. liquid ethane) and takes less than a millisecond for a thin ice layer of ~100 nm. The freezing temperature has to be in the range of at least – 160 ° C to – 170 ° C. A slower freezing results in crystal formation, which makes a further analysis impossible or can even destroy the sample. If after vitrification the temperature raises up to – 140 ° C (devitrification point) the ice would start to crystalize, too. It has to be considered that the pure amplitude contrast is very low in comparison to the negative staining approach. Therefore, the phase contrast is essential for creating a sufficient contrast. The main advantage is that with this approach the high-resolution information and the three-dimensional structure are preserved. Nevertheless, the overall low contrast (especially for smaller proteins) and dose-sensitivity of the biological object limit the achievable resolution.

Theoretical resolution limit

The applied voltages of 200 - 300 kV generate electrons of a wavelength of 0.02 Å to 0.03 Å. The theoretically achievable resolution would be at least in the same region ('Abbe law'; Reimer and Kohl, 2008). However, the resolution is limited by insufficient magnet lenses and image aberrations of the microscope as described before. Beside that, sample movement during exposure, beam induced damage of the sample, incoherent electron beam and the pixel size ('apix', Angstroms per pixel) hamper the

finally achievable resolution. The pixel size at the respective magnification defines the maximal achievable resolution by the sampling theorem and is given by the 'Nyquist frequency' ($f_{\text{nyquist}}^{-1} = 2 \times$ apix). Studies state the theoretically achievable resolution in the range of 1 - 2 Å by taking into account the movement of water molecules, the applied dose and the possible accuracy of the image alignment (Grant and Grigorieff, 2015; Henderson, 1995; McMullan et al., 2015).

2.3.2 Single particle and helical reconstruction

As described above, the actual experimental data are 2D-projections of a 3D-object (single particle or filament, Figure 2.14). The aim is to recover the 3D-information by reconstructing a density map from the projection images. For that purpose, the unknown projection parameters (shifts and angles) per particle have to be estimated. When the parameters are determined, the 3D-structure can be reconstructed from the 2D-projection images (see below in this subsection). For that purpose, up to hundreds of thousands of single particles of different views are needed and averaged to compensate the low signal to noise ratio. The actual reconstruction method is equivalent to the approach used in tomography and is described at the end of this subsection.
Figure 2.14 illustrates an example of a protein sample (single particles) in a thin layer of vitrified ice. Each particle is oriented randomly. Thereby, each recorded single projection of one particle describes the same 3D-object from a different view. All views have to be combined to reconstruct the original structure.

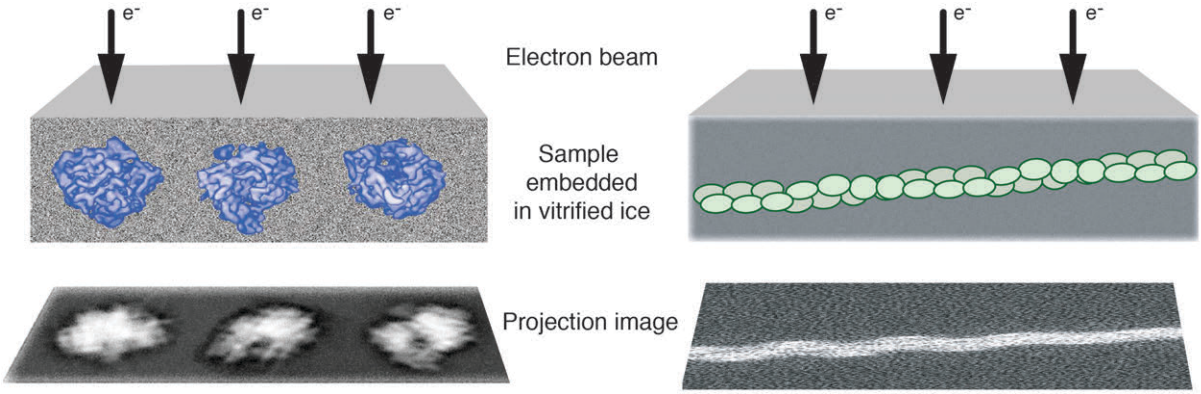

Figure 2.14: Projection image of vitrified samples.

A 3D-object (left: single particle; right: filamentous sample) is embedded and fixed in vitrified ice. The structure is projected to 2D, but the respective projection angles are unknown and have to be estimated to perform a 3D-reconstruction. Left subfigure modified from Frank (2002) and adapted in right subfigure for a filamentous samples.

The methods derived for 'Single Particle Reconstruction' (SPR) can be adapted to determine and refine the projection parameters of a filamentous object (Egelman, 2000; 2010; 2015). For that purpose, the filament is split into single segments, which afterwards can be treated as single particles. Former approaches used a Fourier-Bessel formalism and diffraction pattern from the 2D-projection of a complete filament to reconstruct the 3D-density map (De Rosier and Klug, 1968; Klug and De Rosier, 1966; Klug et al., 1958). These approaches were limited by the requirement of a high-contrast image (for example negatively stained samples) and optimal samples conditions (straight, long, rigid filaments). In order to obtain a high-resolution reconstruction from more flexible filaments, these approaches are not suitable. A more appropriate SPR-adapting approach is called 'Iterative Helical Real Space Refinement (IHRSR)' (Behrmann et al., 2012b; Egelman, 2007).

Besides this single particle approach, the helical symmetry is used for the refinement. The helical symmetry is defined by the axial rise Δz and the azimuthal rotation angle Δϕ between to adjacent asymmetric subunits (Figure 2.15a). As mentioned above, the filament is split into segments for further processing. As the projection angles are unknown, the shifts and angles have to be determined to describe the respective projection view of each segment. On the one hand the centering parameters (x- and y-shifts) and on the other hand the three Euler angles (θ, ϕ, Ψ) have to be iteratively refined (see also section 3.4 in Material and Methods chapter). The out-of-plane angle θ, the projection angle ϕ and the in-plane-rotation angle Ψ define the orientation of the projected segment (Figure 2.15b). In the case of filaments some restrictions can be assumed in comparison to SPR, where no *a priori* information of the angles and shifts are available since each particle is randomly oriented. For example, the filament lies roughly perpendicular to the incident electron beam (limited out-of-plane angle) and the segments of the same filament cannot point in different direction and share thereby a similar in-plane-rotation angle. In principle, the information of the symmetry of the filament should be usable to constrain all projection parameters (shifts and angles) of the segments within the same filament. So far, these constraints based on the helical symmetry are not implemented in the respective programs.

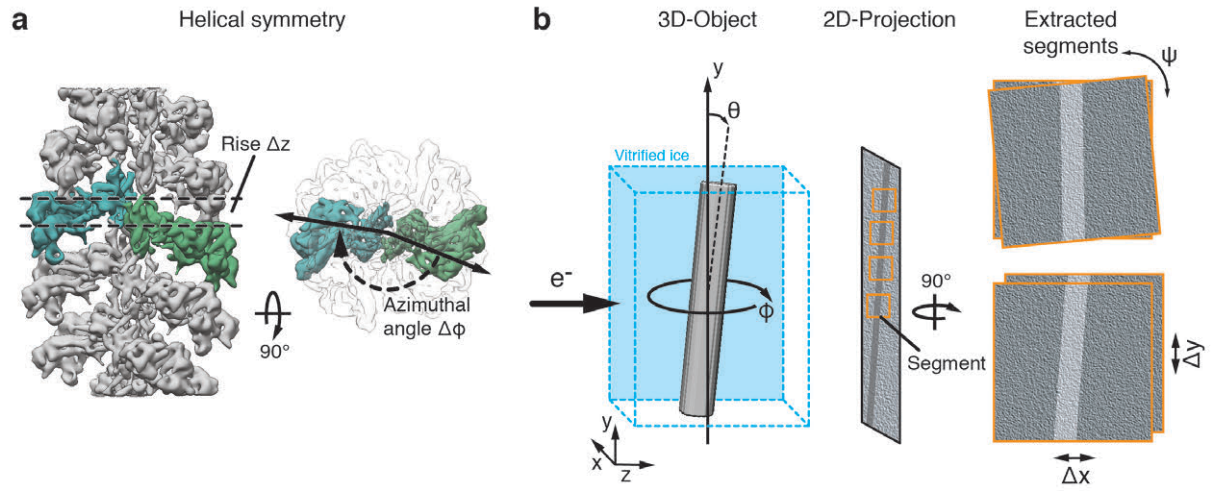

Figure 2.15: Projection parameters and helical symmetry.

a, The symmetry of the particle can be applied during processing. In the case of a filament the symmetry is defined by the rise Δz and the azimuthal rotation angle Δϕ between two adjacent asymmetric subunits (highlighted in tones of green). **b**, In TEM the 3D-object (cylinder as a simplified filament) is embedded in a thin layer of vitrified ice (blue box). The structure is projected to 2D. The filament is extracted and split into single particles (segments) for further processing. The projection parameters (angles and shifts) are unknown and have to be estimated to perform the reconstruction. The filament can be tilted by an out-of-plane angle θ in the y-z plane. In addition, the projection angle ϕ in the x-z-plane and the in-plane-rotation angle Ψ in the x-y-plane are needed. Furthermore, the segments have to be centred in x- and y-direction.

To determine the projection parameters, these assumptions can reduce the space of freedom during 3D-refinement. In Figure 2.16 the general refinement and reconstruction method is shown. Several reference projections are calculated from a reference density map. Subsequently, each segment (in the case of SPR a particle) is compared with and aligned to the reference projections and the respective angles are assigned ('projection matching'). Projection parameters (shifts and angles) are needed for the actual 3D-reconstruction. The subsequent reconstruction method is based on the projection-slice theorem and goes back onto the Randon-transformation (Frank, 2002; Penczek, 2010b; Radon, 1917). The theorem states that a Fourier-transformation of each 2D-projection of a 3D-object describes a single plane (central slice) in Fourier-space of the original 3D-object. Thereby, the Fourier-space can be filled by projections from different views and the 3D-object can be calculated by an inverse Fourier-

transformation (Figure 2.16). Another approach for reconstruction is to back-project the 2D-image to 3D and thereby recover the 3D-density information. Both principles are widely established in other experiments for deriving a reconstruction like in tomography. The advantage in tomography is that the projection parameters are known *a priori*, as the specimen is fixed and each projection image is taken with defined projection angles (McIntosh et al., 2005; Murphy and Jensen, 2007). But tomography is not suitable for a high-resolution reconstruction as the sample gets exposured several times and, as described in the subsection before, the biological sample is sensitive to the overall applied dose. Therefore, only one projection image is recorded per particle in SPR to obtain a high-resolution structure. Moreover, the low signal-to-noise ratio hampers the accuracy of the refinement. Thereby, the assignment of the projection parameters is very challenging. Previously, assigning one set of projection parameters to one particle was widely established. For that purpose, the maximal cross-correlation of a particle to a reference projection was determined. With the growth of computational power, now is possible possible to apply more elaborated methods. It has been shown that applying a probability distribution of projection parameters can perform much better. For that purpose a maximum-likelihood approach ('Bayesian' approach) was introduced, in which each particle is used with a weighted set of projection parameters for the reconstruction (Scheres et al., 2005; Sigworth, 1998; Sigworth et al., 2010; Yin et al., 2003). In theory, both approaches should finally converge in a single set of parameters for each particle, but the iteratively refinement itself is more stable and less prone to misalignments in the case of using a probability distribution of parameters (Scheres and Chen, 2012).

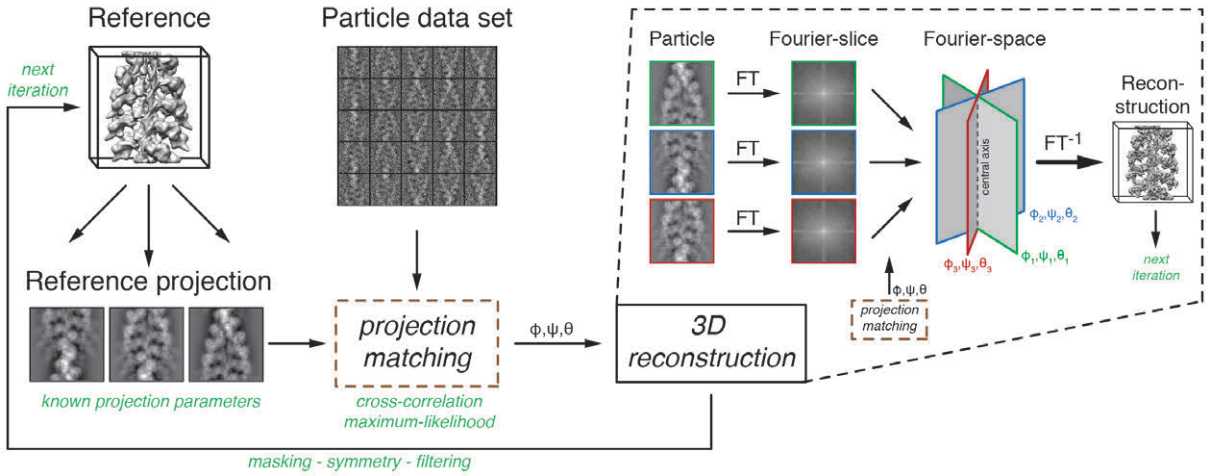

Figure 2.16: Refinement and reconstruction.

From the current 3D-density map several 2D-reference projection are created. In the next step, each segment (particle) is matched and centred (x- and y-direction) to one reference projection and the known projection parameters are assigned to the particle. In the case of a maximum-likelihood approach, not a single (highest cross-correlation) but rather a weighted probability distribution of a set of projection parameters is assigned. Afterwards, the 3D-reconstruction is performed and further used in the next iteration of refinement. The 3D-reconstruction is an inverse Fourier-transformation (FT^{-1}) of the filled Fourier-space. A Fourier-transformation (FT) of each projection image (particle) describes a central slice in Fourier-space of the original 3D-structure and the determined projection parameters (θ_i, ϕ_i, Ψ_i) define the orientation of the slice.

In addition, a splitting of the particles of the data set into two parts has been established and is named 'golden standard approach'. The refinement can be further improved regarding error-proneness by performing the alignment of both halves independently and interpret the reconstruction only up to a certain level, where both reconstructions have a significant agreement (see resolution estimation in subsection 3.4.6; Chen et al., 2013; Scheres and Chen, 2012).

When comparing SPR in TEM with crystallography one major advantage, besides having the sample in its native environment is that it is possible to digitally purify the data. Thereby, samples, which do not crystallize due to heterogeneity or due to a higher degree of flexibility, can be still processed and a structure can be obtained. A digital purification is performed by different classification approaches, in which the single particles can be sorted regarding to their state or conformation (Bai et al., 2015b; Ohi et al., 2004; Penczek et al., 2011; Scheres, 2010; Yang et al., 2012). When these differences are on the level of single domains or even in the range of the size of secondary structure element, a high-resolution structure and data with optimal information (for example a high signal-to-noise ratio) are required to distinguish these differences, which has been made possible recently (see next subsection).

2.3.3 Recent developments in TEM: "resolution revolution"

Single particle cryo-EM has underwent a significant change in the last years. In the past, it was sometimes disparagely called 'blob-ology' since EM was limited to low resolutions in the nanometre range and the published structures looked like a blob in comparison to X-ray crystallography (Cheng, 2015; Gebel Berg, 2015; Zhu and Zhu, 2015). In the end of 2015, *Nature Methods* proclaimed "The end of 'blob-ology': single-particle cryo-electron microscopy (cryo-EM) is now being used to solve macromolecular structures at high-resolution". At the same time, it was designated as the 'Method of the year' by *Nature Methods* (Doerr, 2016; Editorial by Nature Methods, 2016; Eisenstein, 2016; Glaeser, 2016; Nogales, 2016).

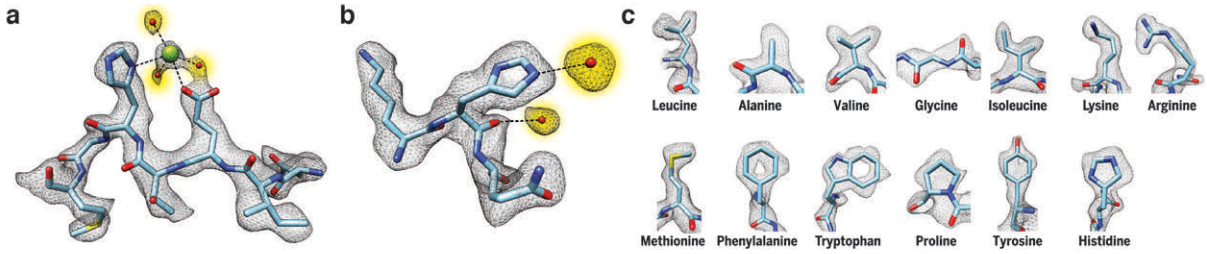

Figure 2.17: Cryo-EM structures at atomic resolution.

a, **b**, Two examples of densities out of a 2.2 Å density map derived from cryo-EM. Bound water molecules and ions (highlighted in yellow) can be identified. **c**, Similar residues can be directly distinguished in the shape of the density map. Subfigures are from Bartesaghi et al. (2015). Reprinted with permission from AAAS.

At the same time in 2014, Werner Kühlbrand heralded the start of a 'new era' of cryo-EM by the so-called 'resolution revolution' (Kühlbrandt, 2014a; 2014b). He reviewed different high-resolution structures revealed by cryo-EM, which were published starting in 2013, showing the advantages of new hardware and improved computational methods for the first time (Allegretti et al., 2014; Amunts et al., 2014; Li et al., 2013a; Liao et al., 2013; Scheres, 2014). So far, the highest resolved structures revealed by cryo-EM were published by the group of Sriram Subramaniam at a resolution up to 2.2 Å (Bartesaghi et al., 2015) and 1.8 Å (Merk et al., 2016). The EM density maps allow directly differentiating between similar amino acids (e.g. Valine and Isoleucine; Phenylalanine and Tyrosine; Lysine and Arginine) and show bound water molecules (Figure 2.17). In addition, Merk et al. could break the 4 Å-barrier for a protein of a size smaller than 100 kDa.

This subsection gives a brief overview of the fundamental developments of the last years making this large progress possible. On the one hand, there was the next generation of cameras and ultra-stable, automated TEMs and on the other hand further software development. At the moment, there are

several reviews published giving a more or less comprehensive overview on these developments (Bai et al., 2015a; Callaway, 2015; Cheng, 2015; Egelman, 2016; Frank, 2015; Nogales and Scheres, 2015; Schröder, 2015; Subramaniam et al., 2016). In addition, Danev and Baumeister recently made a breakthough in using a phase-plate for data collection (Danev and Baumeister, 2016; Khoshouei et al., 2016). This could the next step to 'break the crystal ceiling' even for smaller proteins (Gebel Berg, 2015).

Development of the direct detection camera

Originally, TEM images were recorded on film and afterwards digitized by a scanner. The images had an excellent spatial resolution, which was not limited by the pixel size. It was rather limited by the movement of the specimen during exposure (e.g. beam-induced drift as a result of charging, instable specimen support and movement of the stage of the microscope), the applied dose to get a reasonable contrast and the big effort, which had to be made for the data collection. The 'readout' of one hundred images (recording, developing and scanning) was in the range of two days, while the actual exposure time was just a second. Nevertheless, already with this recording method it was possible to obtain a high-resolution structure with an optimal specimen, best microscopy setup and a substantial personal effort (Jiang et al., 2008; Zhang et al., 2008; 2010; Zhou, 2011; Zhou and Chiu, 2003).

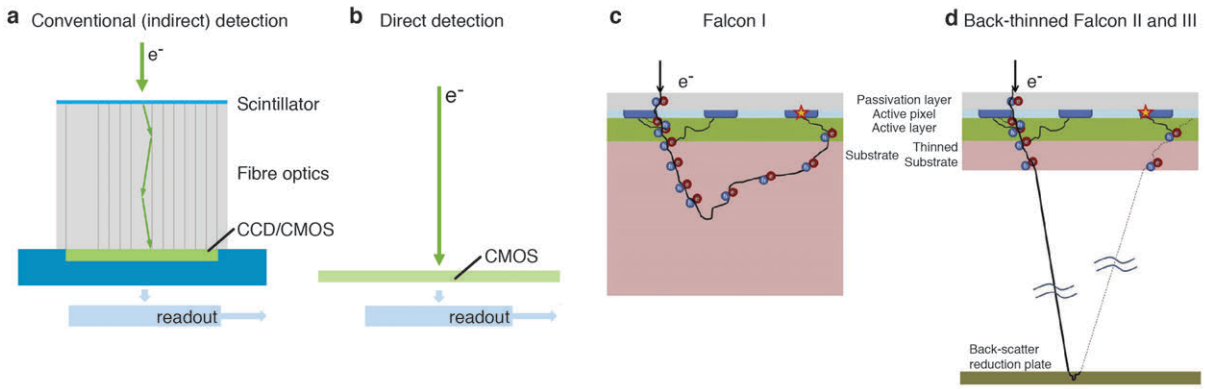

Figure 2.18: Layout of different types of cameras.

The first two panels show the general scheme of a conventional camera (**a**) and a direct detection camera (**b**) (modified from www.gatan.com; Gatan Inc.). The conversion from an electron (e^-) into a photon is spreading the dot-like incidental information (**a**) and back-scattered electron trajectories can induce a displaced signal in addition (**c**). **d**, 'Back-thinning' of the detector substrate significantly reduces these events of back-scattering events and the subsequent wrong signal. The example shows the development from the Falcon I (**c**) to the Falcon II and III (**d**). Reprinted from (Kuijper et al., 2015) with permission from Elsevier.

The film recording was almost replaced by digital cameras (CCD and later CMOS chip) one decade ago. The main advantage was to digitalize an image on a computer at the microscope directly, which could be checked by the user, and in addition a much faster time for recording of the actual data set. Nevertheless, the quality of the image itself was in the same range or worse than of those derived from film. However, in comparison to film the spreading of the incoming, dot-like information (incident electrons) in an image recorded with a camera is quite high. This is because of the transformation of the electron into photons by a scintillator and the fibre optics before the actual detection on the chip ('indirect detection'). Furthermore, the recording time was still in the range of a second to receive enough contrast for image analysis and the resolution was limited by blurring effects due to movements as mentioned before.

At that time, different institutes and companies (see Kühlbrandt, 2014a) started to overcome these problems by trying to invent a camera which can directly detect the incoming electrons without

transformation to photons ('direct detection') and which has a much faster readout time. It took more than ten years before first prototypes were tested (Deptuch et al., 2007; Faruqi et al., 2003; Kühlbrandt, 2014a; Milazzo et al., 2005). Right now, there are three companies, which provide commercially available direct detection cameras: the 'Falcon II' from FEI (Hillsboro, Oregon; 'Falcon III' will be available soon), the 'K2' from Gatan Inc. (Pleasanton, California) and the 'DE-Series' from Direct Electron (San Diego, California). The general setup of a direct detection camera in comparison to a conventional camera is given in Figure 2.18. A more comprehensive overview of all camera specifications and performance are available online or in respective publications (Kuijper et al., 2015; Li et al., 2013b; McMullan et al., 2014; Ruskin et al., 2013).

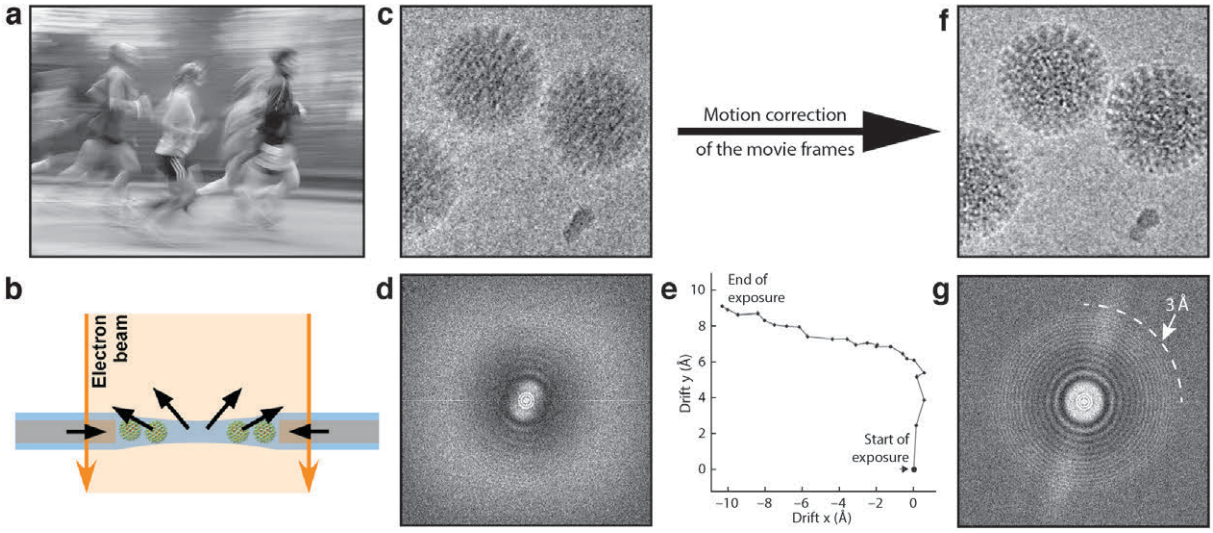

Figure 2.19: Motion correction of movie frames.

a, In all types of image recording, a moving object during exposure leads to a blurring of the information, which can be wanted, as in the given photo (Courtesy to R. Steyernagel; Steyernagel, 2013). **b**, In EM, the applied electron beam leads to beam-induced drift and instable stages to mechanical movement, which results in a blurred image of the specimen (**c**). **d**, Thereby, the power-spectrum - especially at high-resolution - is distorted. **e**, As nowadays a set of single frames instead of an integrated image is recorded, methods can be applied to correct for the drift (see Movie alignment in subsection 3.4.4). Finally, the image is restored (**f**) and the high-resolution information can be recovered (**g**). Subfigures are combined from Brilot et al. (2012, reprinted with permission from Elsevier) in **b**, **c**, **f** and Li et al. (2013a, reprinted by permission from Macmillan Publishers Ltd: Nature Methods) in **d**, **e**, **g**.

Not only the improved signal-to-noise ratio and spatial resolution but also the much higher readout time makes direct detection cameras superior to conventional cameras (Falcon II: 17 readout frames per second (fps); K2: 40 fps; DE-20: 32 fps). The advantage is that instead of recording a single image integrated over the exposure time, a so-called 'movie' is recorded consisting of several single 'movie-frames'. The K2 and die Falcon II differ at the point of exposure time significantly. While the chip of the K2 is very sensitive to a high dose and thereby the overall and single frame exposure time is long (several seconds), the Falcon II works at much higher doses and records in a shorter time (one to two seconds). These movie frames can be used and aligned to reduce drift and motion of the specimen due to the applied beam or the instability of the specimen stage during image recording (see Figure 2.19 and paragraph Movie alignment in subsection 3.4.4). Blurring of the image can be removed with this motion correction and high-resolution information is recovered. Furthermore, it is possible to weight each frame regarding its already incorporated dose. Thereby, the loss of high-resolution information by the dose-dependent radiation damage (e.g. disruption of side-chains, ice-blurring) of the protein sample is reduced, while still low-resolution information (important for the alignment) is preserved (see also subsection 3.4.4).

Several studies tried to quantify and to compare the different detectors and their settings (Grob et al., 2013; Kuijper et al., 2015; Li et al., 2013b; McMullan et al., 2014; Ruskin et al., 2013). The so-called detector 'Quantum efficiency coefficient' (DQE) describes the fraction of detected to incidental information regarding to the spatial frequency. This statistical value is often applied to compare different detectors. However, all quantifications so far were not made with the exact same setup, especially when comparing different types of direct detection cameras. Therefore, the graphs in respective publications have to be taken with caution and can only be used for a general interpretation (one example is given in Figure 2.20). One major difference between the K2 and the Falcon II is that the K2 has a significantly higher DQE at low frequency, while the Falcon II has a better DQE at high frequencies. It seems so that both camera types are the leading edge of detector development and that the K2 produces slightly better results for smaller proteins due to the higher DQE at low resolution, which is mainly important for the alignment.

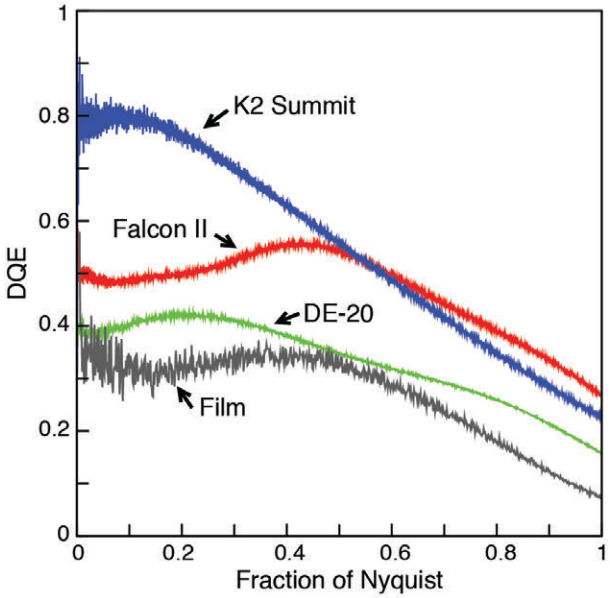

Figure 2.20: DQE of different detectors.

The Quantum efficiency coefficient (DQE) describes the fraction of detected to incidental signal. The experimental data curves show the respective DQE curve of different detectors. The absolute values have to be taken with caution, as all quantifications were performed under different setups. However, all direct detection cameras perform as good or even better than film over the whole frequency spectrum. The K2 shows a significantly higher DQE at low frequencies, while the Falcon II has a slightly better performance at high frequencies. Figure is taken from McMullan et al. (2014).

It has to be considered that the K2 camera is often used with an energy filter (GIF Quantum Energy Filter, Gatan Inc.) or in a 'super-resolution mode', where the pixel size is computational doubled. Thereby, the shown results for the DQE can change in addition. Taking all together, the new camera technologies make it possible to introduce the term of 'electron counting' instead of 'integration' about several detected electrons per pixel. If the readout is fast enough, false events - for example noise - can be discarded and thereby the signal-to-noise ratio significantly enhanced.

Improvements of the setup of TEM data acquisition

The general setup and operation of an EM have not changed. The major improvements are the overall performance (automation of transfer and data collection; stability and running time), the coherence and brightness of the electron beam (high-brightness field emission guns, XFEG), the illumination system (third condenser lens for a parallel illumination and coma-free alignment, ConstantPower™ lenses) and the possibility to correct for the spherical aberration (Cs corrector). FEI is right now the leading company in life science electron microscopy, which provides high-end microscopes for high-resolution cryo-EM. The FEI Titan Krios incorporates all improvements and elements mentioned above. In 2016 over one hundred Titan Krios have been sold and built up around the world. There is not only a technical development, but also improvements in computational power and algorithms as described in the next paragraph.

Software development

Software development was a major part in the resolution revolution. While in the past almost only specialized users were performing cryo-EM reconstructions, there were a clear need for a professional and easy-to-use package. Several software packages can produce high-resolution structures but most of the programs lack a proper interface and documentation. The first software package providing this essential need to the community was 'Relion' (Scheres, 2012). Most of the implemented tools were already published before (Scheres et al., 2005; 2009) and incorporated in 'Xmipp' (Scheres et al., 2008). Programs like 'Sparx' (Hohn et al., 2007) or 'Frealign' (Grigorieff, 2007) were capable to produce a high-resolution structure at the same time, but they were mainly based on command-lines and self-made scripts, were hard to install and no established workflow was described in detail.
Besides providing a GUI, one core requirement is to produce reliable, reproducible and not over-refined structures. Therefore, internal validation are performed and the refinement protocol is less prone to errors. Currently, the 'maximum-likelihood' approach and the 'golden standard' refinement strategy prevent overfitting (see subsection 2.3.2; Scheres and Chen, 2012).
Future requirements will be the automation of the 2D- and 3D-refinement and classifications, improvement in computational power and time (e.g. acceleration through usage of graphics processing units (GPUs) instead of central processing units (CPUs)). Recently, first results were presented using a new version of Relion (version 2.0, unpublished), in which some parts of the software package were accelerated by GPU implementation (Kimanius et al., 2016). Another point will be the automation of the actual model building and improvement of the interface to the refinement of the 3D-reconstruction. It will take some years until the determination of high-resolution cryo-EM structures is on the same highly automated level as X-ray crystallography.

2.4 Aim of this work

The goal of my thesis was to obtain high-resolution structures of a F-actin-tropomyosin complex and a physiological human actomyosin complex with cryo-EM. At the beginning of my doctoral thesis there was neither a high-resolution structure of bare F-actin nor atomic structures of F-actin in complex with tropomyosin or myosin. This hampered our understanding of the interaction and disease-causing mutations of the components of the complexes in atomic detail. Only maps at medium-resolution of entire complexes and high-resolution X-ray structures of the individual components existed. To perform my experiments using TEM, I was supplied with different isoforms of actin, myosin and tropomyosin from different species. All proteins were purified at the Medical School in Hannover in the group of Prof. Dr. Manstein.

My first task was to reconstitute suitable protein complexes and test the conditions by negative stain EM and later on find the best conditions for the vitrification process. Once the best conditions for the preparation were found, I was supposed to record data sets on a high-end electron microscope equipped with a direct detection camera to obtain a high-resolution structure of the complexes. The second part was to develop a new protocol to prepare and to process the obtained EM data. In addition, in collaboration with Prof. Dr. Penczek from the University of Texas another task was to improve the method of processing a filamentous protein sample by performing a constrained search for the projection parameters during refinement using helical symmetry. There was no software package available for that purpose. Then, the workflow should be applied on the data sets. Finally, the aim was to use the EM density maps to build and derive the atomic model of the respective complex and perform the analyses of the structures.

3 Material and Methods

3.1 Protein purification

Different isoforms of F-actin, myosin and tropomyosin were used and screened during the time of my doctoral thesis. Only the finally applied samples are described and listed in Table 3.1. Prof. Dr. Dietmar Manstein and his group from the Institute for Biophysical Chemistry at the Hannover Medical School (MHH) provided all purified protein samples.

3.1.1 Protein samples

	Protein name	Gene	Organism	Tissue	Expressing system	Purified at
Actin	α1-actin	*ACTA1*	*Oryctolagus cuniculus*	skeletal	natively purified	MHH & MPI
Actin	γ1-actin	*ACTG1*	*Homo sapiens*	cytoplasmic	Baculovirus/Sf9-cell	MHH & MPI
Myosin	myosin-IIC	*MYH14*	*Homo sapiens*	cytoplasmic	Baculovirus/Sf9-cell	MHH
Tropomyosin	α1-tropomyosin	*TPM1*	*Mus musculus*	skeletal	Escherichia coli	MHH
Tropomyosin	α3-tropomyosin	*TPM3.1*	*Homo sapiens*	cytoplasmic	Escherichia coli	MHH

Table 3.1: Provided protein samples from F-actin, myosin and tropomyosin isoforms.

All data in this thesis are obtained from the proteins samples listed above. The F-actin-tropomyosin and the F-actin-myosin-tropomyosin complex are composed of α-actin and α1-tropomyosin (white background) or γ-actin, myosin-IIC and α3-tropomyosin (grey background), respectively. All samples were purified at the MHH. The final steps of protein purification of the actin samples were performed at the MPI.

Other isoforms of actin (human cytoplasmic β- and cardiac actin), myosin (myosin-II from *Dictyostelium discoideum*) and tropomyosin (α3-tropomyosin isoform 2) were screened but finally not used for the complex formation.

Actin

Skeletal α-actin (*ACTA1*, Uniprot-ID P68135, α1-actin from *Oryctolagus cuniculus*) was natively purified from rabbit muscle. The purification was performed at the MHH based on the protocol of Pardee and Spudich (Pardee and Spudich, 1982). Fresh skeletal rabbit muscle dealt as the natural source. The derived actin-containing acetone powder was shipped to Dortmund on ice. I performed the separation and purification of G-actin from the acetone powder at the MPI and stored the sample flash-frozen in liquid nitrogen at -80 °C. The protocol is provided in subsection 3.1.2. Cytoplasmic G-actin (γ1-actin, Uniprot-ID P68032, *ACTG1* from *Homo sapiens*) was recombinantly expressed using the baculovirus/Sf9-cell system and purified at the MHH (Müller et al., 2012; Ohki et al., 2009).

Flash-frozen G-actin samples were sent to Dortmund and stored at -80 ˚C. For both cases, frozen G-actin samples were thawed and polymerized to F-actin prior preparation of the specimen at the MPI (see subsection 3.1.3). The final concentration of F-actin for negative staining EM and cryo-EM was adjusted empirically (see sections 3.3 and 4.1). The following buffer nomenclature is used throughout my doctoral thesis:

G-actin buffer or G-buffer:

5 mM Tris-HCl pH 7.5, 1 mM DTT, 0.2 mM $CaCl_2$, 0.5 mM ATP, 2 mM NaN_3

F-actin buffer or F-buffer:

5 mM Tris-HCl pH 7.5, 1 mM DTT, 100 mM KCl, 2 mM $MgCl_2$

If additional ATP was supplemented, the respective concentration is given in the text. All ATP and DTT containing buffers should always be prepared freshly and kept at 4 ˚C.

Myosin

The myosin-IIC (*MYH14*, Uniprot-ID Q7Z406-1, isoform 2 from *Homo sapiens)* sample was recombinantly expressed in the baculovirus/Sf9-cell system and purified via FLAG antibody capture and size exclusion chromatography at the MHH. For more details of the used construct and purification see subsection 4.4.11 Applied methods and the protocols from Heissler and Manstein, 2011. Afterwards, the purified myosin samples were flash-frozen in liquid nitrogen (with additional 10% trehalose as a cryoprotectant) and sent to Dortmund. Prior reconstitution of the protein complexes, a small amount of myosin sample (5 µL of a 75 mM myosin solution) was thawed and diluted with 45 µL of F-buffer. Finally, the dilution was dialyzed against F-buffer to reduce the trehalose concentration to a minimum. Myosin should be kept in a buffer with an ionic strength above 50 mM to prevent aggregation.

Tropomyosin

α1-tropomyosin (*TMP1*, Uniprot-ID P58771, alpha-1 chain from *Mus musculus*) with an alanine-serine extension was recombinantly expressed in *Escherichia coli* and purified based on the protocol of Coulton et al. at the MHH (Coulton et al., 2006). The α1-tropomyosin isoform is abundant in smooth and striated muscles. Cytoplasmic α3-tropomyosin (*TPM3*, Uniprot-ID P06753-2, isoform Tpm3.1 from *Homo sapiens*) was expressed and purified based on the same protocol. Both purified α1- and α3-tropomyosin samples (330 mM and 390 mM, respectively) were flash-frozen in liquid nitrogen and sent to Dortmund. Prior reconstitution of the protein complexes, a small amount of the respective tropomyosin sample (5 µL) was thawed and diluted in F-buffer to different final concentrations (1:10 - 1:200), as the concentration for the reconstitution was adjusted empirically (see sections 3.3 and 4.1).

3.1.2 Purification of G-actin

The purification protocol described below uses muscle acetone powder from rabbit for separation and purification of G-actin. It is commercially available (e.g. from SigmaAldrich or Cytoskeleton, Inc.) and is purified from skeletal muscle from rabbit (Carsten and Mommaerts, 1963; Pardee and Spudich, 1982; Seraydarian et al., 1967). For my doctoral thesis, the muscle acetone powder was prepared at the MHH. If the following protocol does not yield a reasonable amount of G-actin (10 - 15 mg), the

quality of the muscle purification is less sufficient and the starting amount of acetone powder has to be increased.

1 g of muscle acetone powder is resuspended in 25 mL freshly prepared G-buffer and stirred for half an hour at 4 ° C in a small beaker. The solution is vacuum-filtered (filter paper: QT 205, Fisherbrand) and all remaining solid materials are stirred for half an hour in another 25 mL of freshly prepared G-buffer. The filtered solution has to be kept at 4 ° C. Afterwards, the solution is vacuum-filtered as before and the entire actin-containing solution (50 mL) is centrifuged to remove solid impurities (Ti 70, Beckman Rotors; 100.000 g, 1 h, 4 ° C). The polymerisation of the supernatant is induced by a salt-shift to 100 mM KCl and 2 mM $MgCl_2$ with addition of 0.5 mM ATP. The polymerisation is performed for 2 h at room temperature (RT). The solution should significantly turn turbid and more viscous. The F-actin solution is centrifuged (Ti 70, Beckman Rotors; 100.000 g, 3 h, 4 ° C) and 2 L of G-buffer is prepared. The supernatant is discarded and the pellet is washed carefully with G-buffer to remove remaining G-actin and aggregates. Afterwards, the pellet is resuspended in G-buffer, homogenised with a glass homogenizer and transferred to a dialysis membrane tube (SpectraPor-4, cut-off 12-14 kDa, SpectrumLabs). In total, not more than 10 mL G-buffer should be used for this step. The dilution is dialysed against remaining G-buffer at 4 ° C overnight. On the next day, dialyse buffer is replaced with freshly prepared G-buffer (2 L) and left for the day and overnight. Finally, the G-actin-containing solution is centrifuged for a second time (TLA 100.4, Beckman Rotors; 100.000 g, 1 h, 4 ° C). The same protocol for polymerisation (2 h, RT) and a two-day depolymerisation (sample volume: 10 mL; reservoir volume: 2 x 2 L) round is carried out as described above. Finally, the G-actin solution is centrifuged (TLA 100.4, Beckman Rotors; 100.000 g, 1 h, 4 ° C) and the concentration of the supernatant is estimated by absorption spectroscopy (see below). An additional round of polymerisation and depolymerisation can improve the sample purity. For other experiments, a size exclusion chromatography is even more reasonable.

The G-actin concentration is estimated by absorption spectroscopy. As ATP takes a significant part in the absorption at 280 nm, an experimental extension coefficient at 290 nm is used (ε_{290} = 0.63 mL mg^{-1} cm^{-1}; (Hertzog and Carlier, 2005)). The concentration c is estimated by $c = E_{290nm}\ \varepsilon_{290}^{-1}\ d^{-1}$, where E_{290nm} is the measured extinction at 290 nm and $d = 1$ cm for the used device (NanoDrop ND-100, peqlab).

G-actin should be flash-frozen in liquid nitrogen in a range of 50 mM to 150 mM (2-5 mg mL^{-1}) to have a reasonable concentration for polymerisation and to prevent aggregation. The sample can be diluted or concentrated for that purpose before flash freezing. In addition, glycerol (5-10 %) as a cryoprotectant can be added. Flash-frozen G-actin is capable for long time storage at -80 ° C.

3.1.3 Final purification step of G-actin

Before performing the reconstitution experiments of the protein complexes, the respective G-actin sample is thawed (~ 100 µL, 50 - 150 mM G-actin) and resuspended using a pipette. The sample is centrifuged to remove remaining precipitants (TLA 100.1, Beckman Rotors; 100.000 g, 30 min, 4 ° C). Afterwards, the G-actin-consisting supernatant is polymerized by a salt-shift to 100 mM KCl and 2 mM $MgCl_2$ with addition of 0.5 mM ATP. The polymerisation is performed for 2 h at RT and overnight on ice at 4 ° C. On the next day, the F-actin sample is centrifuged (100.000 g, 2 h). For a subsequent depolymerisation step, 100 mL auf G-buffer is freshly prepared. The supernatant is discarded and the pellet is washed carefully with G-buffer to remove remaining G-actin and aggregates. Afterwards, the pellet is resuspended in G-buffer, homogenized and transferred to a

dialysis button (Hampton Research). In total, the pellet is diluted in 50 µL of G-buffer. The dialysis button is covered with a piece of dialysis membrane (SpectraPor-4, cut-off 12-14 kDa, SpectrumLabs) and dialysed against remaining G-buffer overnight at 4 °C. On the next day, the membrane is carefully penetrated with tip of a pipet and the solution is transferred to a tube for centrifugation (100.000 g, 1 h, 4 °C). The polymerisation of the supernatant is performed for 2 h at room temperature (RT) and overnight on ice at 4 °C by applying the same salt-shift as before without additional ATP. On the last day, the F-actin solution is centrifuged (100.000 g, 2 h, 4 °C). The supernatant is discarded and the pellet is washed carefully with F-buffer to remove remaining G-actin and aggregates. Finally, the pellet is resuspended with in total 50 µL F-buffer without addition of ATP, carefully homogenized with a pipette and transferred to 0.5 mL Eppendorf Tube ®. The F-actin solution should be incubated for 1-2 h at RT before preparing the specimen for TEM (see next section 3.2). It depends on the purity of the flash-frozen G-actin, if an additional depolymerisation and polymerisation round is necessary or if the direct usage after the first polymerisation of G-actin is already sufficient for the specimen preparation.

3.2 Sample preparation for TEM

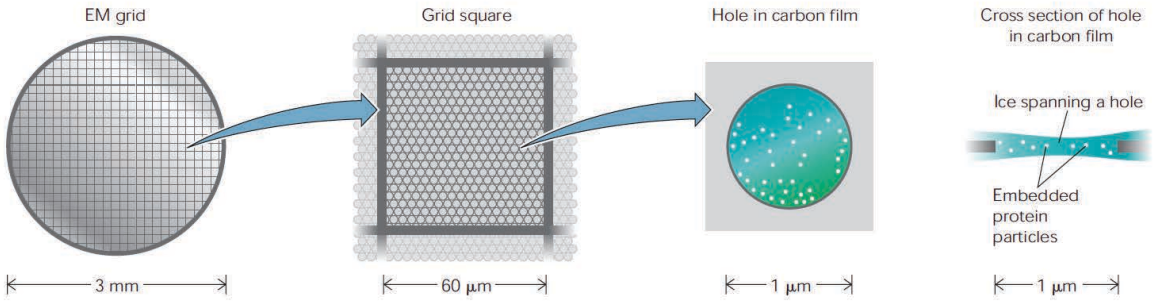

Figure 3.1: EM grid layout.

Scheme of a typical specimen holder (grid) used for transmission electron microscopy. The grid is covered with either a holey carbon layer (shown in this figure) or a continuous carbon layer and is divided in single squares. Protein particles are either analysed on the whole square region (negative staining) or only within holes (cryo-EM). Figure taken from Wang and Sigworth (2006).

Standard biological samples for transmission electron microscopy are prepared in a liquid environment. For investigating these samples (e.g. protein solution) with an electron microscope the solution has to be fixed to a specimen holder. As the microscope column itself has to be at high vacuum to prevent electrons from interfering with air the sample has to be either dried or frozen (see also subsection 2.3.1 Transmission electron microscopy on biological samples). This section describes two protocols for the general sample preparation with either negative staining (3.2.1) or cryo vitrification (3.2.2). Finally optimized procedures are given in the respective paragraphs in Results & Discussion chapter in section 4.1 and in the applied methods subsection of 4.3 and 4.4, respectively.

A copper grid (diameter 3.05 mm) is used as a specimen holder, which is covered by a thin layer of carbon. This layer of carbon is either continuous (for negative staining) or has a holey structure (for cryo vitrification). The grid itself is split into hundreds of squares (see Figure 3.1). EM grids can be purchased commercially either with or without a continuous or holey carbon layer (e.g. from Quantifoil®, C-flat™). In addition, a continuous carbon layer can be added to a bare grid manually (see subsection 3.2.1). Grids for EM vary in their mesh size, hole size and hole spacing. A typical grid is described as for example “C-flat 2/1”, which stands for a hole size and hole spacing of 2 µm and 1 µm, respectively. There are other materials serving as raw material for the grid (e.g. gold or nickel), which are less toxic than copper for growing for example whole living cells on a grid.

3.2.1 Negative staining

Carbon coating of EM grids

Grids for negative staining have to be covered by a continuous carbon layer prior the staining and drying procedure. If not already purchased with carbon layer, the bare cupper grid (G2400C, Plano GmbH) has to be covered with a thin polymer film onto carbon can be coated afterwards. For that purpose, a small amount (2x-3x 25 µL drops) of collodion solution (Fluka) is applied carefully on water in a glass beaker (diameter ~ 30 cm). During this process the water surface should be as still as possible to reduce waves in the final carbon layer. After evaporation of the solvent the bare grids can be manually placed with a forceps on top of the polymer layer. There are several protocols published which demonstrate the optimal grid handling and visualized the whole procedure in detail (Booth et al., 2011; Ohi et al., 2004). When a reasonable amount of grids (~ 40 - 60) are placed on an area of

~ 3x3 cm^2 a piece of lint-free blotting paper is applied from the top. Everything should be sucked to and stabilized by the blotting paper. Unnecessary rest of the polymer film can be cut from the edges from the paper. Finally, the blotting paper with the grids is transferred to a petri dish upside-down for drying for one to two days. Additional filter paper in the petri dish can accelerate the drying process. Once the prepared grids are dried they are transferred to a carbon evaporator machine (Leica EM ACE600, Bal-Tec MED020). In both cases, the chamber for coating is brought to high vacuum (~ 10^{-4} Pa) at first. Afterwards, carbon is evaporated or sputtered from a carbon rod or thread by a high current, respectively. The final carbon layer should be in the range of a 5-15 nm thickness for optimal preparation and contrast.

Preparing of stain solution

Different heavy metal solutions can be applied for negative staining of protein (e.g. uranyl acetate, uranyl formate, sodium phosphotungstate, ammonium molybdate). They differ in their grain size, usable pH range, stability and quality of contrast. Uranyl formate or acetate is used in most cases. Both stain solution are acidic (pH 4 - 4.5) and can have an impact on the protein structure and stability, because proteins can be sensitive to the ph. The main advantage is the quality of the contrast and the small grain size making these staining solution superior to other ones. Uranyl acetate and formate are highly toxic and should be carefully handled and contaminated materials (filter paper, tips) are hazardous waste.

For standard negative staining EM a 0.75 % solution of uranyl formate is prepared. 5 mL of water is boiled and 37.5 mg of uranyl formate (SPI-Chem) is added. Solution is stirred in the dark for five minutes. Afterwards, 6 µL of 5 M sodium hydroxide is added to adjust the pH and stirred again for five minutes in the dark. Finally, the solution is filtered through a 0.22 µm filter syringe to a plastic tube. Adjusting the pH to exactly 4.0 can improve the quality. The staining solution is stable for up to a week, if stored in the dark and heat is avoided. If the solution starts to precipitate it should be filtered again or freshly prepared.

Negative staining of protein samples

The grid has to be cleaned and made hydrophilic by glow-discharging prior to the actual applying of sample and staining. Therefore, the grid is transferred to a plasma-cleaner (FEMTO, Diener electronics GmbH & Co. KG) and an ionising gas charges the surface of the grid.

Best protein concentration differs between protein type and size and has to be optimized during screening (0.01 - 1 mg/mL). Therefore only volumes are given in this section. To get a reasonable negatively stained sample, concentration and stain thickness has to be optimized empirically.

A freshly glow-discharged grid with continuous carbon is fixed in a reverse forceps. Two drops (~10 µL) of washing solution (distilled water or protein buffer) and two drops (~10 µL) of stain solution (0.75 % uranyl formate) are placed on a clean piece of Parafilm® (see Figure 3.2a). A volume of 4 mL of sample solution is applied to the grid and incubated for 30 - 60 s. The solution is blotted with a piece of filter paper (Whatman 4) at the edge of the grid. The first drop of washing solution is adsorbed to the grid a directly blotted as before with filter paper. Afterwards this procedure is applied with the second drop of washing solution and the first drop of stain solution. The second drop of stain solution is only adsorbed to the grid and incubated for another 30 s before blotting with filter paper. The grid is finally air-dried. A small amount of liquid has to be left on the grid during all blotting steps to avoid drying out in the meantime.

Crosslinking prior staining

It is possible to crosslink proteins prior to the actual staining procedure. This can be performed directly on the grid to reduce possible artefacts due to the extreme pH change for proteins, which are normally at a physiological environment around pH 7-8. Therefore, the protein solution is applied to the grid and washed once as before. Then a drop of the used protein buffer with 0.25 % glutardialdehyde is applied for 10 - 30 min on the grid before the standard negative staining procedure with two steps of washing and staining is carried our, respectively. Hepes instead of Tris must be used for the protein buffer for crosslinking studies to avoid crosslinking of the amino group of Tris instead of crosslinking of residues.

3.2.2 Cryo vitrification

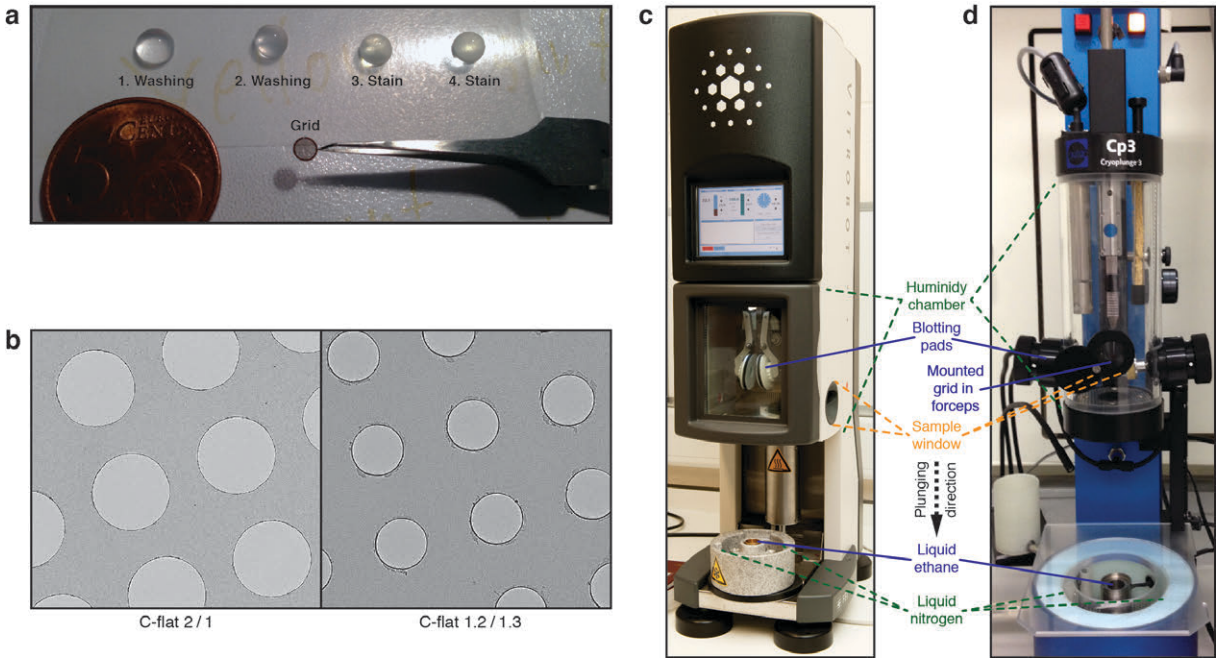

Figure 3.2: Grids and plunge freezers.

a, Standard setup for negative staining of a protein sample. The grid is fixed in a reversed forceps. Two drops for washing and two drops for staining are prepared on a piece of Parafilm®. **b**, Transmission electron microscopy image of two types of holey carbon grids with different hole size (first number in µm) and hole spacing (second number in µm). **c**, **d**, Two of the three mostly used and commercially available plunge freezers; FEI Vitrobot in (**c**), Gatan Cryoplunge Cp3 in (**d**). A Cp3 allows removing of blotting pads to blot manually from one side. Blotting force is motor-driven or created pneumatically for the Vitrobot or Cp3, respectively.

Commercially purchased holey carbon grids are used for vitrification of a protein sample. The aim of the cryo vitrification step is to fix the protein in a thin layer of vitrified ice. The optimal ice thickness depends on the project and is in the range of 20 - 150 nm for single particle EM. The protein has to be within a hole (see Figure 3.1, Figure 3.2b) since the contrast between ice and a biological sample is very low (see also subsection 2.3.1 Transmission electron microscopy on biological samples). Ice thickness influences protein distribution and the air-water interface can induce unwanted preferred orientation of a protein sample. Ice thinner than the analysed protein results in displacing of the protein from the holes. On the other hand the contrast will be reduced significantly by too thick ice. However, a compromise between the ice thickness and sample concentration is needed to obtain best sample distribution and contrast.

Different devices are commercially available for plunge freezing of a protein sample onto an EM grid (Gatan Cryoplunge Cp3, FEI Vitrobot, Leica EM GP; see also Figure 3.2c, d). All devices use liquid ethane as environment for freezing (melting/boiling point: -183 °C / -89 °C) and liquid nitrogen (melting/boiling point: -210 °C / -196 °C) for cooling the ethane. The ethane container of the Gatan Cryoplunge Cp3 can be heated to a temperature higher than the melting point to prevent ethane to become solid. To set up the respective device the user manual should be consolidated. Contamination of ethane with ice crystals should be reduced as much as possible. Therefore, tools should be warmed up and be totally dried prior usage. In addition, high humidity or direct contact to breath must be prevented during all next steps after vitrification of the sample. The general protocol for all these machines is described below.

Plunge freezing protocol

A glow-discharged holey carbon grid (see subsection before) is fixed into a forceps and is mounted into the humidity chamber (Figure 3.2d). Humidity is regulated manually or automatically depending on the used device (should be higher than 90 %). The protein sample is applied to the grid (1 - 4 µL) and can but have not to be incubated for several seconds. Afterwards, the solution on the grid is blotted from either both or only one side with filter paper (Whatman 4) automatically. The blotting time and force depends on the device and can be set independently. In addition, devices differ in their underlying method for applying the blotting force (motor-driven or pneumatically). Finally, only a thin layer of the protein solution is left on the grid and is directly plunge frozen into liquid ethane. Afterwards, the grid is stored in a small grid box. Prepared vitrified sample can be directly transferred to an electron cryomicroscope for screening or can be stored for months in liquid nitrogen.
As mentioned above, best conditions have to be adjusted empirically. Once the optimal condition is found, several grids should be plunged frozen and stored.

Strategies for optimization

Different sizes and spacing of the holes should be checked for optimal conditions. Ice conditions and binding behaviour of proteins can be modified by addition of detergents like Triton or Tween 20 at a concentration of 0.01 - 0.05 % to the protein buffer. If the protein concentration in the holes is too low or the proteins tend to bind only to the surrounding carbon film, saturation of the carbon by applying the sample multiple times can improve the result. Filter paper types differ in their blotting speed and lower values (e.g. Whatman 5) can help to reduce the blotting speed, which is necessary especially for bigger protein complexes or filamentous structures. Although blotting time and force can be set individually, often manual blotting from only the back or front side with a piece of filter paper can lead to optimized sample conditions. In some cases, an additional thin layer of continuous carbon can improve the distribution. It should be checked that the contrast is not reduced too much and that the protein binds not only in preferred orientation to the carbon.

3.3 Screening and data acquisition

3.3.1 Screening with negative staining

Negative staining electron microscopy is the method of choice to perform easy and rapid screening of one or several protein samples. The preparation of one grid is in the range of minutes (see subsection 3.2.1). The quality of a protein sample can be checked with this method already on the level of a micrograph (like overall heterogeneity, aggregation and impurities). In addition, the reproducibility is very high and can deal as a quality control for further EM studies. A data set can be recorded to visualize possible higher level of unwanted heterogeneity like flexibility within a protein or different conformations. Furthermore, a data set can help to reconstruct an initial low-resolution model for further high-resolution refinement of a cryo-EM data set.
For this thesis, negative staining was applied to check for the quality of the filaments and to adjust the protein concentration of F-actin. Furthermore, it was used to optimize the reconstitution of the different protein complexes at the right concentration directly on the grid (see section 4.1 in Results & Discussion). In addition, three data sets of bare F-actin, F-actin decorated with tropomyosin and cross-linked F-actin-tropomyosin were recorded to detect if the staining procedure can modify the tropomyosin position on F-actin (see section 4.3 in Results & Discussion).
All negative stain studies were performed on a JEOL JEM-1400 electron microscope equipped with a LaB_6 cathode operating at a voltage of 120 kV (Figure 3.3a). The sample grid is inserted with a side-entry specimen holder. All images were manually recorded with a 4k x 4k CMOS TemCam F416 (TVIPS). The field of view in were checked in 'search mode' (four fold binned rolling shutter mode) with 400 ms exposure time. Images were finally recorded with an exposure time of 1 s in 'exposure mode' (unbinned mode). The camera is controlled via a computer interface (EMMENU, TVIPS). In addition, a fluorescence screen can be inserted for visualizing the sample.
The whole sample transfer into the microscope is a fragile process and the user has to be trained by the facility manager. In addition the alignment and usage of the microscope has to be trained as well. The next two paragraphs deal as an overview.
Before starting a screening or data collection session on the microscope, a cold trap has to be filled with liquid nitrogen. Especially when bringing several samples after each other into the microscope, the vacuum quality can drop. The beam has to be switched of during sample transfer. The cold trap sits next to the injected sample grid. After stabilization of the temperature the first grid can be placed and fixed to the specimen holder. The specimen holder is not directly inserted to the microscope. An initial evacuation is performed in a pre-chamber. Afterwards, the holder is inserted to the microscope column. The exact vacuum limits, rolling rotation and position of the specimen holder have to be advised during training. After vacuum stabilization in the column, the electron beam can be switched on.
The alignment of a microscope can be split into alignment before and during data acquisition. Firstly, the gun lens system is aligned with the condenser lens system and then the condenser lens system with the object lens system. The main goal is to align the electron beam to the central axis of the microscope. The objective lenses are on axis by definition. Deviation can lead to reduced image quality (especially lost if high-resolution frequencies). In addition, condenser and object apertures have to be centred. Astigmatisms of the condenser lens system (distortion of the beam) and object lens system (distortion of the Fourier-transformation of the image, 'power-spectrum') have to be corrected with

stigmators. All alignments from above are performed before data acquisition. During data acquisition the current position of the grid has to be moved to the eucentric height of the microscope (image position of specimen is independent from tilting of the specimen under 'standard defocus' settings). The focus has to be set to a reasonable defocus value (micrometre range) to allow a good contrast and as much as possible high-resolution information. The astigmatism of the object lens system can be defocus-dependent and should be checked in the power-spectrum. A smaller objective aperture leads to a higher amplitude contrast.

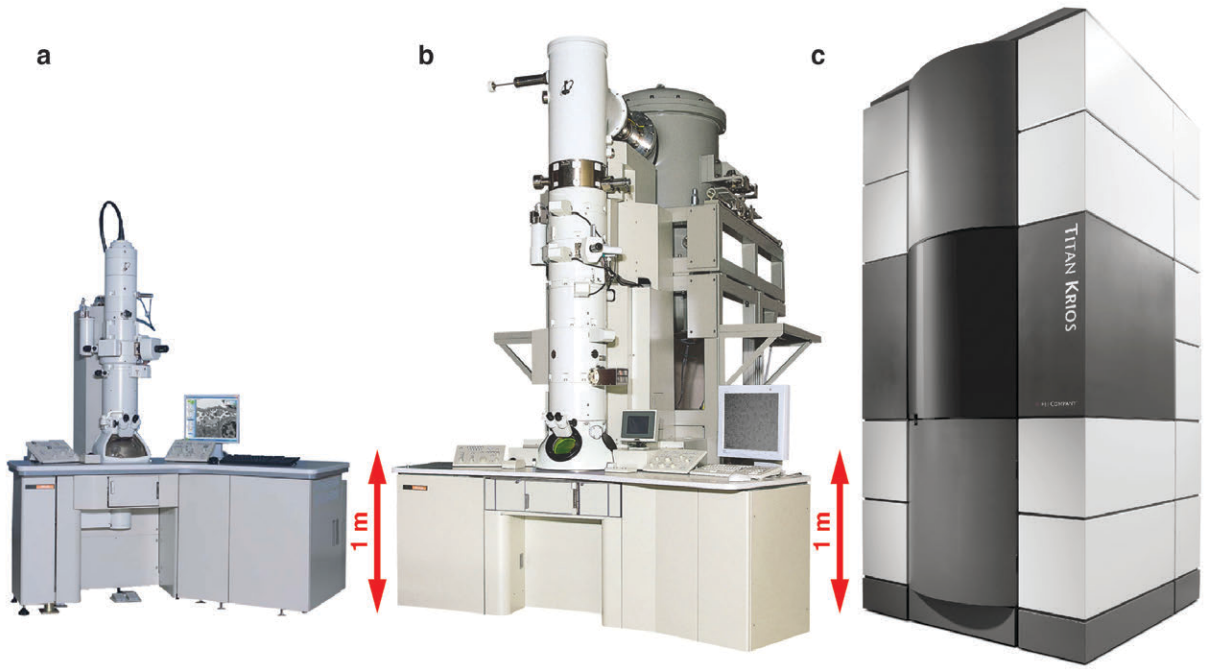

Figure 3.3: Used transmission electron microscopes.

a, Negative staining studies to screen sample quality and to perform reconstitution experiments of the different protein complex were obtained on a JEOL JEM-1400 microscope. **b**, Vitrification settings were checked on a JEOL JEM-3200FSC microscope. Both microscope types are installed at the Max-Planck-Institute in Dortmund. **c**, The final data sets for obtaining a high-resolution structure were collected on a FEI Titan Krios at NeCEN in Leiden (Netherlands).

3.3.2 Screening for cryo-EM sample conditions

Cryo-EM screening was performed manually on a JEOL JEM-3200FSC for determine best blotting and sample conditions at the Max-Planck-Institute in Dortmund (Figure 3.3b), while the final data collection were carried out at a cryo-EM facility in the Netherlands (see next subsection 3.3.3).
The general alignment and sample transfer procedure does not differ from the methods described above. One difference is that the whole sample transfer has to be performed in liquid nitrogen or in a cold nitrogen gas phase at low humidity. A cryo transfer station (EM CPC, Leica) is used to mount up to three grids into the cryo specimen holder. In addition, the microscope itself is cooled with liquid nitrogen. The JEOL JEM-3200FSC is very sensitive to changes of the lens currents and the induced magnetic fields. Therefore, changing for example the magnification, brightness or beam position can lead to strong hysteresis and should be handled with caution. The microscope was run at an operational voltage of 200 kV and images were recorded on an 8k x 8k CMOS TemCam F816 (TVIPS). The ice homogeneity within one grid can differ significantly. Several squares in different regions of the grids were screened to obtain a quality valuation of the respective vitrification settings.

In addition, the JEOL JEM-3200FSC has an omega in-column energy filter, which removes inelastic scattered electron and can be used to estimate the ice thickness by comparing the same field of view with and without filtering.

3.3.3 Data acquisition for high-resolution cryo-EM

Recent developments in cryo-EM make it mandatory to collect a data set on a high-end microscope equipped with a direct detection camera for reconstruction a high-resolution structure (see section 2.3.3 Recent developments in TEM: "resolution revolution"). The high-end electron cryomicroscope (JEOL JEM-3200FSC) of the Max-Planck-Institute was not equipped with a direct detection camera. Therefore, the obtained and processed data sets of this thesis were recorded at the 'National Center for Electron Nanoscopy' (NeCEN) in Leiden in the Netherlands on a FEI Titan Krios TEM (Figure 3.3c). The Titan Krios was operated at 300 kV and is equipped with an extra-high brightness field emission gun (XFEG). All images were recorded with a back-thinned 4k x 4k FEI Falcon II direct detection camera. In addition, the used Titan Krios has a corrector for spherical aberration. The sample grids were prepared and screened at the MPI in Dortmund (see subsection 3.3.2 before). The Titan Krios has the advantage of a fully automatic loading of a grid to the microscope (Autoloader^{TM}, FEI). Up to twelve grids can be mounted to the sample loader cassette under liquid nitrogen. The microscope-cooling tank is filled with nitrogen automatically. After a fast manual pre-screening of each grid, the respective grid for further automatic data collection were chosen. At first, an overview image ('Atlas') of the whole grid is recorded to set up the automatic data collection software (EPU, FEI). Each square can be selected independently and test images are taken. Finally, several squares are chosen for the actual data collection, which can run automatically over several days with only minor external controlling.

The following settings have to be adjusted by the user in the data collection software prior starting. The main settings are the defocus range and step size, how many images per hole should be recorded, how many single subframes ($t_{subframe}$ = 55 ms) should be summed up to one individual frame (in total seven frames could be recorded), when the collection of the frames should start (e.g. deleting of first subframes is possible) and exposure time per position in a hole. The output is directly written to an external hard drive. Per position an integrated image without any correction over the full exposure time ('mrc' file format) is saved, a JPEG-copy of this image is converted and an image stack (so-called movie stack; 'mrcs' file format) of the seven frames is created. In addition, a 'XML'-file holds all metadata information.

The applied settings are given in the respective paragraphs in Results & Discussion chapter in the applied methods subsection of 4.3 and 4.4, respectively. The data sets were recorded within one session over three day in October 2013 for the F-actin-tropomyosin structure and within two sessions in September and October 2014 in about eight days for the actomyosin structure, respectively. The overall raw data set size per session were in the range of ~ 2 TB. The raw data set was backed before starting any further processing step.

3.4 Computational methods in cryo-EM

This section gives a general overview of the applied computational methods and protocols, which are applied to data sets for reconstruct a high-resolution structure with cryo-EM. The ultimately used programs and methods are given in Results & Discussion chapter in the applied methods subsection of 4.3 (F-actin-tropomyosin, first data set, Figure 3.4a) and 4.4 (F-actin-tropomyosin-myosin, second data set, Figure 3.4b), respectively.

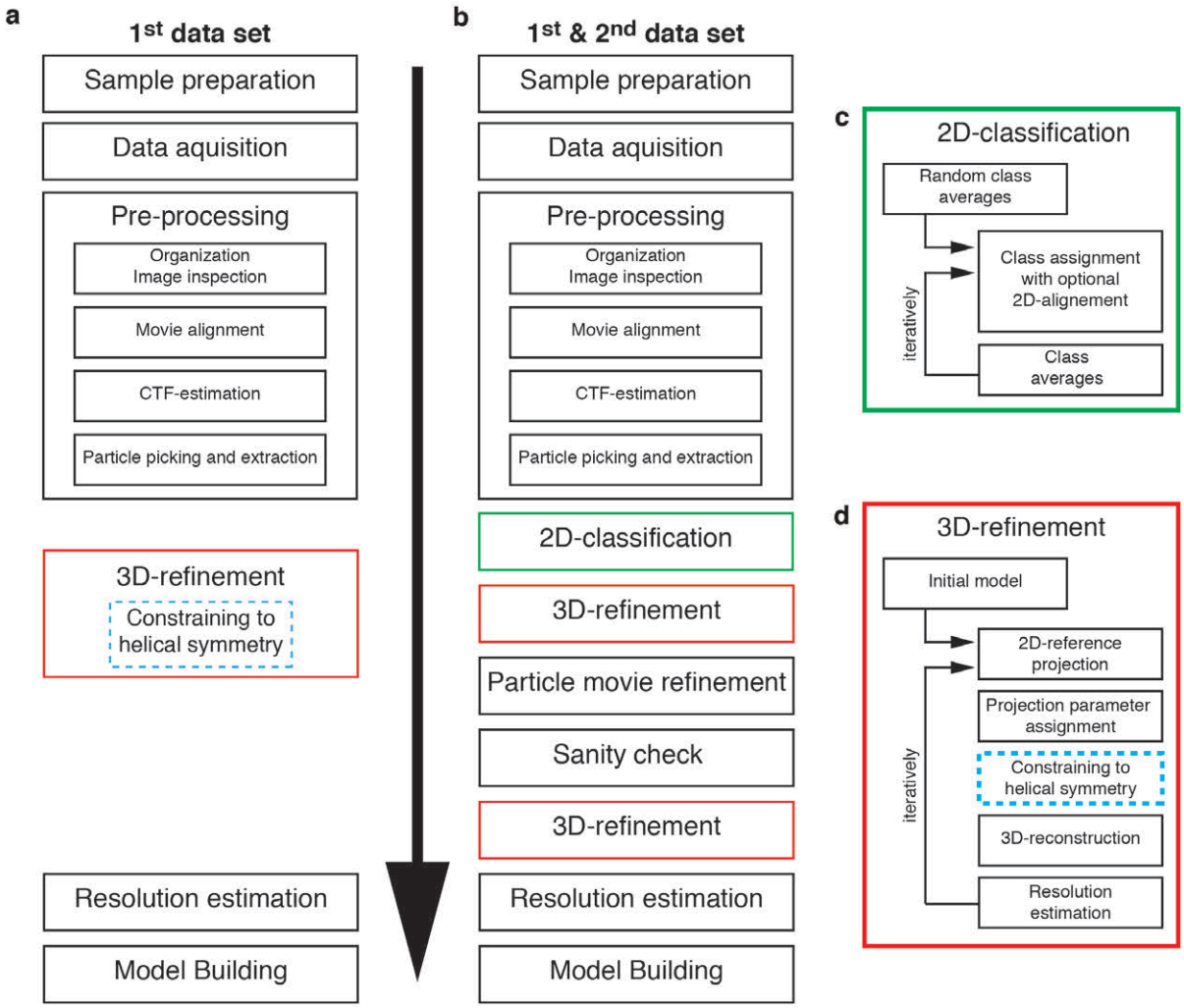

Figure 3.4: Schematic workflow of data processing.

a, **b**, Applied overall workflow for the two processed data sets. Detailed description can be found in the applied methods subsection 4.3.8 and 4.4.11. In addition, the workflow after pre-processing in (**a**) in described in section 4.2 in more detail. The data were prepared the same way (pre-processing), while the workflow differed significantly at the stage of 2D-classification and 3D-refinement. **c**, General idea of an algorithm for 2D-classification. All particles are assigned (and optional aligned) to a set of 2D-classes. Afterwards, new class averages are summed up and taken for the next iteration. **d**, General idea of an algorithm for 3D-refinement. Reference projections are calculated from a current density map (initial model or reconstruction from last iteration). All particles are assigned and aligned to the reference projections. In the case of (**a**) an improved algorithm checks for the projection parameters regarding to the helical symmetry within a filament (see also section 4.2 in Results & Discussion chapter). Finally, a new density map is reconstructed with the assigned projection parameters and the current resolution is estimated.

A main difference was the used software package for the structure classification and refinement (subsections 3.4.2 - 3.4.6). 'SPARX' (Hohn et al., 2007) was used for the first data set and 'RELION' (Scheres, 2012) was applied on the second data set. After processing of the second data set, the derived strategies with Relion were adapted to the first data set and are included in section 4.3

(Figure 3.4b). In addition, the results in section 4.2 Improved helical reconstruction: HELICON describe a software package, which was implemented into Sparx for this thesis (Figure 3.4a, d).
Other commonly applied software packages for single particle or helical refinement and classification are 'FREALIGN' (Grigorieff, 2007; Lyumkis et al., 2013), 'FREALIX' (Rohou and Grigorieff, 2014), 'SPRING' (Desfosses et al., 2014), 'EMAN2' (Ludtke, 2010; Tang et al., 2007), 'IMAGIC' (van Heel et al., 1996) or 'SPIDER' (Shaikh et al., 2008).

3.4.1 Data pre-processing

Organization of the data set and image inspection

Keeping exactly track of each image by a unique image name is very important through the whole data processing steps. Therefore, a single data set name (e.g. 'actaTM') with a running number (e.g. starting '0001') should be applied to each quartet consisting of a 1 s integrated images, a converted JPEG-copy, a XML-file and a image stack with an addition suffix (e.g. '_frames'). Additional data from an extending data collection session should continue from the last number from before.
It is highly recommended to inspect all images manually (particularly by checking the JPG-copy) to delete not suitable images (contaminated, empty or overcrowded holes; destroyed carbon foil areas; images recorded with a strong drift or astigmatism).

Movie alignment

When summing up all frames to one average image, each individual frame of a movie stack has to be aligned to the other frames to improve signal to noise ratio as an initial step of pre-processing (Brilot et al., 2012). Mainly blurring of the image information due to a drifting sample can be reduced by this step (see 2.3.3 Recent developments in TEM: "resolution revolution"). For that purpose different alignment approaches can be applied and are described below. Individual particle movement relative to the rest of an image can be corrected during a later step of processing (see subsection 3.4.4).
Finding a peak in a cross-correlation map between two individual frames can be rather inaccurate or simply wrong. One approach is to calculate all shifts not independent from each other. Therefore, each relative movement between two frames of one movie stack can be used for a redundant measurement (over-determined set of linear equations). Small movements between adjacent frames can still be very inaccurate and therefore only shifts starting with a distance of at least two or more frames are calculated. This approach is implemented in 'motion corr' and runs on a graphics processing unit (GPU; Li et al., 2013a).
Another method to improve the alignment accuracy of a single frame is not to align one frame to another frame but is to align one frame to the sum of all frames. The higher signal-to-noise ratio of the sum of all frames can enhance the peak of a cross-correlation map. Furthermore, this method can be applied iteratively. For that purpose, the shifts per frame estimated in the previous iteration are applied during calculation of the current sum of all frames. This method is implemented in 'unblur' (Grant and Grigorieff, 2015). In addition, this software package can compensate for beam-induced damage (for more details see subsection 3.4.4). There are other tools available but were not applied to the data sets (Abrishami et al., 2015; Rubinstein and Brubaker, 2015). The final output of all programs is one drift-corrected average image of the movie frames.

CTF estimation

Compensation and correction for the contrast-transfer-function (CTF) is essential for obtaining a high-resolution reconstruction (see also section 2.3.1). Therefore, the CTF has to be estimated prior starting any further processing steps. A least square fit can be applied by fitting two parameters (defocus and astigmatism) per image. The voltage, spherical aberration and pixel-size are considered as constants for the calculation. Several software packages are available for that purpose like 'CTFFIND' or 'CTER' (Mindell and Grigorieff, 2003; Penczek et al., 2014; Rohou and Grigorieff, 2015). They base on the same general principle for preparing the individual image for the calculation but use different fitting algorithms or parameter set to describe the CTF model.

All programs cut an image (e.g. 4096x4096 pixels) into sections (e.g. 256x256 pixels), calculate the Fourier-transform of the section and average them to one total Fourier-transform. The simple Fourier-transformation of the original image has a lower signal-to-noise ration than the averaged Fourier-transformation. The CTF function is rotation invariant and a rotational averaged Fourier-transformation is obtained for applying the actual fitting. High drift or strong astigmatism will reduce the quality of this conversion. Therefore, the calculation should be applied on the drift-corrected average of each movie stack. The astigmatism is directly fitted to the averaged 2D-Fourier-transformation or to the rotational averaged curve. This approach can be applied iteratively.

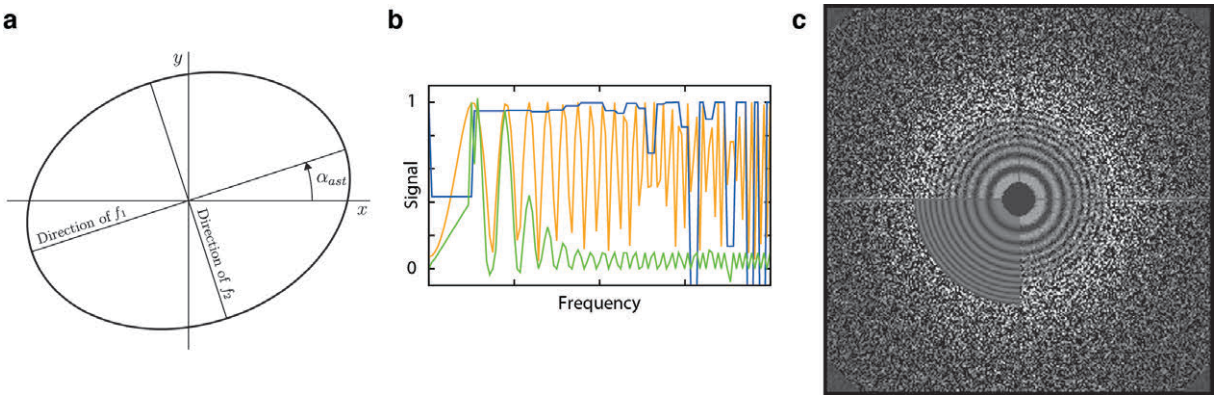

Figure 3.5: CTF parameter set and CTF estimation.

a, The given CTF model is described by an ellipse with its short semi-axis (small defocus value f_2), its long semi-axis (big defocus value f_1) and an astigmatism angle α_{ast} to the x-axis. **b, c**, All programs output statistics for diagnosis. For simplification in both subfigures no astigmatism is present. In (**b**) the plot gives the calculated CTF fit (yellow) and the experimental amplitudes (green) of the rotational averaged 2D-Fourier-transformation. In addition, the accuracy of the fit is given in blue. At high frequencies the accuracy is reduced. The averaged Fourier-transformation of all section of one image is shown in (**c**), while the lower left gives the fitted CTF approximation. Subfigures combined and modified from Rohou and Grigorieff (2015), with permission from Elsevier.

The outputs of different programs base on the same CTF model but use different parameter sets. The CTF model is fully described by a defocus value, an astigmatism angle and amplitude, or by two defocus (smallest and highest) values and an astigmatism angle (latter parameter set is given in Figure 3.5a). Both parameter sets can be converted to each other. Examples of the applied fit and diagnosis of the fit is given in Figure 3.5b, c (more detailed description of the applied algorithms see Penczek et al. (2014) or Rohou and Grigorieff (2015).

Particle picking and extraction

To analyse and reconstruct a structure of a single protein or filament, the actual 'particles' or 'segments' in the case of a filamentous sample have to be selected ('picked') and extracted from each

single image. This process can be totally manual, semi-automatic or automatic. It extremely depends on shape and size, concentration and distribution, and contrast of the sample. As no automatic tools for selection of filaments exists, this paragraph only described the manual selection of filaments with the 'helixboxer' tool ('sxhelixboxer') of Sparx.

As the contrast of the images can be very low and for selecting of the filaments no high-resolution information in the images are needed, the picking of the filaments can be applied on low-pass filtered images (Gaussian low-pass filter with a cut off of 10 Å - 15 Å). Thereby, the contrast is significantly improved as small details are filtered out (filtered areas in Figure 3.6a, b). During selection of the filaments, parts of overlapping or crossing filaments and full bundled filaments (mostly present in the second data set, Figure 3.6b) are leaved out. The position of all filaments within an image is saved as a 'coordinates file', in which pixel of the start and end position of each filament is written to. After selection of all reasonable filaments of all images, the filaments are rotated to the y-axis and separated into single segments automatically. A segment size (several asymmetric subunits, typical range for F-actin: ~ 10 subunits per segment) and a boxing distance (at least one rise) have to be set for the extraction. The segment size has an direct influence on the processing time and an optimal number for asymmetric subunits per segments depends on the respective filamentous sample (Egelman, 2010). Finally, one stack of all segments from the 1 s integrated images and one stack from the drift-corrected average images is extracted.

To apply any constraints to the projection parameters per filament, an identification number (filament ID) or name per filament has to be defined and be tracked through all steps of further refinements (see also section 4.2 Improved helical reconstruction: HELICON).

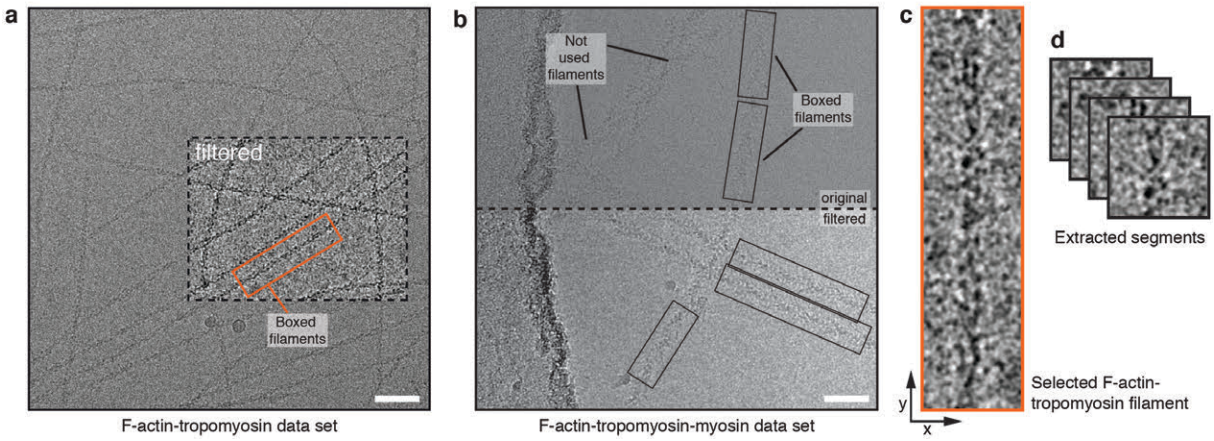

Figure 3.6: Filament selection and extraction.

a, **b**, Representative images of the two data sets. The inlet in (**a**) and the lower panel in (**b**) show examples of the applied low-pass filter for the step of filament selection. **c**, One filament from (**a**) is pre-rotated to the y-axis prior separating into segments with a defined distance and size. **d**, Finally, the extracted segments can be used for further refinements. Scale bars in images are 50 nm. Subfigures combined and modified from von der Ecken et al. (2015 and 2016).

3.4.2 Two-dimensional (2D) classification

A general tool for classifying a stack of particles (or segments in the case of a filamentous sample) is performed in 2D without needing any 3D-reconstruction. The idea of the method is to sum up segments representing the same view of the (unknown) molecule (Figure 3.4c). The resulting so-called 'class averages' of several particles have an enhanced signal-to-noise ratio and can be used for sorting out less suitable particles (e.g. destroyed particles; particles lacking a domain of a molecule;

unspecifically bound compounds or bundled particles). Often it is possible to detect flexible parts (smeared out in an class average) or directly assign parts of the class average to respective parts of a complex. Furthermore, the class averages can be used to perform an initial model of an unknown molecule at low resolution. As several low and medium resolution electron density maps of F-actin exist, the often very essential step of getting a reliable initial model for further 3D-refinement is not needed and is not described.

2D-classifications were applied to check the segment stacks of both data set for their quality (e.g. if secondary structure elements are already visible) and the complex reconstitution (e.g. if tropomyosin is bound to F-actin). In addition, it was applied to sort out less suitable segments in the case of using the pure single particle approach for the second data set and the reprocessing of the first data set in section 4.3.

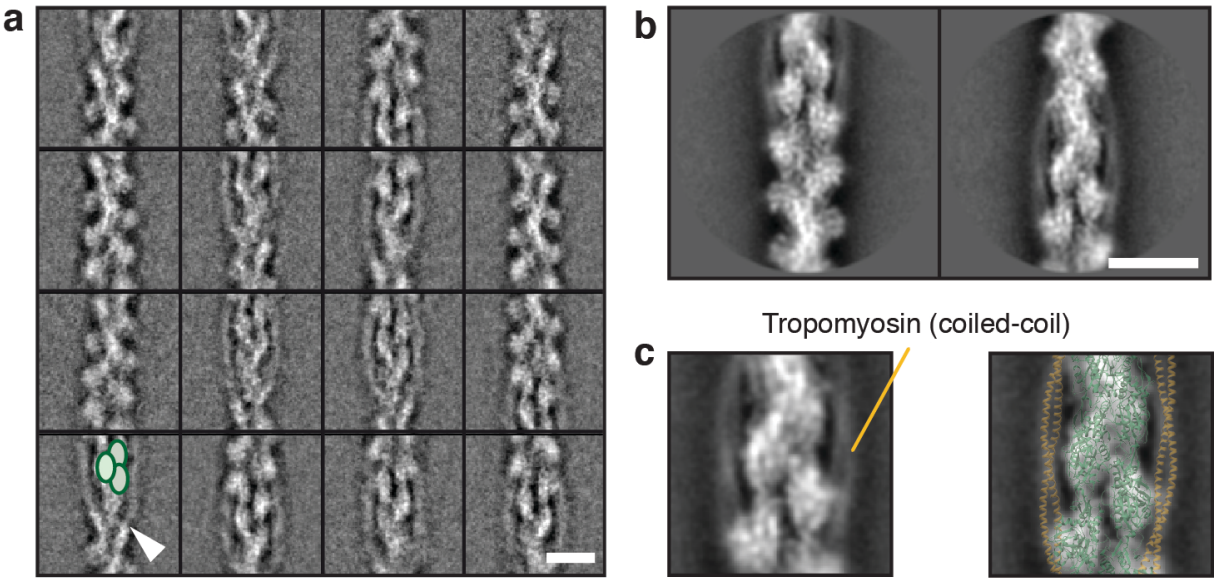

Figure 3.7: Example of 2D-classifications.

a, A classification with Sparx shows aligned segments to the y-axis. F-actin subunits are assignable (green ellipses) and density for tropomyosin is visible (white arrow). **b**, **c**, F-actin filaments are suitable for high-resolution 2D-classification with Relion. Representative class averages show a high degree of details. For example the coiled-coil structure of tropomyosin is already present in the class averages (**c**). Scale bars in class averages are 10 nm. Subfigures combined and modified from von der Ecken et al. (2015 and 2016).

2D-classification can be understood as finding clusters within the unknown projection parameters (in 2D: x- and y-shifts and in-plane rotation). Therefore, a 2D-alignemnt has to be performed before or during the classification. The number of clusters within a data set has to be set by the user. It depends on the data set size, computing power and if the data set is derived from a negatively stained or cryo vitrified sample. In the case of a cryo-EM data set at least 100 particles should be averaged to a single class. Sparx uses a classification method based either on a 'k-means' algorithm (Duda et al., 2012) or a 'Iterative Stable Alignment and Clustering' (ISAC) approach (Yang et al., 2012). The advantage of the latter one is a high reliability due to implemented inner validation and checking of reproducibility. In the case the filamentous sample in this thesis a k-means classification with 'sxk_means' were only applied, because the overall architecture is known and classification was only used to check the alignment quality (Figure 3.7a). Another method in Sparx for a combined alignment and classification in a single program is implemented in a multi-reference alignment ('sxmref_ali2d'). The program needs as an input a stack of references (derived from a k-means classification or calculated reference projection from a 3D-density) to which the particle stack is assigned and aligned.

Relion applies already a maximum likelihood approach for 2D-classifications with or without 2D-alignment (see 2.3.2 Single particle and helical reconstruction) and is superior in the maximal obtainable quality and visibility of details in comparison to Sparx (Figure 3.7). But it can struggle when aligning small particle without any distinct shape (e.g. roundish particles). Furthermore, the centring of a particle can fail, when the centre of mass is not in the centre of the particle dimension or top and side views significantly differ in their size.
In addition, transformed 3D-projection parameters to a 2D parameter set can be applied for a classification without refinement to validate the estimated 3D-parameters. Often it can be utilized to sort out misaligned segments or to perform focused classification on only a part of the molecule or protein complex.
One other method for applying a classification can be performed in three dimensions. The general method is the same but at much higher computational costs. For some projects a 3D-classification can be superior to 2D-classification and improve the sorting and achievable resolution. 3D-classifications could not improve the quality of the final reconstructions of both data sets, as the flexibility and differences are on a level, which is not classifiable.

3.4.3 Three-dimensional (3D) refinement

All commonly applied software packages base on the same methods for obtaining a 3D-reconstruction from 2D-projection of a single particle or filament (Figure 3.4d). They compare calculated reference 2D-projections from the current reconstruction with the experimental 2D-projection (particle stack) and assign either one set of projection parameters to the respective particle (highest cross-correlation peak) or a weighted distribution of several sets of projection parameters (maximum-likelihood distribution). Please consider subsection 2.3.2 Single particle and helical reconstruction in the Introduction for more details regarding the two approaches and how an actual reconstruction is performed.
At the stage of 3D-refinemnt, it has to be distinguished between a pure single particle approach (section 4.4), where no symmetry is applied and a helical reconstruction method (section 4.3), where the symmetry of the filament is used for alignment and symmetrization of the reconstruction. An improved program for the latter one was implemented in 'HELICON' during this thesis and is discussed in section 4.2 Improved helical reconstruction: HELICON. An older program of the latter approach is the 'Iteratively Helical Real Space Refinement' (IHRSR) but were not used anymore for this thesis (Behrmann et al., 2012b; Egelman, 2000; 2010). For the former approach (pure single particle approach) the 3D-refinment and reconstruction algorithm of Relion was used. The next paragraphs describe the overall workflow of a 3D-refinement, while detailed descriptions are part of Results & Discussion chapter in the applied methods subsection 4.3.8 and 4.4.11.
For starting a 3D-refinement an existing starting model is needed. A cylinder with the dimension of the filament or a cylinder filled with Gaussian noise can be used as an initial reference for reconstruction of a filamentous sample. In the case of F-actin, the overall structure is known and a low-resolution density map can be used as an initial model. Furthermore, the refinement can be improved by applying a mask covering only the actual protein density. With an applied mask on respective parts of the density the refinement can be finally focused. Initial masks should be broader and carefully narrowed in later iterations (e.g. starting with a cylindrical mask, continuing with mask

of the full filament, finishing with a mask on the central subunits). As a mask will always cut density in the case of a filamentous sample, the mask should have smoothed edges.
If symmetry is applied during refinement or on the reconstructed volume, the user has to define the symmetry (axial rise and rotation of an asymmetric subunit) before starting the refinement. As the program runs iteratively, a rough idea of the symmetry is sufficient to start the refinement. The symmetry parameters have to be checked from iteration to iteration and should be adjusted if necessary. By this approach the optimal symmetry parameter can be estimated iteratively (Behrmann et al., 2012b; Egelman, 2000; 2010).
The quality and accuracy of assigning of the projection parameter depend on the number of reference projection ('sampling'). This is done either automatically or has to be defined by the user. A step size and step range (for x- and y-shifts) and the step size of the angular sampling should start with broader values allowing a global and exhaustive refinement. Once the overall projection parameters are found, the refinement can be continues with local searches with finer sampling. On the one hand this will save computing time and on the other hand will prevent from being stuck in a local minima. In the case of a filament, it is reasonable to allow only side views to be assigned. As the filament is almost perpendicular to the beam direction, the out-of-plane rotation angle ('tilt' or 'theta') can be restricted. If the filaments are already aligned to the y-axis at the stage of boxing, the possible in-plane rotation angle ('rot' or 'psi') is limited, too. Another parameter, which has to be adjusted for each iteration, is the cut-off frequency of the low-pass filter. The currently applied filter frequency should be always the current resolution of the reconstruction (see also subsection 3.4.6) or even less. By this, the so-call 'over-refinement' can be reduced or completely prevented. Over-refinement describes an artificial improving of the current resolution due to a high correlation of noise (Scheres and Chen, 2012). It depends on the used software packages, if the respective sampling and low-pass filter is adjusted manually or automatically (see also subsection 3.4.6).

3.4.4 Correcting for particle movement and beam-induced damage

As a final step of a high-resolution 3D-refinement, it is possible to perform a particle-based movie refinement to compensate for drift and movement of a single particle. It has to be distinguished from the movie alignment of the whole image (see subsection 3.4.1). At the same level, the total dose of the averaged image should be evaluated. High-resolution information is getting lost with a higher applied dose (see also subsection 2.3.1 Transmission electron microscopy on biological samples). Therefore, each movie frame is weighted dose-dependent. In addition, the sample drift in the beginning of the exposure more than in the end due to the applied beam and charging effects.
Relion has a two-step particle-based movie refinement (Scheres, 2014). In a first step, the drift per frame of each particle is estimated regarding its drifted-corrected averaged particle (Figure 3.8a). In a second step, all estimated shift values are applied, the weighting factors are estimated (Figure 3.8b) and a new particle stacks of 'shiny particles' are written out. All frames can either be weighted or some frames can totally be left out for the shiny particles.
Sparx has no implementation of for a particle-based movie refinement and no particle-based movie refinement was applied for Sparx in this thesis. But it is possible to work with 'shiny particles' derived from Relion. Beside that, a particle stack from weighted averaged movie frames can be used to extract the particles from. The software packages 'unblur' and 'summovie' can calculate a weighted average to

compensate at least for the overall beam-induced damage (Grant and Grigorieff, 2015). In addition, the first frame or first frames could be deleted to remove a strong beam-induced drift.

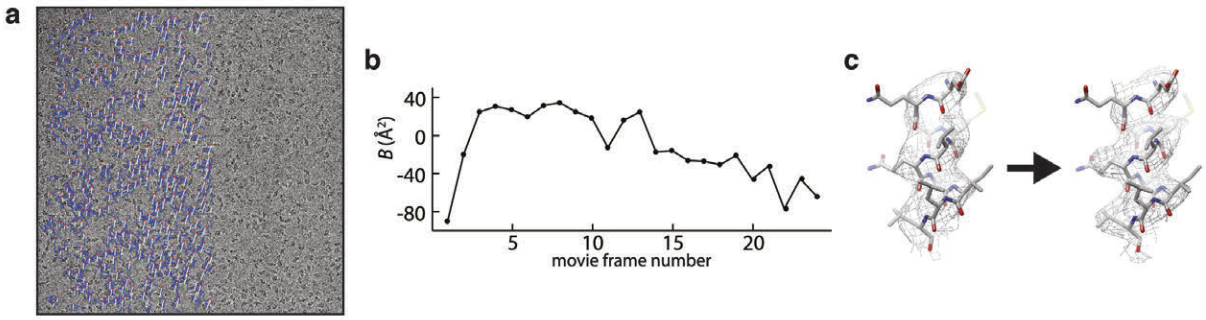

Figure 3.8: Particle-based movie refinement.

a, Example of an image of a single particle project. The drift (indicated by up-scaled arrows) is not unique throw-out the whole image. The right part of the image is the raw image for comparison. **b**, The so-called B-factor is estimated per frame to perform weighting regarding the frame quality. A lower value indicates worse high-resolution information due to high beam-induced drift (first frames) or beam damage (high dose in the last frames). **c**, Secondary structure elements (like the turn of a helix) become more clearly visible density map by applying a particle-based movie refinement and dose-dependent weighting. Figure modified from Scheres (2014).

3.4.5 Methods for sanity check of projection parameters of filamentous samples

No information from adjacent particles can be utilized when performing a 3D-refinement for a single particle. The particle orientation is random. In the case of a segment, which is part of a filament, adjacent or even the whole filament information can be taken into account to define the projection parameters. One simple example is that all segments within a filament have to point either up or down, when aligned to the y-axis. In addition, all other parameters (angles and shifts) should depend on each other. In theory, all other parameters of the same filament could be estimated by knowing the projection parameters of one segment. In reality, a filament is always flexible and not totally rigid. The degree of flexibility is highly sample-dependent. So far, no single particle approach has take this into account. Old single particle approaches (IHRSR; Behrmann et al., 2012b; Egelman, 2000; 2010) did not make use of it and the information was lost once the filament was segmented. Therefore, a new software package was implemented into Sparx (section 4.2). At the same time two other approaches addressed same ideas ('FREALIX', Rohou and Grigorieff, 2014; 'SPRING', Desfosses et al., 2014).
For the pure single particle approach with Relion (applied in section 4.4), after performing 3D-refinement and particle-based movie refinements the final projection parameters were checked regarding the helical consistency within each filament. Therefore, the filaments were split to sub-filaments in the size of ten segments. Within each sub-filament, the median out-of-plane and in-plane rotation angles were estimated and outliers were discarded. By choosing different cut-off values the optimal subset of segments can be established. In theory, only filaments showing no flexibility at all could be used, but this will result in a large reduction of size of the data set.

3.4.6 Post-processing and resolution estimation

After 3D-refinement the actual resolution of the reconstruction has to be determined. Furthermore, the details of the reconstruction can be improved by amplifying of low frequencies, which are under-

represented due to the envelope function ('b-factor sharpening'), and by correction of the MTF of the detector (see also subsection 2.3.1 Transmission electron microscopy on biological samples). The same method for estimation of the resolution can also be applied during refinement to get suitable values for the low-pass filtering (see section before). While in Sparx the user has to set the value manually, in Relion the resolution estimation during refinement is performed automatically.

A 'Fourier-Shell-Correlation' (FSC) is calculated for assigning a resolution value for validation of the quality of a reconstruction. Therefore, the data set is split into two equally sized halves and one reconstruction is performed for each part of the data set. These halves are then compared by a FSC. The FSC describes the correlation value (1 = high correlation; 0 = no correlation) of the two halves regarding a given Fourier-shell (summed up frequency range). A defined cut-off for the correlation value gives the current resolution of the reconstruction. Two different cut-off criteria are applied depending on the 3D-refinement strategies.

The 0.5-criteria ($FSC_{0.5}$) is chosen, when the data set was processed as a whole in each iteration of 3D-refinement and when the two half reconstruction are performed only for the actual FSC calculation (Penczek, 2010c; van Heel and Schatz, 2005). The 0.143-criteria ($FSC_{0.143}$) is applied, when the 3D-refinement is performed by the golden standard approach (Scheres and Chen, 2012; see 2.3.2 Single particle and helical reconstruction).

The resolution of a reconstruction does not have to be homogenous throughout the structure, as for example different regions of a protein or protein complex can be more flexible than other and thereby make it impossible to achieve a high-resolution in that region. A mask of different parts of the reconstruction can be manually applied to get local resolution values. Software packages are available to perform a local resolution map of the full reconstruction ('ResMap', Kucukelbir et al., 2014; 'sxlocres' in Sparx). These resolution maps can be used to either colour the reconstruction (example 'Color suface' in 'Chimera' (Pettersen et al., 2004)) or to filter the reconstruction regarding their local resolution ('sxfilterlocal' in Sparx).

3.5 Model building and refinement

Once a high-resolution reconstruction of a protein or protein complex is obtained, a molecular model ('coordinate' or 'protein data bank' (PDB) file) has to be derived. Different strategies, methods and program packages exist to generate these models. If no model or a homolog structure exists and the structure is totally unknown, the average resolution has to be in the range of 3.5 Å or better to build up the model *ab initio*. If homolog models or parts of the protein complex already exist (like in the case of F-actin, tropomyosin and myosin), these models can be directly utilized to create the new model. Even at lower resolution levels, the resulting models are sufficient for structural interpretation and analysis. A general overview of applicable strategies and programs are given in this section.

3.5.1 Preparation of the EM density map

In comparison to (X-ray) crystallography, the experimental data (EM density map) is at its final stage and is not changed during model building and refinement. Established tools can be adapted, which were originally implemented for data coming from crystallography. Therefore, the EM density map has to be Fourier-transformed to structure factors and phases ('mtz' file, standard file format for software applied in crystallography), which then can be directly used for model building and refinement. Programs in the CCP4 suite were originally used for that purpose (Winn et al., 2011). Recently, protocols for the conversion were published (Brown et al., 2015) and were applied from that time on ('map2mtz' or 'mrc2mtz'). Some of the applied programs need the density map in the 'CCP4'-file format, which can be created using standard image and map handling software packages (e.g. 'e2proc3d' of EMAN2; Tang et al., 2007).

3.5.2 Model building

Ab initio model building

If the resolution of the reconstruction is sufficient and the structure is unknown, the model must be build manually into the EM density map. One major problem is to find the right register or a starting point, if the structure is not known. Often secondary structure predictions can be used to identify respective regions in the protein sequence (Artimo et al., 2012). In addition, tools are available to find secondary structure elements automatically in the density map, which afterwards can be assigned to regions in the density map (Terwilliger, 2010a; 2010b; 2010c). Programs ('Coot', Emsley et al., 2010); 'O', Jones, 2004) exist to build the structure residue by residue and than fit and refine the derived model into the EM density map in real-space. Secondary structure restraints or the 'Ramachandran-plot' (Ramachandran et al., 1963) can often help to find the right conformation of the rotamer. Performing model building, when parts of the model are known can be less complicated and is described in the next paragraphs.

Sequence alignment and homology modeling

If a model or parts from homologous structures exist, these models can be used to generate a homology model. Search of the target sequence ('sequence blast') and a sequence alignment can be applied to find these homolog structures. Programs for a sequence blast are implemented and performed on online servers (Pettersen et al., 2004; UniProt Consortium, 2015). To identify the respective regions, the

sequence can be aligned directly to a reference sequence with 'ClustalOmega' (Sievers et al., 2011). Once a homolog sequence or structure is detected, the model can deal as a reference model to create a homology model with the respective target sequence using 'Modeller' (Sali and Blundell, 1993). A whole online library ('ExPASy') exists for those kinds of bioinformatics tools (Artimo et al., 2012).

Flexible fitting

When a homology model of the structure of interest or when the structure already exists in another conformation, these structures can deal as a starting model (for example crystal structures of myosin or monomeric actin). This starting model has to be flexible fitted into the EM density map. Several program packages exist to perform the calculation. As an input, a model and the respective EM density map is needed. Filter frequency, allowed flexibility and restraints are the main parameters, which have to be adjusted and which will resuls in different performances of the programs. 'DireX' using a 'Deformable Elastic Network (DEN)' approach (Wang and Schröder, 2012) or 'iMODFIT' performing a 'Normal Mode Analysis' (Lopéz-Blanco and Chacón, 2013) were successfully applied for that purpose in this thesis. Finally, the whole model can be manually refined, optimised and missing residues added using Coot (see paragraph *ab initio* model building). Once the overall model is fitted and built, the model has to be finally refined to the original EM density map.
The program suite 'Phenix' has an implemented program for a real-space refinement ('phenix.real_space_refine'; Adams et al., 2011). This tool does not only fit the model into the EM density, but also refines the model to improve the overall geometry of the model. In addition, non-crystallographic symmetry (NCS) restraints (for example different subunits of F-actin) can be applied during refinement and a model for automatically creating reference restraints can be added. The resulting model should carefully checked for overfitting, as no geometry weights can be set in comparison to the refinement described in the next subsection.

3.5.3 Model refinement and validation

Model refinement is essential in crystallography, since the unknown phases are determined and refined during the actual electron density map is created (see section 2.3 Electron microscopy). For a density map derived by cryo-EM, this refinement is performed only to optimize the model into the density and improve the geometry, while the phases of the experimental data remain unchanged. At the same step, the model is evaluated and overall quality is defined including the so-called 'R-factor' (reliability factor, agreement between experimental data and build model; Morris et al., 1992). In addition, the following refinements can use external restraints derived from known high-resolution crystal structures to improve the performance. Furthermore, they are highly tuneable and general protocols were recently published for the software packages 'ProSMART' (Nicholls et al., 2014) and 'Refmac' (Vagin et al., 2004) by Brown et al. (2015). ProSMART is used to generate secondary structure and reference restraints for the refinement. In addition, NCS restraints can be created. REFMAC performs the actual refinement. The refinement depends on different geometry weights, which have to be set by the user. For example a weight defines, how much the model is allowed to change with respect to the input and how much the given restraints are take into account. This weights has to be established before the model is finally refined.

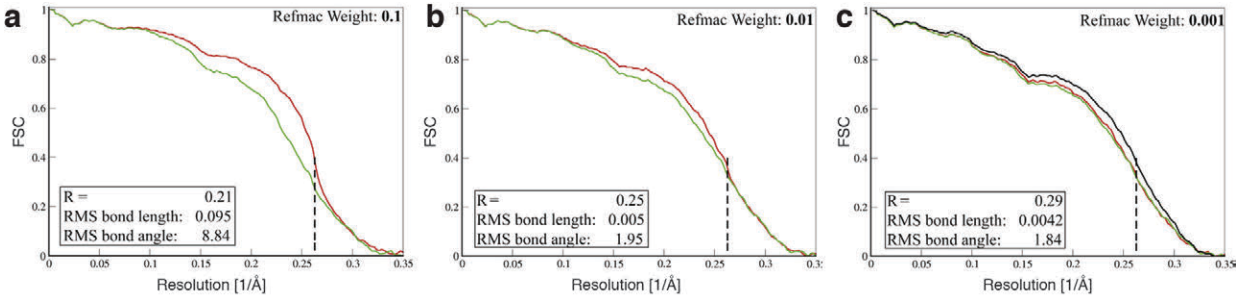

Figure 3.9: Define geometry weights in model refinement.

The geometry weights have to be defined prior the final model refinement is applied. Therefore, the model has to be refined (here performed with Refmac) with different settings using only one derived half reconstruction. Afterwards, the refined model is compared with both halves by calculating a FSC. FSC curves (**a**, **b**) show an overfitting (significant variation of both curves) into the half reconstruction used for refinement (red curve) in comparison to the other half (green curve). With a lower weight in (**c**) both FSC curves of each half reconstruction overlay well indicating a reasonable set of geometry weights. Finally, the model is refined to the full reconstruction (black curve in **c**) with the established settings. Dotted line indicates the estimated resolution of the reconstruction. Especially in (**a**) the overfitting is significant up to the indicated resolution. Some of the value derived for validation of the model (here: R-factor, Rms deviation) can help to identify an improvement of the geometry or overfitting. Figure modified from Fernández et al. (2014).

In cryo-EM the following protocol is widely exempted to define the geometry weights (Amunts et al., 2014; Bai et al., 2013; Fernández et al., 2014; Greber et al., 2014). Two independent reconstructions of two halves exist, as in most cases the 3D-refinement is performed by using the golden standard approach (see 2.3.2 Single particle and helical reconstruction). Initially, only one half reconstruction is taken into account to refine the model. In addition, all atoms of the model are randomly displaced (by 0.5 Å to 1 Å) to prevent already introduced bias. After a refinement with one set of geometry weights to one half, the model is compared to both halves with a FSC. For the FSC-calculation the refined model is converted to a density map with the respective pixel size with Chimera ('molmap') or EMAN2 ('pdb2mrc'). If the FSC do significantly differ, the geometry weights were too unconstrained and the model was overfitted to the half reconstruction, which was used for the refinement (Figure 3.9a, b). After establishing the right geometry weights, the obtained parameters are used to refine the model against the full map (Figure 3.9c). Most models are refined by these strategies either with Refmac (Vagin et al., 2004) or 'phenix.refine' (Adams et al., 2011).

After the refinement of the model, the result has to be validated by estimation using the 'Ramachandran-statistics', 'Rms deviation' and 'Clashscore'. Online servers like 'MolProbity' (Chen et al., 2010) or 'wwPDB' (Berman et al., 2003) perform the validation.

3.6 Tools for visualization and characterization of a protein structure

A variety of techniques and protocols exist for interpreting a derived protein model. Reasonable methods highly depend on the context. In the case of a protein complex undergoing conformational changes, the mainly applied tools are methods for analysis and visualization of the interfaces and for performing conformational changes.

The program suite 'Chimera' was used for all visualisations and rendering of videos (Pettersen et al., 2004). In addition, it incorporates several interfaces to other methods (e.g. homology modelling with Modeller, see section before). 'PyMOL', a similar visualisation tool, was not applied for this thesis but is widely used in structural biology (The PyMOL Molecular Graphics System, Schrodinger LLC.). Both programs can handle density maps and coordinate files of a protein model.

For all surface depictions the model was first protonated at the respective pH using the H++ online server (Anandakrishnan et al., 2012). The derived protonated model was further used to colour the surface regarding its electrostatic Coulomb potential ('Coulombic surface coloring' in Chimera). In addition, the protonated model was used to visualize the hydrophobicity. For that purpose, for each amino acid an additional attribute was defined ('Define attribute' in Chimera) using the scale derived by Hessa et al. (Hessa et al., 2005). Especially when analysing different states of a molecule (e.g. in the case of myosin states), a morph can be obtained to determine, understand and visualize the conformational changes. For overlaying the different conformational states, the 'MatchMaker' tool implemented in Chimera can be applied. When the aligned models differ significantly, it has to be evaluated, which domain is superimposed. The 'Morph Conformations' tool implemented in Chimera can finally calculate morphs between two or more superimposed models. It has to be pointed out that the derived morphs do not have to reflect the actual trajectory of the conformational changes. More reliable for that propose are molecular dynamics (MD) simulations. These calculations are computationally intensive but can give more insights into the actual movement with a higher reliability.

All figures of my doctoral thesis were created and assembled with Adobe Illustrator and Adobe Photoshop CS6.

4 Results & Discussion

As described in Material and Methods chapter in section 3.1, different protein isoforms as well as proteins from different species were provided by the Manstein group (MHH) to obtain structures of a F-actin-tropomyosin and a human F-actin-myosin-tropomyosin complex. The protein samples used for the performed reconstructions in my doctoral thesis are listed in Table 3.1 in subsection 3.1.1. I performed different reconstitution experiments (section 4.1) to obtain suitable protein complexes to achieve high-resolution structures presented later in section 4.3 (F-actin-tropomyosin complex) and section 4.4 (F-actin-myosin-tropomyosin complex). In section 4.2 I give an overview on the improved helical reconstruction workflow implemented in HELICON. Finally, I summarize my results in a comprehensive discussion and outlook in section 4.5.

4.1 Reconstitution of the protein complexes

A first task was to obtain suitable actin filaments, which were further decorated with tropomyosin. Tropomyosin stabilizes the filaments and improves the filament quality and distribution on the EM specimen. Negative staining experiments were performed to evaluate the filament quality of F-actin and to obtain an appropriate binding of tropomyosin to F-actin. These experiments are described in subsection 4.1.1 and 4.1.2. The subsequent vitrification process and further difficulties of cryo-EM on filaments are given in subsection 4.1.3.
The human F-actin-myosin-tropomyosin structure was obtained by decorating the F-actin-tropomyosin filaments with myosin. The same experiments introduced above could be used to create a human F-actin-tropomyosin complex. The decoration of these filaments with myosin introduces strong bundling, which cannot be prevented by a short incubation time. Therefore, the reconstitution of the actomyosin complex was optimized. To reduce the bundling effect, an on-the-grid decoration with myosin was the best strategy, which I already developed during my master thesis (von der Ecken, 2013). The results are presented in subsection 4.1.4.

4.1.1 Evaluation of F-actin with negative staining EM

Negative staining EM was used for an initial evaluation of the sample condition and quality as well as to adjust the concentration to obtain a suitable distribution. All protein samples were prepared as described in Material and Methods chapter. As reproducibility is an important issue, a pre-screening with negative staining EM was performed to ensure the same starting point for further cryo-EM experiments (later in this section).

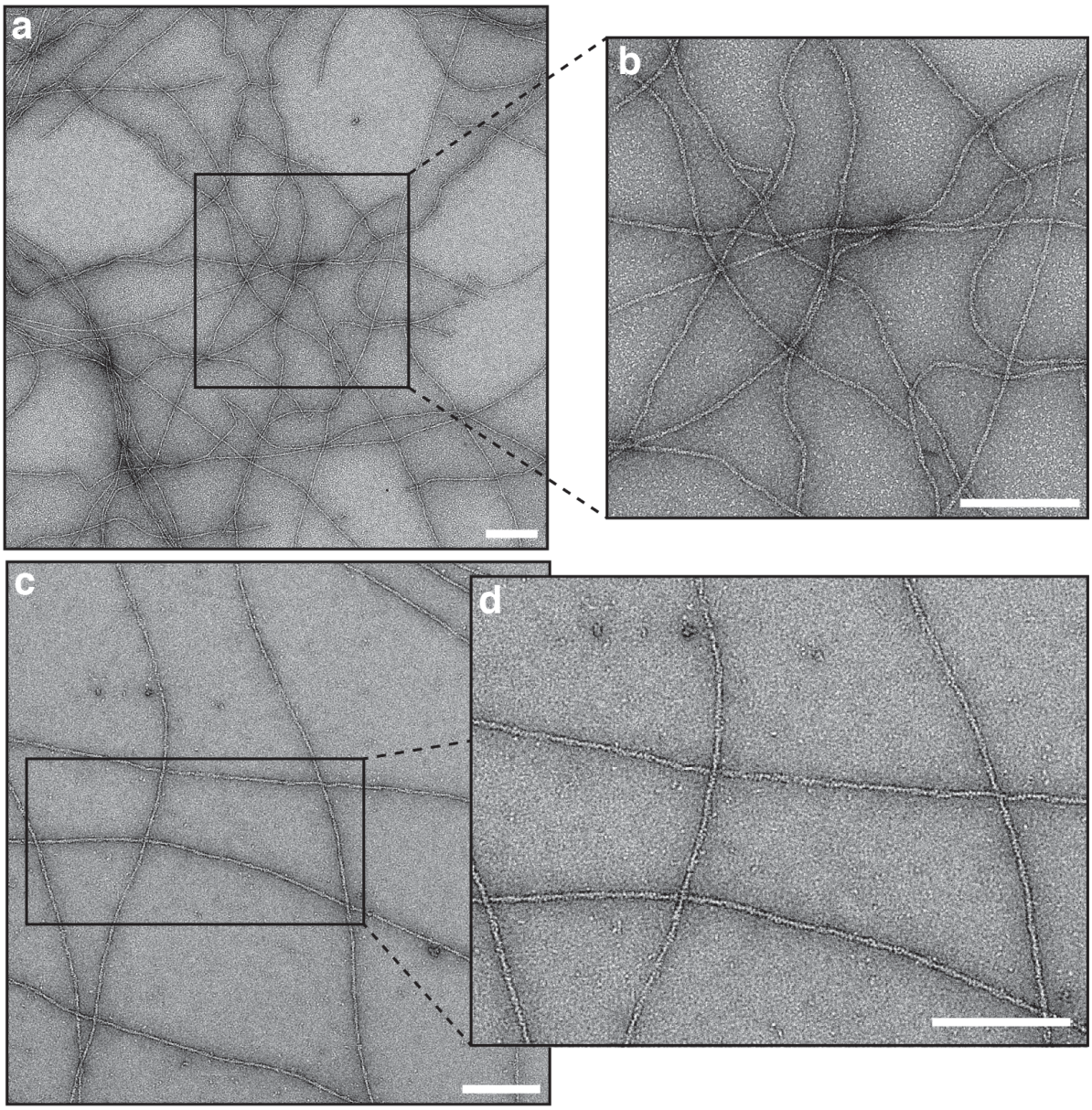

Figure 4.1: Evaluation of the quality and concentration of F-actin sample.

Micrographs of negatively stained F-actin samples at slightly different concentrations (**a** higher than **c**). The concentration was adjusted empirically. Examples show reasonable distribution on the grid. The filaments are long (> 1µm) and show the characteristic features of F-actin (e.g. visible subunits). A distribution like this is suitable for further tests like tropomyosin binding or on-the-grid decoration with myosin. Scale bars 200 nm.

In Figure 4.1 a representative optimal F-actin sample is given with respect to the filament concentration and distribution. A F-actin concentration similar to the one shown in Figure 4.1c was used for further decoration experiments with tropomyosin and myosin. Moreover, to judge over the quality of the filaments their length as one criterion (> µm) and if F-actin characteristics were visible (double-stranded helix, narrow and wider areas, subunits) were checked. In addition, the background should only show a few aggregates (G-actin monomers or oligomers). Furthermore, an optimal sample should show almost no bundled F-actin filaments, because they will most probably not be decorated with tropomyosin or myosin, as the individual filaments block each other. If the filament quality did not meet all criteria, the purification was repeated starting with stored G-actin samples and applying polymerization and depolymerisation rounds.

4.1.2 Reconstitution of the F-actin-tropomyosin complex

All experiments were performed with freshly polymerized F-actin samples and the highest concentration was used initially, which was obtained after the final purification step of F-actin (resuspended F-actin pellet, see subsection 3.1.3). However, standard absorptions measurements give inaccurate results for the concentration of filamentous samples like F-actin. Therefore, not only the concentration of F-actin but also the concentration of tropomyosin empirically had to be adjusted. To obtain a suitable F-actin-tropomyosin complex the total tropomyosin amount was stepwise increased.

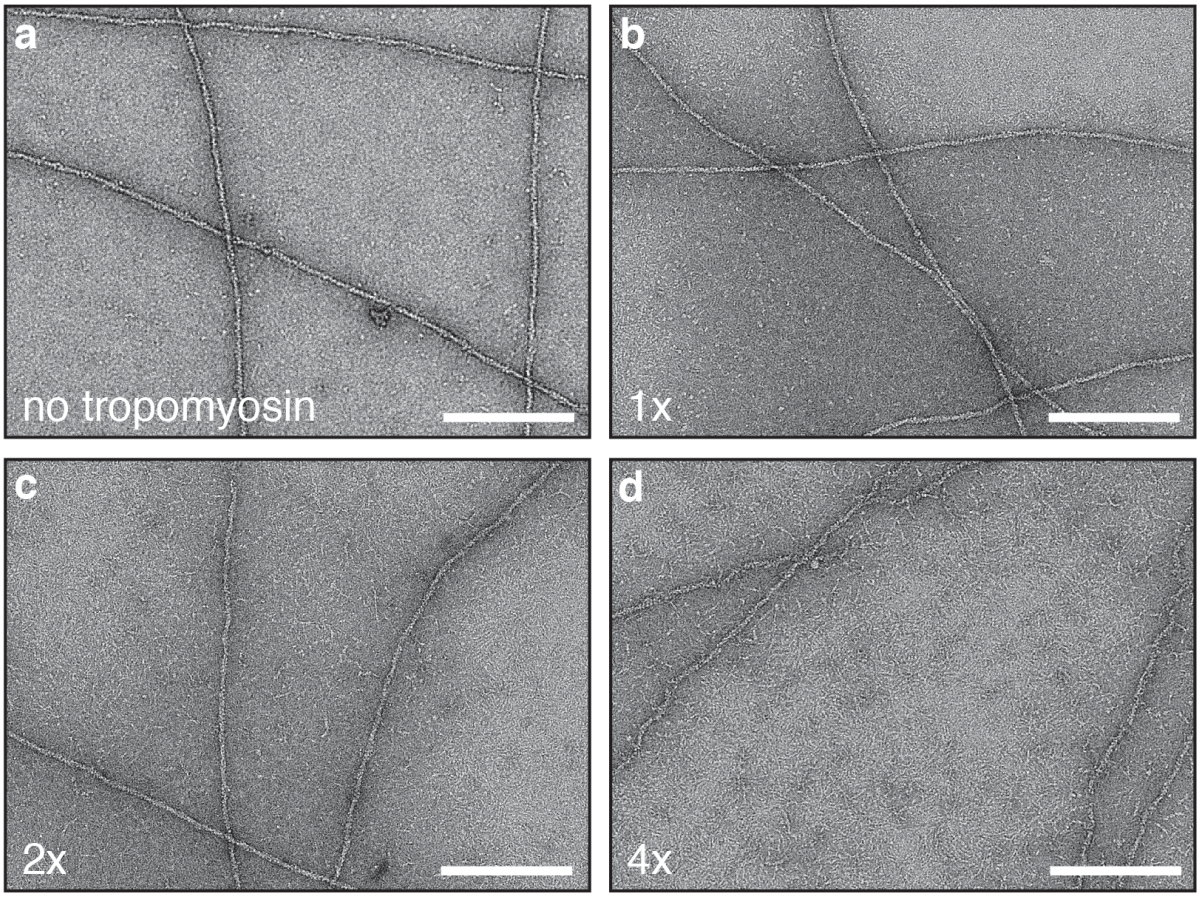

Figure 4.2: Empirical adjustment of tropomyosin concentration.

The four representative images illustrate the empirical adjustment of the tropomyosin concentration. **a**, The sample as shown in Figure 4.1c shows only small particles in the background (most probably G-actin monomers or oligomers). **b-d**, Same F-actin concentration but with increased amount of tropomyosin (1- in **b** to 4-fold in **d**). For further studies a tropomyosin concentration similar to the one shown in **c** is chosen, as yet several tropomyosin molecules (elongated particles) are visible in the background but do not harm the filament quality as they do in **d**.

The respective amount of tropomyosin with F-actin in solution was incubated for at least half an hour before diluting it to the established F-actin concentration as shown in Figure 4.1c. This whole reconstitution experiment with different tropomyosin concentrations is illustrated in Figure 4.2. The filament concentration of all subfigures was adjusted to the one of bare F-actin shown in Figure 4.2a. Afterwards, the best actin-to-tropomyosin ratio was chosen. Therefore, an F-actin-tropomyosin sample was used, which showed a clear amount of unbound tropomyosin molecules in the background (Figure 4.2c) while the filaments were still stable and unaffected. If the tropomyosin concentration was too low, it cannot be ruled out that the filaments are only partly decorated (Figure 4.2b). When the

concentration of tropomyosin was too high, tropomyosin destroys the filament during applying the solution to the grid or drying (Figure 4.2d). In addition, the high amount of unbound tropomyosin molecules could reduce the contrast in the final cryo-EM images.

4.1.3 Vitrification of F-actin complexes

Although the concentration was roughly adjusted with the help of negative staining EM before, the optimal F-actin concentration has to be optimized during the vitrification procedure for every protein complex. Especially, the applied amount of protein solution and the blotting conditions have a great impact on the concentration as well as sample distribution on the holey-carbon grids (also see subsection 3.2.2). Furthermore, the sample concentration is increased trough the process of manual backside blotting, as the filament solution gets sucked though the holes and the filaments stick to the carbon edges.

In Figure 4.3 several examples of different concentrations and distributions of the F-actin filaments as well as ice conditions are given. One essential aspect of the vitrification process is rapid freezing as well as storage of the sample at liquid nitrogen temperature to avoid crystallisation of the ice. Nevertheless, it is possible that areas of the grid still show crystalline ice (Figure 4.3a), as the freezing procedure is not homogenous. Therefore, these areas should not be used for data collection. Furthermore, F-actin filaments can be harmed (fragmented and destroyed) by shear forces, which arise during the blotting process (Figure 4.3b). This often happens when automatic blotting is performed or small holes sizes are used (e.g. box size of 1.2 µm).

The filament concentration depends on the ice thickness and vice versa. Once a protein concentration similar to the given example in Figure 4.3c is obtained, the concentration can be fine-tuned. A simple reduction of the concentration by diluting the sample or an increase of the blotting time can result in empty holes. Furthermore, as a thin ice layers (< 50 nm) are often instable at low concentration of filaments, a small amount of detergent (0.01-0.04 % Tween®20, Sigma-Adrich) was added to change the surface tension and viscosity of the solution. Thereby, a thin film of solution can spread and remain in the hole while getting frozen. It is not possible to obtain a very thin ice layer in the holes, as at the same time the ice thickness has an impact on the F-actin distribution. If the ice thickness is less than 30 nm, the filaments will be displaced accordingly to the ice thickness gradient. Consequently, areas with very thin ice do not contain any filaments (example given in the centre of Figure 4.3d, e). A gradient of the ice thickness can be recognized by a gradient in brightness of the image. Interestingly, the filaments can stabilize the ice layer. Thereby, a compromise between thin ice (to obtain the highest contrast) and filament concentration (to get a high yield of particles per image) has to be found. Figure 4.3f gives an example of a reasonable compromise, as the concentration is not too high and the filaments are still separated and not bundled. In addition, the filaments are spread over the entire hole indicating that the ice is thicker than 30 nm and thus does not influence the filament distribution.

The given strategies were applied to obtain the best vitrification conditions for the F-actin-tropomyosin complex. The final protocol is described in the Applied Methods subsection 4.3.8. The same conditions of F-actin were used to prepare the human F-actin-tropomyosin complex decorated with myosin (see next subsection).

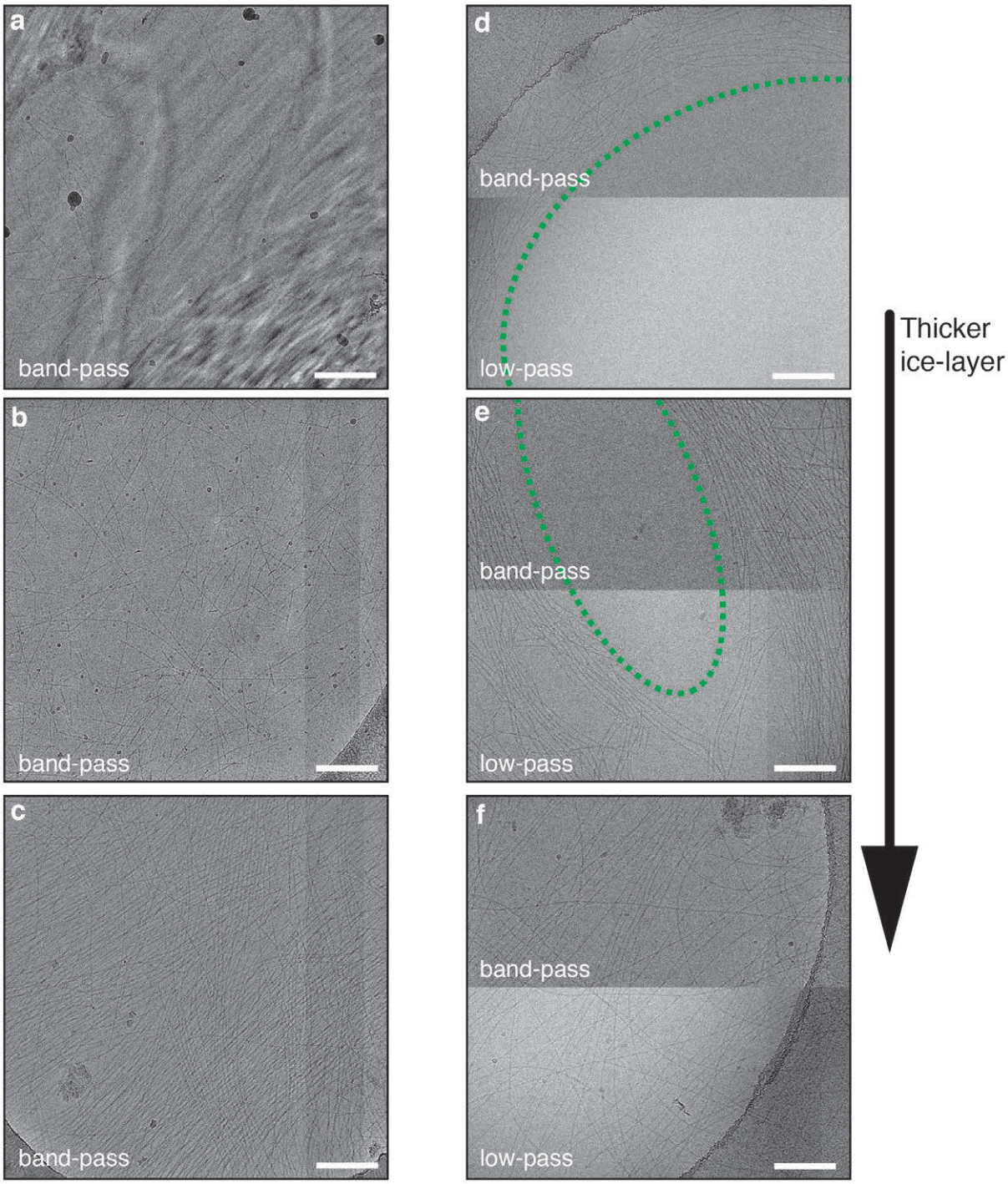

Figure 4.3: Screening for best vitrification conditions for F-actin-tropomyosin.

a-b, Examples of vitrified samples with insufficient ice and sample quality. **a**, Areas or the whole grid suffer from crystalline ice. **b**, In some cases, F-actin gets fragmented, as for example often when using an automatic blotting device instead of manually blotting. **c-f**, The ice thickness and actin concentration depend on each other. **c**, The concentration of F-actin is too high to perform any further structural analysis but the ice thickness is in the desired range (~40-60 nm). **d**, The ice layer is too thin (<25 nm) and the filament concentration too low. Consequently, F-actin gets pushed to the edges of the holes, which leads to an empty central part of the hole (highlighted by green doted line). **e**, A higher concentration of actin stabilizes thin layers of ice and makes it therby possible to obtain thinner ice layers occupied with filaments. Nevertheless, the central part is still too thin and empty (highlighted by green doted line). **f**, Compromise between F-actin concentration and ice thickness. The illustrated condition was the one I used for data collection of the F-actin-tropomyosin data set. For a better visualization all micrographs are band-pass filtered and the lower half of micrographs in **d-f** are low-pass filtered in addition. Darker vertical column in some images (**b**, **c**, **e**, **f**) on the right originates from incorrect gain references. Scale bars are 200 nm.

4.1.4 Decoration of F-actin with myosin in cryo-EM

As introduced above, several problems were encountered when incubating myosin with F-actin in solution. In particular, the main problem was that with myosin decorated F-actin-tropomyosin filaments tend to bundle. These bundles are not suitable for structural analyses with TEM. Therefore, the decoration protocol were changes to a preincubation of the F-actin filaments on the grid and adding myosin solution on-the-grid subsequently.

As described in subsection 2.2.1, a decoration of F-actin with the head region of myosin forms a characteristic arrow shape. Thereby, the naming as pointed and barbed end were introduced for F-actin (see also subsection 2.2.2). This prominent shape can be used to judge the quality and homogeneity of decoration. Furthermore, as filaments decorated with myosin heads have more than twice the diameter, the ice thickness must be thicker than for actin-tropomyosin filaments.

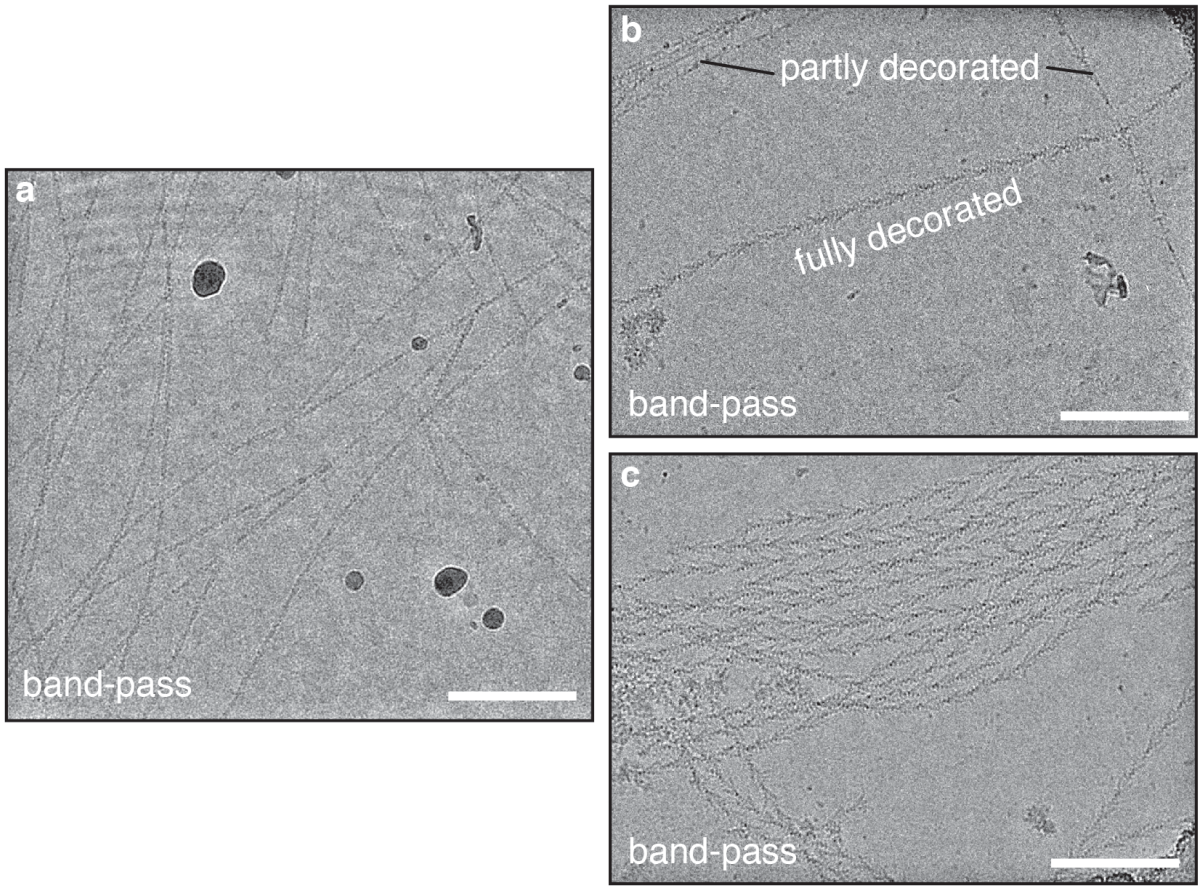

Figure 4.4: Decoration of F-actin with myosin.

a, Evaluation of quality and concentration of the initial F-actin sample, which was used for the reconstitution experiments with myosin. The F-actin concentration similar to the sample illustrated in Figure 4.3f. **b**, Applying myosin to the preincubated filaments at a low concentration, results in a partial decoration of the filaments. Interestingly, myosin is not equally distributed over all filaments indicating the a cooperativity of myosin binding to F-actin (especially when tropomyosin is bound to the actin filament before). **c**, When using a higher concentration of myosin (~ 1 - 5 µM) all filaments are fully decorated. All micrographs are band-pass filtered for a better visualization. Scale bars 200 nm.

Figure 4.4a illustrates the starting point, which is a pure F-actin-tropomyosin sample going along with optimized vitrification conditions (see subsection above). The filaments are prefixed over the holes on the carbon edges. Although the filaments are preincubated on the grid and most of the protein solution is blotted, an excess of protein solution always remains on the grid. This solution contains

filaments, which are not attached to the carbon surface of the grid. Consequently, it is not possible to completely suppress the bundling effect of myosin, which is applied afterwards.

After a preblotting step of the F-actin-tropomyosin solution (see also final protocol in Applied Methods in subsection 4.4.11) a small amount of myosin solution was applied directly on the grid (1-2 µL). The concentration has to be sufficiently high to decorate all actin filaments, while the myosin in the background is still minimal, as it decreases the contrast of the images. The decoration of F-actin with myosin is a very fast process. Therefore, the incubation time can be neglected, as binding happens during the time, which is needed to perform the vitrification procedure. A too high concentration can lead to a total loss of all filaments (the filaments get flushed by the strong myosin flow). In Figure 4.4b an example of an image is given showing an intermediate concentration of myosin solution applied to the F-actin-tropomyosin. At this concentration some filaments start to be fully decorated while others are either partly decorated or bare. This concentration is not yet sufficient but should be further increased. As the myosin molecules are not equally distributed over all filaments at this intermediate concentration of myosin, it is reasonable to assume that the myosin binding occurs in a cooperative manner, especially when tropomyosin is bound before blocking the position (see open or Apo-state in subsections 2.2.1, 4.3.6 and 4.3.7). This behaviour (of having either totally decorated or bare filaments) allows the usage of heterogeneous sample, as the data can be digitally purified during filament selection or by other methods (for example by evaluating the filament diameter in 2D-classifications). It was shown that two different reconstructions (one with and one without bound myosin) derived from the same sample and data set could be obtained in parallel (performed by Behrmann et al; 2012a).

The aim was a complete decoration of all actin filaments, as the overall yield was always quite low. Another issue was, that the sample often contained lots of bundled filaments although the bundling was reduced by the on-the-grid decoration (Figure 4.4c). To achieve the results presented in section 4.4, around 70 % of the micrographs were deleted because of insufficient decoration, filament concentration or ice quality. Therefore, all grids were screened with caution before starting the actual data collection to improve the overall yield.

4.2 Improved helical reconstruction: HELICON

Analysing helical assemblies or complexes (in my case F-actin filaments) requires its own methods to determine the projection parameters when performing a reconstruction. First pioneers in this field applied a Fourier-Bessel approach to process helical objects (De Rosier and Klug, 1968). This method needs long, straight and rigid filaments to determine required information in Fourier space, which is not given for a variety of biological samples. In the last two decades, single particle methods have been used with great success to reconstruct 3D-density maps of single molecules (Frank, 2015) (see also subsection 2.3.2). These methods have been adapted to proteins with helical symmetry (filaments) by the IHRSR (iterative helical real space refinement) algorithm (Egelman, 2000). In this approach the filament is split into single segments, which are treated as single particles from then on. The respective programs were recently implemented in the software package Sparx (Behrmann et al., 2012b; Hohn et al., 2007). For a more general introduction see subsection 2.3.2 and section 3.4 and Material and Methods chapter, respectively.

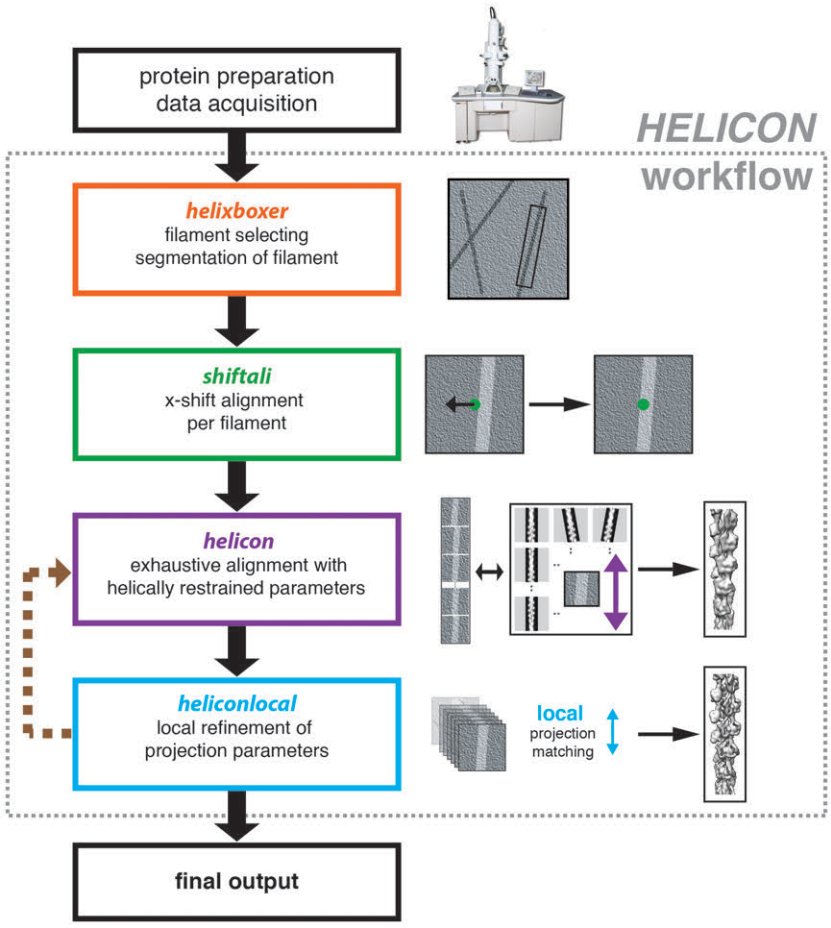

Figure 4.5: The *HELICON* workflow.

Overview of the image processing workflow of HELICON for helical objects (filaments) implemented in the software package Sparx. The helical symmetry parameters are taken into account during the alignment precedure. The HELIcal symmetry CONstrains (HELICON, helical geometrically constrained reconstruction) the projection parameters of each segment within a filament.

So far, no single particle approach utilizes the symmetry within a filament to restrain the projection parameters during refinement. Therefore, we wanted optimize the helical reconstruction approach in collaboration with Prof. Dr. P.A. Penczek of the University of Texas (Houston). For that purpose, we

implemented and derived a new workflow into the software package Sparx and improved each step of the procedure starting with the extraction of the segments (helixboxer), over pre-centering of the segments (shiftali) and the actual 3D-refinement using helicon and heliconlocal (see subsections 4.2.1 and 4.2.2). The overall workflow of the HELICON package (HELIcal CONstrains, helical geometrically constrained reconstruction) is given in Figure 4.5 and described in this section. Afterwards, I successfully applied the derived protocol on my F-actin-tropomyosin data set (see next section 4.3). In addition, the performance was tested on MAVS filaments (Wu et al., 2014). P.A. Penczek and his postdoctoral fellow J. Fang performed the development of the code. I continuously supported the development by applying new routines on my structural data, debugging and testing the code and introducing new ideas to solve problems when having data of an actual biological sample in contrast to simulated data.

The HELICON workflow needs as an input the micrographs and the symmetry parameters of the respective filamentous sample. The symmetry parameter can be estimated by an evaluation of the power spectrum averaged over all segments (not discussed). Thereby, symmetry specific reflection lines (layer lines) arise which can be analysed to estimate the rise and azimuthal rotation (Egelman, 2014; 2015). In addition, the CTF information of each micrograph is imported to the header during the extraction of the segments (see also subsection 3.4.1).

4.2.1 Helixboxer and shiftali

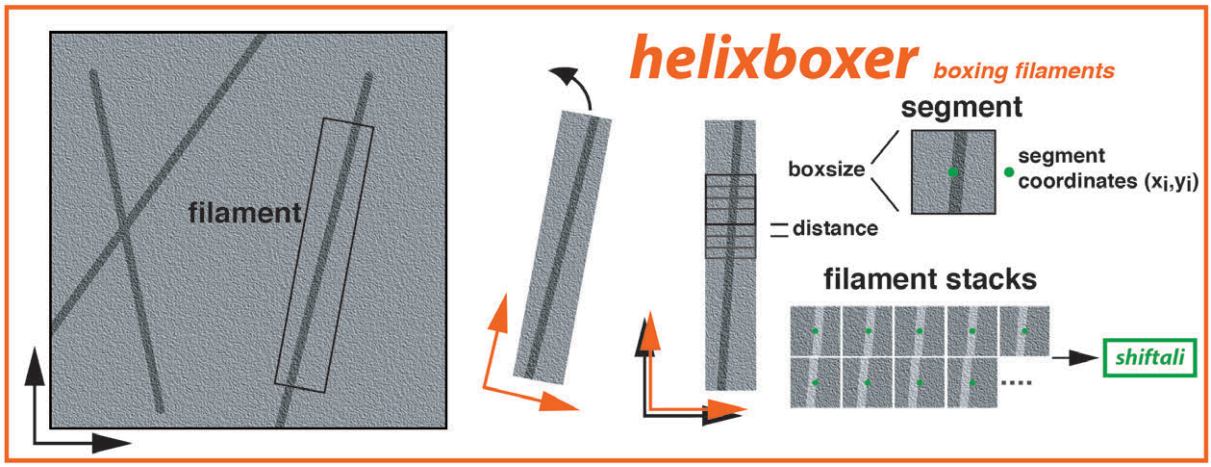

Figure 4.6: *Helixboxer* - manual boxing of filaments.

After a manual selection of individual filaments, they get pre-rotate relative to the filament axis. Next, respective segments are automatically extracted with a defined box size and distance. The coordinates (x_i, y_i) define the position of each segment within a micrograph and filament stack. The coordinates per segment and an ID per filament are necessary for determination of the projection parameters and to constrain the parameters with respect to the helical symmetry of each filament.

The first step, as well in single particle reconstruction, is the selection of the filaments (see also subsection 3.4.1) and scheme in Figure 4.6. Two pairs of x-y-coordinates, which represent the start and end pixel position of each filament, define the filament position. Afterwards, each filament is rotated to the longitudinal axis of the box, which is the filament axis. The axis can be slightly off-centred and not totally parallel to the actual filament due to the manual selection procedure. In the next step, each filament is split into single segments with a defined box size and distance of adjacent sitting boxes automatically. The distance has to be at least the size of the rise of the filament (definition of the symmetry parameters of a helical object see subsection 2.3.2).

A unique identification number per filament (filament ID) is added to the header to enable the application of constraints in a further step within the same filament. In addition, the original coordinates of each segment are saved in the header. Thereby, the belonging of each segment to a filament and the order of segments within one filament are stored and recoverable.
As the reliability of the projection parameter restrains, which are calculated from all segments belonging to one filament, increases with the number of segments, filaments with only a few segments are discarded. In conclusion, the whole data set can be interpreted as a data set of single filament stacks defined by filament ID. In some cases, in particular for strongly curved filaments, the overall alignment quality can be later improved by splitting the filaments into shorter parts. For that purpose the respective filament IDs can be extended by an index (e.g. a, b, c ...). For the initial refinement it can be useful to bin the data set to saves computation time. To maintain the filament information the coordinates of each segment have to be rescaled accordingly.

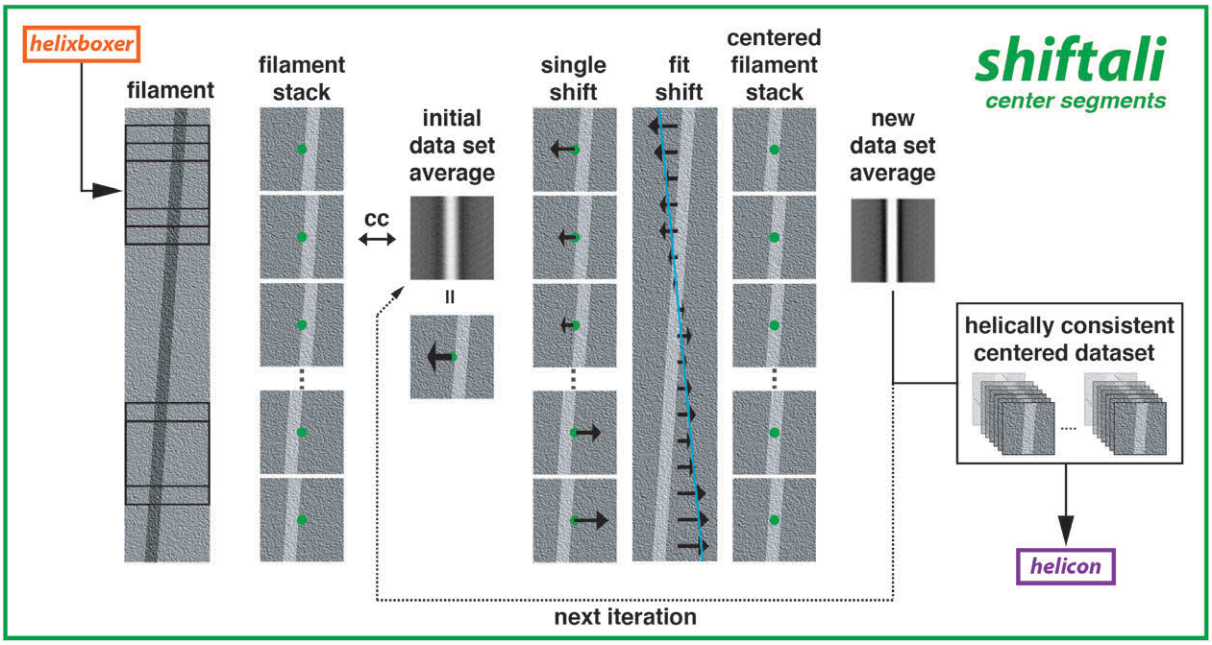

Figure 4.7: *Shiftali* - centering the segments.

Each segments is centred with respect to the rest of the filament. A x-shift (indicated by an arrow) is determined for each segment by a peak search in a cross-correlation (cc) of each segment with the average of all segments of the data set. Afterwards, based on the calculated shifts of all segments belonging to one filament a linear fit is calculated (blue line), which is be used to replace incorrectly estimated shifts of single segments. This procedure is performed iteratively. Finally, all x-shift are applied to the data set to create a centred stack. The centred filament stacks are still consistent with the helical architecture of the filament.

Due to the manual selection of the filaments extracting can result in off-centred segments. Therefore, all segments are centred with shiftali in plane subsequently. Shiftali is the first program (Figure 4.7), which uses the filament information to constrain the search of the x-shift (black arrows in Figure 4.7). The determination of each shift bases on a peak search of a cross-correlation (cc) of each segment with the average of all segments of the data set. But the shift of a single segment can be prone to alignment errors. Therefore, to compensate for outliers a least square fit over all estimated shifts per filament is calculated (blue line in Figure 4.7). Shiftali is executed iteratively until it converges. The comparison of the initial average of all segments with the resulting average illustrated the successful centering. To prevent interpolation errors the shifting is performed in integers of pixel. Finally, the shifts are physically applied on the image. The resulting filament stacks are still consistent with the architecture

of the filament and directly serve as an input for the program helicon, which performs the initial 3D-refinement.

4.2.2 Helicon and heliconlocal

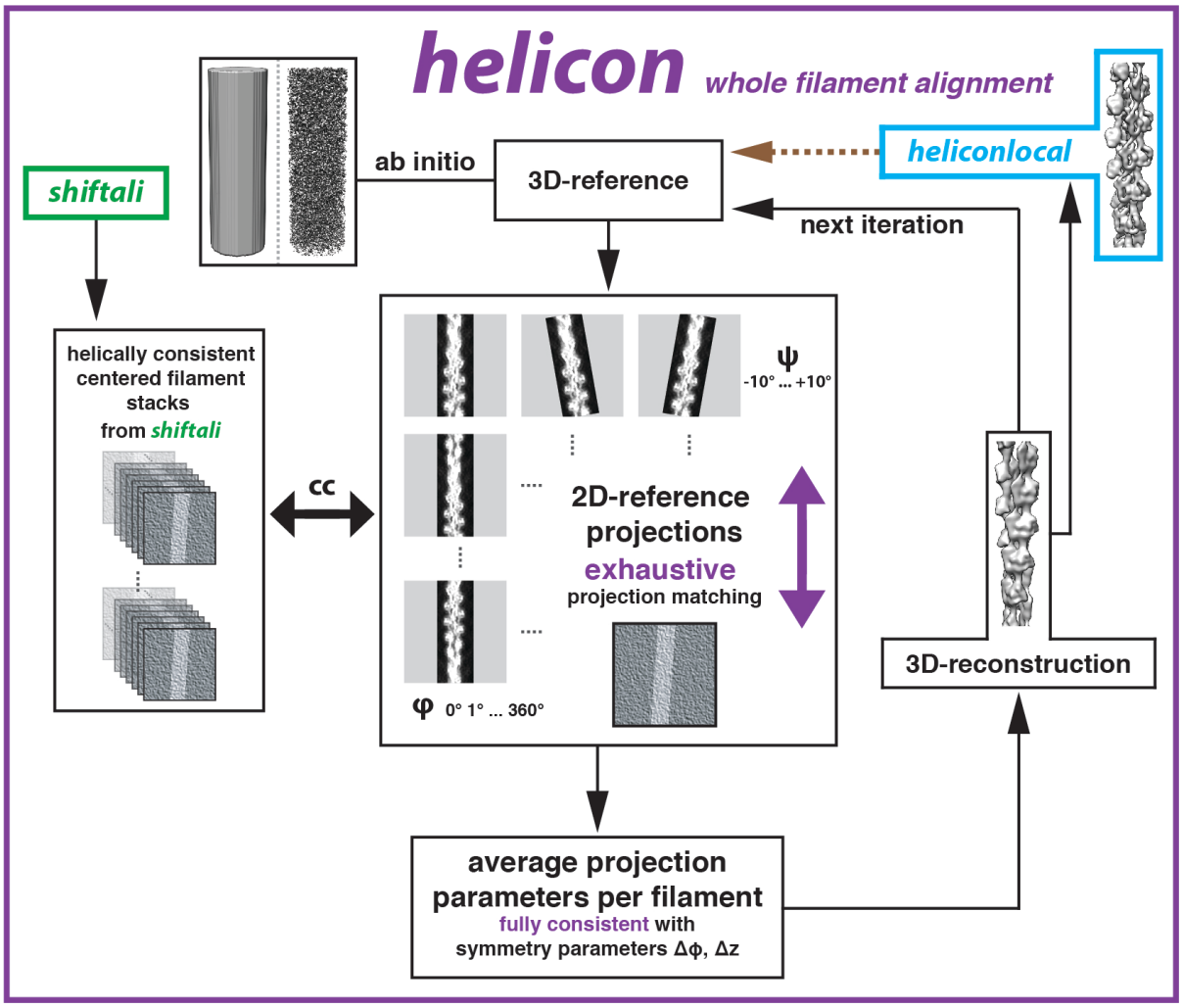

Figure 4.8: *Helicon* – initial aligning of the segments.

Helicon is the first part of the 3D-refinement, in which all segments within the same filament are aligned with respect to its helical symmetry. The search for the projection parameters is exhaustive and the resulting projection parameters are fully consistent with the symmetry parameters (rise Δz and azimuthal rotation angle $\Delta\Phi$).

Helicon is the first part of the 3D-refinement (Figure 4.8). Analogue to single particle reconstruction methods an initial 3D-reference is needed. For a filament with a known helical symmetry a cylinder (or cylinder filled with Gaussian noise) is sufficient and deals as an initial 3D-reference. Almost all projection parameters (x-, y-shifts; in-plane angle Ψ and projection angle φ) are estimated. The out-of-plane angle is kept at 90 ° during the refinement with helicon, as the filament is almost perpendicular to the transmission direction (see Figure 2.15 and subsection 2.3.2, parallel to the ice layer). The respective parameters are determined per segment. The search is exhaustive (all reference projections are considered as possible candidates). In addition, the step sizes of shifts and angles for the reference projection are rather big (e.g. at least integer pixel and angles, see also Figure 2.15 and subsection 2.3.2). The in-plane rotation is limited to a maximal value, as the filaments should already be relatively well aligned due to the pre-rotation during extraction of the segments. Therefore, the

maximal in-plane rotation angle depends on the quality of the prior manual selection, the performance of shiftali and should be in the range of a maximal angle of 10 ° to 15 °. A least square fit of the projection angle φ and the x-/y- shifts is performed after each iteration in helicon. The in-plane rotation angle constraint of the current version of helicon is limited to the orientation of the segments of one filament, as they should all point into the same direction (up or down). Furthermore, the y-shift should not exceed the half of the rise in both directions when using the step size of a rise to perform the extracting of the segments. In helicon no relaxing to the determined fit should be allowed (only optionally). In theory all projection parameters could be derived from one set of parameters representing one segment per filament, if the filaments would be perfectly rigid and symmetric. Finally, a 3D-reconstruction is calculated and deals as a reference for the next iteration of refinement or used as an input for heliconlocal. In the current version there is no convergence criteria implemented. In a future version the resolution could be considered as a possible criterion (see also section 4.5).

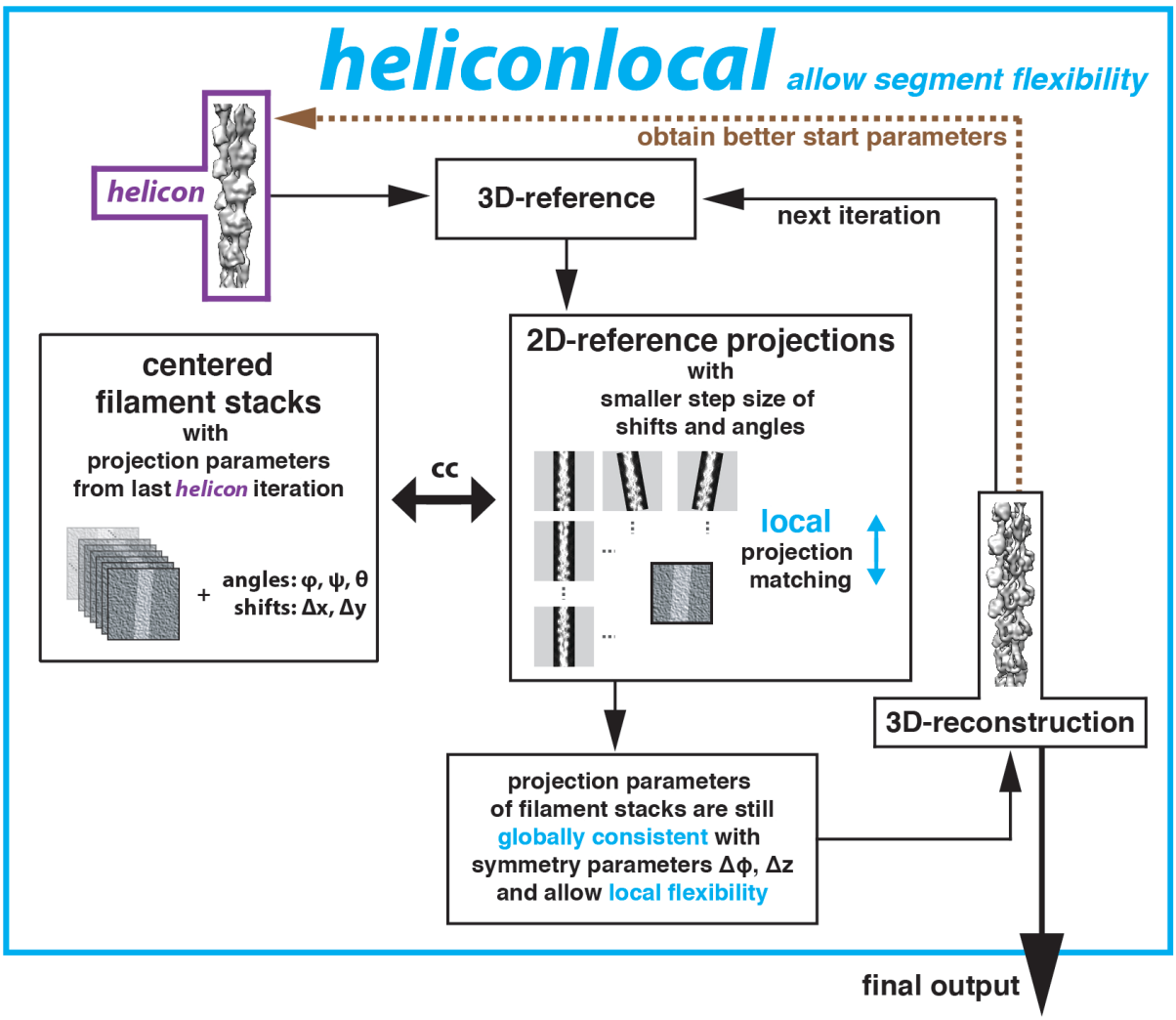

Figure 4.9: Heliconlocal - allowing flexibility to the segments within a filament.

Heliconlocal is the second part of the 3D-refinement, in which all segments within the same filament are still refined with respect to the helical symmetry but small variation are allowed. Thereby, the search for the projection parameters is locally relaxed and the resulting projection parameters can take account of flexibility.

Helicon is used to establish the overall projection parameters while keeping them consistent with the filament architecture. Due to physiological variations and flexibility of the biological sample, these parameters need to be relaxed to obtain and recover high-resolution features of the structure. In heliconlocal this idea is realized by broadening the allowed range of parameters within the final fit of all parameters within one filament. In addition, the step sizes of projection angles and shifts used for the 2D-reference projections are reduced. In contrast to helicon the out-of-plane angle is no longer fixed to 90 ° but also determined via projection matching. The out-of-plane angle is not constrained within a filament. As the overall orientation is already determined, the possible candidates during the projection matching for all parameters can be limited to the neighbourhood (local refinement) to reduce the processing time. Analogue to helicon the refinement is performed iteratively and the final 3D-reconstruction represents the final electron density map or is used to obtain better start parameters with helicon by starting from the beginning (indicated by brown arrows in Figure 4.8 and Figure 4.9).

In the software package Sparx, consequently also for helicon and heliconlocal, an user-defined function is needed to perform the 3D-refinement (see Sparx wiki for further details, http://sparx-em.org). The user function enables the user, for example, to apply a mask to the map during the refinement (cylinder or soft-edge mask of the filament structure), to amplify underrepresented frequencies (detector specific) to recover high-resolution information (power spectrum adjustment) and to define a filter frequency per iteration representing the current resolution. Although the overall workflow of HELICON is developed to have a simple strategy to reconstruct a filamentous sample, each step has to be evaluated with caution (e.g. checking for overfitting or noise-alignment) and the user has to be trained how to use the workflow in an appropriate manner. My results, which I present in the next section 4.3, proved the potential and strength of HELICON. Nevertheless, this is only the first version and can be further improved (see section 4.5 Comprehensive discussion and outlook).

4.3 Structure of a skeletal F-actin-tropomyosin complex

This section was original published in *Nature* in 2015 as:

von der Ecken J., Müller M., Lehman W., Manstein D.J., Penczek P.A., and Raunser S. (2015): *Structure of the F-actin—tropomyosin complex.* Nature 519, 114-117.

Online version: http://www.nature.com/nature/journal/v519/n7541/full/nature14033.html

The manuscript was submitted on the 25th of August 2014 and was accepted on 7th of November of the same year after undergoing a peer review procedure. It was published online on the 1st of December 2014 and available in the printed journal on the 5th of March 2015.
The original publication was reformatted to the format of the thesis (e.g. text font, figure numbering). The supplementary discussion is included at the respective paragraph. In addition, some extended data figures were moved to the main text, party split or combined to improve the quality of reading, respectively. Respective references to other chapters or sections are inserted. Some figures and tables were moved to the Appendix. Subsection 4.3.8 gives an overview on the methods in the publication. More generalized and optimized protocols are given in Material and Methods and sections 3.2 and 4.2 of this chapter, respectively. Supplementary videos are not included in this thesis but can be downloaded from the online version of the paper (von der Ecken et al., 2015).

4.3.1 Abstract

Filamentous actin (F-actin) is the major protein of muscle thin filaments, and actin microfilaments are the main component of the eukaryotic cytoskeleton. Mutations in different actin isoforms lead to early-onset autosomal dominant non-syndromic hearing loss (van Wijk et al., 2003), familial thoracic aortic aneurysms and dissections (Milewicz et al., 2008), and multiple variations of myopathies (Sparrow et al., 2003). In striated muscle fibres, the binding of myosin motors to actin filaments is mainly regulated by tropomyosin and troponin (Gordon et al., 2000; Sparrow et al., 2003). Tropomyosin also binds to F-actin in smooth muscle and in non-muscle cells and stabilizes and regulates the filaments there in the absence of troponin (Pittenger et al., 1994; see also subsection 2.2.1). Although crystal structures for monomeric actin (G-actin) are available (Kabsch et al., 1990), a high-resolution structure of F-actin is still missing, hampering our understanding of how disease-causing mutations affect the function of thin muscle filaments and microfilaments (see also subsection 2.2.2). Here we report the three-dimensional structure of F-actin at a resolution of 3.7 Å in complex with tropomyosin at a resolution of 6.5 Å, determined by electron cryomicroscopy. The structure reveals that the D-loop is ordered and acts as a central region for hydrophobic and electrostatic interactions that stabilize the F-actin filament. We clearly identify map density corresponding to ADP and Mg^{2+} and explain the possible effect of prominent disease-causing mutants. A comparison of F-actin with G-actin reveals the conformational changes during filament formation and identifies the D-loop as their key mediator. We also confirm that negatively charged tropomyosin interacts with a positively charged groove on F-actin. Comparison of the position of tropomyosin in F-actin–tropomyosin with its position in our previously determined F-actin–tropomyosin–myosin structure (Behrmann et al., 2012a) reveals a

myosin-induced transition of tropomyosin. Our results allow us to understand the role of individual mutations in the genesis of actin- and tropomyosin-related diseases and will serve as a strong foundation for the targeted development of drugs.

4.3.2 Structure of F-actin-tropomyosin

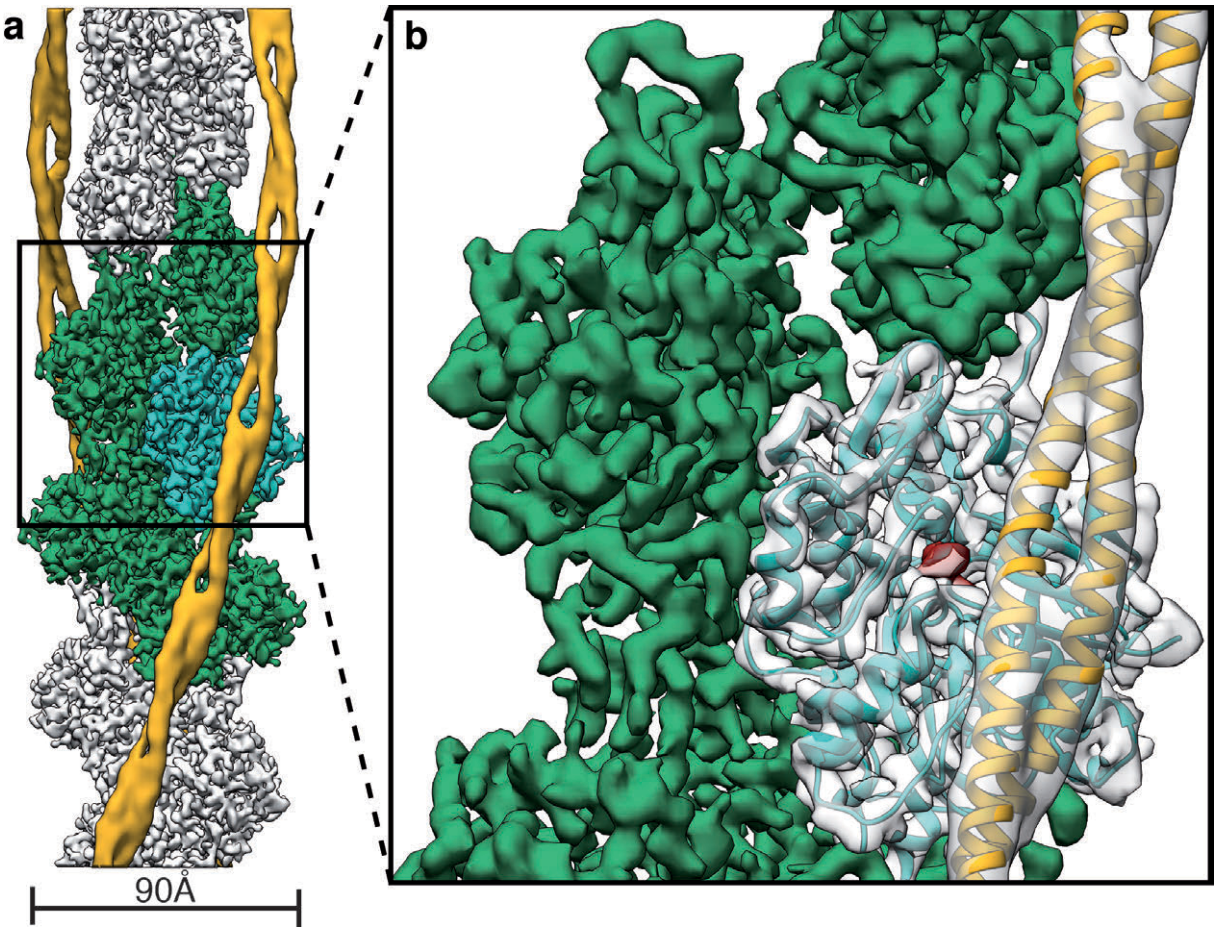

Figure 4.10: Cryo-EM structure of F-actin decorated with tropomyosin.

a, Full cryo-EM reconstruction of F-actin (grey, with five central subunits in green and one subunit in cyan) decorated with tropomyosin (yellow). **b**, Close-up view of **a** with the atomic and molecular model of an F-actin subunit (cyan) and tropomyosin (yellow) and their corresponding densities, respectively. The density corresponding to ADP is depicted in red.

To determine the structure of F-actin is inherently difficult because of its flexibility and its resistance to crystallization. Therefore, the only structural models of F-actin so far have been determined either from medium-resolution electron cryomicroscopy (cryo-EM) maps (Fujii et al., 2010; Galkin et al., 2010; Holmes et al., 1990; Murakami et al., 2010; Sousa et al., 2013) or by interpreting X-ray fibre diffraction data (Oda et al., 2009), which has certain limitations (see also subsection 2.2.2). Using a direct electron detector and drift correction and by improving the image processing of helical specimens (see subsection 4.3.8), we have determined the structure of F-actin in complex with tropomyosin at an average resolution of 3.7 Å for F-actin and 6.5 Å for tropomyosin using cryo-EM (Figure 4.10a, Figure 4.11).

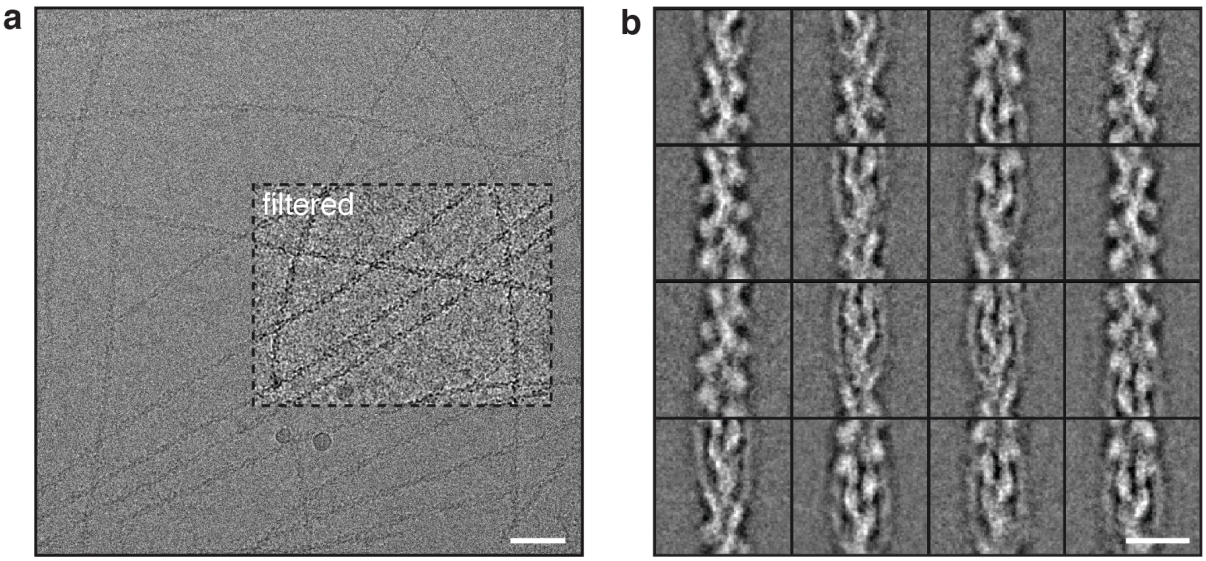

Figure 4.11: Micrograph and 2D-classification of the cryo-EM dataset.

a, b, Representative digital micrograph and corresponding representative 2D class averages of F-actin decorated with tropomyosin in amorphous ice (in total 300 class averages of randomly chosen 40,000 phase-flipped segments of in total 109,242 segments from 689 images). Scale bars, 50 nm (**a**) and 10 nm (**b**).

During refinement the helical parameters - that is, the rise per subunit and the azimuthal rotation - were estimated to be 27.5 Å and 166.4 °, respectively (see subsection 4.3.8). The side-chain densities of most actin residues were clearly resolved and allowed us to build an atomic model of F-actin (Figure 4.10b, Figure 4.12). The first four residues of the amino terminus and the last four residues of the carboxy terminus were not resolved (Figure 4.23 in subsection 4.3.8), indicating that these regions are disordered in the filament. However, we could clearly identify map density corresponding to ADP and the coordinated cation, which is most probably Mg^{2+} (Figure 4.10b, Figure 4.12a).

The overall organization of F-actin is similar to that described in previous structures and models (Fujii et al., 2010; Oda et al., 2009). However, given the superior resolution of our structure, we could clearly identify many salt bridges and therefore directly reveal intra- and intermolecular interactions of the F-actin filament in detail (Table A6.1).

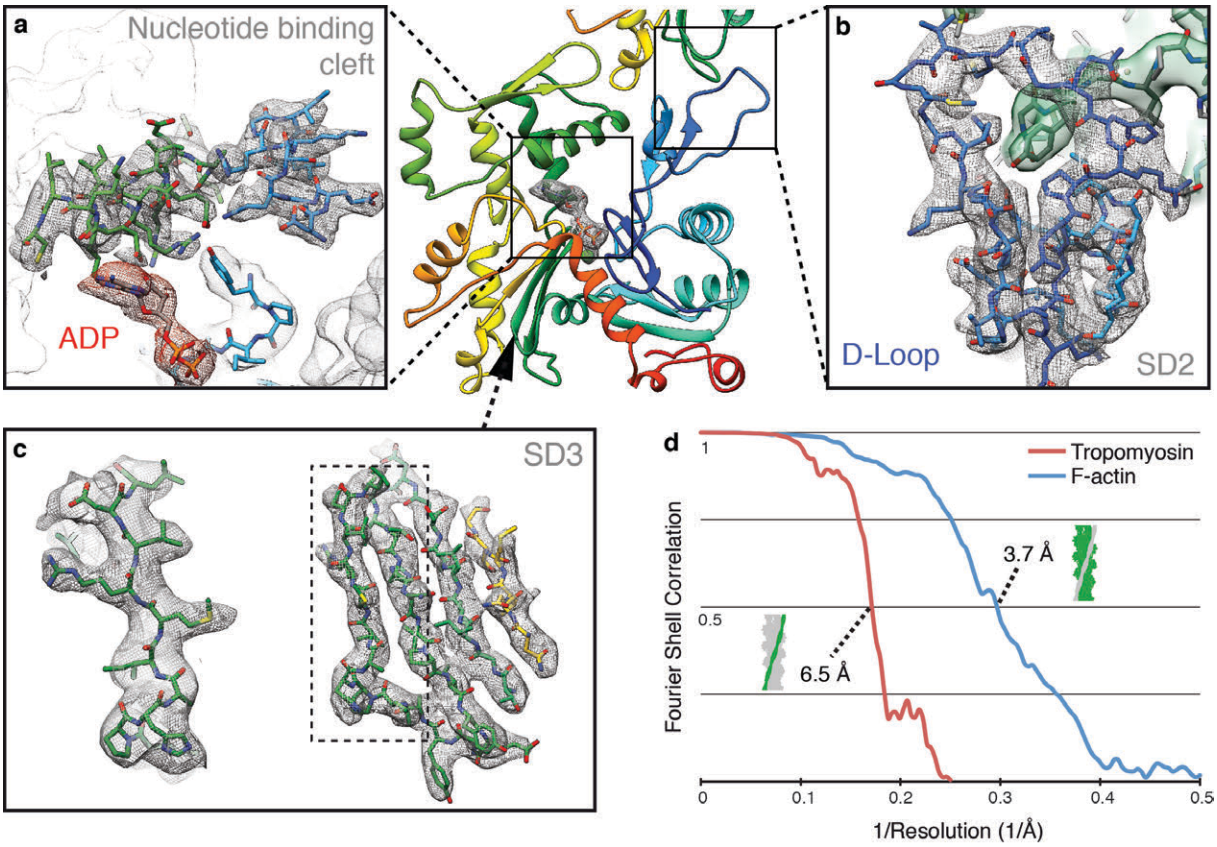

Figure 4.12: Representative regions and resolution of the F-actin cryo-EM map.

a-c, Close-ups and overview of the atomic model of an F-actin subunit rainbow-coloured from the N terminus (blue) to the C terminus (red). Amino acids, ADP and the coordinated cation, probably Mg^{2+}, are depicted inside their corresponding map densities. ADP is well resolved in the α-helical nucleotide binding cleft (**a**). Interface between the D-loop (SD2) and the SD3 of the adjacent actin subunit (**b**). Beside α-helices (**a**), β-sheets (**b**) are well defined in our reconstruction. **d**, FSC curves of different areas of interest (green) by masking (see subsection 4.3.8). The resolution of tropomyosin was estimated using the twice down-sampled data set (2.24 Å per pixel). The $FSC_{0.5}$ criterion indicates that the tropomyosin density map has a resolution of 6.5 Å. The resolution of the final F-actin density map is estimated at a resolution of 3.7 Å.

4.3.3 Intra- and Interstrand contacts of the F-actin filament

F-actin is composed of two long-pitch helical strands. Interactions between actin subunits of the same strand and the opposing strand - the so-called intrastrand and interstrand interactions, respectively - stabilize the F-actin filament (Figure 4.13, Figure 4.14, Figure A6.1 and Table A6.1). Intrastrand contacts are mediated by subdomains SD2 and SD4 of one actin subunit with the SD3 of the adjacent actin subunit of the same strand (Figure 4.13a, b). Besides several salt bridges between the edges of SD4 and SD3 (Figure 4.13b), the major site of interstrand interaction is between the D-loop and the bottom of the beta-sheet of SD3 (Figure 4.13c–f, Figure 4.14). The D-loop encloses tyrosine 169 of the neighbouring subunit, resembling a lock-and-key interaction (Figure 4.13c). In addition, adjacent residues fit snugly into the groove formed by regions next to the D-loop around isoleucine 64 (Figure 4.13d) and a prominent hydrophobic patch in the D-loop interacts with a hydrophobic groove on the neighbouring F-actin subunit (Figure 4.13e, f). Thus, the intrastrand interface at this position is large and is stabilized not only by electrostatic and hydrophobic interactions but also by geometric surface complementarity. As expected, mutations at this site (which, for instance, induce charges at

hydrophobic interfaces) hamper F-actin polymerization and stability (Figure 4.14) and can lead to different forms of nemaline myopathy (Gordon et al., 2000; Laing et al., 2009; Table A6.1).

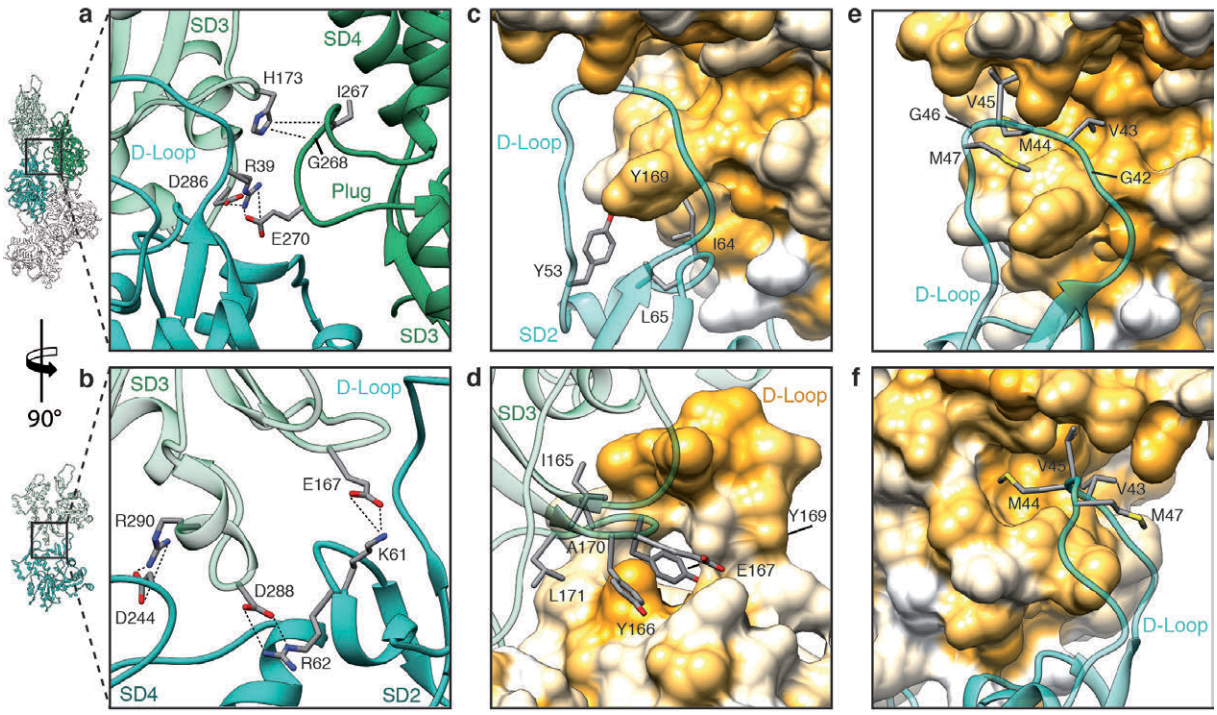

Figure 4.13: Filament stability by intrastrand and interstrand interactions.

a–f, Neighbouring F-actin subunits stabilize the F-actin filament by interaction through salt bridges (**a, b**) and by hydrophobic interactions (**c-f**). The central F-actin subunit is depicted in cyan, and adjacent subunits are shown in shades of green. Surfaces are coloured from high (yellow) to low (white) hydrophobicity. Interactions between amino acids are highlighted with dotted lines. **a**, Interstrand and intrastrand salt bridges of three actin subunits involving the plug. **b**, Several intrastrand salt bridges at the actin–actin interface. **c-f**, Front view (**c, e**), back view (**d**) and side view (**f**) of the D-loop interacting with the SD3 of the neighbouring intrastrand F-actin subunit. The D-loop wraps around Y169 of the neighbouring subunit and other residues snugly fit into the groove formed by regions adjacent to the D-loop (**c, d**), resembling a lock-and-key interaction. In addition, a prominent hydrophobic patch in the D-loop interacts with a hydrophobic groove on the neighbouring F-actin subunit (**e, f**).

4.3.4 The D-loop and its key function for the filament stability

In contrast to most G-actin structural models, in which the D-loop is not resolved owing to its high flexibility, the D-loop is well defined in our structure (Figure 4.12b), corroborating its importance in mediating actin–actin interaction. It also contrasts with results of medium-resolution cryo-EM data (Galkin et al., 2010) and disulphide cross-linking studies (Oztug Durer et al., 2010) that suggested the presence of multiple D-loop conformational states. In addition, these and other studies (Crosbie et al., 1994; Strzelecka-Gołaszewska et al., 1995) suggested a close interaction of the D-loop with the C terminus of actin. Although the C terminus is located next to the D-loop, it is not resolved in the cryo-EM density (Figure 4.23b in subsection 4.3.8), indicating that the interaction between these two regions is either transient or structurally flexible.

Our structural determination also gives a possible explanation for the recently described F-actin disassembly by Mical, a multidomain cytosolic actin regulator (Hung et al., 2010) Mical post-translationally oxidizesmethionine 44 within the D-loop of actin (Hung et al., 2011), leading to the less flexible and more hydrophilic sulfoxide. The increased polarity could lead to a weakening of the

hydrophobic actin–actin interaction (Figure 4.14c) and consequently to a Mical-induced disassembly of the F-actin filament.

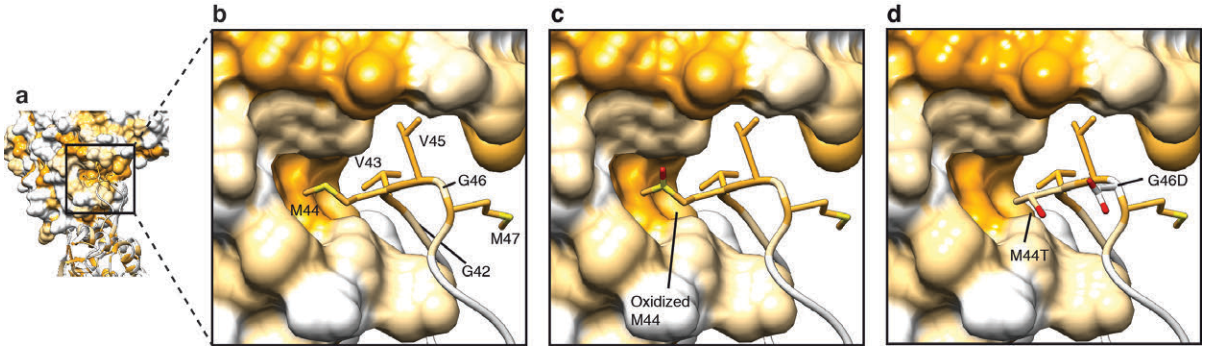

Figure 4.14: Destabilization of the D-loop binding.

a, Overview of the D-loop bound to the hydrophobic cleft in SD3 of the F-actin molecule on top. Surfaces and residues are coloured from high (yellow) to low (white) hydrophobicity. **b**, Involved hydrophobic residues of the D-loop. **c**, **d**, Modifications in the D-loop, like oxidation of methionine 44 (d) or mutations of methionine 44 and glycine 46 (M44T, G46G; Hung et al., 2011; Laing et al., 2009) (**e**) change the polarity or insert charges and consequently weaken the hydrophobic interactions. Thus, this destabilization of the intrastrand contact is connected to anomalous actin filament assembly and nemaline myopathies.

The F-actin structure confirms that the so-called hydrophobic plug (Holmes et al., 1990) connects three F-actin subunits with each other (Figure 4.13a). However, as suggested previously (Fujii et al., 2010), this interstrand interaction is formed by salt bridges (Figure 4.13a), not by hydrophobic interactions (Figure A6.1a-e). A large part of the plug is negatively charged on the surface, electrostatically interacting with a positively charged patch on the opposing actin, with histidine 173 and lysine 284 at its centre (Figure A6.1c-e). Another possible salt bridge connects two neighbouring actins at lysine 113 of SD1 and glutamate 195 of SD4 (Figure A6.1f). However, the interface at this position is quite small and not surrounded by other prominent electrostatic or hydrophobic interactions. In general, the two strands of F-actin are held together by only a few contacts, and a large empty space is maintained between the strands. This is probably an important requisite for the flexibility of F-actin filaments.

4.3.5 G- to F-actin transition

As previously described ((Fujii et al., 2010; Holmes et al., 1990; Oda et al., 2009), F-actin is more flattened than is G-actin because of a rotation of SD1 and particularly SD2 (Figure 4.15a). New salt bridges between SD1, SD4 and SD2 stabilize the new interface between the opposing subdomains at the nucleotide binding cleft (Figure 4.15b–f and Table A6.2).

Nucleotide binding and hydrolysis

The coordination of ADP and the divalent cation in the nucleotide binding cleft by nearby residues is very similar to that in G-actin (Figure 4.15b, Figure A6.2a). However, glutamine 137, which has been shown to play a central role in ATP hydrolysis (Iwasa et al., 2008) , is clearly moved closer to ADP, coordinating not only the cation (as in G-actin) but also the nucleotide beta-phosphate (Figure A6.2b, c). Interestingly, the presence of ATP instead of ADP in the nucleotide-binding site would be sterically unfavourable (Figure A6.2c), suggesting that a different intermediate conformation exists for F-actin-ATP. High-resolution crystal structures of non-vertebrate actin showed that glutamine 137 positions the nucleophilic water that attacks the gamma-phosphate of ATP (Vorobiev et al., 2003).

Therefore, as previously suggested (Oda et al., 2009), the shorter distance of glutamine 137 to gamma-phosphate probably induces ATP hydrolysis and then afterwards the cation takes the position of the gamma-phosphate in the finally resulting ADP-binding-state (Figure A6.2d). A mutation of glutamine 137 connected to nemaline myopathy (Koy et al., 2007) further highlights the importance of this residue in the proper function of F-actin (Figure A6.2e).

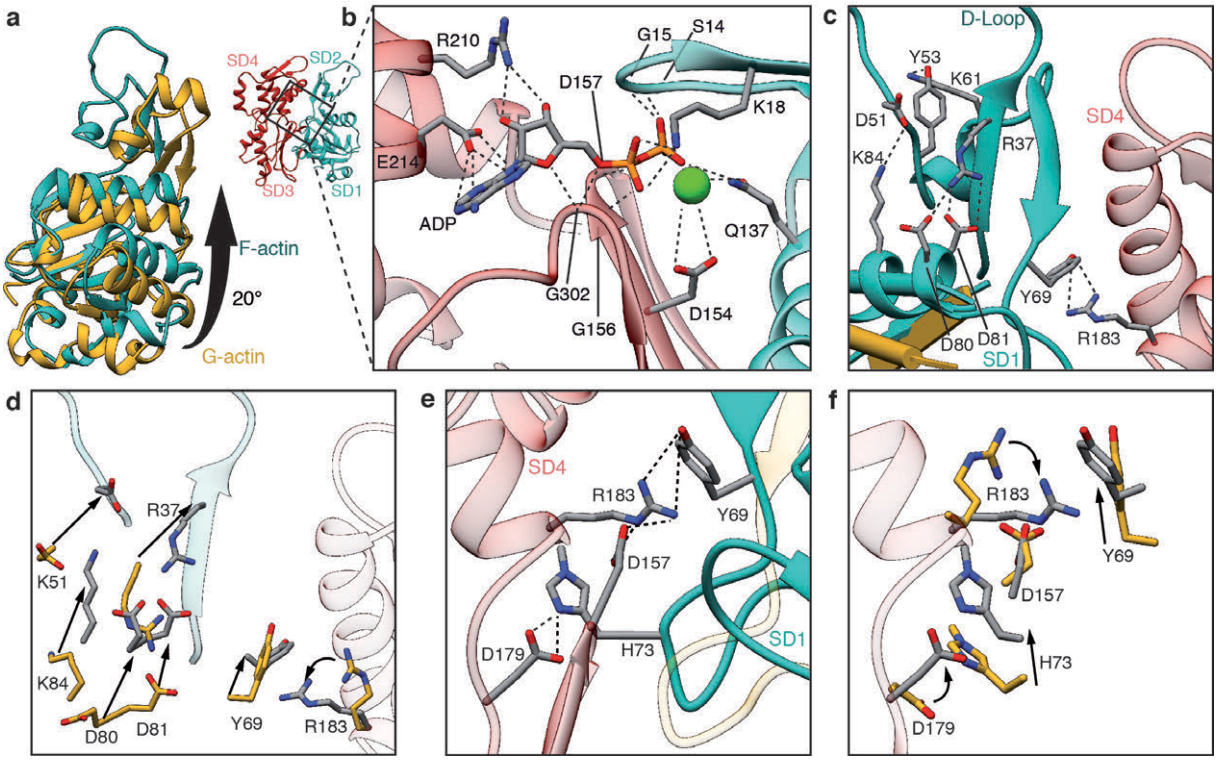

Figure 4.15: G-actin to F-actin transition.

a, A global rotation of SD1 and SD2 leads to a flattening of G-actin (yellow) during transition to F-actin (cyan). **b**, Coordination of ADP and a cation in the nucleotide binding cleft in F-actin (SD1–SD2 cyan, SD3–SD4 red). The cation is most probably Mg^{2+}. However, Ca^{2+} cannot be excluded as the coordinated cation because the actin was purified in Ca^{2+}-containing buffer. **c**–**f**, The conformation of F-actin is finally stabilized by intramolecular interactions between SD2, SD1 and SD4 (**c**, **e**). Most of the residues involved in the stabilization of the F-actin conformation show a considerable movement during the transition between G-actin andF-actin (**d**, **f**). **a**, G-actin with defined D-loop for better visualization; PDB accession code 1J6Z. **c**–**f**, ATP-bound G-actin; PDB accession code 3EL2.

Barbed end binding

The comparison of the structures of F-actin with that of G-actin (PDB accession codes 3EL2 and 1J6Z; Nair et al., 2008; Otterbein et al., 2001), which represent the start and end points of filament formation, allows describing the possible conformational changes during polymerisation. Initial intrastrand binding of G-actin to the barbed end of F-actin probably happens at the interface between SD4 of G- and SD3 of the F-actin (Figure 4.16a). This process is accompanied by an interstrand binding between SD4 of G-actin and SD1 of the terminal actin of F-actin (Figure 4.16b). By an induced fit mechanism the flexible D-Loop and the other regions of SD2 then interact strongly with SD3 at the barbed end forming the second major interface (Figure 4.16c). This results in a straightening of SD2 and consequently of SD1, which leads to the flattening of the newly bound actin subunit and an activation of the ATPase as described before (Figure 4.16d, e). The interstrand contacts are less affected by the G- to F-actin transition, which suggests that the opposite strand guides the newly binding G-actin to its position and thereby determines the symmetry of the filament.

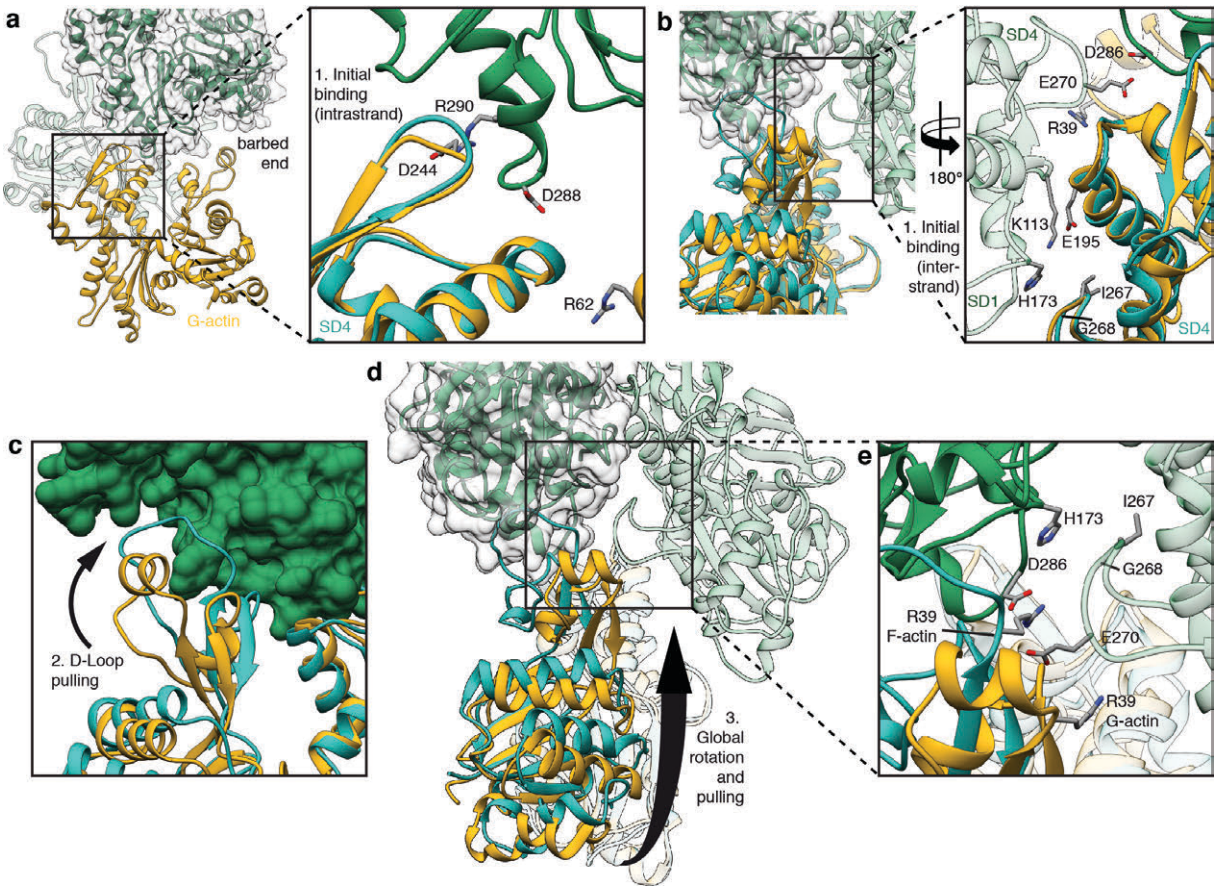

Figure 4.16: Model of barbed end binding and G- to F-actin transition.

a, **b**, Binding of new G-actin (yellow, PDB accession code 3EL2) at the barbed end of F-actin (green) is initiated by the intrastrand binding of SD4 of G-actin to SD3 of F-actin (**a**, side view) and the interstrand binding of SD4 and SD1 (**b**, front view), respectively. G-actin is overlaid with a subunit of the structure found in F-actin (cyan). The main interstrand contacts are already present at the start of the transition and thereby guide the binding G-actin to its correct position, determining the symmetry of the filament. **c**, After initial binding the D-loop is trapped in the hydrophobic cleft of SD3 of F-actin and pulls on SD2. F-actin is depicted in surface representation (green). **d**, Finally, the SD2 and concomitantly SD1 are rotated and the final F-actin conformation is stabilized by various intramolecular interactions (see Figure 4.13c–f, Figure 4.15c–f and Table A6.2). **e**, Owing to the relatively large distance from the SD1 and SD2 subdomains of the newly bound G-actin to the subunit of the opposite strand, the only influence of the opposite strand on the binding of G-actin is at the docking position of the D-loop. The transition of R39 illustrates well the docking of the D-loop. The residue is depicted in both states (G-actin and F-actin).

Pointed end binding

It is more difficult to explain the binding of G-actin to the pointed end of F-actin. Whereas the differences between G- and F-actin are mainly at the upper subdomains (SD2 and SD4), the lower subdomains (SD1 and SD3) are very similar in both conformations (Figure 4.17a-c). Thus, if the conformation of the pointed end of F-actin and is very similar to that of G-actin, it follows that the surfaces would be very similar at the pointed and barbed end and consequently the binding affinity for further actins would only slightly differ. However, this is not the case. The actin-actin affinity at the pointed end is much lower than at the barbed end (Brieher, 2013). We therefore assume that the actins at both ends of the filament have very similar conformations resulting in different interacting surfaces and affinities and hence propose the following mechanism. Similarly to barbed end binding, interstrand contacts between the newly bound G-actin and F-actin exist right from the beginning (Figure 4.17a-c). Initial intrastrand contacts are mediated by the D-Loop of F-actin at the pointed end. Although it has the overall conformation of a central F-actin, it is still flexible and binds G-actin

by an induced fit mechanism (Figure 4.17d). This results in a pulling of the tyrosine 169 loop of G-actin and straightening of the central beta-sheet of SD3 (Figure 4.17e), which initiates an amplifying domino effect by displacement of helices in SD1 (Figure 4.17e, f). Finally, SD2 rotates (Figure 4.17f) and new interactions between SD1, SD4 and SD2 stabilize the final conformation (Figure 4.15c-f).

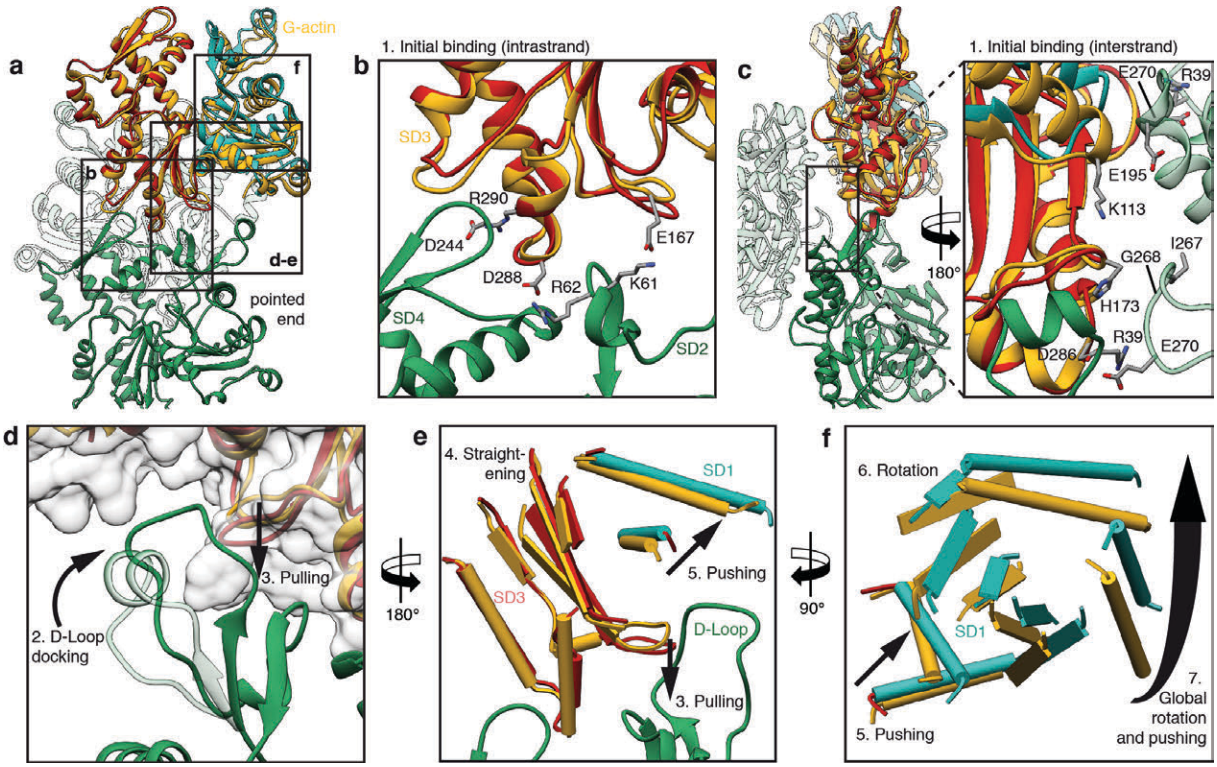

Figure 4.17: Model of pointed end binding and G- to F-actin transition.

a–**c**, Binding of new G-actin (yellow, PDB accession code 3EL2) at the pointed end of F-actin (green) is initiated by initial intrastrand binding (**b**) of SD3 of G-actin to SD4 of F-actin at the pointed end and interstrand binding of SD4 to SD3 (**c**), respectively. Again, the main interstrand contacts are available before the transition of G-actin (yellow) to F-actin (SD1 and SD2 in cyan, SD3 and SD4 in red). **d**, During binding to F-actin the transition from G-actin to F-actin is initiated by an induced fit of the F-actin D-loop to the hydrophobic cleft of the newly bound G-actin. This leads to a pulling down of the central beta-sheet of SD3 of G-actin. **e**, The beta-sheet is thereby straightened and pushes up two adjacent helices of SD1. **f**, The slight dislocation of these helices is transmitted to other regions of SD1 and thereby emphasized. This leads to a global rotation of SD1, which results in a considerable rotation of SD2 by an angle of 20° and a closure of the nucleotide binding cleft (Figure 4.15).

4.3.6 Tropomyosin position on F-actin in an Apo-state

The F-actin filaments were completely decorated by tropomyosin (Figure 4.10a, Figure 4.11). Although tropomyosin consists of seven pseudo-repeating units, applying the helical symmetry of F-actin for the reconstruction of the F-actin–tropomyosin complex results in a reduced resolution of tropomyosin and the overlap region of the N and C termini is not visible in the map (see subsection 4.3.8). However, densities corresponding to the helices of the coiled-coil were well resolved (Figure 4.10) and allowed us to fit a previous chimeric model of tropomyosin derived from X-ray, nuclear magnetic resonance and molecular dynamics simulation data (Li et al., 2011) and to determine the register of the chains of tropomyosin. Together with the atomic resolution of F-actin, this allows us to describe the interaction between actin and tropomyosin in greater detail and with higher accuracy than previous studies.

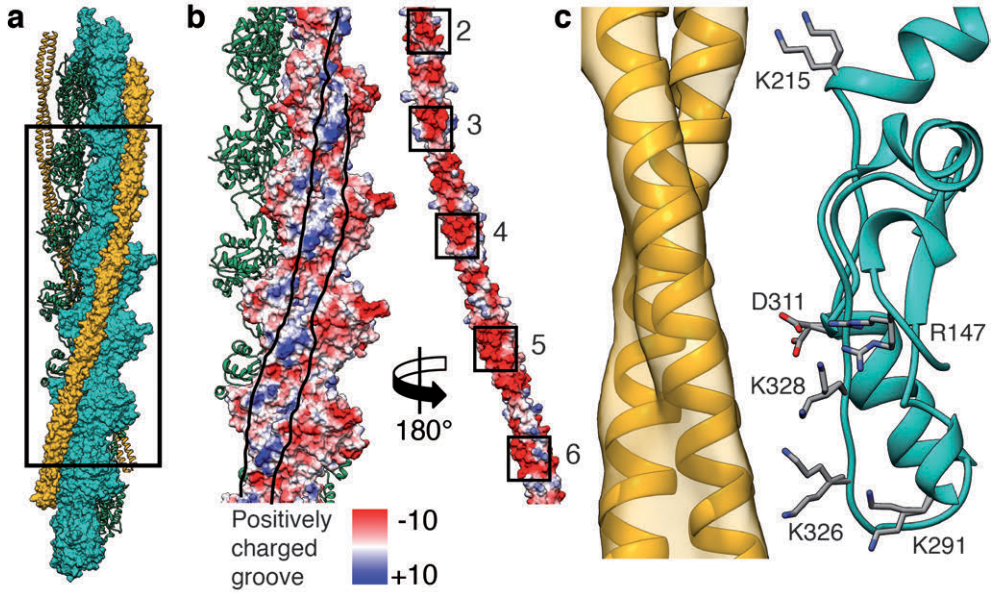

Figure 4.18: F-actin interaction with tropomyosin.

a, Structural overview of an F-actin filament (green and cyan) decorated with tropomyosin (yellow). Half of the filament is shown in surface representation. The N and C termini of F-actin are included in this model. **b**, Surface of F-actin and tropomyosin (pseudo-repeats 2–6) with the electrostatic Coulomb potentials ranging from -10 kcal mol^{-1} to +10 kcal mol^{-1} at pH 7.5. Tropomyosin was rotated by 180° and shifted to the right to allow a better view on the F-actin–tropomyosin interface, which is delimited by lines drawn onto the surfaces. The overall negatively charged tropomyosin interacts with a positively charged groove on F-actin. **c**, Several charged residues of actin are within distances that would make it possible to interact with tropomyosin via putative salt bridges. Different rotamers of the same residue are shown to indicate how F-actin subunits could adjust to the surfaces of different tropomyosin pseudo-repeats.

Tropomyosin, which is mainly negatively charged on its surface, interacts with a positively charged groove on F-actin, confirming previous predictions (Lehman et al., 2013b; Li et al., 2011; Lorenz et al., 1995; Figure 4.18a, b and Table A6.3). In particular, lysines 326 and 328 on F-actin strongly interact with the different pseudo-repeats of tropomyosin (Figure 4.18c). The distance between tropomyosin and actin varies depending on the position along the filament between 38 Å and 40 Å. The distance would allow for direct interactions of opposing residues (Figure 4.18c) and is similar to the distance in the M-state (Behrmann et al., 2012a) and to what was previously suggested for the other states of tropomyosin (Lorenz et al., 1995; Poole et al., 2006). The interactions between tropomyosin and F-actin probably determine the position of tropomyosin on F-actin in the Apo-state (A-state), a term we recently introduced to describe the position of tropomyosin in the absence of troponin, myosin or Ca2+ (Lehman et al., 2013b).

The position of tropomyosin in the A-state in our structure (Figure 4.18a, Figure 4.19a) is close to that described by Sousa et al. (Sousa et al., 2013), but differs from a previous positioning based on negative staining data and molecular dynamics simulations (Li et al., 2011). To determine the source of this discrepancy, we first repeated the negative staining work (Figure 4.22 in subsection 4.3.8) and indeed reproduced the different position (Figure 4.19b). However, when we cross-linked the sample before staining, tropomyosin was in the same position as in our cryo-EM structure (Figure 4.19c-f, Figure 4.22 in subsection 4.3.8). This shows that negative staining rather than cryo-preparation results in a change of the tropomyosin position on F-actin. The relatively low pH of the stain (pH 4) probably induces repulsions at the F-actin–tropomyosin interface and forces tropomyosin to change its position (Figure 4.19g). In any case, the change in position depending on preparative conditions confirms the striking ability of tropomyosin to translocate azimuthally across the actin filament at low energy cost (Lehman et al., 2013b).

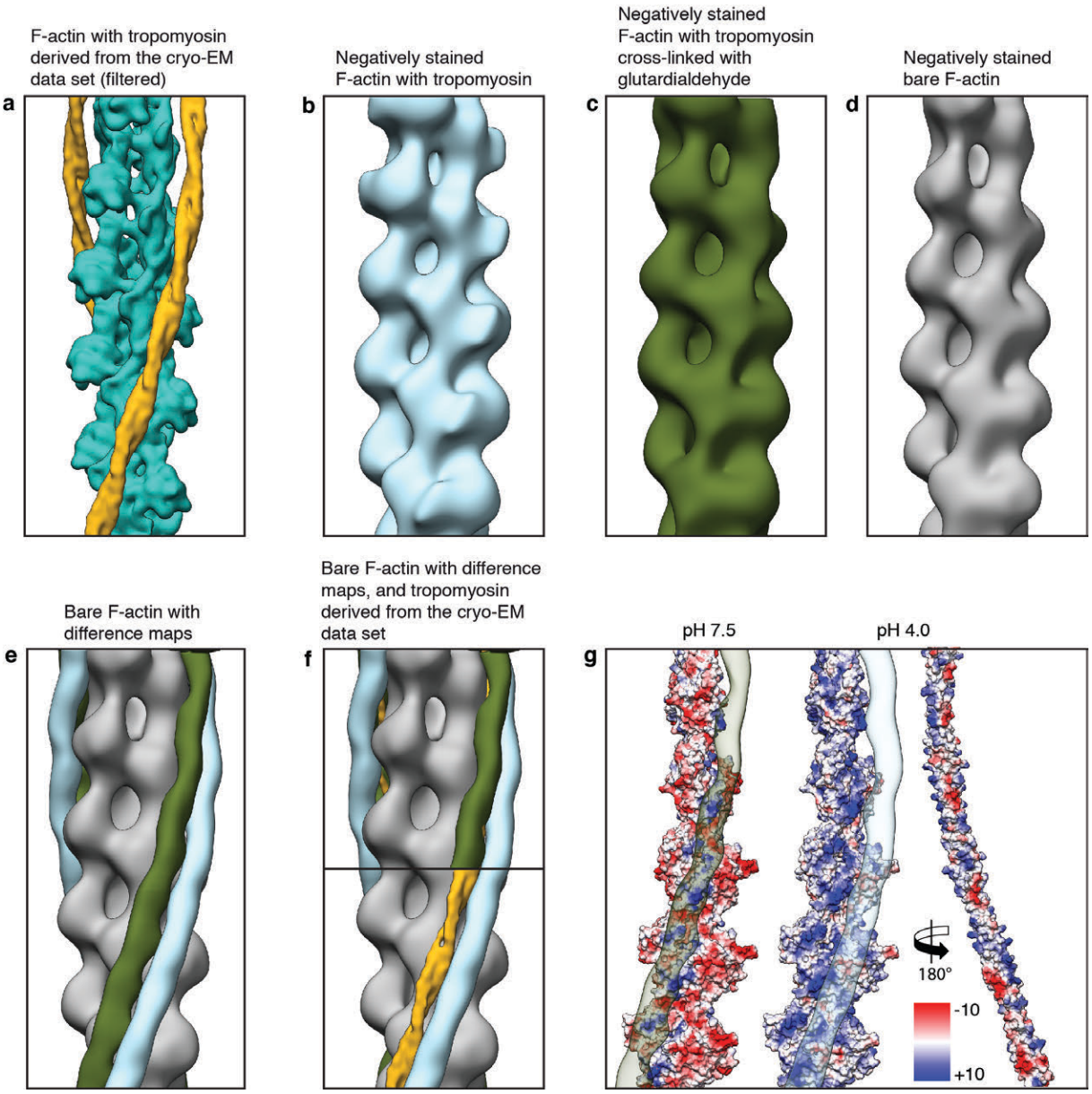

Figure 4.19: Comparison of reconstructions regarding the tropomyosin position on F-actin.

a–**d**, Reconstructions of F-actin decorated with tropomyosin calculated from: the cryo-EM data set filtered to 15 Å (**a**), from a negatively stained data set (**b**), from a negatively stained data set after cross-linking with glutardialdehyde (**c**), and from negatively stained bare F-actin (**d**). **e**, By calculating a difference map between tropomyosin–bare F-actin (blue) and glutardialdehyde–bare F-actin (green), differences in the tropomyosin position on bare F-actin (grey) are visualized. **f**, Overlay of difference maps showing that the position of tropomyosin in the cryo-EM reconstruction (yellow) corresponds to the tropomyosin position of the negatively stained data set with the cross-linked complex (green). **g**, Surface of F-actin and tropomyosin (pseudo-repeats 2--6) with the electrostatic Coulomb potentials at pH 7.5 and pH 4, ranging from -10 kcal mol^{-1} (red) to +10 kcal mol^{-1} (blue) (see also Figure 4.18b). Tropomyosin was rotated by 180 ° and shifted to the right to allow a better view of the F-actin–tropomyosin interface. Difference maps of the glutardialdehyde–bare F-actin and the tropomyosin–bare F-actin map are shown on the F-actin surface at pH 7.5 (left) and pH 4.0 (middle), respectively.

4.3.7 Model of tropomyosin transition by myosin binding

In comparison to the previously assumed position of tropomyosin in the A-state, the new position blocks only minor regions of the myosin binding site on F-actin. This supports our previous model of myosin binding to actin filaments in the absence of troponin (Behrmann et al., 2012a) even more

strongly. If the current position of tropomyosin is the default state for tropomyosin, then only loop 4 and the cardiomyopathy loop of myosin would be sterically hindered from binding to the F-actin filament (Figure 4.20a-d) and probably allows for a weak binding of myosin, especially with its lower 50-kDa domain. Actin induced cleft closure of myosin would then move tropomyosin to its M-state (Behrmann et al., 2012a; Figure 4.20b-g).

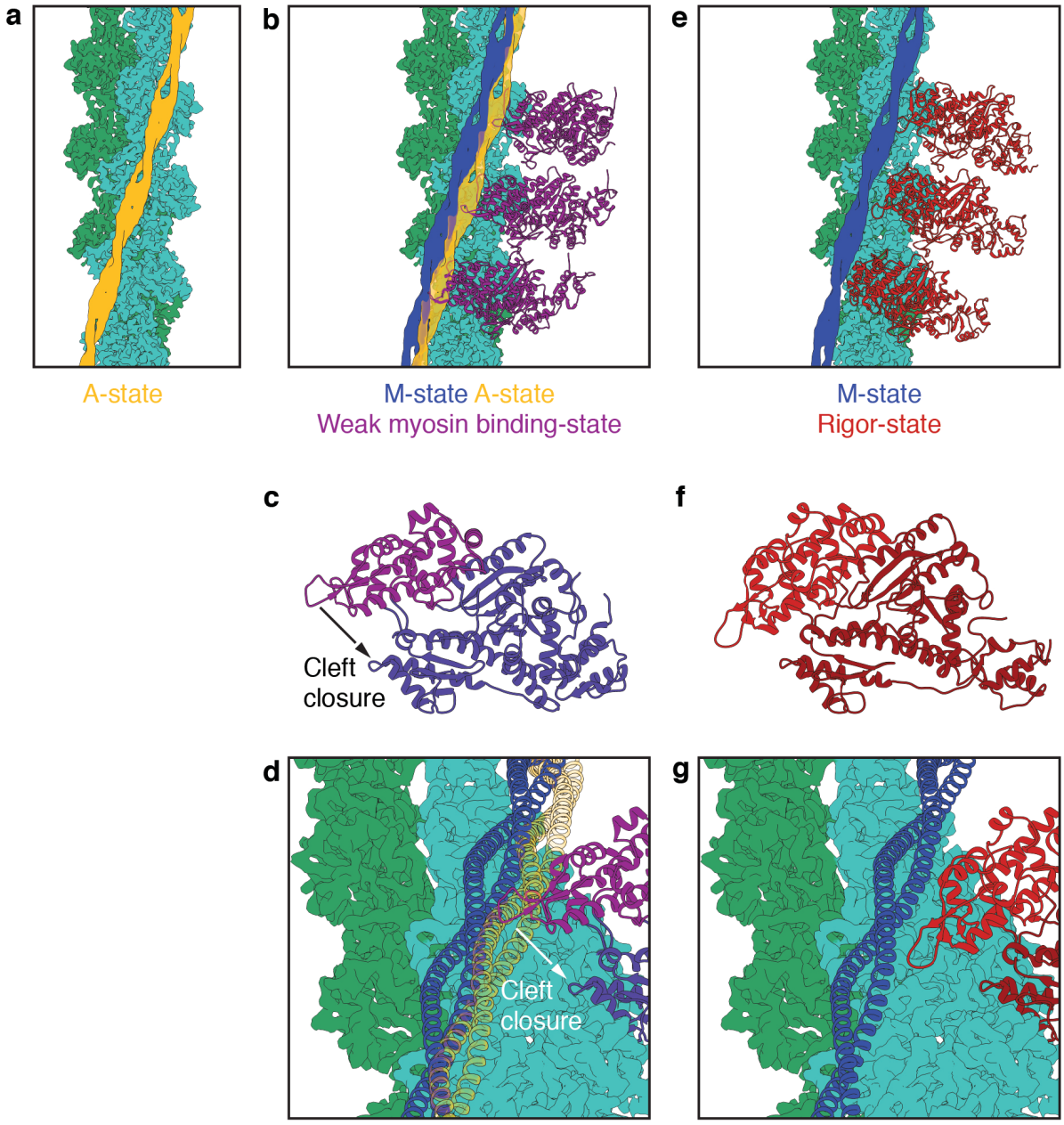

Figure 4.20: Tropomyosin transition on F-actin induced by myosin binding.

a, Cryo-EM structure of the F-actin–tropomyosin complex with tropomyosin in the A-state. Tropomyosin (yellow, A-state), F-actin (green). **b**–**d**, Initial weak binding of myosin (magenta, PDB accession code 1LKX) to the F-actin–tropomyosin filament in the absence of troponin. Most of the myosin binding sites on F-actin are not occupied by tropomyosin and only loop 4 and the cardiomyopathy loop are sterically hindered from binding to the F-actin filament (**b**). Actin-induced closure of the 50-kDa cleft of myosin (**c**) results in a strong binding of myosin and tropomyosin moves to its M-state position (blue) (**d**). **e**–**g**, F-actin-tropomyosin-myosin complex in the rigor state (PDB accession code 4A7H). Myosin is shown in red.

Comparing the position of tropomyosin in the new A-state with the M-state (Figure 4.21a), we find two possible transitions between the states. Either tropomyosin rolls on the F-actin filament by an

azimuthal rotation of about 16 ° and a left-handed rotation of about 70 ° or a right-handed rotation of about 110 ° along its own axis (Figure 4.21b, c) or tropomyosin shifts by about 37 Å (half the length of a pseudo-repeat) along the actin filament (Figure 4.21d, e) or a mixture of the two effects occurs. The distance of tropomyosin to the filament axis of F-actin is not altered during the transition. Gestalt-binding and rigidity of tropomyosin (Holmes and Lehman, 2008) support a shifting mechanism, whereas the spatial limitations inside the sarcomere make a shift of 37 Å rather unlikely. However, direct localization of the N/C-terminal overlap of tropomyosin will be needed to discriminate between the two possibilities.

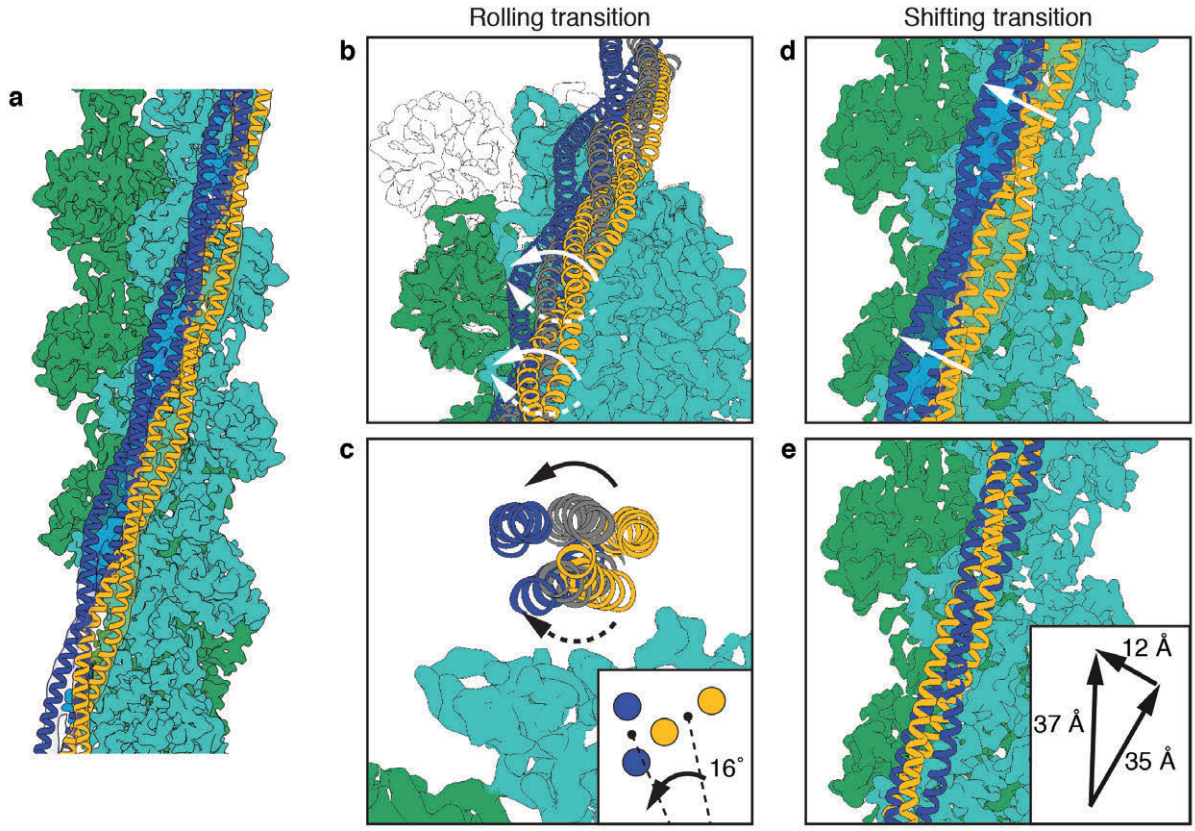

Figure 4.21: Model of tropomyosin transition on F-actin during myosin binding.

a–e, There are two possible ways for the transition of tropomyosin from the A-state to the M-state. Tropomyosin either rolls (**b**, **c**) or slides (**d**, **e**) from one to the other position. Rolling would involve an azimuthal rotation of 16 ° with respect to the F-actin axis (inset of **c**) and a left-handed rotation of 70 ° (indicated by solid arrows) or a right-handed rotation of 110 ° (indicated by dotted arrows) with respect to its own axis (**b**, **c**). Sliding would imply not only an azimuthal shift of 12 Å (indicated by white arrows in **d**), but also a tremendous shift of a half tropomyosin repeat (that is 35 Å) along the F-actin filament (**d**, **e**). The radius to the filament axis would be preserved in both situations. The inset of **e** depicts the vectors for a shifting transition of tropomyosin: an azimuthal and longitudinal shift of 12 Å and 35 Å, resulting in an overall shift of 37 Å.

In summary, the structure of the F-actin-tropomyosin complex shows how F-actin filaments are stabilized in health and destabilized in certain diseases. Our results provide the structural framework for further experiments towards resolving the molecular details of actin polymerization and its interaction with actin-regulating proteins such as tropomyosin.

4.3.8 Applied methods

Protein expression and purification (see also section 3.1 in Material and Methods)

F-actin was isolated from rabbit skeletal muscle acetone powder and purified with several polymerization and depolymerization steps as described previously (Pardee and Spudich, 1982). The composition of the G-actin buffer was 5 mM Tris pH 7.5, 1 mM DTT, 0.2 mM $CaCl_2$. Recombinant α-tropomyosin (Mus musculus, alpha-1 chain, Uniprot-ID P58771) with an alanine-serine extension was purified from Escherichia coli, based on the protocol of Coulton et al. (Coulton et al., 2006). The α-tropomyosin isoform we used is abundant in smooth and striated muscles. The actin–tropomyosin complex was prepared by mixing F-actin with tropomyosin initially at a molar ratio of 7:1 in filament buffer (5 mM Tris-HCl pH 7.5, 1 mM DTT, 100 mM KCl, and 2 mM $MgCl_2$). The final concentration of tropomyosin for either negatively stained or frozen specimens was then adjusted empirically to obtain complete decoration and only few unbound tropomyosins in the background. For the cross-linking studies between F-actin and tropomyosin, samples were prepared in filament buffer containing 5 mM HEPES (pH 7.5).

Preparation for negative staining EM (see also subsection 3.2.1 in Material and Methods)

To stabilize and straighten the F-actin filaments (this is important for image processing), we decorated them with tropomyosin. Actin-tropomyosin complexes were directly prepared before the negative staining procedure. 4 ml of sample was applied on a freshly glow-discharged copper grid (Agar Scientific; G2400C) with an additional thin and continuous carbon film. After incubation for 60 s on the grid the sample was blotted using filter paper (Whatman no. 4), washed twice with filament buffer and stained with 0.75 % uranyl formate (pH 4.0) for 30 s. For cross-linking studies, after incubation for 60 s of the sample solution on the grid and one washing step, a droplet of filament buffer with 0.25 % glutardialdehyde was applied for 30 min on the grid before negative staining to avoid putative pH-induced artefacts. All images were taken with a JEOL JEM-1400 electron microscope equipped with a $LaBB_6$ cathode at an operation voltage of 120 kV. Micrographs were recorded manually with a 4,000 x 4,000 pixel CMOS TemCam F416 (TVIPS) camera under minimal dose conditions.

Image processing of negatively stained filaments (see also section 3.4 in Material and Methods)

All micrographs had a pixel size of 2.32 Å per pixel and filaments were boxed with a boxing distance of 13 pixels (overlap ~ 90%) and a total box size of 128 pixels. We analysed 8,371 segments from 40 images of bare F-actin, 27,926 segments from 111 images of F-actin decorated with tropomyosin, and 27,011 segments from 81 images of F-actin decorated with tropomyosin and cross-linked with glutardialdehyde. Subsequently, all segment stacks were aligned and classified independently using reference-free alignment and k-means classification procedures as implemented in SPARX (Hohn et al., 2007; Figure 4.22). During the helical refinement and reconstruction using the HELICON package implemented in SPARX, a cylinder filled with Gaussian noise was used as an initial three-dimensional template. The position of tropomyosin was determined in the resulting three-dimensional maps. The difference maps of tropomyosin-bare F-actin and glutardialdehyde-bare F-actin were calculated with the 'vop subtract' command in Chimera (Pettersen et al., 2004; Figure 4.19c–g).

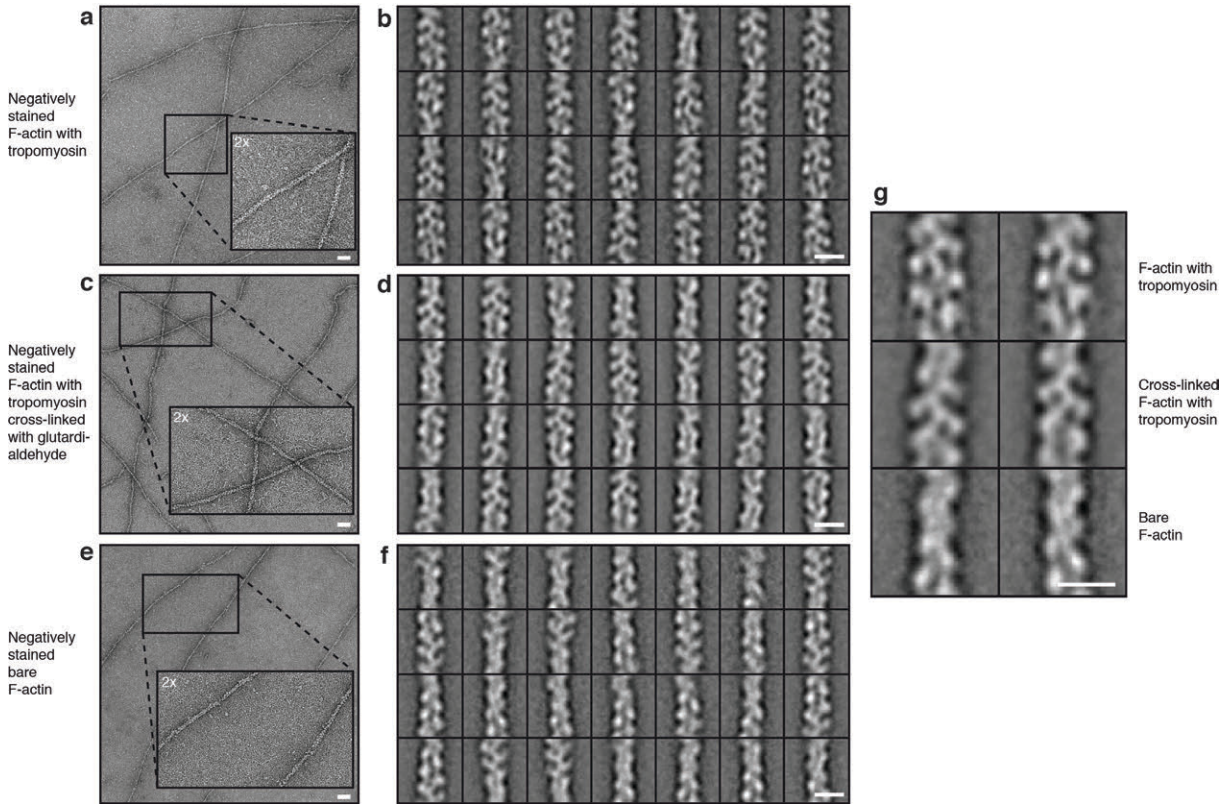

Figure 4.22: Micrographs and two-dimensional classification with negative staining EM.

a–**f**, Representative digital micrographs and corresponding representative two-dimensional class averages of F-actin decorated with tropomyosin negatively stained (in total 300 class averages of 27,926 segments from 111 images) (**a**, **b**), negatively stained after cross-linking with glutardialdehyde (in total 300 class averages of 27,011 segments from 81 images) (**c**, **d**), and a micrograph of negatively stained bare F-actin (in total 100 class averages of 8,371 segments from 40 images) (**e**, **f**). Scale bars, 50 nm. Each class average 70–90 single segments. Scale bars, 10nm. Insets in **a**, **d** and **e** show magnified regions of the digital micrographs. **g**, Comparison of representative class averages of the three negatively stained data sets. Class averages of the data sets with tropomyosin (top panels) show additional density and a larger diameter than bare F-actin (bottom panel). Scale bar, 10 nm.

Grid preparation and image acquisition for cryo-EM (see also subsection 3.2.2 in Material and Methods)

A 1.5 ml sample was applied to a glow-discharged holey carbon grid (C-flats 2/1, Protochips), incubated for 10 s and manually blotted for 3 s from the backside with filter paper (Whatman no. 5), before vitrification by plunging the grid into liquid ethane using a cryo plunger Cp3 (Gatan). Screening for the best sample and blotting conditions was performed on a JEOL JEM 3200FSC electron microscope equipped with a field emission gun and operated at a voltage of 200 kV. The omega in-column energy filter of the microscope was used to estimate the best ice conditions (~ 40-60 nm thickness). Finally, a data set was taken with a spherical-aberration corrected FEI Titan Krios transmission electron microscope equipped with an extra-high brightness field emission gun (XFEG) and operated at a voltage of 300 kV. Images were recorded with a back thinned 4k x 4k FEI Falcon 2 direct detection camera under minimal dose conditions using the automatic data collection software EPU (FEI). Within each selected grid-hole, three different positions were imaged, each with a total exposure of 1 s and a frame time of 55 ms. Seven frames from 85 ms to 475 ms with a total dose of 14.6 electrons per $Å^2$ and one total average with an electron dose of 30.7 electrons per $Å^2$ were used for image processing. The defocus range of the data set was 0.8-2.6 µm. The pixel size was 1.14 Å per pixel, based on the reflection of gold at the same magnification. Since the inaccuracy of pixel size determination is about 2 % with this method, we used the well-defined rise per subunit of F-actin

(27.6 Å) from fibre diffraction studies (Dominguez and Holmes, 2011; Oda et al., 2009) instead to calibrate the pixel size, which was then 1.12 Å per pixel.

Image processing of the cryo-EM data set (see also section 3.4 in Material and Methods)

As a first quality control, all 1,311 frame averages were manually inspected and only 689 images with high filament and ice quality (Figure 4.11a) were used for further processing. Frames were aligned and afterwards summed up using motion correction (Li et al., 2013a). Filaments were manually selected with helixboxer in SPARX. A total of 109,242 segments from 7,854 filaments were extracted with a box size of 256 pixels and a boxing distance of 29 pixels (overlap ~ 90 %). Thus, the approximate distance between them (~ 32 Å) slightly exceeded the rise of the helical assembly of actin (~ 27-28 Å), as required by the helicon design. The defocus and astigmatism and the accuracy of both were determined by cter in SPARX (Penczek et al., 2014). All segments were aligned and classified using reference-free alignment and k-means classification procedures implemented in SPARX (Figure 4.11b). For the initial reconstruction, the data set was binned twice to a pixel size of 2.24 Å and a box size of 128 pixels. We used a cylinder filled with Gaussian noise as a three-dimensional initial template for the helical refinement and reconstruction in helicon. After adjusting the pixel size as described above, the helical symmetry parameters converged to a rise per subunit of 27.5 Å and an azimuthal rotation of 166.4 °. Initially, the entire F-actin–tropomyosin map was used as the reference during the first rounds of refinement, using the helical symmetry parameters of F-actin. However, tropomyosin spans over seven actin subunits and therefore has a symmetry different to that of actin. Nevertheless, because it is divided into seven pseudo-repeating units, each of which binds to a successive actin subunit along F-actin, the symmetry of F-actin could be used for reconstructions of actin-tropomyosin complexes of up to 6 Å resolution, accepting that the overlap region of the N and C termini of tropomyosin would not be discernible in these maps. Once the refined map reached a resolution of 6.5 Å, as determined by the FSC0.5 criterion (Penczek, 2010c), we masked out tropomyosin in the reference volume before continuing with high-resolution refinements of F-actin. In the last refinement iteration, we used only filaments derived from summed up frames with a drift of less than 7 Å, as estimated in the motion correction step and with a sufficient content of high-resolution information, as determined by cter in SPARX. This yielded a subset of 74,228 segments for the final map, which corresponded to ~120,000 asymmetric subunits. The segments' statistics are given in (Table A6.4). Since an electron microscope map of a filament is truncated at the edges of the cubic volume of the box (here 256 voxels), a mask with Gaussian edges must be applied for resolution estimation to minimize artefacts. Therefore, Fourier shell correlation (FSC) analysis was performed within the central area of the volume, resulting in a nominal resolution of 3.7 Å ($FSC_{0.5}$ criterion) for the F-actin cryo-EM density map (Figure 4.12d). The map of F-actin was then sharpened using a negative b factor of -50 $Å^2$ and filtered to its nominal resolution. Finally, the tropomyosin map filtered to 6.5 Å was merged with the final F-actin map to obtain a map of the entire F-actin-tropomyosin complex.

Model building and refinement of F-actin (see also section 3.5 in Material and Methods)

The central F-actin subunit (chain A) shows all available contacts to adjacent chains (B, C, D, E) and was therefore used for further structural analysis. In a first step, five central subunits (chains A–F) of an F-actin model (PDB accession code 4A7N) were rigid-body fitted into the electron microscope map, using 'Fit in Map' and the map was initially segmented with 'Split Map' in Chimera (Pintilie et al., 2010). Homology modelling was performed using MODELLER (Sali and Blundell, 1993) and the

resulting model of the central subunit was then flexibly fitted into its corresponding part of the density using DireX (Wang and Schröder, 2012). Finally, the flexibly fitted subunit was used to create a starting F-actin model of five adjacent subunits (hereafter referred to as the 'pentamer') for further model building. The cryo-EM density was converted to structure factors with the CCP4 program suite (Winn et al., 2011). The model and the map were then used for real space refinement and model building in COOT (Emsley et al., 2010). After a single iteration of model building of the central F-actin subunit, its part of the map was further used for an initial automatic reciprocal space refinement using PHENIX.refine (Adams et al., 2011). Since this part was less well resolved in the N and C terminus, and model building was difficult for a part of the D-loop, we deleted amino acids 1–4, 42–50 and 372–375 from the model. Owing to the high reliability of the experimental phases of the cryo-EM map, we were able to apply experimental phase restraints during refinement in PHENIX. After refinement the output model was again manually refined in COOT using the original cryo-EM map to minimize model bias. Rebuilding of the N or C terminus was not possible even in the refined map (Figure 4.23). However, after refinement in PHENIX the definition of the D-loop improved, so ultimately it could be manually rebuilt *ab initio*.

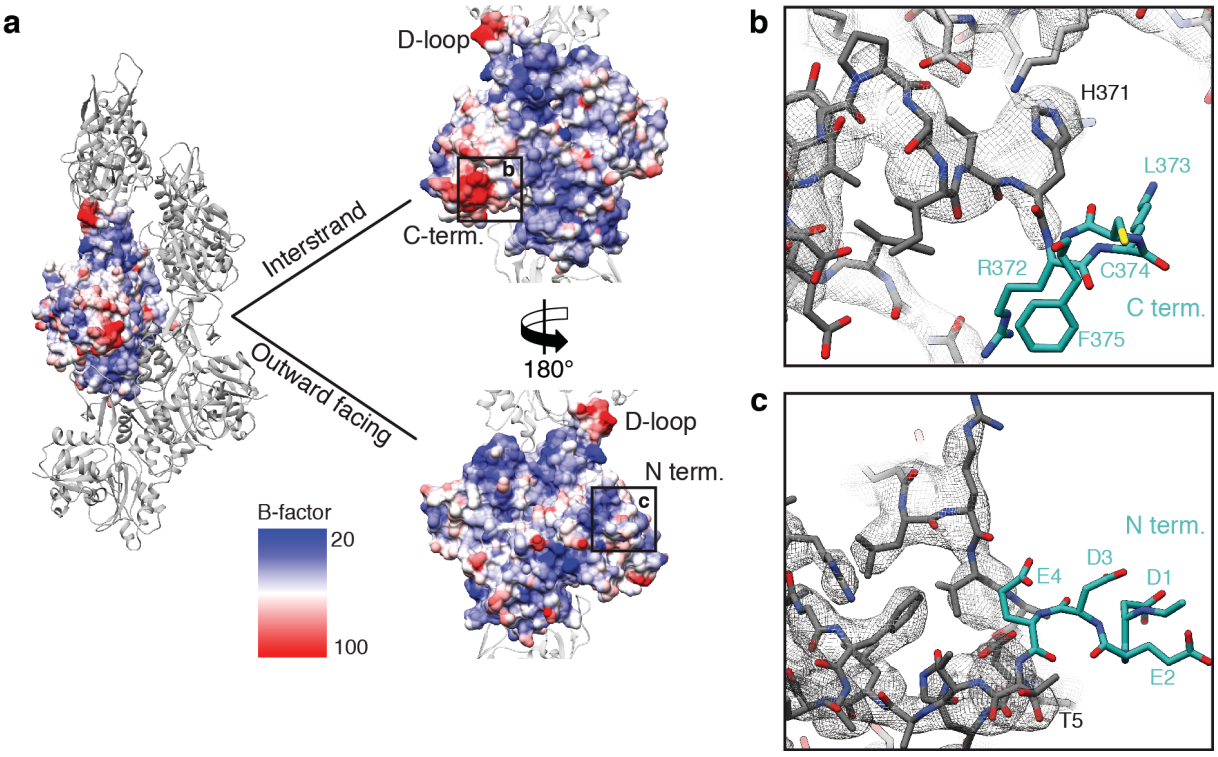

Figure 4.23: B-factor distribution and not resolved N and C termini.

a, Surfaces of F-actin with B-factors (high is red, low is blue) estimated by the reciprocal space refinement in PHENIX. A side view as well as top views on the inward- and outward-facing surfaces, that is, facing the adjacent F-actin subunit inside the filament and oriented to the periphery, respectively, are shown. **b**, **c**, Putative structures of the C and N termini (cyan). Map density is missing in these regions.

After refinement of the subunit had converged and model building was completed, the resulting subunit was used to assemble the F-actin pentamer and the respective full map of the central pentamer was then segmented. The molecular model and the respective original density were then used as input for PHENIX.refine. Again, we alternated manual model building and refinement steps. Finally, the resulting model was validated using MOLPROBITY (Chen et al., 2010; see data statistics in Table A6.4). For further structural analysis we used the final model and the cryo-EM map of the actin pentamer.

Structure analysis and visualization (see also section 3.5 in Material and Methods)

To describe the interaction between F-actin and tropomyosin, a chimaeric molecular model of tropomyosin (Li et al., 2014) was initially rigid body fitted into the cryo-EM density of F-actin–tropomyosin. Subsequently, the respective density of tropomyosin was extracted as described above using Chimera. The molecular model of tropomyosin was then flexibly fitted into the resulting density using DireX. Furthermore, during flexible fitting, in order to preserve its electrostatically preferred position on F-actin we fixed tropomyosin in its vertical position on the filament. Atomic clashes and stereochemistry were repaired using PHENIX.geometry_minimization (Adams et al., 2011). Since the tropomyosin N/C-terminal overlap is not fully understood (Lehman et al., 2013a), we reduced the model to the five central pseudo-repeats. Owing to the limited resolution of the cryo-EM density in the region of tropomyosin, we avoided interpretation of tropomyosin on the single-amino-acid level.

We used the refined actin pentamer and the modelled tropomyosin to reconstruct a full filament for visualization of the actin–tropomyosin interaction (Figure 4.18). The filament was protonated using H++ (Anandakrishnan et al., 2012) at different pH values and the electrostatic coulomb potential of the filament surface was calculated to range from -10 kcal mol-1 to +10 kcal mol-1 in Chimera (Figure 4.18b, Figure 4.19g). For visualization of the hydrophobicity per amino acid residue, we used 'Define attribute' in Chimera and generated amino-acid-specific scores (Hessa et al., 2005). Point mutations were introduced via COOT or Chimera to show charge-induced repulsions and changes in hydrophobicity. The HGMD library was browsed to find mutations in regions of interest (Stenson et al., 2014).

For detailed analyses of intra- and intermolecular interactions in F-actin, we applied PISA tools (Krissinel and Henrick, 2007) and distance measurements in Chimera. The G- to F-actin transition within a monomer/subunit was visualized and interpreted with the 'Morph Conformations' in Chimera. Furthermore, the hinge region and the global rotation angle were detected with the DynDom Sever (Hayward and Lee, 2002) using an atomic model of G-actin (PDB accession code 1J6Z (Otterbein et al., 2001)) and one subunit of our F-actin model (Figure 4.15, Figure 4.16, Figure 4.17).

4.4 Structure a human cytoplasmic actomyosin complex

This section was original published in *Nature* in 2016 as:

von der Ecken J., Heissler S.M, Pathan-Chhatbar S., Manstein D.J., and Raunser S. (2016): *Cryo-EM structure of a human cytoplasmic actomyosin complex at near-atomic resolution.* Nature 534, 724-728.

Online version: http://www.nature.com/nature/journal/v534/n7609/full/nature18295.html

The manuscript was submitted on the 16th of February 2016 and was accepted on 29th of April of the same year after undergoing a peer review procedure. It was published online on the 20st of June 2016 and available in the printed journal on the 30th of the same month.
The original publication was reformatted to the format of the thesis (e.g. text font, figure numbering). Some extended data figures were moved to the main text, party split or combined to improve the quality of reading, respectively. Respective references to other chapters or sections are inserted. Some figures and tables were moved to the Appendix. Subsection 4.4.11 gives an overview on the methods in the publication. More generalized and optimized protocols are given in Material and Methods and sections 4.1 of this chapter, respectively. Supplementary videos are not included in this thesis but can be downloaded from the online version of the paper (von der Ecken et al., 2016).

4.4.1 Abstract

The interaction of myosin with actin filaments is the central feature of muscle contraction (Huxley, 1969) and cargo movement along actin filaments of the cytoskeleton (Heissler and Manstein, 2012). The energy for these movements is generated during a complex mechanochemical reaction cycle (Lymn and Taylor, 1971; Sweeney and Houdusse, 2010a; see also subsection 2.2.1). Crystal structures of myosin in different states have provided important structural insights into the myosin motor cycle when myosin is detached from F-actin (Coureux et al., 2004; Gulick et al., 1997; Llinas et al., 2015). The difficulty of obtaining diffracting crystals, however, has prevented structure determination by crystallography of actomyosin complexes. Thus, although structural models exist of F-actin in complex with various myosins (Behrmann et al., 2012a; Holmes et al., 2003; Lorenz and Holmes, 2010; Rayment et al., 1993a), a high- resolution structure of the F-actin–myosin complex is missing (see also subsection 2.2.2). Here, using electron cryomicroscopy, we present the structure of a human rigor actomyosin complex at an average resolution of 3.9 Å. The structure reveals details of the actomyosin interface, which is mainly stabilized by hydrophobic interactions. The negatively charged amino (N) terminus of actin interacts with a conserved basic motif in loop 2 of myosin, promoting cleft closure in myosin. Surprisingly, the overall structure of myosin is similar to rigor-like myosin structures in the absence of F-actin, indicating that F-actin binding induces only minimal conformational changes in myosin. A comparison with pre-powerstroke and intermediate (P_i-release; Llinas et al., 2015) states of myosin allows us to discuss the general mechanism of myosin binding to F-actin. Our results serve as a strong foundation for the molecular understanding of cytoskeletal diseases, such as autosomal dominant hearing loss and diseases affecting skeletal and cardiac muscles, in particular nemaline myopathy and hypertrophic cardiomyopathy.

4.4.2 Structure of the ATM complex

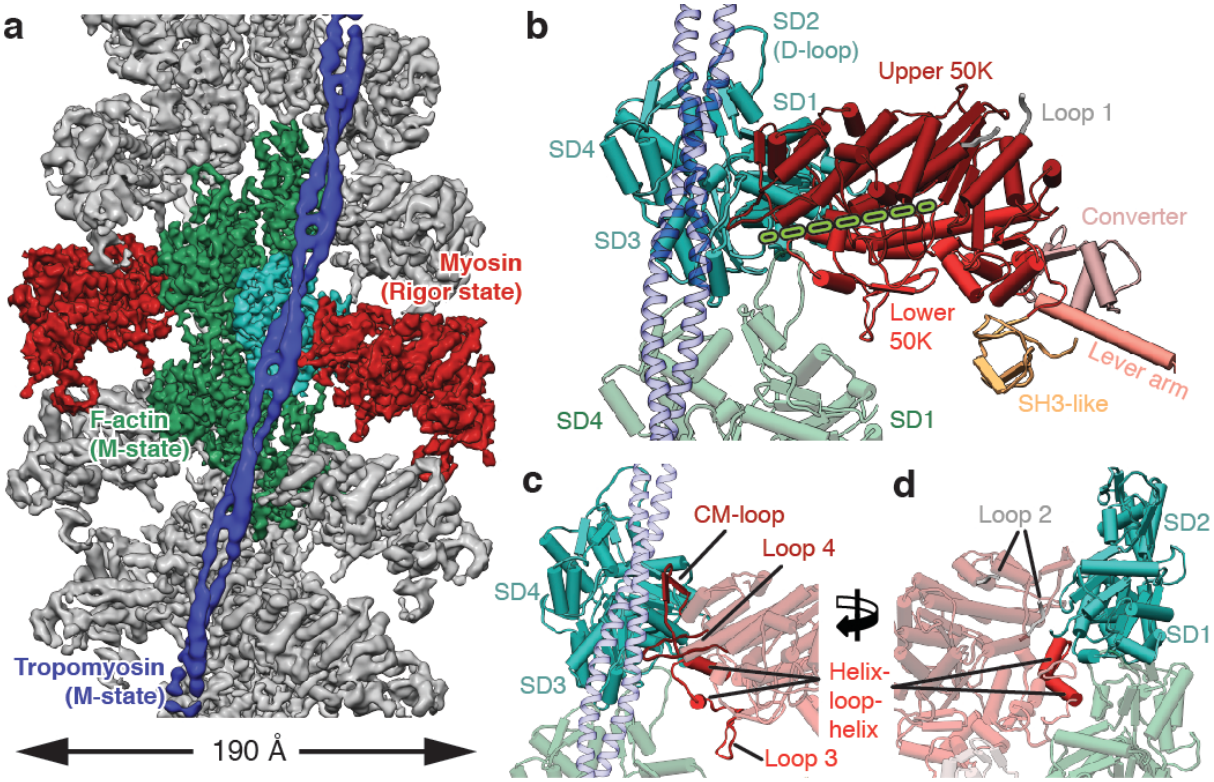

Figure 4.24: Structure and model of the ATM complex.

a, Cryo-EM reconstruction of F-actin (five central subunits in green and cyan) decorated with tropomyosin (blue) and myosin (central molecules in red). The peripheral densities (shown in grey) and tropomyosin were low- pass filtered and symmetrized for better visualization. **b**, Subdomain organization of F-actin and myosin head region. The closed actin- binding cleft between L50 (red) and U50 (dark red) domains is indicated with a dotted line. **c**, **d**, Front and back views of the F-actin–myosin interface. Involved structural parts of myosin are highlighted in red. For all figures and videos, we use a general colour code for each protein and state, if not labelled differently. The central F-actin subunit is shown in cyan (M-state) and yellow (A-state); surrounding F-actin subunits are depicted in green (M-state) and in darker yellow (A-state); rigor state myosin (red), P_i-release state myosin (blue) and PPS state myosin (purple). Less relevant parts of models or densities in respective figures are depicted in grey or faded out.

Using electron cryomicroscopy (cryo-EM) and single-particle-based analysis of helical specimens (subsection 4.4.11), we determined the structure a human actomyosin–tropomyosin (ATM) complex, composed of the motor domain of non-muscular myosin-2C (NM-2C), cytoplasmic γ1-F-actin and cytoplasmic tropomyosin 3.1 (Figure 4.24, Figure 4.25 and subsection 4.4.11). We also reprocessed our previous F-actin–tropomyosin data set (von der Ecken et al., 2015) and obtained an improved reconstruction at 3.6 Å resolution (Figure 4.36a in subsection 4.4.11). The density of tropomyosin did not improve in both data sets and is limited to ~7 Å as described previously (von der Ecken et al., (2015) and section 4.3).

The ATM structure reveals that myosin interacts intimately with F-actin (Figure 4.24a). The overall organization of the ATM complex is similar to that described in our previous structure of the complex between *Dictyostelium discoideum* myosin-IE, skeletal α-F-actin and α-tropomyosin (Behrmann et al., 2012a). However, given the superior resolution of our present structure, we could clearly identify large side chains and therefore reveal most intermolecular interactions between F-actin and myosin in detail. The large interface between the two proteins is formed mainly between the helix–loop–helix (HLH) motif and surface loops of myosin (CM-loop, loop 2, loop 3, loop 4, and 'activation' loop; Várkuti et al., 2012) and the subdomain (SD) 1 and 2 of one actin subunit and SD2 (D-loop) of the adjacent

actin subunit as previously predicted (Behrmann et al., 2012a; Holmes et al., 2003; Rayment et al., 1993a; Figure 4.24b-d).

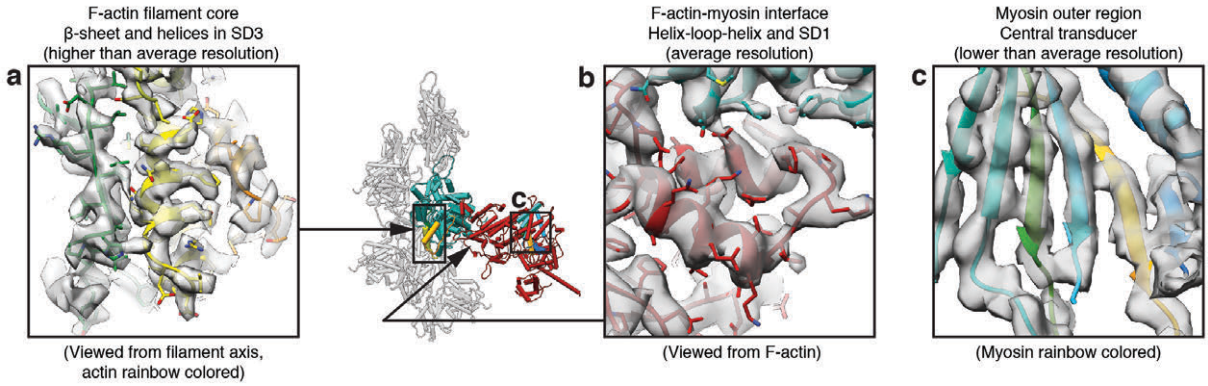

Figure 4.25: Resolution range of the density map.

a–**c**, Representative regions with higher than the average resolution (~3.5 Å) in the F-actin filament core (**a**), the average resolution of 3.9 Å at the interface (**b**) and lower resolution (~ 4 - 5 Å) in outer myosin parts (**c**).

Tpm3.1, which is resolved to ~7 Å, is in the same position as skeletal muscle tropomyosin 1.1 (Tpm1.1) in our previous structure, namely the M-state (Behrmann et al., 2012a), interacting with loop 4 of myosin and SD3 of actin (Figure 4.24b, c, Figure 4.27a). Interestingly, although Tpm3.1 is shorter (stretching over six actin subunits) than Tpm1.1 (stretching over seven actin subunits), the pitch of the coiled-coil structure is equivalent. Tpm3.1, which is mainly negatively charged on its surface, interacts with arginine 384 of loop 4, indicating electrostatic interactions (Figure 4.27a). In addition, the negatively charged residue D387 on loop 4 (N377–D393) interacts with a positively charged region on F-actin (K325, K327) (Figure 4.27b). Notably, in the absence of myosin, these actin residues directly interact with tropomyosin (A-state; von der Ecken et al., 2015).

4.4.3 Helix-loop-helix motif as the key binding region

The HLH motif (L550–E575) in the lower 50-kDa (L50) domain of NM-2C plays an essential role in strong binding of myosin to F-actin (Figure 4.24c, d, Figure 4.26, Figure 4.27c, d). It enters a hydrophobic groove on actin that is formed between two adjacent actin subunits comprising SD1 and SD3 of one and the D-loop (R38–V53) of the adjacent subunit. In particular, the hydrophobic loop of the HLH motif interacts with the hydrophobic groove and F560 is completely immersed into a hydrophobic cavity resembling a lock-and-key interaction (Figure 4.26a-d, Figure 4.27d). The key role of F560 for the actomyosin interaction has also been shown by mutational analyses in which a F560A mutation resulted in a complete disruption of motility, whereas alanine mutants of the directly adjacent W559 and P561 showed only one-tenth the motility compared with wild type (Onishi et al., 2006). Interestingly, compared with its position in the pre-powerstroke (PPS) state the loop is the only part of the HLH motif that alters its position upon actin binding, stressing its important role in the actin-myosin interaction (Figure 4.26a, c).

In addition to the hydrophobic contacts, there are also two electrostatic interactions that stabilize the HLH motif binding to F-actin. E570 probably forms a salt bridge with K49 of the D-loop and E556 interacts with the backbone of S349 and T350 in SD1 of F-actin (Figure 4.26b, e, andFigure 4.27c). Both residues are part of a highly conserved acidic patch in several myosin classes (Figure 4.26e,

Figure A6.3), and a single point mutation (E556Q) in myosin results in a tenfold reduced F-actin binding affinity (Furch et al., 2000).

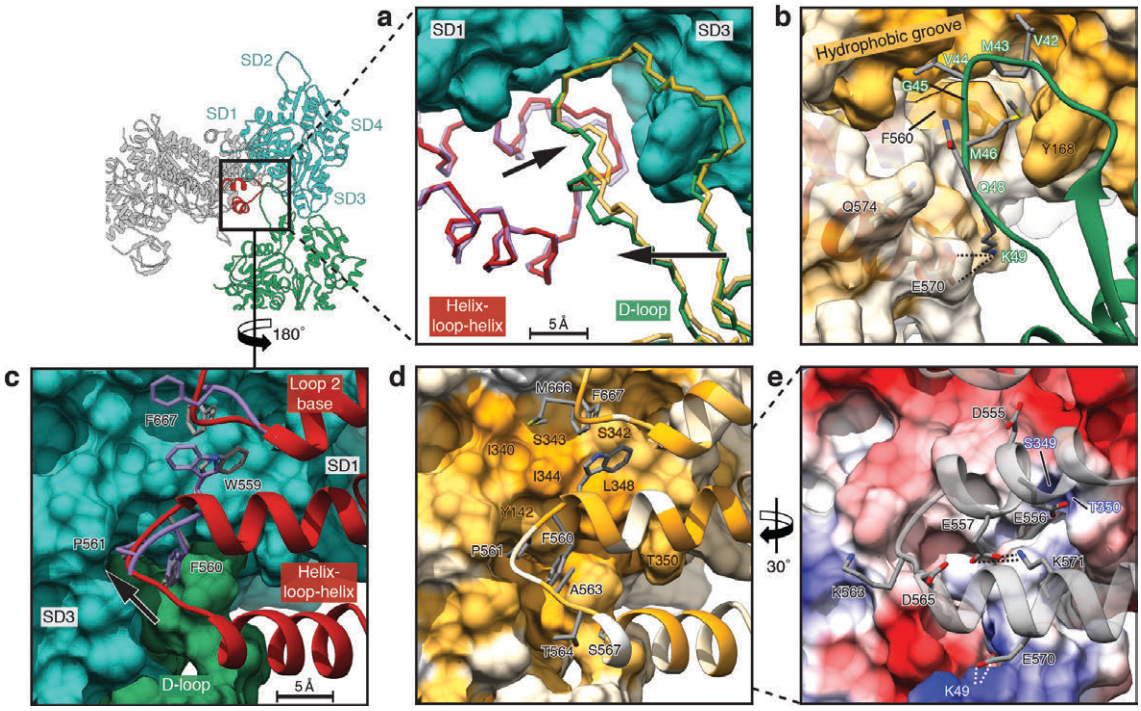

Figure 4.26: Helix-loop-helix motif bound to F-actin.

a, Front view of F-actin and the HLH motif of the L50 domain of myosin show only small changes in loop regions while helices do not alter between weak (PPS state in purple, PDB accession number 5I4E) and strong binding (rigor state in red). The D-loop is moved towards the binding interface and is stabilized (A-state in yellow, M-state in green). Arrows indicate changes and scale bar is given. **b**, Same view as before shows the interface of myosin and F-actin in the rigor state. One possible salt bridge is highlighted with dotted lines. Surfaces are coloured from low (white) to high (yellow) hydrophobicity. **c**–**e**, Back view of the HLH motif and the base of loop 2 bound to central (SD1, SD3) and adjacent (D-loop) F-actin subunits. Comparison of rigor (red) and PPS state (purple, PDB accession number 5I4E) shows main differences (**c**). Final interaction of fully bound myosin is given in **d**, **e**. Possible electrostatic interactions are indicated by dotted lines. F-actin surface is depicted per subunit colour (**c**), by hydrophobicity (**d**) or electrostatic Coulomb potential (**e**, -10 kcal mol^{-1} in red to +10 kcal mol^{-1} in blue). In all subfigures, coloured residue labels belong to F-actin.

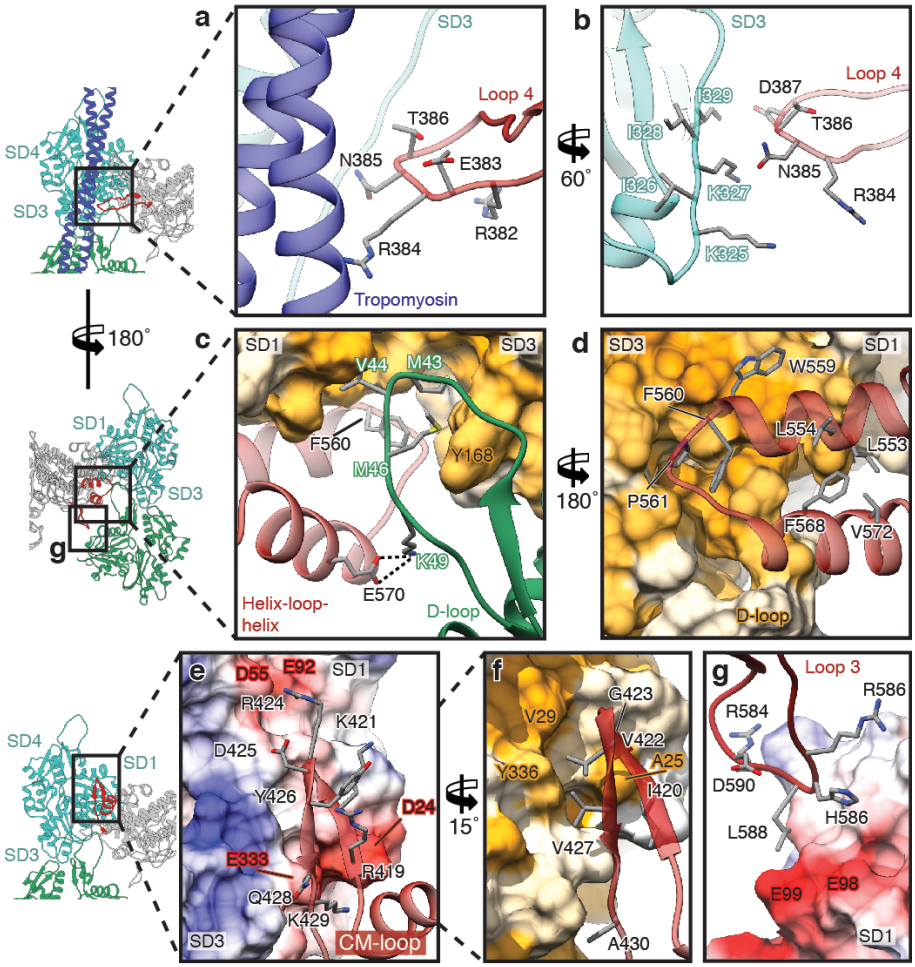

Figure 4.27: Interfaces of the ATM complex.

a, **b**, Interface of loop 4 with tropomyosin (blue) and SD3 of one F-actin subunit (cyan). **c**, **d**, Interaction of the HLH motif of myosin (red) with hydrophobic groove formed by the D-loop of one F-actin subunit (green ribbon in **c** and as surface in **d**) and SD1 and SD3 of the adjacent subunit (surfaces depicted by low (white) to high (yellow) hydrophobicity). Hydrophobic residues at the interface (**c**, **d**) and a possible electrostatic interaction (dotted lines in **c**) are highlighted. **e**, **f**, The CM-loop (red) binds to a region formed by SD1 and SD3 of F-actin. Charged (**e**) and hydrophobic (**f**) residues of myosin. **g**, Loop 3 (red) interacts with SD1 of an adjacent F-actin subunit forming the Milligan contact. The F-actin surface is coloured either by hydrophobicity (**f**) or electrostatic Coulomb potential from -10 kcal mol^{-1} (red) to +10 kcal mol^{-1} (blue) (**e**, **g**). In all panels, coloured residue labels depict residues of F-actin.

4.4.4 Cardiomyopathy loop completes the rigor interface

The cardiomyopathy loop (CM-loop), forming one antiparallel β-strand pair (T417–T432), is the major site of the myosin upper 50-kDa (U50) domain that interacts with actin (Figure 4.24c, Figure 4.27e, f). The CM-loop is fully ordered and the interface with actin is mainly stabilized by hydrophobic interactions (Figure 4.27f), supported by weak electrostatic interactions at the tip and the base of the CM-loop (Figure 4.27e). K429, which is found in all myosin-II isoforms (Figure 4.28), interacts with a negatively charged patch on F-actin formed mainly by D24 and E333 in SD1 and SD3, respectively (Figure 4.27e). In addition, the positively charged tip (R424) interacts with the negatively charged region around E55 and D92 of F-actin (Figure 4.27e). However, residue 424 is only positively charged in smooth and non-muscular isoforms of myosin (Figure 4.28b) and therefore does not play a role in skeletal and cardiac muscles. Importantly, we did not find any prominent possible salt bridges that would stabilize the contacts between the CM-loop and F-actin, supporting previous mutagenesis

studies suggesting that charged residues, in particular the highly conserved residue D425, play a minor role in this interface (Onishi et al., 2006; Sasaki et al., 1999).

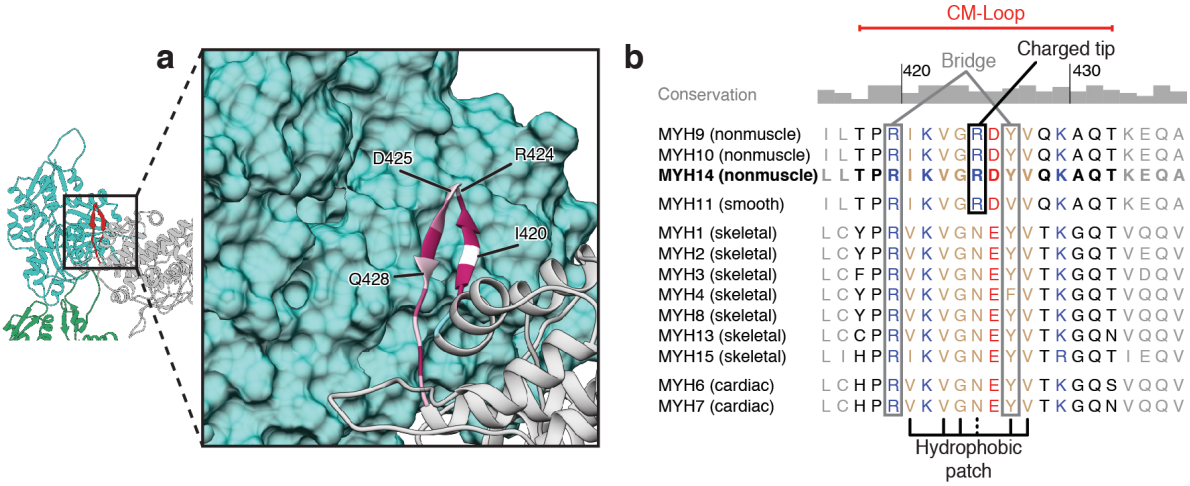

Figure 4.28: Cardiomyopathy loop.

a, Conservation of the CM-loop in the human myosin-II class is visualized as a model on F-actin (cyan) from low (white) to high (purple) conservation. **b**, Sequence alignment of the CM-loop region of the human myosin-II class. Important functions at the F-actin–myosin interface are highlighted and labelled. Residue numbering refers to our published structure belonging to the sequence of NM-2C (depicted in bold type). Tissue localization of myosin-II is written in parentheses. We refer to the different myosin isoforms according to the nomenclature for the genes encoding the respective myosin heavy chains.

As speculated previously (Lorenz and Holmes, 2010), the highly conserved and disease-related residue R419 (R403 in β-cardiac myosin) indeed does not directly interact with F-actin (Figure 4.27e,Figure 4.28b and Table A6.5a, b). In our structure, R419 clearly interacts with Y426 on the opposing strand of the CM-loop, thereby bridging and stabilizing the conformation of the loop (Figure 4.27e). Both residues are highly con- served, suggesting that this bridge is present in all myosin-II isoforms (Figure 4.28b). Many disease-causing mutations are found in the region of the CM-loop, demonstrating the high importance of the CM-loop for the strong binding between actin and myosin (Figure 4.28b and Table A6.5).

4.4.5 Role of loop 2 in initial binding

Several studies showed that loop 2, connecting the L50 and U50 domains in myosin (W638–T669), plays a major role in the initial binding to F-actin (Furch et al., 2000; Joel et al., 2001; Murphy and Spudich, 1999; Onishi et al., 2006; Uyeda et al., 1994). We see clear density for loop 2 in the ATM structure. However, whereas the base of the loop is ordered, the rest of the loop is more flexible (Figure 4.29a, b). It occupies a large predominantly hydrophobic surface of the actin SD1 domain (Figure 4.29c, Figure A6.4a, b).

A conserved hydrophobic patch at the carboxy (C)-terminal base of loop 2 (G665–F667) and the tip of helix-R (W559) (Figure 4.29c, Figure A6.3) interacts with a hydrophobic groove of actin SD1 (Figure 4.26d, Figure 4.29c). Mutagenesis studies showed that especially W559 is essential for forming the F-actin–myosin interface and obtaining motility (Kojima et al., 2001; Onishi et al., 2006). Compared with their position in the PPS state, these residues orient towards actin to stabilize the newly formed interface (Figure 4.31a).

Interestingly, the adjacent conserved positively charged region (R661–R664) interacts with the acidic N terminus of actin and a negatively charged area (D23, D24) of SD1 (Figure 4.29d, Figure A6.4b).

While one of the conserved arginines (R663) forms a possible salt bridge with actin E3 (Figure 4.29d), the other one (R664) interacts with D640 and D642 at the other end of loop 2, forming an electrostatic belt that stabilizes the base of loop 2 (Figure 4.29c). Notably, D640 and D642 are only conserved in myosins with a long loop 2 (Figure A6.4c), suggesting that the electrostatic belt is not required for myosins with a shorter loop 2.

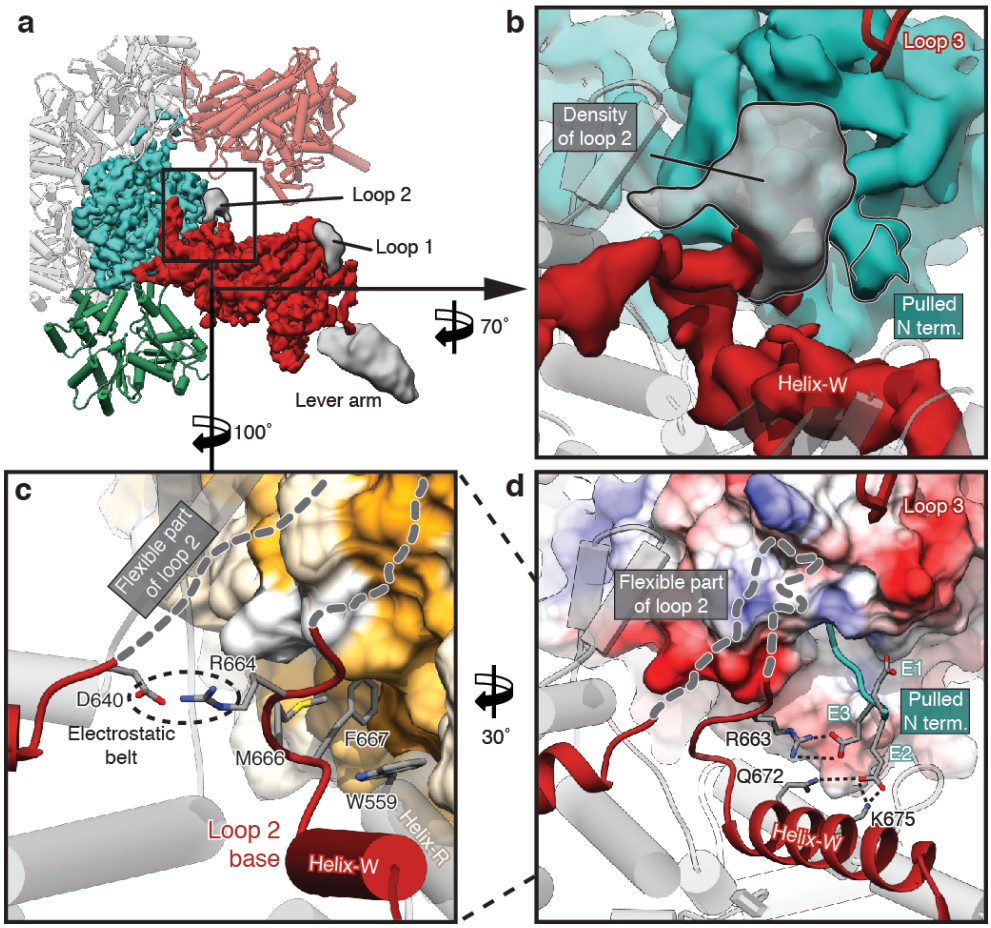

Figure 4.29: Stabilization of loop 2.

a, Myosin densities of lower resolution (grey) are shown together with more highly resolved regions of myosin (red) and F-actin (cyan). The densities can be assigned to more flexible parts of loop 1, loop 2 and the outer lever arm, respectively. **b**, Close-up view onto region of the density map corresponding to loop 2. Loop 3 of the adjacent myosin does not interact with loop 2 (red). **c**, **d**, Interaction of the stabilized base of loop 2 with SD1 of F-actin (coloured by hydrophobicity in **c** or by electrostatic Coulomb potential in **d**). The flexible part of loop 2 and possible electrostatic interactions are indicated by different dotted lines.

4.4.6 Loop 3 as an assistant

In line with our previous observation (Behrmann et al., 2012a), loop 3 (Q576–D593) forms the so-called Milligan-contact (Milligan et al., 1990; Rayment et al., 1993a) connecting the L50 domain to SD1 of the adjacent actin subunit (Figure 4.24c, Figure 4.27g, Figure A6.4d, e). The small interface is only formed by complementary charged surfaces and not by specific salt bridges as previously expected (Figure 4.27g). The weak nature of the interactions, and the fact that not all myosin isoforms have a long loop 3 that can form this contact (Van Dijk et al., 1999), suggest that, for most myosin proteins, loop 3 plays only an ancillary role in strong F-actin binding.

4.4.7 Supporting instead of activation loop

Several studies suggested that a proline-rich loop in the L50 domain, a so-called activation loop (I541–G549), is directly involved in activation of myosin by interacting with the negatively charged N terminus of actin (Várkuti et al., 2012; 2015). Our ATM structure confirms that this loop is part of the actomyosin interface. Together with helix-W and the base of loop 2, it forms a positively charged basin that interacts with the negatively charged N terminus of actin (Figure 4.29d, Figure 4.30a, b). However, R543, which is the only positively charged residue of the loop and conserved in myosin-II (Figure A6.5a), points away from the interface and therefore cannot be involved in a direct interaction with the glutamates of the actin N terminus (Figure 4.31b, Figure 4.30c).

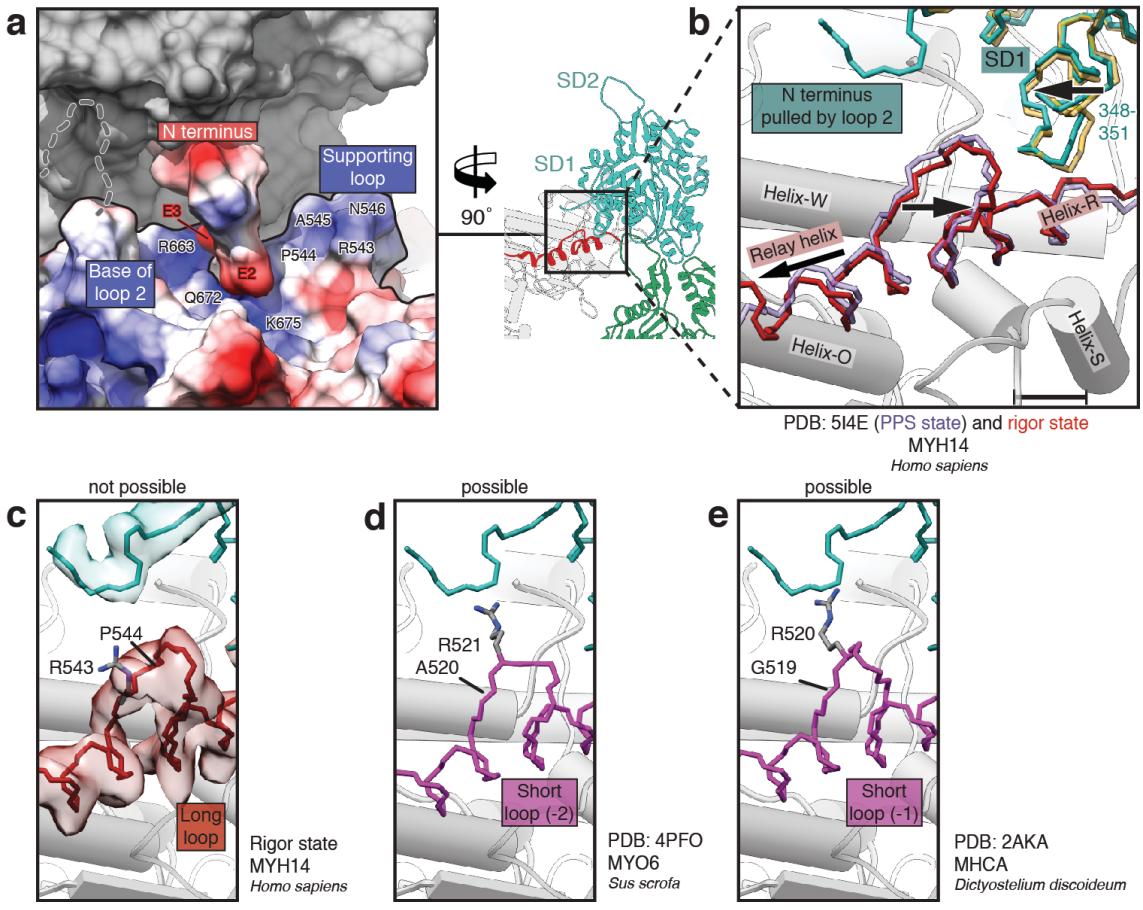

Figure 4.30: Sequence-dependent interaction of supporting loop with N terminus of F-actin.

a, Surface of myosin and N terminus is depicted by electrostatic Coulomb potential (-10 kcal mol^{-1} in red to +10 kcal mol^{-1} in blue). Involved charged residues are labelled. **b**, Position of the proline-rich loop (supporting loop) located between relay helix and helix-R slightly differs between the PPS (purple, PDB accession number 5I4E) and rigor state (red) and shows no direct interaction with the N terminus of F-actin. Regions at the surface of SD1 are pulled to the actomyosin interface indicated by an arrow and a scale bar is given (F-actin in A-state is depicted in yellow; F-actin in M-state is depicted in cyan). **c**–**e**, Comparison of prominent properties in the supporting loop of different myosin classes (comparative models in purple) and their ability to undergo a direct interaction with the N terminus. Main differences are length of loop (numbers give absent amino acids relative to long loop) and position of the prominent positive-charged amino acid (R or K). Only an arginine or lysine sitting on the top would allow a direct interaction (**d**–**e**), while a sideward-oriented arginine (**d**) disables or reduces a possible interaction. In addition, respective densities (**c**) of the cryo-EM map are displayed. Sequence alignment in Figure A6.5a.

In other myosins with shorter activation loops, namely myosin-V, myosin-VI or *Dictyostelium* myosin-II, the position of the positively charged residue is shifted by one position and would therefore allow a direct interaction with the N terminus (Figure A6.5a, b, Figure 4.30d, e). Compared with the PPS

conformation, the proline-rich loop orients slightly closer to F-actin (Figure 4.30b). Since the actin-induced conformational changes in the proline-rich loop and the adjacent relay helix are minor, we conclude that they are probably not responsible for a direct activation of myosin and therefore suggest using the term supporting loop rather than activation loop.

4.4.8 Myosin-induced conformational changes in F-actin

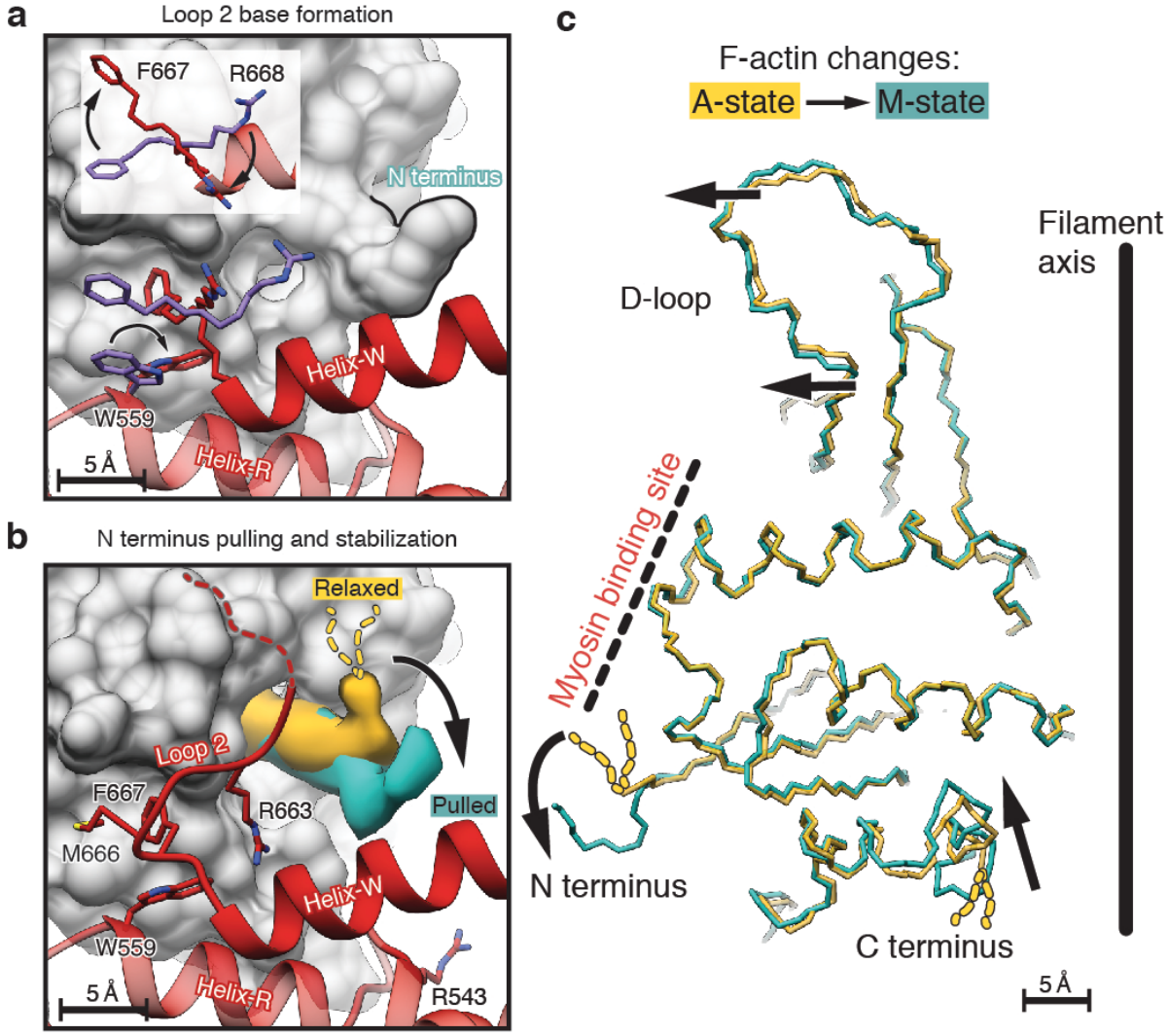

Figure 4.31: Comparison of PPS and rigor state and induced changes in F-actin.

a, Involved residues of loop 2 and helix-R undergo changes in rotamer orientation during base stabilization of loop 2 (PPS state (purple), PDB accession number 5I4E; rigor state (red)). The F-actin surface is shown in grey. Inset shows a top view of rotating residues of loop 2. F667 rotates to SD1, R668 rotates outwards to the U50 of myosin. **b**, Density comparison of the N terminus between myosin-unbound F-actin (yellow, A-state) and myosin-bound F-actin (cyan, M-state) illustrates the pulled conformation of the terminus induced by loop 2 interaction. The flexible N terminus (1–4 in α-actin) in the A-state is depicted as dotted lines. **c**, Superposition of SD1 and SD2 of F-actin in the A-state (yellow) and M-state (cyan) visualizing the myosin-induced changes in F-actin (indicated by arrows).

To identify myosin-induced conformational changes in F-actin, we compared the ATM structure with our reprocessed F-actin–tropomyosin structure. As expected from our previous observations (Behrmann et al., 2012a), the overall changes are minimal. Whereas the D-loop and other interface regions orient slightly towards myosin (Figure 4.26a, Figure 4.31c), areas interacting with the CM-loop and more distal regions of actin only move marginally away from the interface (Figure A6.6a-c).

The most prominent changes occur at the N and C termini of actin (Figure 4.31b, c, Figure A6.6d-k). The highly conserved and negatively charged N terminus (Figure A6.6c), which is only partly resolved in F-actin (von der Ecken et al., 2015), but essential for myosin binding (Cook et al., 1993; Miller et al., 1996; Sutoh et al., 1991), is completely ordered in the ATM structure and pulled into a positively charged basin on the myosin structure (Figure 4.30a, Figure 4.31b, c). Two glutamates at its tip (E2, E3) are potentially involved in salt bridges with positively charged residues on helix-W and loop 2 (Figure 4.29d). The conformational change of the N terminus is partly transmitted to the nucleotide-binding pocket (Figure A6.6e, f). Actin residues D10 and K17 slightly change their position (Figure A6.6f ,g); however, this does not considerably alter the position of ADP and Mg^{2+} (Figure A6.6f, h). Interestingly, although the actin C terminus does not participate in forming the actomyosin interface, it is completely ordered in the ATM structure and orients towards the SD1 domain (Figure 4.31c, Figure A6.6i-k). This is in line with previous studies showing that myosin binding to F-actin results in quenching of fluorescence of pyrene-labelled actin at C373 (C374 in α-actin) (Onishi et al., 2006). The higher myosin-induced stability of the D-loop, N terminus and surrounding regions is probably responsible for the stabilization of the C terminus, which is not well ordered in the F-actin–tropomyosin structure (von der Ecken et al., 2015; Figure A6.6j). We believe that the minimal but substantial myosin-induced conformational changes are exemplary for most actin-myosin interactions. We therefore suggest using the term M-state for F-actin bound to myosin in contrast to A-state for bare F-actin (Figure 4.24a, Figure 4.31c).

4.4.9 Actin-induced conformational changes in myosin

To understand which conformational changes F-actin binding induces in myosin, we compared our rigor ATM structure with rigor-like crystal structures (Figure 4.32). Surprisingly, the overall structures of the different rigor-like states are very similar compared with that of the rigor state (Figure 4.32a, b), indicating that F-actin induces only minimal conformational changes in myosin as previously predicted (Coureux et al., 2003; Holmes et al., 2003). Differences are found at actin-interacting loops that are partly ordered in the crystal structures and are stabilized by actin in the ATM structure (Figure 4.32c). In addition, we found that the converter and lever arm regions differ in their position relative to the rest of the protein (Figure 4.32d). Importantly, the comparison between rigor and rigor-like structures shows that F-actin stabilizes the closed conformation of myosin, but does not induce major additional conformational changes.

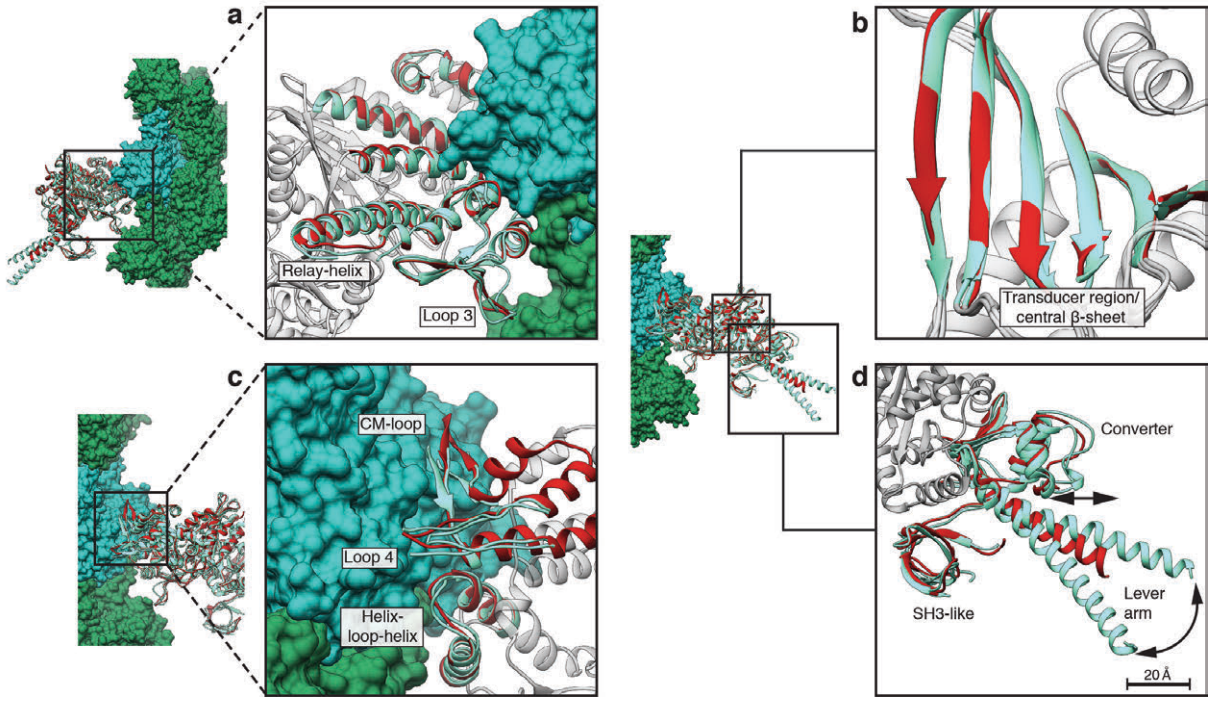

Figure 4.32: Comparison of rigor and rigor-like myosin structures.

a–**d**, Close-ups of superimposed models from rigor-like structures (nucleotide-free myosin crystal structures in light green, PDB accession number 4PD3 (Münnich et al., 2014) and 1OE9; (Coureux et al., 2003)) with our rigor cryo-EM structure (red). F-actin is shown as surface model (green, cyan). Illustrated domains are labelled and coloured, while the rest of myosin is shown in grey from the rigor state model. Most regions do not show conformational differences (**a**, **b**), but the surface loops of myosin (CM-loop, loop 3 and loop 4) interacting with F-actin differ slightly in the rigor from the rigor-like structures (**a**, **c**). In contrast to the cryo-EM structure, loops at the interface (**a**, **c**) between F-actin and myosin are not always resolved in crystal structures. Major structural differences in the lever arm and converter regions are indicated by arrows and a scale bar is given (**d**).

4.4.10 Mechanism of myosin binding to F-actin

To gain further insight into how actin accommodates first a weak and then a strong myosin-binding state, we compared our rigor NM-2C structure with the crystal structure of the same protein in the PPS state. On the basis of recently determined crystal structures of the motor domain of myosin-VI in the P_i-release state, an important intermediate state, a detailed mechanism of myosin binding to F-actin has been proposed (Llinas et al., 2015). To obtain the best possible approximation for an F-actin-NM-2C complex in the P_i-release state, we used a two-step approach. First, we calculated a homology model of the Pi-release state of NM-2C on the basis of the atomic model of myosin-VI (Llinas et al., 2015). On the basis of the positions of actin and myosin in our rigor actomyosin structure and the myosin PPS structure, we then performed different alignments of the P_i-release state model to obtain a model for the actomyosin complex in its P_i-release state (Figure 4.33, Figure A6.7). Exclusive alignment to the U50 domain in all states would cause steric clashes with F-actin in the P_i-release state (Figure A6.7a). Alignment to the L50 domain would result in a rotation of the U50 away from F-actin before the final strong binding (Figure A6.7b). We therefore chose a combined alignment instead (Figure A6.7c) to describe the possible global conformational changes during myosin binding (Figure 4.33, Figure 4.34). We aligned the P_i-release state model first to the L50 domain of the rigor state. The PPS state was then aligned to the U50 domain of the P_i-release state.

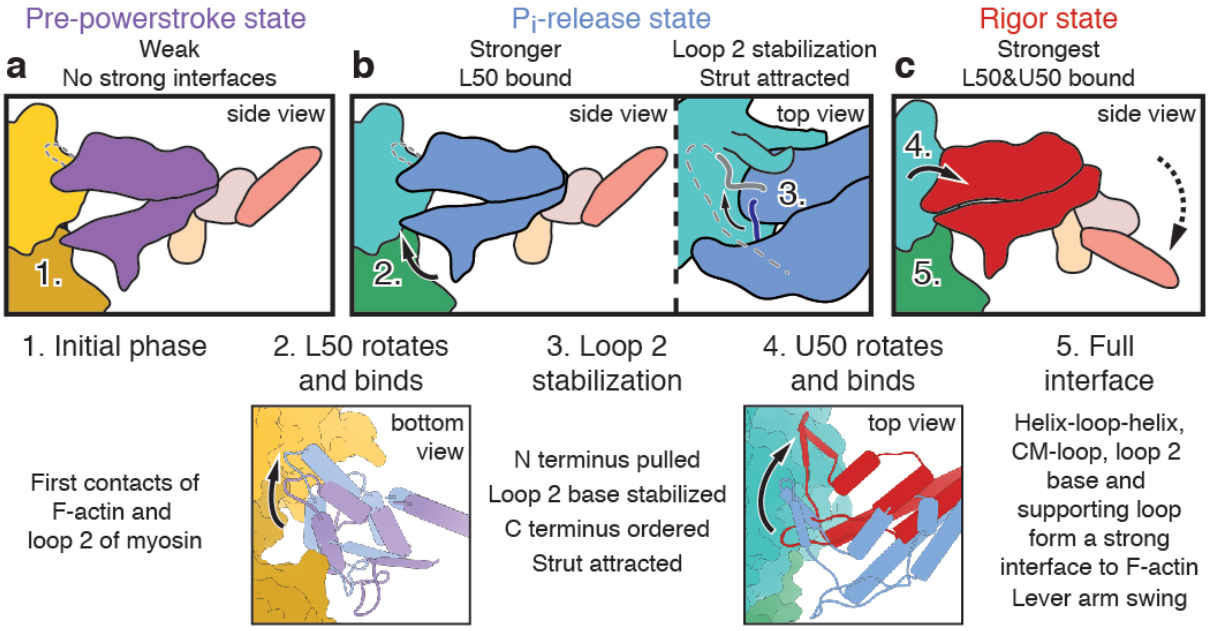

Figure 4.33: Model of myosin binding to F-actin.

a–**c**, Cartoon representation of the myosin–F-actin-binding mechanism. Numbers refer to different steps of the actomyosin interaction and are directly described in the lower panel. U50 and L50 domains are coloured according to their respective myosin state: PPS (purple, PDB accession number 5I4E), P_i-release (blue, homology model of PDB accession number 4PFO) and rigor state (red). Other domains are coloured as in Figure 4.24b. F-actin subunit colours give their current state (A-state, yellow; M-state, cyan and green). Loop 2 (grey) and strut (dark blue) are shown as lines. Flexibility in loop 2 is indicated by dotted lines. Arrows highlight rotations and binding of domains.

There is general agreement that loop 2 initiates weak binding of myosin-ADP-P_i to F-actin by interacting with the SD1 and SD3 of one actin subunit (Furch et al., 2000; Joel et al., 2001; Murphy and Spudich, 1999; Onishi et al., 2006; Uyeda et al., 1994, Figure 4.34a). This brings both the L50 and U50 close to F-actin (Figure 4.33a). As proposed in Llinas et al. (2015), the L50 domain rotates and binds to actin, resulting in the P_i-release state that represents the initial strong binding state of myosin. The interface is mainly mediated by hydrophobic interactions of the HLH domain with SD1, SD3 and the D-loop and hydrophilic interactions with the N terminus of actin, in line with our previous prediction (Behrmann et al., 2012a; Figure 4.33b). On the basis of our results, we propose that this process stabilizes the base of loop 2 (Figure 4.33b, Figure 4.34b), creating a positively charged patch to which the negatively charged strut (bridge between L50 and U50) is attracted (Figure 4.33b, Figure 4.34c). Thus, the base of loop 2 acts as a key region that shifts the equilibrium between the open and closed actin-binding cleft (Klein et al., 2008) towards the closed conformation, in which F-actin directly interacts with the CM-loop and loop 4 of the U50 domain (Figure 4.33c). Notably, both the strut and the highly conserved basic region at the base of loop 2 have previously been shown to be essential for strong binding (Coureux et al., 2003; Joel et al., 2001; Sasaki et al., 2000). In our model, the closure of the cleft is mediated by a rotation of the U50 domain towards F-actin and not by a back-rotation of the L50 domain (Figure 4.33c).

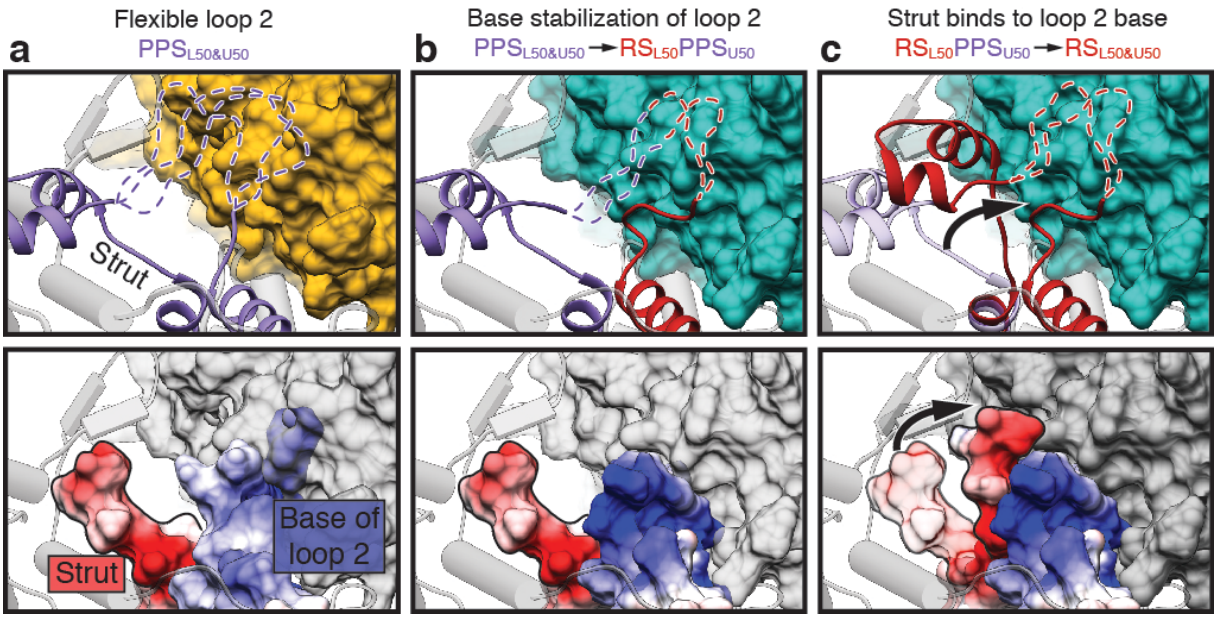

Figure 4.34: Strut attraction to the base of loop 2 promotes cleft closure.

a–**c**, Binding mechanism of the strut, connecting L50 and U50 domains, to the stabilized base of loop 2. To illustrate the conformational changes, the respective regions in the PPS state (PPS, purple, PDB accession number 5I4E) and rigor state (RS, red) of myosin have been partly overlaid. The rest of myosin is shown in grey. L50 binds to F-actin (A-state, yellow) (**a**, **b**). The base of loop 2 is stabilized by F-actin (**b**) and attracts the negatively charged strut with its positive patch. This promotes the binding of the strut, shifting the equilibrium to a closed conformational state of myosin (**c**). Flexible parts of loop 2 are indicated as dotted lines. Lower panels show surfaces of the same regions as in the upper panels coloured by electrostatic Coulomb potential. For better visualization, the upper parts of the strut were removed. Surface of F-actin is depicted in transparent grey.

As described before (reviewed in Sweeney and Houdusse, 2010a), cleft closure results in the strong binding of myosin to actin, providing the necessary anchoring of the motor domain for the subsequent powerstroke (Figure 4.33c). The time point and effect of P_i and ADP release during this process is highly debated (Llinas et al., 2015; Muretta et al., 2015). Because we lack high-resolution structures of intermediate states of myosin bound to F-actin, we cannot determine whether P_i is released before or after the powerstroke. However, our observation that the rigor state is very similar to the rigor-like state suggests that actin promotes and stabilizes the closed conformation of myosin, ultimately resulting in the release of phosphate and ADP.

4.4.11 Applied methods

Protein expression and purification (see also section 3.1 in Material and Methods)

G-actin (γ1-actin, *ACTG1* from *Homo sapiens*) was recombinantly expressed using the baculovirus/*Sf9-cell* system and purified as described previously (Müller et al., 2012; Ohi et al., 2004; see also section 3.1). Afterwards, the sample was polymerized to F-actin by increasing the salt concentration to 100 mM KCl and 2 mM $MgCl_2$. Tropomyosin 3.1 (*TPM3* from *H. sapiens*, isoform Tpm3.1) was expressed and purified from *Escherichia coli* on the basis of the protocol of (Coulton et al., 2006) with no additional modifications. The motor domain of non-muscular myosin-2C (MYH14, isoform 2 from H. sapiens) consisting of amino acids 1–799 was directly fused to an artificial lever arm (spectrin repeats 1 and 2 from α-actinin) and a C-terminal Flag-tag (Heissler and Manstein, 2011). The protein was recombinantly overproduced in the Sf9/baculovirus system as previously described (Heissler and Manstein, 2011) and purified via Flag capture and size-exclusion chromatography on a Superdex 26/60–200 prep grade column. Before grid preparation for electron microscopy studies, the F-actin sample was spun down (100,000g) and carefully suspended in nucleotide-free F-actin buffer (5 mM Tris-HCl pH 7.5, 1 mM DTT, 100 mM KCl, and 2 mM $MgCl_2$). The actomyosin complex was prepared by mixing F-actin with tropomyosin initially at a molar ratio of 7:1. The final concentration of tropomyosin for frozen specimens was then adjusted empirically to obtain complete decoration and only little unbound tropomyosin in the background by standard negative staining studies as described previously (von der Ecken et al., 2015; see also section 4.3). The F-actin–tropomyosin filaments were decorated with myosin during preparation of vitrified sample grids (see below).

Optimized grid preparation and image acquisition for cryo-EM (see also 3.3 in Material and Methods)

Best conditions for reconstituting the F-actin–tropomyosin complex were screened by using the negative staining protocol as described above. When myosin was incubated in solution with the optimized F-actin–tropomyosin sample before applying the sample to the grid, we always obtained only bundles of fully myosin-decorated actin filaments. Because of this, we optimized the protocol to reconstitute the full actomyosin filaments with reduced bundling on a grid. Therefore, the normal cryo-preparation protocol was changed. First we applied 2 µl of F-actin-tropomyosin solution to a glow-discharged holey carbon grid (C-flats 2/1, Protochips), incubated for 20 s and manually blotted from the backside for less than a second with filter paper. A thin layer of solution stayed on the grid and the filaments where pre-straightened in the holes. Afterwards, 1.5 µl of myosin solution (3 µM in F-actin buffer without nucleotide) were added directly on the grid, incubated for 10 s and then manually blotted for 5 s from the backside with filter paper (Whatman no. 5), before vitrification by plunging the grid into liquid ethane using a Cp3 plunger (Gatan).
Screening for the best sample and blotting conditions was performed on a JEOL JEM 3200FSC electron microscope equipped with a field emission gun and operated at a voltage of 200 kV. The omega in-column energy filter of the microscope was used to estimate best ice conditions (~70–100 nm thickness). Finally, a data set was taken with a spherical aberration-corrected FEI Titan Krios transmission electron microscope equipped with an extra-high brightness field emission gun (X-FEG) and operated at a voltage of 300 kV. Although the sample preparation protocol was optimized, we had to screen and choose usable grid squares extensively. Images were recorded with a back-thinned

4k × 4k FEI Falcon 2 direct detection camera under minimal dose conditions using the automatic data collection software EPU (FEI). Within each selected grid hole, three different positions were imaged, each with a total exposure of 1 s and a frame recording time of 55 ms. Seven frames from 85 to 475 ms with a total dose of ~16 electrons per square angstrom and one total average (integrated image) with an electron dose of ~35 electrons per square angstrom were used for image processing. The used magnification of 125,000 (nominal magnification of 59,000) corresponds to a pixel size of 1.1 Å. The defocus range of the data set was 0.7–2.8 µm (Table A6.6).

Image processing of the cryo-EM data set (see also section 3.4 in Material and Methods)

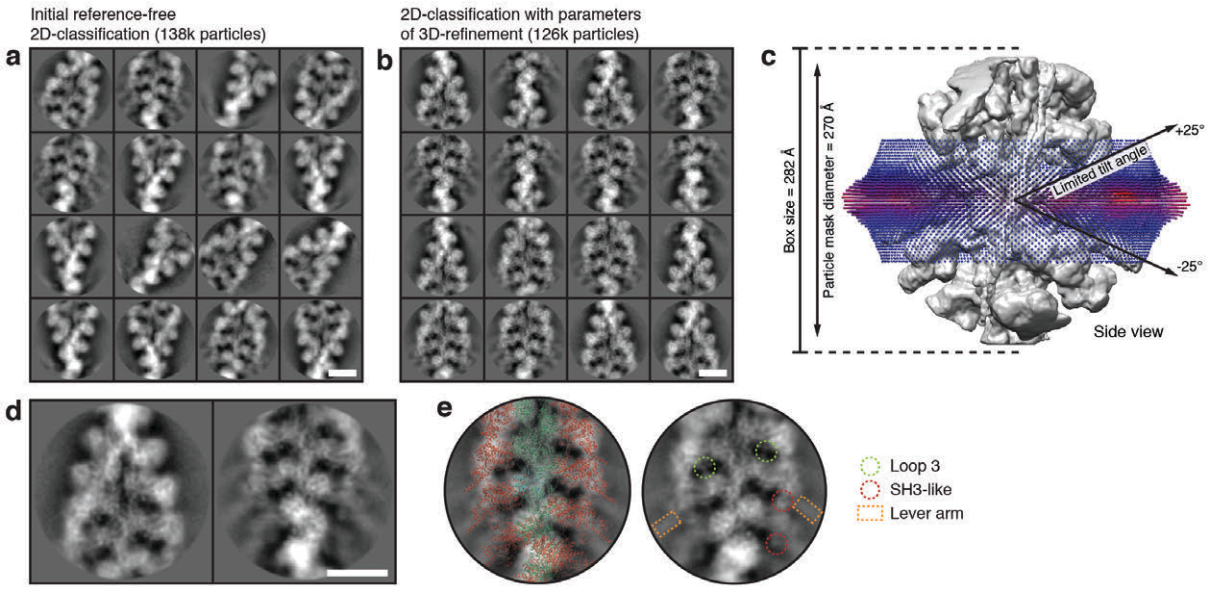

Figure 4.35: Two-dimensional classifications and three-dimensional refinement.

a, **b**, Representative of 200 two-dimensional class averages of the F-actin–tropomyosin–myosin data set before (**a**) and after (**b**) three-dimensional refinement, respectively. **c**, Box dimension and angular distribution during three-dimensional refinement in side view. Histogram (few in blue to many in red) shows distribution of projection direction of each boxed segment relative to the three- dimensional reconstruction (grey). **d**, Example of two class averages out of a that show secondary structure elements. **e**, Fit of F-actin–myosin model to assign characteristic domains of myosin (see coloured circles and boxes). Scale bars in micrograph and class averages are 50 nm and 10 nm, respectively.

In total, we collected ~6,300 images in two sessions. Despite the extensive pre-screening of grid squares before starting automatic data collection (see above), we deleted ~68% of the recorded images because of bundled filaments, contaminations or bad ice quality. Resulting frames were aligned and afterwards summed up using motion correction (Li et al., 2013a). The drift- corrected averages were used for determination of defocus and astigmatism values with CTFFIND3 (Mindell and Grigorieff, 2003). Filaments were manually selected (Figure 3.6 in subsection 3.4.1) and exported from the 1 s integrated images using sxhelixboxer in SPARX (Hohn et al., 2007) without changing the orientation of the filaments to the y-axis. A total of ~138,000 segments were extracted with a box size of 256 pixels and a boxing distance of 29 pixels (overlap ~90%). Thus, the approximate distance between them (~ 32 Å) slightly exceeded the rise of the helical assembly of actin (~ 27 – 28 Å). The same procedure was applied to the drift-corrected average and all individual frames. Afterwards all segments were transformed to Relion-readable image stack formats and initial metadata files were created for further refinement steps in Relion (Scheres, 2012).

First, two-dimensional reference-free classification and sorting of bad classes from the integrated images led to a resulting data set of 126,000 particles (Figure 4.35a). The resulting data set was used in several rounds of three- dimensional auto-refinements with particles from the integrated images and local three-dimensional auto-refinements with the particles from the drift-corrected averages. The refinement showed an expected Gaussian distribution of projection direction around the filament axis (Figure 4.35c). To improve processing time, we limited the tilt angle afterwards. Finally, we applied a particle-based movie refinement and frame weighting (Scheres, 2014) and continued three-dimensional auto-refinements with the resulting contrast-enhanced particles (see also subsection 3.4.4). We did not make use of helical symmetry during refinement but masked F-actin and myosin in the outer regions to focus the refinement on the central parts. Initially, we applied a standard spherical mask (diameter 270 Å, Figure 4.35c) to the reconstruction. After a global refinement with the spherical mask, we continued with local refinement and a mask at the size of seven F-actin subunits and six myosin molecules. We used a preliminary model and the 'Colour zone' and 'Split Map' options in CHIMERA (Pettersen et al., 2004; Pintilie et al., 2010) to extract the central part of the map from the current density map. From this part of the map we calculated a smoothed mask with the 'relion_mask_create' function in Relion.

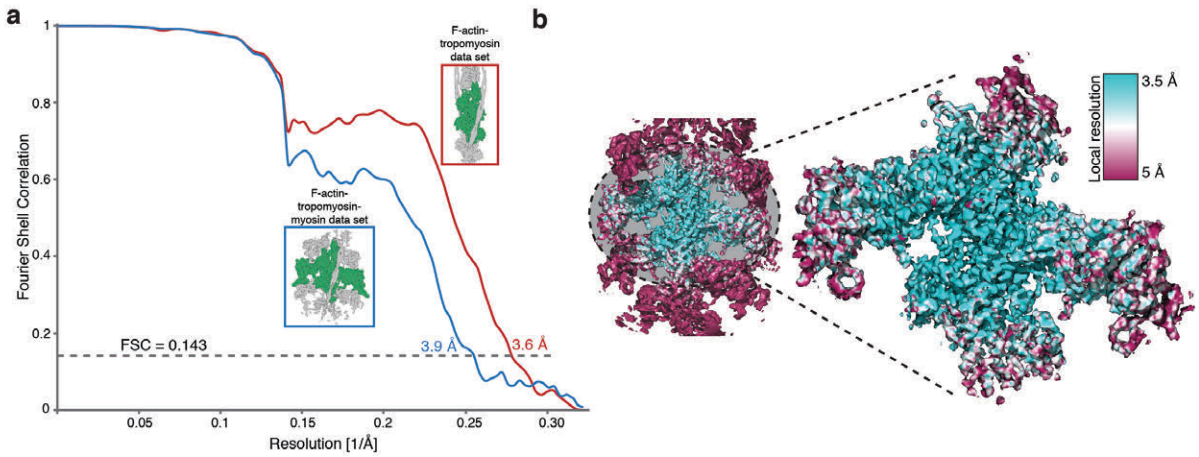

Figure 4.36: Average and local resolution.

a, FSC curves of the cryo-EM reconstruction of the F-actin–tropomyosin–myosin data set (blue) and the reprocessed data set of F-actin–tropomyosin (red). The average resolution ($FSC_{0.143}$) of the final electron density maps (central parts, green in subfigures) is estimated at 3.9 Å and 3.6 Å, respectively. **b**, Colour-coded local resolution of the full map and only finally refined part of the map of actomyosin.

To evaluate the results, we again performed a two-dimensional classification with projection parameters derived from three-dimensional refinement (Figure 4.35b). In single class averages, we could already detect secondary structure elements (Figure 4.35d, e). As a final sorting step, we deleted particles, which were outliers with respect to their neighbouring segments coming from the same filament. Therefore, we kept track throughout the whole processing steps to know to which filament each particle belongs. This resulted in 118,000 particles, which we used for a local three-dimensional auto-refinement. In the final iteration, we applied a mask of the central five F-actin subunits and two central myosin molecules (coloured region in Figure 4.24a). This mask was created as described above for the mask of seven F-actin subunits and six myosin molecules. Outer regions of the lever arm were also excluded.

Fourier shell correlation (FSC) analysis was performed within the central area (five F-actin subunits and two myosin molecules) of the volume, resulting in an average resolution of 3.9 Å ($FSC_{0.143}$ criterion

(Scheres and Chen, 2012)) for the F-actin–myosin electron density map (Figure 4.36a). The density map of F-actin–myosin was then sharpened using a negative *b* factor of –200 Å^2 and filtered to its nominal resolution. Because tropomyosin was masked out during refinements as we did before[12], we filtered the tropomyosin density map to ~7 Å and merged it with the final F-actin–myosin map to obtain a map of the entire F-actin–myosin–tropomyosin complex.

Local resolution was estimated using ResMap (Kucukelbir et al., 2014) on the full density map without masking (Figure 4.36b), revealing a resolution gradient from higher (~3.5 Å, F-actin core) to lower (4.5 Å - 5 Å, outer myosin domains) values, which could be a result of induced forces from the protruded lever arm (Figure 4.25). We converted the local resolution map to absolute frequencies and applied a local filtering algorithm on the final map with sxfilterlocal in SPARX. To estimate and confirm the helical symmetry of the actomyosin complex, we used the symmetry search function of sxhelicon_utils in SPARX.

We reprocessed our previous F-actin–tropomyosin (von der Ecken et al., 2015; see also section 4.3) data set with the same protocol as described above (see Figure 3.7b, c in subsection 3.4.2) and obtained an improved reconstruction at an average resolution of 3.6 Å for the central five F-actin subunits (Figure 4.36a). During the helical reconstruction approach, several asymmetrical units are averaged by symmetrization. This results in a decrease of resolution in flexible and bent regions. However, using the single particle approach, we refine only on the central region, thereby probably decreasing the influence of flexibility induced by the bending of the filament. This probably improves the resolution of the resulting reconstruction.

For each data set, we provide two density maps in the Electron Microscopy Data Bank (EMDB) databank. One entry contains the map after 'post-processing' in Relion without masking, the other one the same map locally filtered, masked and merged with the filtered tropomyosin density map at its respective position (as described above).

Atomic model building and refinement (see also section 3.5 in Material and Methods)

The central F-actin subunit (chain A) and the central myosin molecules (chain F, G) show all available contacts to adjacent chains (B, C, D, E) and were therefore used for further structural analysis. We used our previous F-actin model (von der Ecken et al., 2015) as a starting model for F-actin and the highly homologous model of rigor-like NM-2B (PDB accession number 4PD3; Münnich et al., 2014) for myosin. We performed homology modelling with the respective sequences of both proteins using MODELLER (Sali and Blundell, 1993). Derived models were rigid-body fitted into the density map, using 'Fit in Map' and the map was segmented with 'Split Map' in CHIMERA. Additionally, models were flexibly fitted with iMODFIT (Lopéz-Blanco and Chacón, 2013) into the respective density maps. Finally, the flexibly fitted models were used to create a starting F-actin-myosin model. The electron density was converted to structure factors with the CCP4 program suite (Winn et al., 2011). The model and the density map were then used for real space refinement and model building in COOT (Emsley et al., 2010). Flexible parts of the N terminus (residues 1–49), loop 1 (residues 222–232), loop 2 (residues 640–661) and lever arm (residues 817–1039) of myosin were deleted from the model. Some parts (especially surface loops and termini) of F-actin and myosin were built de novo. Domains showing resolution lower than 4.5 Å (outer myosin regions) were not manually changed and only the backbone trace was optimized.

The resulting model was refined in REFMAC, using the modified version of the program for cryo-EM maps (Brown et al., 2015) and applying secondary structure and reference restraints derived by

ProSMART (Nicholls et al., 2014). In addition, we added non-crystallographic symmetry symmetry restraints for F-actin (chain A–E) and myosin (chain F and G). To prevent overfitting, we first determined refinement settings by refining the model (atoms randomly displaced by 0.5 Å) only versus a density map belonging to one half of the data set and compared the FSC curves of the refined model with both half maps (Figure 4.37a). Finally, the model was refined versus the full map with the derived refinement parameters, which did not show significant differences in the two FSC curves (Figure 4.37a). We used MOLPROBITY (Chen et al., 2010) to evaluate the resulting atomic model. The data statistics are given in Table A6.6.

For the reprocessed F-actin–tropomyosin data set, we used the same refinement strategies as for the actomyosin data set. The final data statistics are given in Table A6.6.

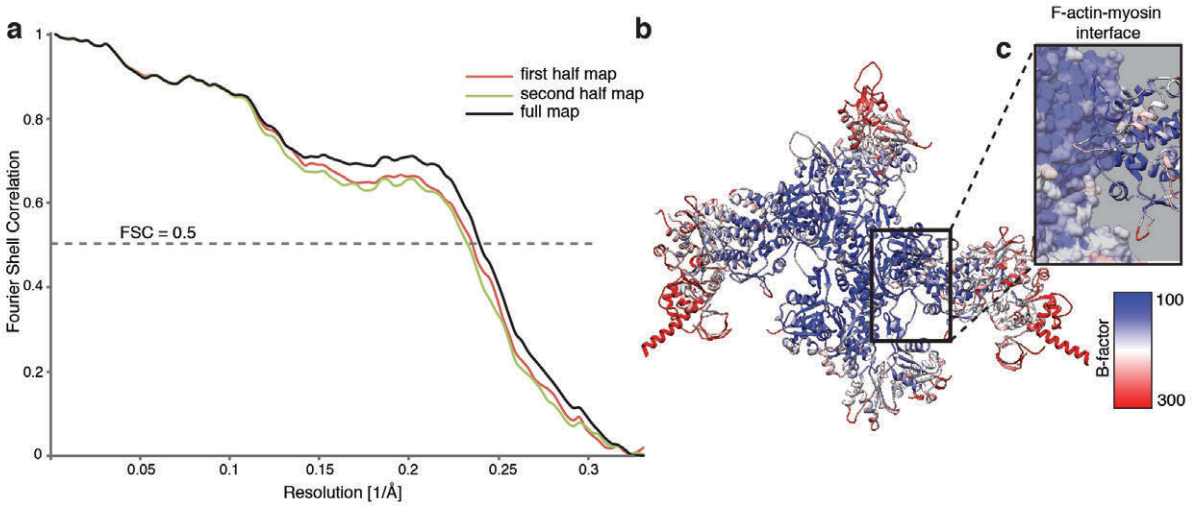

Figure 4.37: Model refinement and B-factor distribution.

a, FSC curves of the model to each half map to check for overfitting, when the model was only refined versus the first half map. Black curve shows FSC between refined model and full map, when the model was refined against the full map (see Methods). **b**, **c**, B-factor distribution of final model from low (blue) to high (red) values. The absolute value strongly depends on the sharpening factor of the map, while the distribution shows the same gradient as the local resolution in Figure 4.36**b**.

Fit of the tropomyosin models (see also section 3.5 in Material and Methods)

To describe the interaction between F-actin–myosin and tropomyosin, we used the tropomyosin model from our previous structure (Behrmann et al., 2012a). As already described in the main text, the pitch of the coiled-coil structure is equivalent. We directly rigid-body fitted the tropomyosin model (PDB accession number 4A7F) into the density map, using 'Fit in Map' in CHIMERA. We reduced the model to the five central pseudo-repeats as before (Behrmann et al., 2012a) and shifted the residue numbering regarding the differences from long Tpm1.1 to the shorter Tpm3.1. Owing to the limited resolution of the cryo-EM density in the region of tropomyosin, we avoided interpretation of tropomyosin at the single amino-acid level.

For the reprocessed F-actin–tropomyosin model, we could use the tropomyosin model from our previous model (PDB accession number 3JA8), as the structure and resolution in that region did not differ.

Structure analysis and visualization (see also section 3.5 in Material and Methods)

For visualization of models and density maps in all figures and videos, we used CHIMERA. The actomyosin complex was protonated using H++ (Anandakrishnan et al., 2012) at pH 7.5, and the

electrostatic Coulomb potential of the filament surface was calculated ranging from −10 to +10 kcal mol−1. For visualization of the hydrophobicity per amino-acid residue, we used 'Define attribute' in CHIMERA and generated amino-acid-specific scores (Hessa et al., 2005). The densities of flexible parts of myosin were detected by using the 'Colour Zone' function on a low-pass-filtered density map in CHIMERA. For comparison of differences in density of A-state and M-state F-actin, we low-pass filtered both density maps to the same resolution of 3.9 Å. Sequence alignments were performed using the ClustalOmega online server (Sievers et al., 2011). The HGMD (Stenson et al., 2014) library and UNIPROT (UniProt Consortium, 2015) were browsed to find mutations in regions of interest. For creating a homology model of NM-2C in the P_i-release state, we used MODELLER in the CHIMERA 'Multalign viewer'-interface with NM-2C as target sequence and the coordinates of the previously determined crystal structure of the P_i-release state of myosin-VI (PDB accession number 4PFO; Llinas et al., 2015) as reference structure.

4.5 Comprehensive discussion and outlook

My aim of my doctoral thesis was to obtain high-resolution structures of a F-actin-tropomyosin and a human actomyosin complex. The results presented in section 4.3 and 4.4 show that I could successfully reconstruct the cryo-EM maps of both complexes and analyse the derived molecular models at atomic level. Besides that a task was to improve the workflow of processing a filamentous protein sample to obtain high-resolution structures. An overview of this workflow (HELICON) is given in section 4.2. The program was applied to reconstruct the F-actin-tropomyosin structure to high-resolution. However, while continuing with the reconstruction of the actomyosin structure limitations of the program were encountered and a maximum-likelihood approach in Relion was further applied.
In this section the structures of F-actin-tropomyosin and actomyosin are validated and the reliability is compared with other published cryo-EM structures (subsection 4.5.1). Furthermore, perspectives are given regarding both structures and possible adaption of the established methods on other F-actin complexes are presented (subsection 4.5.2). Finally, general perspectives of cryo-EM like improvements at the software (e.g. further improvements of HELICON) and hardware (e.g. development of TEMs) level are being discussed (subsection 4.5.3).

4.5.1 Validation of the results

Validation of cryo-EM data and in particular of the derived molecular model was and is an open discussion. There is no general agreement on how the refinement of the atomic model should be performed, as there are no defined validation values like the ones existing for crystallography.
Right now, several groups use the described methods (see section 3.5) of deriving the restraints for refinement by the usage of only one half map of a golden standard refinement. Not only the validation of the final refinement of the atomic model but also the entire refinement of the initial reconstruction of the EM density is still being reconsidered. For that purpose, the golden standard approach is widely accepted (see also subsection 2.3.2). But there is still a need for validation tools during processing of the data. Indeed, once the secondary structure is visible there is no doubt about the reliability of the density map. Nevertheless, especially medium-resolution structures (in the range of 5 - 8 Å) still struggle in terms of how reliable these maps are. But also high-resolution structures should be taken with caution, as the atomic model could be overfitted into the electron density map.
Besides that, because cryo-EM reaches atomic resolution and several atomic models at this quality are published, there is a general impression among researchers that all published models in the database have this high reliability. But it is very important to check the respective model regarding to the local resolution and if the respective residue or loop is actually resolved. For example in the actomyosin structure, the F-actin core is in the range of atomic resolution (3.2-3.5 Å) while the outer regions of myosin have only medium resolution of 4-5 Å (see Figure 4.25). Therefore, an interpretation of single residues in these outer regions was not possible. Furthermore, not resolved parts of myosin (e.g. loop 1 and 2) were deleted to prevent an overinterpretation of the results in those regions. It is very important to establish a reliability value to the atomic model as soon as possible that also non-specialised researchers can evaluate the published structures and interpret the information of single residues only to a respective limit. The local resolution of the density map could be a possible value for that purpose, which could be incorporated in the coordinates file of the atomic model.

Recently, an approach for an automatic model building into EM destiny was introduced (DiMaio et al., 2015; Wang et al., 2015). The software suite Rosetta was used for that purpose (Leaver-Fay et al., 2011). Rosetta becomes more and more popular to create the atomic model. Furthermore, Rosetta was recently applied by the Lander group (Scripps Research Institute, San Diego, CA, USA) to evaluate all recently published cryo-EM structures with respect to their model to map convergence (http://www.scripps.edu/lander/convergence/). They analysed reconstructions and models, which had at least a resolution of 5 Å using Rosetta.

Their applied protocol generates one hundred models for each reconstruction based on the published atomic model. Afterwards, all these models are sorted by different scores (e.g. 'Rosetta score', clash score, Ramachandran plot, MolProbity score). The best ten models are taken and refined with a real-space refinement with Phenix into the EM density map (Adams et al., 2011). Finally, the RMSD (root mean square deviation) of the Cα-atoms of the resulting ten models are estimated.

With this protocol the Lander lab has statistically analysed the published atomic models derived by cryo-EM (unpublished) and show preliminary results online in their 'Dirty Laundry Server'. The respective results of the actomyosin and the reprocessed F-actin-tropomyosin structures from section 4.4 are illustrated in Figure 4.38. The F-actin-tropomyosin model of section 4.3 was not evaluated by the server, as it was not processed as a single-particle and a helical symmetry is not supported so far. In addition, tropomyosin is not being evaluated in both cases, as it is resolved at a lower resolution and no atomic model exists.

The overall sizes of RMSD indicate a high reliability of the derived atomic models. As expected, high RMSD are in the D-loop region in the F-actin model (Figure 4.38a), which showed a lower resolution and a higher B-factor (Figure 4.23). However, only the central subunits were used to build the model, as the density in the periphery was less well resolved. Thereby, the D-loops of the upper subunits have an expected higher RMSD.

The overall actomyosin model is in the same quality range but the average RMSD is higher (see also broader distribution in histograms in Figure 4.38b). This represents the slightly lower resolution and the lower resolution in the outer regions of myosin. However, when using only the F-actin model and the interface region of myosin, which is mainly discussed in this thesis, the RMSD distribution should be at least at good as for the F-actin from the F-actin-tropomyosin structure. In comparison to the F-actin structure, the D-loops of the central subunits have a lower RMSD, which correspond to the higher resolution in this region as it is stabilized in the actomyosin complex by the helix-loop-helix motif of myosin (Figure 4.26).

The Lander group evaluated almost ninety published models with their respective density maps of different resolution (1.8 Å to 4.9 Å). Thereby, they could analyse the dependency of average RMSD to the resolution. A plot of all derived data points (average RMSD per structure) is given in Figure 4.38c. The average RMSD lowers with a higher resolution. To illustrate this behaviour a regression line is given while assuming a proportional relationship between average RMSD and resolution. The respective average RMSD at a given resolution can indicate how good and how reliable the respective atomic model is and can be an indicator for over- or underestimation of the actual resolution. Interestingly, both of the obtained models in this thesis lay significantly lower than the regression line (red data points) indicating the high quality of the models with respect to other models at the same resolution.

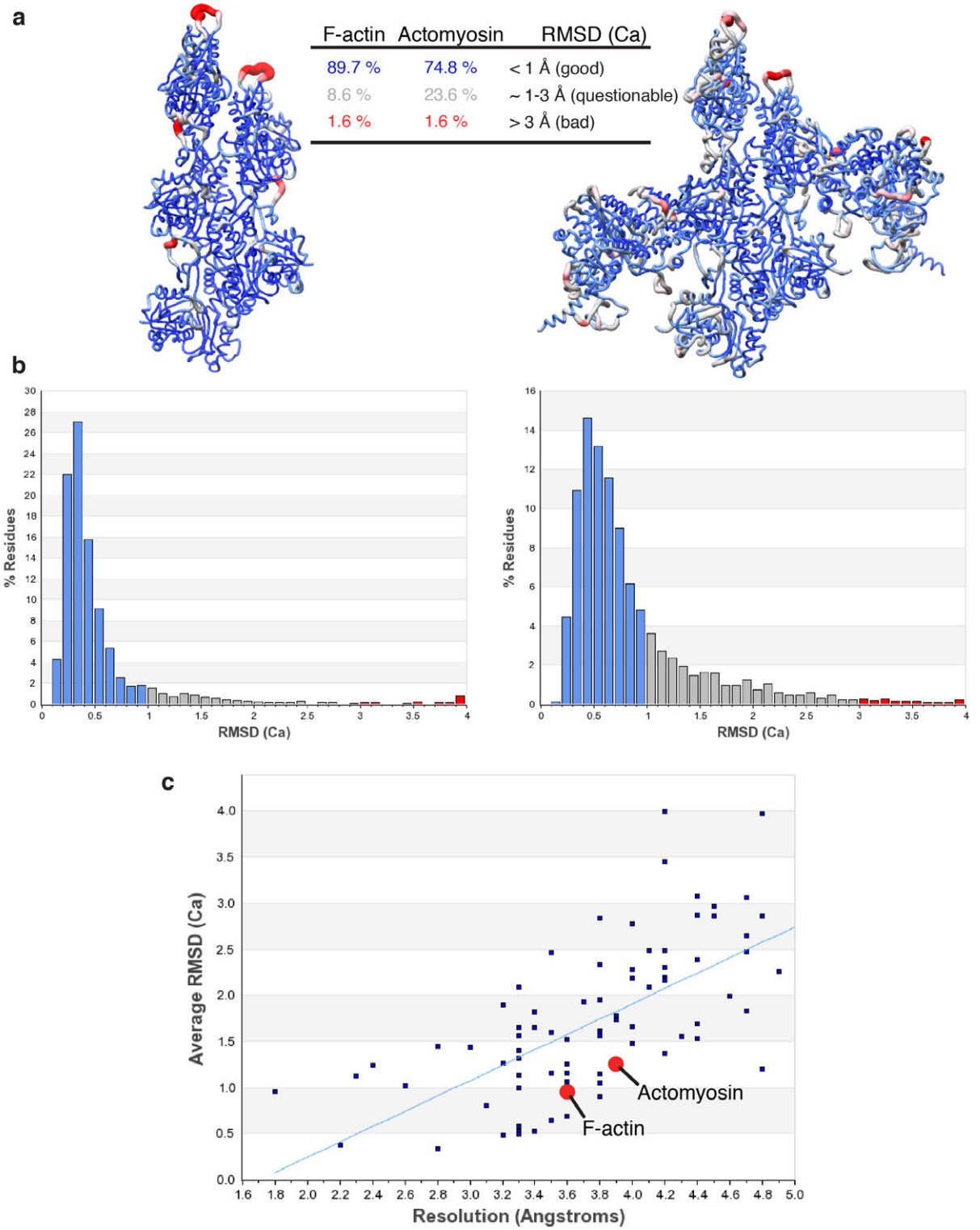

Figure 4.38: Fitting of atomic model to EM density by the 'Dirty laundry server'.

The given results are taken from 'The Dirty Laundry Server' of the Lander Lab (Scripps Research Institute, San Diego, CA, USA; http://www.scripps.edu/lander/convergence/). **a**, **b**, On the left side the results of F-actin and on the right side the results of actomyosin are shown. The models in **a** and the histograms in **b** are coloured by the RMSD (root mean square deviation) of the Cα(Ca)-atoms in blue over grey to red of the top ten scoring atomic models. The y-axes have a different scale in **b**. **c**, Until now (fetch of the data on the 15.07.2016) almost ninety published atomic models and the respective cryo-EM density maps were evaluated and presented by the online server. The reported resolutions are between 1.8 Å and 4.9 Å. The blue line gives a regression line indicating that the overall RMSD of Cα-atoms decreases with a higher resolution of the density map. The red data points belong to the F-actin and actomyosin structures. In both cases, tropomyosin was not considered, as it is not resolved to a high-resolution and no atomic model exists.

4.5.2 The results and their perspectives

In the Introduction an historical overview of resolved structures and derived models of actin, myosin, F-actin and actomyosin are given (see subsection 2.2.2). Only high-resolution structures and atomic models of the individual proteins and lower resolved structures and models of the entire complexes existed so far. In particular, results of studies on F-actin complexes based only on simulated or best-fit models or obtained density maps at low to medium resolution with cryo-EM. The presented two structures in this thesis are the first direct visualization of the F-actin-tropomyosin and actomyosin complex at high-resolution.

F-actin-tropomyosin structure

Based on the structure of F-actin-tropomyosin previously made assumptions could be verified (e.g. inter- and intrastrand contacts), but furthermore the derived molecular model gave more insights into the filament organization and formation (e.g. key-player function of the D-loop, G- to F-actin form transition, structural model of polymerization). In addition, data from kinetic and mutagenesis studies were combined with the structural information. Several mutations were already mapped within the structure and their possible impacts were described and analysed (for example induced charges at the hydrophobic D-loop, Figure 4.14). The F-actin-tropomyosin structure and the established methods can now deal as a starting point for further studies on individual residues (e.g. site-directed mutagenesis) at the interface of F-actin subunits to reveal their importance for filament formation and stability. Thereby, disease-causing mutations and how single mutations can induce dysfunction of the interfaces could be better understood.

Besides the structure of F-actin, the position of tropomyosin on the filament was analysed in detail. Tropomyosin in the F-actin-tropomyosin structure is in an Apo-state position on F-actin. This position was recently observed at a lower resolution with cryo-EM, but not further evaluated (Sousa et al., 2013). Interestingly, this Apo-state position has not been expected. Former studies applying negative staining EM and molecular dynamics simulations obtained models, in which tropomyosin is positioned in a B-state (see subsection 2.2.1). To further verify and understand the position of tropomyosin in comparison to these previous studies three reconstructions with negative staining EM were performed in this thesis (Figure 4.19). It was shown that the different positions are induced by the low pH of the staining solution (pH ~ 4) and the position observed in the cryo-EM structure can be preserved in negative staining by a prefixation with glutaraldehyde. Therefore, the position of tropomyosin in the cryo-EM structure is thought to be the native conformation. Furthermore, a comparison with the M-state of tropomyosin showed that tropomyosin has to undergo a significant shift or rotation on the actin filament (Figure 4.20, Figure 4.21). The need of this large movement was not expected as well and cannot be easily explained. Taken together, not only the position as well the need of the greater conformational change will enhance the discussion of the native position of tropomyosin on the actin filament and how the transition between the different states proceeds.

To shed more light onto both points and to further elucidate the described pH-dependency of the tropomyosin position, experiments of cryo-negatively stained F-actin-tropomyosin filaments or a negative staining procedure with PTA (Phosphotungstate) at physiological pH could be performed. Furthermore, in the case of skeletal and cardiac actins troponin plays a major role in tropomyosin positioning (see subsection 2.2.1). Therefore, structures are needed of F-actin-tropomyosin with bound troponin while calcium is available or not to promote a closed and blocked state, respectively. So far,

there are no structural data of the complex at high-resolution. Low resolution models obtained with negative staining exist but could be affected by staining artefacts and the low pH as well (Mun et al., 2014; Poole et al., 2006; Yang et al., 2014).

Studies could use the obtained model to restrain their molecular dynamics simulation and perform and renew the energy landscaping of the F-actin surface for tropomyosin (Orzechowski et al., 2014a; Zheng et al., 2016) and come up with models how the tropomyosin transition happens (Rynkiewicz et al., 2015). However, this will only result in models of the mechanism. To sufficiently answer this question, high-resolution structures of tropomyosin on F-actin in different states are needed. With these structures the exact position of tropomyosin would be known and thereby it could be directly revealed if tropomyosin shifts, roles or performs a combination of both movements between different states. In addition, these structures could give more insights into how the N and C termini overlap is organized. As described in the Introduction in subsection 2.2.1, the binding and transition of tropomyosin is highly cooperative ('Gestalt-Binding'; Lehman et al., 2013b) and the communication of the adjacent tropomyosin molecules is unknown.

To obtain these F-actin-tropomyosin structures with cryo-EM and to derive the atomic model obstacles have to be overcome. So far, during processing the alignment is focussed on the F-actin part of the structure and therefore all high-resolution features of tropomyosin are merged out, because one tropomyosin molecule is only pseudo-symmetric to F-actin. Therefore only the coiled-coil structure is preserved and can be unambiguously observed in the reconstruction. Afterwards, as crystal structures of tropomyosin exist, they can be fitted into the tube-like densities but the exact register on F-actin stays unknown.

One approach to improve the resolution of tropomyosin could be a change in the processing procedure. The whole procedure would have to be applied on the asymmetric subunit of tropomyosin. This subunit is fourteen times longer than for F-actin as tropomyosin stretches over seven actins subunits of only one strand. In addition, a single-particle approach should be used without applying symmetry. Furhtermore, the box size should be much bigger, since several subunits are needed within a box. To technically realize this approach, the selecting of particles has to be further optimized, as the tropomyosin molecule is not visible within an image. If the molecule is selected on the wrong height, two half molecules could be within one boxed particle. These difficulties could be solved by an artificial label to recognize the individual molecules or by an exhaustive 2D-classification after a random selection. Another obstacle, which will hamper the selection process, is that it is unknown if in an *in vitro* reconstitution both tropomyosin tubes are bound in the same register. Therefore, it has to be further evaluated if this can be solved by using natively purified actin filaments or by addition of troponin, which could mediate between both tropomyosin strands. Once the selecting problem is solved standard single-particle reconstruction should allow obtaining high-resolution structures and open questions of the tropomyosin mechanism on F-actin could be answered with the derived tropomyosin model. Afterwards, the same methods could be applied on F-actin-tropomyosin complexes with bound troponin.

Actin is one of the most conserved and abundant proteins and the differences are only minimal on the amino acid level. However, different actin isoforms are present in for example muscle cells or the cytoskeleton. Therefore, the different isoforms must have specific properties to fulfil the respective purpose. It could be possible that these differences do not only impact for example the ATP-hydrolysis activity but also lead to changes on the level of the structure. Besides the differences of actin isoforms, there are a lot more isoforms of tropomyosin (Geeves et al., 2014). In particular, some tropomyosin

isoforms are short tropomyosins (stretching over only six actins instead of seven) or have different influences on the F-actin stability and polymerization. These properties probably have a structural and functional reason. Therefore other F-actin and F-actin-tropomyosin structures could be obtained by applying cryo-EM and the molecular models could be derived. Finally, a comparison of these models could give more insights into how different properties of isoforms are promoted by the structure.
Furthermore, as described in the Introduction in subsection 2.2.1, different nucleotide binding states of F-actin exist but only the kinetics are understood, while the structural differences are lacking. The presented structure is in the ADP state. A next step could be to try to stabilize a single F-actin state (e.g. ADP-Pi or ATP state) by oversaturation or using non hydrolysable analogues (AMP-PNP, ADP or ATP with beryllium fluoride or orthovanadate) as it was performed for an actin-like filament from bacteria but at much lower resolution (Bharat et al., 2015). If intermediate states of the subunit with F-actin are known the polymerization and hydrolysis mechanism could be fully elucidated and the proposed models (subsections 4.3.4 and 4.3.5) verified and extended.
Taken together, the structure of the F-actin-tropomyosin structure and the established methods open a wide range of perspectives to further analyse and understand fundamental mechanisms regarding F-actin and F-actin-tropomyosin complexes.

Actomyosin structure

After obtaining the high-resolution structure of the F-actin-tropomyosin complex the same computational methods were applied on a human actomyosin complex with tropomyosin. Some problems during processing (e.g. struggling with stronger flexibility and resolution gradient within a segment) were encountered and therefore another refinement approach was applied by applying a pure single particle approach (discussion see next subsection). In addition, although the bundling of actomyosin filaments was reduced by optimizing the vitrification procedure (see subsection 4.4.11) almost three quarters of the original raw micrographs were discarded. Nevertheless, a high-resolution structure of the actomyosin complex is obtained and a molecular model derived. By analysing the actomyosin model not only most of the pioneering work were confirmed in greater detail but also for example the curiosity of loop 2 (half rigid and half flexible, Figure 4.29) were observed for the first time and an explanation for how actin promotes the activation of myosin (e.g. attraction of the strut, Figure 4.34) was introduced. Besides that, the misleading name of the previously called ‘activation’ loop (Figure 4.30) was discussed. Furthermore, for the first time the myosin-induced differences in the structure of F-actin were directly visualized and an Apo- and a myosin-state of one F-actin subunit were suggested like it is already existing for the tropomyosin states (Van Dijk et al., 2002; Vibert et al., 1972). These points give only some highlights of section 4.4. The results represent the next milestone in studying the fundamental interaction of actin and myosin.
As for the F-actin-tropomyosin structure the model was analysed and brought into context with other published works. There are several disease-causing mutants known and their impact on the actin-myosin binding has been observed. Based on biomechanical analyses amino acids with high importance for the actin-myosin binding and stability of the interface have been previously identified (Furch et al., 2000; Giese and Spudich, 1997; Kojima et al., 2001; Onishi et al., 2006). But in these studies, the interface was only indirectly elucidated by measurements of the binding-performance of point-mutated myosins and actins. These results can further be directly interpreted and understood with the presented actomyosin structure. For example, it was known before that the helix-loop-helix motif plays an essential role in F-actin binding of myosin. But now, in the obtained structure the densities of the

immersion of the motif into the hydrophobic cleft of F-actin and the unknown function in the base stabilization of loop 2 (Figure 4.26, Figure 4.27, Figure 4.29) could be directly observed and described in great detail.

Besides the evaluation of the actin-myosin interface, one major part of the interpretation of the results was to derive a model of myosin binding to F-actin (Figure 4.33). As the whole cross-bridge cycle is highly dynamic (Figure 2.6 Figure 2.7, subsection 2.2.1 of the Introduction) and as there are several states of myosin on F-actin, the rigor state structure had to be analysed in context to other intermediate states of myosin to derive this model. For that purpose, crystal structures of these intermediate states were taken into account and manually aligned to the actin filament, as no structures bound to F-actin exist. Recently, a detailed model of myosin binding to actin was proposed while introducing a structure of a P_i-released state (Llinas et al., 2015). Therefore, this state was included to the model of myosin binding to F-actin in addition. Interestingly, the model of the Llinas et al. could be partly falsified by comparing different kinds of model fittings (Figure A6.7). Their superposition of the myosin states would lead to clashes with F-actin during cleft closure of myosin (Figure A6.7a). Finally, a new detailed model considering these issues were presented in this thesis, but the mechanism has to be further evaluated by obtaining high-resolution structures of intermediate states of myosin bound to F-actin.

To obtain these structures the established methods for refinement should be suitable to obtain high-resolution structures. Moreover, the main task will be to stabilize these low affinity states on F-actin (e.g. by crosslinking or using non hydrolysable analogues of nucleotide). Therefore, the next aim for structural analysis of actomyosin could be to obtain a high-resolution structure of a starting point of myosin-binding to F-actin (weak binding state; e.g. ADP-Pi or ADP bound to myosin in a pre-powerstroke conformation), a late myosin-binding state (weak binding state; e.g. ATP bound to myosin in a post-rigor conformation) or an intermediate myosin-binding state (strong binding state; e.g. ADP bound to myosin before or after the powerstroke). Only when more states are resolved, the highly complex mechanochemical reaction cycle can be understood from a structural point of view and the derived mechanism can be further evaluated.

The quality of the reconstructed density map showed a higher flexibility to the periphery of myosin and a resolution gradient was observed (Figure 4.36). Recently, another group used an comparable actomyosin complex have obtained a density map with an equivalent, prominent resolution gradient while having a much lower average resolution (Wulf et al., 2016). This higher flexibility of myosin resulting in a resolution gradient seems to be a general problem. Therefore, to obtain higher resolution reconstruction of the actomyosin complexes the data set size, in particular the total amount of segments, has to be at least as the size of presented actomyosin structure to further compensate for the flexibility. Another approach could be to further stabilize the myosin motor domain. For example the used myosin construct had a protruding lever arm, which should be depleted to reduce the flexibility. In addition, surface loops, which do not take part into the interface of actin-myosin (e.g. loop 1), could be shortened.

Besides solving different intermediate states to high-resolution, there are several other myosin isoforms and myosin classes, which show different properties when interacting with actin and could be a possible target for further structural studies. As described for the different isoforms of actin and tropomyosin, high-resolution structures of for example a skeletal myosin isoform could explain how in comparison to cytoskeleton myosin the different kinetics are represented on the level of the structure. It could be possible that loop 2 is fully ordered or loop 3 creates a stronger Milligan-contact to the

adjacent F-actin subunit. Thereby, the binding strength could be enhanced. In addition, as in different tissues not only the myosin isoform can differ, the isoform of the F-actin filament should be considered as well. One major difference between non-muscular and muscular actin isoforms is the different lengths of the N terminus (Figure A6.6d). There is an additional negative charged residue (aspartic or glutamic acid) in muscular isoforms of actin, which could promote a stronger binding of myosin by a faster stabilization of the base of loop 2. But these assumptions can only be proven, when high-resolution structures of myosin in complex with actin are obtained to give the structural interpretation in addition to data derived from kinetics studies, as it was shown with the actomyosin structure in this thesis.

4.5.3 General perspectives of cryo-EM

As described in the introduction of this section, the HELICON workflow could be successfully applied on the F-actin-tropomyosin data set and a high-resolution structure was obtained. However, for solving the structure of the actomyosin complex I switched to the software package Relion since a reconstruction with HELICON did not result in a high-resolution structure. In addition, by using Relion the resolution of the F-actin-tropomyosin reconstruction could be slightly improved in comparison to the previous obtained reconstructions with HELICON (see subsections 4.4.2 and 4.4.11). In Relion the segments of a filament are treated as independent single particles without restraints to the projection parameters within a filament and no symmetrization of the density maps are applied during refinement. In addition, Relion uses a maximum-likelihood approach for assignment of a distribution of projection parameters, while HELICON uses a single set of projection parameters (cross-correlation approach, see also subsection 2.3.2). Therefore, it seems that a pure single-particle approach with maximum-likelihood statistics is superior to a helical reconstruction approach with cross-correlation statistics. However, it could be shown that applying helical restraints to the projection parameters in addition improved the reconstruction and its resolution in the single-particle approach in Relion. For that purpose, particle within the same filament, which did not go in line with other particles of the same filament (e.g. strong deviation between in- or out-of-plane angles), were sorted out in the final steps of refinement (see subsection 4.4.11). Taken together, a combination of a maximum-likelihood approach implemented in HELICON could be an even more superior method to obtain high-resolution structures of filamentous protein samples with cryo-EM.

Besides mechanistic questions of the interplay of the described proteins in this thesis (see subsection before), there are more than a hundred of actin-binding proteins, which could be interesting for further studies applying cryo-EM in the context of F-actin. It was shown by obtaining the structure of actomyosin in this thesis that the structure of a symmetrically binding protein to F-actin can be solved by the established methods. Therefore, these methods can deal as a strong foundation to obtain further F-actin structures in complex with actin-binding proteins and to analyse the molecular models at atomic level. Actin-binding proteins have a variety of functions like for example in promoting of muscle contraction in muscle cells or regulation of the actin cytoskeleton (Dominguez and Holmes, 2011). By solving these structures while interacting with an actin filament the function and disease-caused dysfunction could be better understood. Thereby, new starting points for a medication could be possibly found.

Moreover, new technologies in cryo-EM could improve the quality of the data sets and provide new technical approaches. In particular, the development of the phase-plate (see subsection 2.3.3) and

recent results in applying it on single particle reconstruction are very promising (Chua et al., 2016; Danev and Baumeister, 2016; Khoshouei et al., 2016). When images are recorded with the phase-plate the contrast is significantly enhanced over the entire frequency spectrum (Glaeser, 2013). Thereby, smaller data sets and having fewer particles are sufficient for obtaining the same resolution as without the addition contrast. This could lead to an enormous reduction of the required data set size, which is currently in the size of at least several terabytes. Furthermore, as the contrast is also enhanced for low frequencies representing larger features of the structure, smaller proteins (< 100 kDa) are visible and can be analysed with standard reconstruction software. The same effect of an improved contrast for small proteins will make it possible to classify conformational changes of for examples domains of larger protein complexes. In the case of actomyosin complexes this could help to sort different intermediate states of myosin on actin within one sample preparation. Right now, the respective conformational state has to be stabilized and be the only one within a sample. This is still a limiting factor in solving the structures of other possible intermediate states of the cross-bridge cycle.

The currently used reconstitution of the actomyosin complex when analysing it with cryo-EM is based on binding of isolated head regions (motor domain) of myosin to F-actin. This leads to an artificial decoration of the actin filaments resulting in a typical arrow-like shape (see subsection 0), which is not possible in vivo as myosin is organized for example as a thick filament in muscle cell. Therefore, a next step in understanding the interaction and organisation of actomyosin in a more physiological complex could be to analyse natively purified thin and thick filaments directly within a sarcomere. This large sample of interest could be 3D-visualized by cryo tomography. Recently, the resolution and contrast of obtained tomograms were significantly improved by a combination of FIB-milling and the usage of the above discussed phase-plate (Mahamid et al., 2016). A focus ion beam (FIB) is used to cut (mill) a single slice of 200-300 nm of the vitrified tissue of interest. This method is still not capable to obtain sub nanometre resolution, but can answer questions of the organisation of proteins within the tissue (e.g. sarcomere) at medium resolution.

Further developments of cryo-EM to improve the quality of the data could be a change of the setup of the electron emitter of TEMs. At the moment, conventional TEMs are working at a constant electron beam using field emissions guns (see section 2.3). During one exposure of the sample the total exposure time is split into frames by recording subframes by the detector (see also subsection 3.3.3). Instead of trying to improve only the readout time of the detectors to record shorter frames another approach could be to change from a constant illumination to a pulsed illumination. A pulsed electron source would be needed for that purpose (personal communication with Prof. Dr. Dwayne Miller; Max-Planck-Institute for the Structure and Dynamics of Matter in Hamburg). Thereby, the exposure time of the sample could be minimized more than it is currently technically possible with standard direct electron detectors. One exposure would be split not in subframes rather than in subexposures. Short subexposures could lead to a reduction of drifting effects within one image as shown for shorter subframes.

One other change of the setup of conventional TEMS for cryo-EM could be the used cooling temperature. Using the medium of liquid nitrogen is the worldwide standard for cryo-EM, but it was shown that cryo-EM at liquid helium temperature can result in high-resolution reconstructions (McMullan et al., 2015; Unwin, 2005). It has to be further analysed how the lower temperature when using helium can impact the particle drift or beam damage of the biological sample. This can lead to an enhanced contrast and improved high-resolution features of the particles, which, as explained for the phase-plate above, would reduce the needed size of the data set.

Besides technical developments of TEMs, the specimen-supporting grid, although produced mechanically nowadays, has almost not changed since the beginning of cryo-EM. As described in the thesis obtaining suitable conditions for negative staining and vitrification of the sample can be a time consuming task as it is performed manually (sections 3.3 and 4.1). At least, the preparation for vitrified samples becomes more and more reproducible as the plunge-freezing devices became more optimized and automated. To reduce the effort of the manual screening process, groups try for example to automate the actual sample screening by applying several conditions on different areas on a grid (Mulligan et al., 2015; Tan et al., 2016). This grid with multiple conditions is then screened automatically and the best conditions can be chosen instead of preparing one grid per condition. To obtain the structure of the actomyosin complex an exhaustive screening was manually performed. Nevertheless, 70 % of the raw data was finally discarded. Therefore, an automated screening could help to find even better conditions and thereby improve the yield.

Several technical developments of the microscopes and detectors can improve the time of data collection by reducing the amount of data and are already described in this section. However, the actual processing time of the data set can take months. The algorithms for processing cryo-EM data are constantly improved. For example there is already a transformation going on with respect to the usage of GPUs instead of CPUs (see also subsection 2.3.3). Some image operations are being faster performed on a GPU system. Thereby, the processing time will be further reduced in the future, which will help to analyse more structures in shorter time.

All in all, cryo-EM just started its very promising future and will be more and more the method of choice to obtain molecular structures at high-resolution of proteins, which are not easily resolvable by other methods like crystallography.

5 References

Abrishami, V., Vargas, J., Li, X., Cheng, Y., Marabini, R., Sorzano, C.Ó.S., and Carazo, J.M. (2015). Alignment of direct detection device micrographs using a robust Optical Flow approach. Journal of Structural Biology 189, 163–176.

Adams, P.D., Afonine, P.V., Bunkóczi, G., Chen, V.B., Echols, N., Headd, J.J., Hung, L.-W., Jain, S., Kapral, G.J., Grosse Kunstleve, R.W., et al. (2011). The Phenix software for automated determination of macromolecular structures. Methods 55, 94–106.

Adelman, M.R., Borisy, G.G., Shelanski, M.L., Weisenberg, R.C., and Taylor, E.W. (1968). Cytoplasmic filaments and tubules. Fed. Proc. 27, 1186–1193.

Agrawal, P.B., Strickland, C.D., Midgett, C., Morales, A., Newburger, D.E., Poulos, M.A., Tomczak, K.K., Ryan, M.M., Iannaccone, S.T., Crawford, T.O., et al. (2004). Heterogeneity of nemaline myopathy cases with skeletal muscle alpha-actin gene mutations. Ann. Neurol. 56, 86–96.

Allegretti, M., Mills, D.J., McMullan, G., Kühlbrandt, W., and Vonck, J. (2014). Atomic model of the F420-reducing [NiFe] hydrogenase by electron cryo-microscopy using a direct electron detector. Elife 3, e01963.

Amunts, A., Brown, A., Bai, X.-C., Llácer, J.L., Hussain, T., Emsley, P., Long, F., Murshudov, G., Scheres, S.H.W., and Ramakrishnan, V. (2014). Structure of the yeast mitochondrial large ribosomal subunit. Science 343, 1485–1489.

Anandakrishnan, R., Aguilar, B., and Onufriev, A.V. (2012). H++ 3.0: automating pK prediction and the preparation of biomolecular structures for atomistic molecular modeling and simulations. Nucleic Acids Research 40, W537–W541.

Artimo, P., Jonnalagedda, M., Arnold, K., Baratin, D., Csardi, G., de Castro, E., Duvaud, S., Flegel, V., Fortier, A., Gasteiger, E., et al. (2012). ExPASy: SIB bioinformatics resource portal. Nucleic Acids Research 40, W597–W603.

Asano, S., Engel, B.D., and Baumeister, W. (2016). In Situ Cryo-Electron Tomography: A Post-Reductionist Approach to Structural Biology. J. Mol. Biol. 428, 332–343.

Bai, X.-C., Fernández, I.S., McMullan, G., and Scheres, S.H.W. (2013). Ribosome structures to near-atomic resolution from thirty thousand cryo-EM particles. Elife 2, e00461.

Bai, X.-C., McMullan, G., and Scheres, S.H.W. (2015a). How cryo-EM is revolutionizing structural biology. Trends Biochem. Sci. 40, 49–57.

Bai, X.-C., Rajendra, E., Yang, G., Shi, Y., and Scheres, S.H.W. (2015b). Sampling the conformational space of the catalytic subunit of human γ-secretase. Elife 4, 1485.

Banga, I., and Szent-Györgyi, A. (1940). Structure-Proteins. Science 92, 514–515.

Banga, I., Guba, F., and Szent-Györgyi, A. (1947). Nature of myosin. Nature 159, 194.

Bartesaghi, A., Merk, A., Banerjee, S., Matthies, D., Wu, X., Milne, J.L.S., and Subramaniam, S. (2015). 2.2 Å resolution cryo-EM structure of β-galactosidase in complex with a cell-permeant inhibitor. Science 348, 1147–1151.

Bathe, F.S., Rommelaere, H., and Machesky, L.M. (2007). Phenotypes of myopathy-related actin mutants in differentiated C2C12 myotubes. BMC Cell Biol. 8, 2.

Behrmann, E., Müller, M., Penczek, P.A., Mannherz, H.G., Manstein, D.J., and Raunser, S. (2012a). Structure of the rigor actin-tropomyosin-myosin complex. Cell 150, 327–338.

Behrmann, E., Tao, G., Stokes, D.L., Egelman, E.H., Raunser, S., and Penczek, P.A. (2012b). Real-space processing of helical filaments in SPARX. Journal of Structural Biology 177, 302–313.

Berman, H., Henrick, K., and Nakamura, H. (2003). Announcing the worldwide Protein Data Bank. Nature Structural Biology 10, 980–980.

Bharat, T.A.M., Murshudov, G.N., Sachse, C., and Löwe, J. (2015). Structures of actin-like ParM filaments show architecture of plasmid-segregating spindles. Nature 523, 106–110.

Bigge, M. (2002). Westfalenstadion. download on 15.07.2016, Creative-Commons 3.0, https://upload.wikimedia.org/wikipedia/commons/5/52/ Westfalenstadion_070_17.jpg.

Binder, B.P., Cornea, S., Thompson, A.R., Moen, R.J., and Thomas, D.D. (2015). High-resolution helix orientation in actin-bound myosin determined with a bifunctional spin label. Proc. Natl. Acad. Sci. U.S.a. 112, 7972–7977.

Blanchard, E., Seidman, C., Seidman, J.G., LeWinter, M., and Maughan, D. (1999). Altered crossbridge kinetics in the alphaMHC403/+ mouse model of familial hypertrophic cardiomyopathy. Circ. Res. 84, 475–483.

Blanchoin, L., Boujemaa-Paterski, R., Sykes, C., and Plastino, J. (2014). Actin dynamics, architecture, and mechanics in cell motility. Physiological Reviews 94, 235–263.

Booth, D.S., Avila-Sakar, A., and Cheng, Y. (2011). Visualizing proteins and macromolecular complexes by negative stain EM: from grid preparation to image acquisition. Journal of Visualized Experiments : JoVE.

Brieher, W. (2013). Mechanisms of actin disassembly. Molecular Biology of the Cell 24, 2299–2302.

Briggs, J.A.G. (2013). Structural biology in situ--the potential of subtomogram averaging. Current Opinion in Structural Biology 23, 261–267.

Brilot, A.F., Chen, J.Z., Cheng, A., Pan, J., Harrison, S.C., Potter, C.S., Carragher, B., Henderson, R., and Grigorieff, N. (2012). Beam-induced motion of vitrified specimen on holey carbon film. Journal of Structural Biology 177, 630–637.

Brown, A., Long, F., Nicholls, R.A., Toots, J., Emsley, P., and Murshudov, G. (2015). Tools for macromolecular model building and refinement into electron cryo-microscopy reconstructions. Acta Crystallogr. D Biol. Crystallogr. 71, 136–153.

Brown, J.H., Kim, K.H., Jun, G., Greenfield, N.J., Dominguez, R., Volkmann, N., Hitchcock-Degregori, S.E., and Cohen, C. (2001). Deciphering the design of the tropomyosin molecule. Proc. Natl. Acad. Sci. U.S.a. 98, 8496–8501.

Brown, J.H., and Cohen, C. (2005). Regulation of muscle contraction by tropomyosin and troponin: how structure illuminates function. Adv. Protein Chem. 71, 121–159.

Bykov, Y.S., Cortese, M., Briggs, J.A.G., and Bartenschlager, R. (2016). Correlative light and electron microscopy methods for the study of virus-cell interactions. FEBS Lett. n/a–n/a.

Callaway, E. (2015). The revolution will not be crystallized: a new method sweeps through structural biology. Nature 525, 172–174.

Carsten, M.E., and Mommaerts, W.F. (1963). A study of actin by means of starch gel electrophoresis. Biochemistry 2, 28–32.

Chapman, H.N., Fromme, P., Barty, A., White, T.A., Kirian, R.A., Aquila, A., Hunter, M.S., Schulz, J., DePonte, D.P., Weierstall, U., et al. (2011). Femtosecond X-ray protein nanocrystallography. Nature 470, 73–77.

Chen, S., McMullan, G., Faruqi, A.R., Murshudov, G.N., Short, J.M., Scheres, S.H.W., and Henderson, R. (2013). High-resolution noise substitution to measure overfitting and validate resolution in 3D structure determination by single particle electron cryomicroscopy. Ultramicroscopy 135, 24–35.

Chen, V.B., Arendall, W.B., Headd, J.J., Keedy, D.A., Immormino, R.M., Kapral, G.J., Murray, L.W., Richardson, J.S., and Richardson, D.C. (2010). MolProbity: all-atom structure validation for macromolecular crystallography. Acta Crystallogr. D Biol. Crystallogr. 66, 12–21.

Cheng, Y. (2015). Single-Particle Cryo-EM at Crystallographic Resolution. Cell 161, 450–457.

Chua, E.Y.D., Vogirala, V.K., Inian, O., Wong, A.S.W., Nordenskiöld, L., Plitzko, J.M., Danev, R., and Sandin, S. (2016). 3.9 Å structure of the nucleosome core particle determined by phase-plate cryo-EM. Nucleic Acids Research gkw708.

Clark, R., Ansari, M.A., Dash, S., Geeves, M.A., and Coluccio, L.M. (2005). Loop 1 of transducer region in mammalian class I myosin, Myo1b, modulates actin affinity, ATPase activity, and nucleotide access. J. Biol. Chem. 280, 30935–30942.

Coluccio, L.M. (2007). Myosins - A Superfamily of Molecular Motors (Dordrecht: Springer Science & Business Media).

Cook, R.K., Root, D., Miller, C., Reisler, E., and Rubenstein, P.A. (1993). Enhanced stimulation of myosin subfragment 1 ATPase activity by addition of negatively charged residues to the yeast actin NH2 terminus. J. Biol. Chem. 268, 2410–2415.

Cope, M.J., Whisstock, J., Rayment, I., and Kendrick-Jones, J. (1996). Conservation within the myosin motor domain: implications for structure and function. Structure 4, 969–987.

Costa, C.F., Rommelaere, H., Waterschoot, D., Sethi, K.K., Nowak, K.J., Laing, N.G., Ampe, C., and Machesky, L.M. (2004). Myopathy mutations in alpha-skeletal-muscle actin cause a range of molecular defects. J. Cell. Sci. 117, 3367–3377.

Coulton, A., Lehrer, S.S., and Geeves, M.A. (2006). Functional homodimers and heterodimers of recombinant smooth muscle tropomyosin. Biochemistry 45, 12853–12858.

Coureux, P.-D., Sweeney, H.L., and Houdusse, A. (2004). Three myosin V structures delineate essential features of chemo-mechanical transduction. The EMBO Journal 23, 4527–4537.

Coureux, P.-D., Wells, A.L., Ménétrey, J., Yengo, C.M., Morris, C.A., Sweeney, H.L., and Houdusse, A. (2003). A structural state of the myosin V motor without bound nucleotide. Nature 425, 419–423.

Crosbie, R.H., Miller, C., Cheung, P., Goodnight, T., Muhlrad, A., and Reisler, E. (1994). Structural connectivity in actin: effect of C-terminal modifications on the properties of actin. Biophys. J. 67, 1957–1964.

Cuda, G., Fananapazir, L., Zhu, W.S., Sellers, J.R., and Epstein, N.D. (1993). Skeletal muscle expression and abnormal function of beta-myosin in hypertrophic cardiomyopathy. J. Clin. Invest. 91, 2861–2865.

D'Amico, A., Graziano, C., Pacileo, G., Petrini, S., Nowak, K.J., Boldrini, R., Jacques, A., Feng, J.-J., Porfirio, B., Sewry, C.A., et al. (2006). Fatal hypertrophic cardiomyopathy and nemaline myopathy associated with ACTA1 K336E mutation. Neuromuscul Disord 16, 548–552.

Daehmlow, S., Erdmann, J., Knueppel, T., Gille, C., Froemmel, C., Hummel, M., Hetzer, R., and Regitz-Zagrosek, V. (2002). Novel mutations in sarcomeric protein genes in dilated cardiomyopathy. Biochemical and Biophysical Research Communications 298, 116–120.

Danev, R., and Baumeister, W. (2016). Cryo-EM single particle analysis with the Volta phase plate. Elife 5, 439.

Dausse, E., Komajda, M., Fetler, L., Dubourg, O., Dufour, C., Carrier, L., Wisnewsky, C., Bercovici, J., Hengstenberg, C., and al-Mahdawi, S. (1993). Familial hypertrophic cardiomyopathy. Microsatellite haplotyping and identification of a hot spot for mutations in the beta-myosin heavy chain gene. J. Clin. Invest. 92, 2807–2813.

De Rosier, D.J., and Klug, A. (1968). Reconstruction of three dimensional structures from electron micrographs. Nature 217, 130–134.

Deptuch, G., Besson, A., Rehak, P., Szelezniak, M., Wall, J., Winter, M., and Zhu, Y. (2007). Direct electron imaging in electron microscopy with monolithic active pixel sensors. Ultramicroscopy 107, 674–684.

Desfosses, A., Ciuffa, R., Gutsche, I., and Sachse, C. (2014). SPRING - An image processing package for single-particle based helical reconstruction from electron cryomicrographs. Journal of Structural Biology 185, 15–26.

DiMaio, F., Song, Y., Li, X., Brunner, M.J., Xu, C., Conticello, V., Egelman, E., Marlovits, T.C., Cheng, Y., and Baker, D. (2015). Atomic-accuracy models from 4.5-Å cryo-electron microscopy data with density-guided iterative local refinement. Nature Methods 12, 361–365.

Doerr, A. (2016). Single-particle cryo-electron microscopy. Nature Methods 13, 23.

Dominguez, R., Freyzon, Y., Trybus, K.M., and Cohen, C. (1998). Crystal structure of a vertebrate smooth muscle myosin motor domain and its complex with the essential light chain: visualization of the pre-power stroke state. Cell 94, 559–571.

Dominguez, R. (2016). The WH2 Domain and Actin Nucleation: Necessary but Insufficient. Trends Biochem. Sci. 41, 478–490.

Dominguez, R., and Holmes, K.C. (2011). Actin structure and function. 40, 169–186.

Dubochet, J., and McDowall, A.W. (1981). Vitrification of pure water for electron microscopy. Journal of Microscopy 124, 3–4.

Dubochet, J., Adrian, M., Chang, J.J., Homo, J.C., Lepault, J., McDowall, A.W., and Schultz, P. (1988). Cryo-electron microscopy of vitrified specimens. Quarterly Reviews of Biophysics 21, 129–228.

Duda, R.O., Hart, P.E., and Stork, D.G. (2012). Pattern Classification (John Wiley & Sons).

Durer, Z.A.O., Kudryashov, D.S., Sawaya, M.R., Altenbach, C., Hubbell, W., and Reisler, E. (2012). Structural states and dynamics of the D-loop in actin. Biophys. J. 103, 930–939.

Editorial by Nature Methods (2016). Method of the Year 2015. Nature Methods 13, 1.

Edwards, M., Zwolak, A., Schafer, D.A., Sept, D., Dominguez, R., and Cooper, J.A. (2014). Capping protein regulators fine-tune actin assembly dynamics. Nature Reviews. Molecular Cell Biology 15, 677–689.

Egelman, E.H. (1985). The structure of F-actin. J. Muscle Res. Cell. Motil. 6, 129–151.

Egelman, E.H. (2000). A robust algorithm for the reconstruction of helical filaments using single-particle methods. Ultramicroscopy 85, 225–234.

Egelman, E.H. (2007). The iterative helical real space reconstruction method: surmounting the problems posed by real polymers. Journal of Structural Biology 157, 83–94.

Egelman, E.H. (2010). Reconstruction of helical filaments and tubes. Methods in Enzymology 482, 167–183.

Egelman, E.H., and DeRosier, D.J. (1991). Angular disorder in actin: is it consistent with general principles of protein structure? J. Mol. Biol. 217, 405–408.

Egelman, E.H., Francis, N., and DeRosier, D.J. (1982). F-actin is a helix with a random variable twist. Nature 298, 131–135.

Egelman, E.H., Francis, N., DeRosier, D.J., and Klug, A. (1983). Helical disorder and the filament structure of F-actin are elucidated by the angle-layered aggregate. J. Mol. Biol. 166, 605–623.

Egelman, E.H. (2014). Ambiguities in helical reconstruction. Elife 3.

Egelman, E.H. (2015). Three-dimensional reconstruction of helical polymers. Archives of Biochemistry and Biophysics 581, 54–58.

Egelman, E.H. (2016). The Current Revolution in Cryo-EM. Biophys. J. 110, 1008–1012.

Eisenstein, M. (2016). The field that came in from the cold. Nature Methods 13, 19–22.

Emsley, P., Lohkamp, B., Scott, W.G., and Cowtan, K. (2010). Features and development of Coot. Acta Crystallogr. D Biol. Crystallogr. 66, 486–501.

Epstein, N.D., Cohn, G.M., Cyran, F., and Fananapazir, L. (1992). Differences in clinical expression of hypertrophic cardiomyopathy associated with two distinct mutations in the beta-myosin heavy chain gene. A 908Leu----Val mutation and a 403Arg----Gln mutation. Circulation 86, 345–352.

Erdmann, J., Daehmlow, S., Wischke, S., Senyuva, M., Werner, U., Raible, J., Tanis, N., Dyachenko, S., Hummel, M., Hetzer, R., et al. (2003). Mutation spectrum in a large cohort of unrelated consecutive patients with hypertrophic cardiomyopathy. Clin. Genet. 64, 339–349.

Erickson, H.P. (2001). Cytoskeleton. Evolution in bacteria. Nature 413, 30–30.

Faruqi, A.R., Cattermole, D.M., Henderson, R., Mikulec, B., and Raeburn, C. (2003). Evaluation of a hybrid pixel detector for electron microscopy. Ultramicroscopy 94, 263–276.

Fernández, I.S., Bai, X.-C., Murshudov, G., Scheres, S.H.W., and Ramakrishnan, V. (2014). Initiation of translation by cricket paralysis virus IRES requires its translocation in the ribosome. Cell 157, 823–831.

Fisher, A.J., Smith, C.A., Thoden, J.B., Smith, R., Sutoh, K., Holden, H.M., and Rayment, I. (1995). X-ray structures of the myosin motor domain of Dictyostelium discoideum complexed with MgADP.BeFx and MgADP.AlF4-. Biochemistry 34, 8960–8972.

Fletcher, D.A., and Mullins, R.D. (2010). Cell mechanics and the cytoskeleton. Nature 463, 485–492.

Frank, J. (1973). The envelope of electron microscopic transfer functions for partially coherent illumination. Optik 38, 519–536.

Frank, J. (1996). Three-Dimensional Electron Microscopy of Macromolecular Assemblies (Academic Press).

Frank, J. (2002). Single-particle imaging of macromolecules by cryo-electron microscopy. Annual Review of Biophysics and Biomolecular Structure 31, 303–319.

Frank, J. (2015). Generalized single-particle cryo-EM - a historical perspective. Microscopy (Oxf) dfv358.

Fujii, T., Iwane, A.H., Yanagida, T., and Namba, K. (2010). Direct visualization of secondary structures of F-actin by electron cryomicroscopy. 467, 724–728.

Furch, M., Geeves, M.A., and Manstein, D.J. (1998). Modulation of actin affinity and actomyosin adenosine triphosphatase by charge changes in the myosin motor domain. Biochemistry 37, 6317–6326.

Furch, M., Remmel, B., Geeves, M.A., and Manstein, D.J. (2000). Stabilization of the actomyosin complex by negative charges on myosin. Biochemistry 39, 11602–11608.

Galkin, V.E., Orlova, A., and Egelman, E.H. (2012). Actin filaments as tension sensors. Curr. Biol. 22, R96–R101.

Galkin, V.E., Orlova, A., Schröder, G.F., and Egelman, E.H. (2010). Structural polymorphism in F-actin. Nat. Struct. Mol. Biol. 17, 1318–1323.

Gao, M., Berghaus, M., von der Ecken, J., Raunser, S., and Winter, R. (2015). Condensation agents determine the temperature-pressure stability of F-actin bundles. Angew. Chem. Int. Ed. Engl. 54, 11088–11092.

Gatsogiannis, C., Hofnagel, O., Markl, J., and Raunser, S. (2014). Structure of Mega-Hemocyanin Reveals Protein Origami in Snails. Structure.

Gavira, J.A. (2015). Current trends in protein crystallization. Archives of Biochemistry and Biophysics.

Gebel Berg, E. (2015). Breaking the Crystal Ceiling. ACS Cent. Sci. 1, 283–285.

Geeves, M.A., and Holmes, K.C. (1999). Structural mechanism of muscle contraction. Annu. Rev. Biochem. 68, 687–728.

Geeves, M.A. (2016). The ATPase mechanism of myosin and actomyosin. Biopolymers.

Geeves, M.A., Hitchcock-DeGregori, S.E., and Gunning, P.W. (2014). A systematic nomenclature for mammalian tropomyosin isoforms. J. Muscle Res. Cell. Motil. 1–7.

Geisterfer-Lowrance, A.A., Kass, S., Tanigawa, G., Vosberg, H.P., McKenna, W., Seidman, C.E., and Seidman, J.G. (1990). A molecular basis for familial hypertrophic cardiomyopathy: a beta cardiac myosin heavy chain gene missense mutation. Cell 62, 999–1006.

Geuze, H.J. (1999). A future for electron microscopy in cell biology? Trends in Cell Biology 9, 92–93.

Giese, K.C., and Spudich, J.A. (1997). Phenotypically selected mutations in myosin's actin binding domain demonstrate intermolecular contacts important for motor function. Biochemistry 36, 8465–8473.

Glaeser, R.M. (2013). Invited review article: Methods for imaging weak-phase objects in electron microscopy. Rev Sci Instrum 84, 111101.

Glaeser, R.M. (2016). How good can cryo-EM become? Nature Methods 13, 28–32.

Gordon, A.M., Homsher, E., and Regnier, M. (2000). Regulation of contraction in striated muscle. Physiological Reviews 80, 853–924.

Graceffa, P., and Dominguez, R. (2003). Crystal structure of monomeric actin in the ATP state. Structural basis of nucleotide-dependent actin dynamics. J. Biol. Chem. 278, 34172–34180.

Grant, T., and Grigorieff, N. (2015). Measuring the optimal exposure for single particle cryo-EM using a 2.6 Å reconstruction of rotavirus VP6. Elife 4, e06980.

Graziano, C., Bertini, E., Minetti, C., and Porfirio, B. (2004). Alpha-actin gene mutations and polymorphisms in Italian patients with nemaline myopathy. Int. J. Mol. Med. 13, 805–809.

Greber, B.J., Boehringer, D., Leibundgut, M., Bieri, P., Leitner, A., Schmitz, N., Aebersold, R., and Ban, N. (2014). The complete structure of the large subunit of the mammalian mitochondrial ribosome. Nature 515, 283–286.

Greber-Platzer, S., Marx, M., Fleischmann, C., Suppan, C., Dobner, M., and Wimmer, M. (2001). Beta-myosin heavy chain gene mutations and hypertrophic cardiomyopathy in Austrian children. J. Mol. Cell. Cardiol. 33, 141–148.

Greenberg, M.J., Arpağ, G., Tüzel, E., and Ostap, E.M. (2016). A Perspective on the Role of Myosins as Mechanosensors. Biophys. J. 110, 2568–2576.

Grigorieff, N. (2007). FREALIGN: high-resolution refinement of single particle structures. Journal of Structural Biology 157, 117–125.

Grob, P., Bean, D., Typke, D., Li, X., Nogales, E., and Glaeser, R.M. (2013). Ranking TEM cameras by their response to electron shot noise. Ultramicroscopy 133C, 1–7.

Gulick, A.M., Bauer, C.B., Thoden, J.B., and Rayment, I. (1997). X-ray structures of the MgADP, MgATPgammaS, and MgAMPPNP complexes of the Dictyostelium discoideum myosin motor domain. Biochemistry 36, 11619–11628.

Gunning, P., O'Neill, G., and Hardeman, E. (2008). Tropomyosin-based regulation of the actin cytoskeleton in time and space. Physiological Reviews 88, 1–35.

Gunning, P., Weinberger, R., and Jeffrey, P. (1997). Actin and tropomyosin isoforms in morphogenesis. Anatomy and Embryology 195, 311–315.

Gunning, P.W., Ghoshdastider, U., Whitaker, S., Popp, D., and Robinson, R.C. (2015a). The evolution of compositionally and functionally distinct actin filaments. J. Cell. Sci. 128, 2009–2019.

Gunning, P.W., Hardeman, E.C., Lappalainen, P., and Mulvihill, D.P. (2015b). Tropomyosin - master regulator of actin filament function in the cytoskeleton. J. Cell. Sci. jcs.172502.

Gyimesi, M., Tsaturyan, A.K., Kellermayer, M.S.Z., and Malnasi-Csizmadia, A. (2008). Kinetic characterization of the function of myosin loop 4 in the actin-myosin interaction. Biochemistry 47, 283–291.

Harris, J.R. (2000). The future of transmission electron microscopy (TEM) in biology and medicine. Micron 31, 1–3.

Hartman, M.A., Finan, D., Sivaramakrishnan, S., and Spudich, J.A. (2011). Principles of unconventional myosin function and targeting. Annual Review of Cell and Developmental Biology 27, 133–155.

Hatano, S., and Oosawa, F. (1966). Extraction of an actin-like protein from the plasmodium of a myxomycete and its interaction with myosin A from rabbit striated muscle. J. Cell. Physiol. 68, 197–202.

Hayashi, T., and Ip, W. (1976). Polymerization polarity of actin. J Mechanochem Cell Motil 3, 163–169.

Hayward, S., and Lee, R.A. (2002). Improvements in the analysis of domain motions in proteins from conformational change: DynDom version 1.50. J. Mol. Graph. Model. 21, 181–183.

Heissler, S.M., and Manstein, D.J. (2011). Comparative kinetic and functional characterization of the motor domains of human nonmuscle myosin-2C isoforms. J. Biol. Chem. 286, 21191–21202.

Heissler, S.M., and Manstein, D.J. (2012). Nonmuscle myosin-2: mix and match. Cellular and Molecular Life Sciences : CMLS.

Hell, S.W., and Wichmann, J. (1994). Breaking the diffraction resolution limit by stimulated emission: stimulated-emission-depletion fluorescence microscopy. Opt Lett 19, 780–782.

Helliwell, J.R. (2013). How to solve protein structures with an X-ray laser. Science 339, 146–147.

Henderson, R. (1995). The potential and limitations of neutrons, electrons and X-rays for atomic resolution microscopy of unstained biological molecules. Quarterly Reviews of Biophysics 28, 171–193.

Hertzog, M., and Carlier, M.F. (2005). Functional characterization of proteins regulating actin assembly. Current Protocols in Cell Biology / Editorial Board, Juan S. Bonifacino ... [Et Al.] 13.

Hessa, T., Kim, H., Bihlmaier, K., Lundin, C., Boekel, J., Andersson, H., Nilsson, I., White, S.H., and Heijne, von, G. (2005). Recognition of transmembrane helices by the endoplasmic reticulum translocon. Nature 433, 377–381.

Hodge, T., and Cope, M.J. (2000). A myosin family tree. J. Cell. Sci. 113 Pt 19, 3353–3354.

Hohn, M., Tang, G., Goodyear, G., Baldwin, P.R., Huang, Z., Penczek, P.A., Yang, C., Glaeser, R.M., Adams, P.D., and Ludtke, S.J. (2007). SPARX, a new environment for Cryo-EM image processing. Journal of Structural Biology 157, 47–55.

Holmes, K.C. (1997). The swinging lever-arm hypothesis of muscle contraction. Curr. Biol. 7, R112–R118.

Holmes, K.C., Popp, D., Gebhard, W., and Kabsch, W. (1990). Atomic model of the actin filament. Nature 347, 44–49.

Holmes, K.C., and Lehman, W. (2008). Gestalt-binding of tropomyosin to actin filaments. J. Muscle Res. Cell. Motil. 29, 213–219.

Holmes, K.C., Angert, I., Kull, F.J., Jahn, W., and Schröder, R.R. (2003). Electron cryo-microscopy shows how strong binding of myosin to actin releases nucleotide. Nature 425, 423–427.

Houdusse, A., Szent-Gyorgyi, A.G., and Cohen, C. (2000). Three conformational states of scallop myosin S1. Proc. Natl. Acad. Sci. U.S.a. 97, 11238–11243.

Hung, R.-J., Pak, C.W., and Terman, J.R. (2011). Direct redox regulation of F-actin assembly and disassembly by Mical. Science 334, 1710–1713.

Hung, R.-J., Yazdani, U., Yoon, J., Wu, H., Yang, T., Gupta, N., Huang, Z., van Berkel, W.J.H., and Terman, J.R. (2010). Mical links semaphorins to F-actin disassembly. Nature 463, 823–827.

Huxley, H., and Hanson, J. (1954). Changes in the cross-striations of muscle during contraction and stretch and their structural interpretation. Nature 173, 973–976.

Huxley, H.E. (1953). Electron microscope studies of the organisation of the filaments in striated muscle. Biochimica Et Biophysica Acta 12, 387–394.

Huxley, H.E. (1963). Electron microscope studies on the structure of natural and synthetic protein filaments from striated muscle. J. Mol. Biol. 7, 281–308.

Huxley, H.E. (1969). The mechanism of muscular contraction. Science 164, 1356–1365.

Ilkovski, B., Nowak, K.J., Domazetovska, A., Maxwell, A.L., Clement, S., Davies, K.E., Laing, N.G., North, K.N., and Cooper, S.T. (2004). Evidence for a dominant-negative effect in ACTA1 nemaline myopathy caused by abnormal folding, aggregation and altered polymerization of mutant actin isoforms. Hum. Mol. Genet. 13, 1727–1743.

Ishikawa, H., Bischoff, R., and Holtzer, H. (1969). Formation of arrowhead complexes with heavy meromyosin in a variety of cell types. J. Cell Biol. 43, 312–328.

Iwasa, M., Maeda, K., Narita, A., Maéda, Y., and Oda, T. (2008). Dual roles of Gln137 of actin revealed by recombinant human cardiac muscle alpha-actin mutants. J. Biol. Chem. 283, 21045–21053.

Jain, R.K., Jayawant, S., Squier, W., Muntoni, F., Sewry, C.A., Manzur, A., Quinlivan, R., Lillis, S., Jungbluth, H., Sparrow, J.C., et al. (2012). Nemaline myopathy with stiffness and hypertonia associated with an ACTA1 mutation. Neurology 78, 1100–1103.

Jégou, A., and Romet-Lemonne, G. (2016). Single Filaments to Reveal the Multiple Flavors of Actin. Biophys. J. 110, 2138–2146.

Jiang, W., Baker, M.L., Jakana, J., Weigele, P.R., King, J., and Chiu, W. (2008). Backbone structure of the infectious epsilon15 virus capsid revealed by electron cryomicroscopy. Nature 451, 1130–1134.

Joel, P.B., Trybus, K.M., and Sweeney, H.L. (2001). Two conserved lysines at the 50/20-kDa junction of myosin are necessary for triggering actin activation. J. Biol. Chem. 276, 2998–3003.

Jones, T.A. (2004). Interactive electron-density map interpretation: from INTER to O. Acta Crystallogr. D Biol. Crystallogr. 60, 2115–2125.

Jontes, J.D., Wilson-Kubalek, E.M., and Milligan, R.A. (1995). A 32 degree tail swing in brush border myosin I on ADP release. Nature 378, 751–753.

Kabsch, W., Mannherz, H.G., Suck, D., Pai, E.F., and Holmes, K.C. (1990). Atomic structure of the actin:DNase I complex. Nature 347, 37–44.

Kamisago, M., Sharma, S.D., DePalma, S.R., Solomon, S., Sharma, P., McDonough, B., Smoot, L., Mullen, M.P., Woolf, P.K., Wigle, E.D., et al. (2000). Mutations in sarcomere protein genes as a cause of dilated cardiomyopathy. N. Engl. J. Med. 343, 1688–1696.

Khoshouei, M., Radjainia, M., Phillips, A.J., Gerrard, J.A., Mitra, A.K., Plitzko, J.M., Baumeister, W., and Danev, R. (2016). Volta phase plate cryo-EM of the small protein complex Prx3. Nat Commun 7, 10534.

Kimanius, D., Forsberg, B.O., Scheres, S.H.W., and Lindahl, E. (2016). Accelerated cryo-EM structure determination with parallelisation using GPUs in RELION-2. bioRxiv.

Kirschner, M.W. (1980). Implications of treadmilling for the stability and polarity of actin and tubulin polymers in vivo. J. Cell Biol. 86, 330–334.

Klar, T.A., Engel, E., and Hell, S.W. (2001). Breaking Abbe's diffraction resolution limit in fluorescence microscopy with stimulated emission depletion beams of various shapes. Phys Rev E Stat Nonlin Soft Matter Phys 64, 066613.

Klein, J.C., Burr, A.R., Svensson, B., Kennedy, D.J., Allingham, J., Titus, M.A., Rayment, I., and Thomas, D.D. (2008). Actin-binding cleft closure in myosin II probed by site-directed spin labeling and pulsed EPR. Proc. Natl. Acad. Sci. U.S.a. 105, 12867–12872.

Klug, A., and De Rosier, D.J. (1966). Optical filtering of electron micrographs: reconstruction of one-sided images. Nature 212, 29–32.

Klug, A., Crick, F.H.C., and Wyckoff, H.W. (1958). Diffraction by helical structures. Acta Crystallographica 11, 199–213.

Knoll, M., and Ruska, E. (1932a). Beitrag zur geometrischen Elektronenoptik. I. Ann. Physik 404, 607–640.

Knoll, M., and Ruska, E. (1932b). Beitrag zur geometrischen Elektronenoptik. II. Ann. Physik 404, 641–661.

Kojima, S., Konishi, K., Katoh, K., Fujiwara, K., Martinez, H.M., Morales, M.F., and Onishi, H. (2001). Functional roles of ionic and hydrophobic surface loops in smooth muscle myosin: their interactions with actin. Biochemistry 40, 657–664.

Kollmar, M., Dürrwang, U., Kliche, W., Manstein, D.J., and Kull, F.J. (2002). Crystal structure of the motor domain of a class-I myosin. The EMBO Journal 21, 2517–2525.

Koy, A., Ilkovski, B., Laing, N., North, K., Weis, J., Neuen-Jacob, E., Mayatepek, E., and Voit, T. (2007). Nemaline myopathy with exclusively intranuclear rods and a novel mutation in ACTA1 (Q139H). Neuropediatrics 38, 282–286.

Krissinel, E., and Henrick, K. (2007). Inference of macromolecular assemblies from crystalline state. J. Mol. Biol. 372, 774–797.

Kucukelbir, A., Sigworth, F.J., and Tagare, H.D. (2014). Quantifying the local resolution of cryo-EM density maps. Nature Methods 11, 63–65.

Kuijper, M., van Hoften, G., Janssen, B., Geurink, R., De Carlo, S., Vos, M., van Duinen, G., van Haeringen, B., and Storms, M. (2015). FEI's direct electron detector developments: Embarking on a revolution in cryo-TEM. Journal of Structural Biology.

Kukulski, W., Schorb, M., Welsch, S., Picco, A., Kaksonen, M., and Briggs, J.A.G. (2012). Precise, correlated fluorescence microscopy and electron tomography of lowicryl sections using fluorescent fiducial markers. Methods Cell Biol. 111, 235–257.

Kühlbrandt, W. (2014a). Biochemistry. The resolution revolution. Science 343, 1443–1444.

Kühlbrandt, W. (2014b). Cryo-EM enters a new era. Elife 3, e03678.

Laing, N.G., Dye, D.E., Wallgren-Pettersson, C., Richard, G., Monnier, N., Lillis, S., Winder, T.L., Lochmüller, H., Graziano, C., Mitrani-Rosenbaum, S., et al. (2009). Mutations and polymorphisms of the skeletal muscle alpha-actin gene (ACTA1). Hum. Mutat. 30, 1267–1277.

Lankford, E.B., Epstein, N.D., Fananapazir, L., and Sweeney, H.L. (1995). Abnormal contractile properties of muscle fibers expressing beta-myosin heavy chain gene mutations in patients with hypertrophic cardiomyopathy. J. Clin. Invest. 95, 1409–1414.

Leaver-Fay, A., Tyka, M., Lewis, S.M., Lange, O.F., Thompson, J., Jacak, R., Kaufman, K., Renfrew, P.D., Smith, C.A., Sheffler, W., et al. (2011). ROSETTA3: an object-oriented software suite for the simulation and design of macromolecules. Methods in Enzymology 487, 545–574.

Lehman, W., Li, X.E., Orzechowski, M., and Fischer, S. (2013a). The structural dynamics of alpha-tropomyosin on F-actin shape the overlap complex between adjacent tropomyosin molecules. Archives of Biochemistry and Biophysics.

Lehman, W., Orzechowski, M., Li, X.E., Fischer, S., and Raunser, S. (2013b). Gestalt-binding of tropomyosin on actin during thin filament activation. J. Muscle Res. Cell. Motil. 34, 155–163.

Ley, T.J., Mardis, E.R., Ding, L., Fulton, B., McLellan, M.D., Chen, K., Dooling, D., Dunford-Shore, B.H., McGrath, S., Hickenbotham, M., et al. (2008). DNA sequencing of a cytogenetically normal acute myeloid leukaemia genome. Nature 456, 66–72.

Li, X.E., Tobacman, L.S., Mun, J.Y., Craig, R., Fischer, S., and Lehman, W. (2011). Tropomyosin position on F-actin revealed by EM reconstruction and computational chemistry. 100, 1005–1013.

Li, X., Mooney, P., Zheng, S., Booth, C.R., Braunfeld, M.B., Gubbens, S., Agard, D.A., and Cheng, Y. (2013a). Electron counting and beam-induced motion correction enable near-atomic-resolution single-particle cryo-EM. Nature Methods.

Li, X.E., Orzechowski, M., Lehman, W., and Fischer, S. (2014). Structure and flexibility of the tropomyosin overlap junction. Biochemical and Biophysical Research Communications 446, 304–308.

Li, X., Zheng, S.Q., Egami, K., Agard, D.A., and Cheng, Y. (2013b). Influence of electron dose rate on electron counting images recorded with the K2 camera. Journal of Structural Biology 184, 251–260.

Li, Y., Mui, S., Brown, J.H., Strand, J., Reshetnikova, L., Tobacman, L.S., and Cohen, C. (2002). The crystal structure of the C-terminal fragment of striated-muscle alpha-tropomyosin reveals a key troponin T recognition site. Proc. Natl. Acad. Sci. U.S.a. 99, 7378–7383.

Liao, M., Cao, E., Julius, D., and Cheng, Y. (2013). Structure of the TRPV1 ion channel determined by electron cryo-microscopy. Nature 504, 107–112.

Llinas, P., Isabet, T., Song, L., Ropars, V., Zong, B., Benisty, H., Sirigu, S., Morris, C., Kikuti, C., Safer, D., et al. (2015). How actin initiates the motor activity of Myosin. Dev. Cell 33, 401–412.

Lodish, H., Berk, A., Kaiser, C., Krieger, M., Scott, M., Bretscher, A., Ploegh, H., and Matsudaira, P. (2008). Molecular Cell Biology (New York: W. H. Freeman and Company).

Lopéz-Blanco, J.R., and Chacón, P. (2013). iMODFIT: efficient and robust flexible fitting based on vibrational analysis in internal coordinates. Journal of Structural Biology 184, 261–270.

Lorenz, M., Poole, K.J., Popp, D., Rosenbaum, G., and Holmes, K.C. (1995). An atomic model of the unregulated thin filament obtained by X-ray fiber diffraction on oriented actin-tropomyosin gels. J. Mol. Biol. 246, 108–119.

Lorenz, M., Popp, D., and Holmes, K.C. (1993). Refinement of the F-actin model against X-ray fiber diffraction data by the use of a directed mutation algorithm. J. Mol. Biol. 234, 826–836.

Lorenz, M., and Holmes, K.C. (2010). The actin-myosin interface. Proc. Natl. Acad. Sci. U.S.a. 107, 12529–12534.

Ludtke, S.J. (2010). 3-D structures of macromolecules using single-particle analysis in EMAN. Methods Mol Biol 673, 157–173.

Lymn, R.W., and Taylor, E.W. (1970). Transient state phosphate production in the hydrolysis of nucleoside triphosphates by myosin. Biochemistry 9, 2975–2983.

Lymn, R.W., and Taylor, E.W. (1971). Mechanism of adenosine triphosphate hydrolysis by actomyosin. Biochemistry 10, 4617–4624.

Lyumkis, D., Brilot, A.F., Theobald, D.L., and Grigorieff, N. (2013). Likelihood-based classification of cryo-EM images using FREALIGN. Journal of Structural Biology 183, 377–388.

Mahamid, J., Pfeffer, S., Schaffer, M., Villa, E., Danev, R., Cuellar, L.K., Förster, F., Hyman, A.A., Plitzko, J.M., and Baumeister, W. (2016). Visualizing the molecular sociology at the HeLa cell nuclear periphery. Science 351, 969–972.

Mamidi, R., Michael, J.J., Muthuchamy, M., and Chandra, M. (2013). Interplay between the overlapping ends of tropomyosin and the N terminus of cardiac troponin T affects tropomyosin states on actin. FASEB Journal : Official Publication of the Federation of American Societies for Experimental Biology.

Manstein, D.J., and Mulvihill, D.P. (2016). Tropomyosin-mediated Regulation of Cytoplasmic Myosins. Traffic.

Marian, A.J., Wu, Y., Lim, D.S., McCluggage, M., Youker, K., Yu, Q.T., Brugada, R., DeMayo, F., Quinones, M., and Roberts, R. (1999). A transgenic rabbit model for human hypertrophic cardiomyopathy. J. Clin. Invest. 104, 1683–1692.

McIntosh, R., Nicastro, D., and Mastronarde, D. (2005). New views of cells in 3D: an introduction to electron tomography. Trends in Cell Biology 15, 43–51.

McLaughlin, P.J., Gooch, J.T., Mannherz, H.G., and Weeds, A.G. (1993). Structure of gelsolin segment 1-actin complex and the mechanism of filament severing. Nature 364, 685–692.

McMullan, G., Faruqi, A.R., Clare, D., and Henderson, R. (2014). Comparison of optimal performance at 300keV of three direct electron detectors for use in low dose electron microscopy. Ultramicroscopy 147, 156–163.

McMullan, G., Vinothkumar, K.R., and Henderson, R. (2015). Thon rings from amorphous ice and implications of beam-induced Brownian motion in single particle electron cryo-microscopy. Ultramicroscopy 158, 26–32.

Merk, A., Bartesaghi, A., Banerjee, S., Falconieri, V., Rao, P., Davis, M.I., Pragani, R., Boxer, M.B., Earl, L.A., Milne, J.L.S., et al. (2016). Breaking Cryo-EM Resolution Barriers to Facilitate Drug Discovery. Cell.

Mertens, H.D., and Svergun, D.I. (2010). Structural characterization of proteins and complexes using small-angle X-ray solution scattering. Journal of Structural Biology 172, 128–141.

Meusch, D., Gatsogiannis, C., Efremov, R.G., Lang, A.E., Hofnagel, O., Vetter, I.R., Aktories, K., and Raunser, S. (2014). Mechanism of Tc toxin action revealed in molecular detail. Nature 508, 61–65.

Milazzo, A.-C., Leblanc, P., Duttweiler, F., Jin, L., Bouwer, J.C., Peltier, S., Ellisman, M., Bieser, F., Matis, H.S., Wieman, H., et al. (2005). Active pixel sensor array as a detector for electron microscopy. Ultramicroscopy 104, 152–159.

Milewicz, D.M., Guo, D.-C., Tran-Fadulu, V., Lafont, A.L., Papke, C.L., Inamoto, S., Kwartler, C.S., and Pannu, H. (2008). Genetic basis of thoracic aortic aneurysms and dissections: focus on smooth muscle cell contractile dysfunction. Annu Rev Genomics Hum Genet 9, 283–302.

Miller, C.J., Wong, W.W., Bobkova, E., Rubenstein, P.A., and Reisler, E. (1996). Mutational analysis of the role of the N terminus of actin in actomyosin interactions. Comparison with other mutant actins and implications for the cross-bridge cycle. Biochemistry 35, 16557–16565.

Milligan, R.A. (1996). Protein-protein interactions in the rigor actomyosin complex. Proc. Natl. Acad. Sci. U.S.a. 93, 21–26.

Milligan, R.A., and Flicker, P.F. (1987). Structural relationships of actin, myosin, and tropomyosin revealed by cryo-electron microscopy. The Journal of Cell Biology 105, 29–39.

Milligan, R.A., Whittaker, M., and Safer, D. (1990). Molecular structure of F-actin and location of surface binding sites. Nature 348, 217–221.

Mindell, J.A., and Grigorieff, N. (2003). Accurate determination of local defocus and specimen tilt in electron microscopy. Journal of Structural Biology 142, 334–347.

Mohiddin, S.A., Begley, D.A., McLam, E., Cardoso, J.-P., Winkler, J.B., Sellers, J.R., and Fananapazir, L. (2003). Utility of genetic screening in hypertrophic cardiomyopathy: prevalence and significance of novel and double (homozygous and heterozygous) beta-myosin mutations. Genet. Test. 7, 21–27.

Moolman, J.C., Brink, P.A., and Corfield, V.A. (1993). Identification of a new missense mutation at Arg403, a CpG mutation hotspot, in exon 13 of the beta-myosin heavy chain gene in hypertrophic cardiomyopathy. Hum. Mol. Genet. 2, 1731–1732.

Moolman-Smook, J.C., De Lange, W.J., Bruwer, E.C., Brink, P.A., and Corfield, V.A. (1999). The origins of hypertrophic cardiomyopathy-causing mutations in two South African subpopulations: a unique profile of both independent and founder events. Am. J. Hum. Genet. 65, 1308–1320.

Moore, P.B., Huxley, H.E., and DeRosier, D.J. (1970). Three-dimensional reconstruction of F-actin, thin filaments and decorated thin filaments. J. Mol. Biol. 50, 279–295.

Morris, A.L., MacArthur, M.W., Hutchinson, E.G., and Thornton, J.M. (1992). Stereochemical quality of protein structure coordinates. Proteins 12, 345–364.

Morton, W.M., Ayscough, K.R., and McLaughlin, P.J. (2000). Latrunculin alters the actin-monomer subunit interface to prevent polymerization. Nat. Cell Biol. 2, 376–378.

Mulligan, S.K., Speir, J.A., Razinkov, I., Cheng, A., Crum, J., Jain, T., Duggan, E., Liu, E., Nolan, J.P., Carragher, B., et al. (2015). Multiplexed TEM Specimen Preparation and Analysis of Plasmonic Nanoparticles. Microsc. Microanal. 21, 1017–1025.

Mun, J.Y., Previs, M.J., Yu, H.Y., Gulick, J., Tobacman, L.S., Beck Previs, S., Robbins, J., Warshaw, D.M., and Craig, R. (2014). Myosin-binding protein C displaces tropomyosin to activate cardiac thin filaments and governs their speed by an independent mechanism. Proc. Natl. Acad. Sci. U.S.a. 111, 2170–2175.

Murakami, K., Yasunaga, T., Noguchi, T.Q., Gomibuchi, Y., Ngo, K.X., Uyeda, T.Q., and Wakabayashi, T. (2010). Structural basis for actin assembly, activation of ATP hydrolysis, and delayed phosphate release. Cell 143, 275–287.

Muretta, J.M., Rohde, J.A., Johnsrud, D.O., Cornea, S., and Thomas, D.D. (2015). Direct real-time detection of the structural and biochemical events in the myosin power stroke. Proc. Natl. Acad. Sci. U.S.a. 112, 14272–14277.

Murphy, C.T., and Spudich, J.A. (1999). The sequence of the myosin 50-20K loop affects Myosin's affinity for actin throughout the actin-myosin ATPase cycle and its maximum ATPase activity. Biochemistry 38, 3785–3792.

Murphy, G.E., and Jensen, G.J. (2007). Electron cryotomography. BioTechniques 43, 413–415–417passim.

Müller, M.P., and Goody, R.S. (2016). Review: Ras GTPases and myosin: Qualitative conservation and quantitative diversification in signal and energy transduction. Biopolymers 105, 422–430.

Müller, M., Mazur, A.J., Behrmann, E., Diensthuber, R.P., Radke, M.B., Qu, Z., Littwitz, C., Raunser, S., Schoenenberger, C.-A., Manstein, D.J., et al. (2012). Functional characterization of the human α-cardiac actin mutations Y166C and M305L involved in hypertrophic cardiomyopathy. Cellular and Molecular Life Sciences : CMLS 69, 3457–3479.

Münnich, S., Pathan-Chhatbar, S., and Manstein, D.J. (2014). Crystal structure of the rigor-like human non-muscle myosin-2 motor domain. FEBS Lett. 588, 4754–4760.

Nair, U.B., Joel, P.B., Wan, Q., Lowey, S., Rould, M.A., and Trybus, K.M. (2008). Crystal structures of monomeric actin bound to cytochalasin D. J. Mol. Biol. 384, 848–864.

Nannenga, B.L., Shi, D., Leslie, A.G.W., and Gonen, T. (2014). High-resolution structure determination by continuous-rotation data collection in MicroED. Nature Methods 11, 927–930.

Narita, A., Oda, T., and Maéda, Y. (2011). Structural basis for the slow dynamics of the actin filament pointed end. The EMBO Journal 30, 1230–1237.

Nicholls, R.A., Fischer, M., McNicholas, S., and Murshudov, G.N. (2014). Conformation-independent structural comparison of macromolecules with ProSMART. Acta Crystallogr. D Biol. Crystallogr. 70, 2487–2499.

Nogales, E. (2016). The development of cryo-EM into a mainstream structural biology technique. Nature Methods 13, 24–27.

Nogales, E., and Scheres, S.H.W. (2015). Cryo-EM: A Unique Tool for the Visualization of Macromolecular Complexity. Mol. Cell 58, 677–689.

Nowak, K.J., Wattanasirichaigoon, D., Goebel, H.H., Wilce, M., Pelin, K., Donner, K., Jacob, R.L., Hübner, C., Oexle, K., Anderson, J.R., et al. (1999). Mutations in the skeletal muscle alpha-actin gene in patients with actin myopathy and nemaline myopathy. Nat. Genet. 23, 208–212.

Nürnberg, A., Kitzing, T., and Grosse, R. (2011). Nucleating actin for invasion. Nat. Rev. Cancer 11, 177–187.

Oda, T., and Maéda, Y. (2010). Multiple Conformations of F-actin. Structure 18, 761–767.

Oda, T., Iwasa, M., Aihara, T., Maéda, Y., and Narita, A. (2009). The nature of the globular- to fibrous-actin transition. Nature 457, 441–445.

Ohi, M., Li, Y., Cheng, Y., and Walz, T. (2004). Negative Staining and Image Classification - Powerful Tools in Modern Electron Microscopy. Biological Procedures Online 6, 23–34.

Ohki, T., Ohno, C., Oyama, K., Mikhailenko, S.V., and Ishiwata, S. (2009). Purification of cytoplasmic actin by affinity chromatography using the C-terminal half of gelsolin. Biochemical and Biophysical Research Communications 383, 146–150.

Ohlsson, M., Tajsharghi, H., Darin, N., Kyllerman, M., and Oldfors, A. (2004). Follow-up of nemaline myopathy in two patients with novel mutations in the skeletal muscle alpha-actin gene (ACTA1). Neuromuscul Disord 14, 471–475.

Onishi, H., Mikhailenko, S.V., and Morales, M.F. (2006). Toward understanding actin activation of myosin ATPase: the role of myosin surface loops. Proc. Natl. Acad. Sci. U.S.a. 103, 6136–6141.

Orlova, A., and Egelman, E.H. (1995). Structural dynamics of F-actin: I. Changes in the C terminus. J. Mol. Biol. 245, 582–597.

Orzechowski, M., Moore, J.R., Fischer, S., and Lehman, W. (2014a). Tropomyosin movement on F-actin during muscle activation explained by energy landscapes. Archives of Biochemistry and Biophysics 545C, 63–68.

Orzechowski, M., Li, X.E., Fischer, S., and Lehman, W. (2014b). An atomic model of the tropomyosin cable on F-actin. Biophys. J. 107, 694–699.

Otterbein, L.R., Graceffa, P., and Dominguez, R. (2001). The crystal structure of uncomplexed actin in the ADP state. Science 293, 708–711.

Oztug Durer, Z.A., Diraviyam, K., Sept, D., Kudryashov, D.S., and Reisler, E. (2010). F-actin structure destabilization and DNase I binding loop: fluctuations mutational cross-linking and electron microscopy analysis of loop states and effects on F-actin. J. Mol. Biol. 395, 544–557.

Pardee, J.D., and Spudich, J.A. (1982). Purification of muscle actin. Methods in Enzymology 85 Pt B, 164–181.

Penczek, P.A. (2010a). Image restoration in cryo-electron microscopy. Methods in Enzymology 482, 35–72.

Penczek, P.A. (2010b). Fundamentals of three-dimensional reconstruction from projections. Methods in Enzymology 482, 1–33.

Penczek, P.A. (2010c). Resolution measures in molecular electron microscopy. Methods in Enzymology 482, 73–100.

Penczek, P.A., Kimmel, M., and Spahn, C.M. (2011). Identifying conformational states of macromolecules by eigen-analysis of resampled cryo-EM images. Structure 19, 1582–1590.

Penczek, P.A., Fang, J., Li, X., Cheng, Y., Loerke, J., and Spahn, C.M.T. (2014). CTER-rapid estimation of CTF parameters with error assessment. Ultramicroscopy 140, 9–19.

Perrot, A., Schmidt-Traub, H., Hoffmann, B., Prager, M., Bit-Avragim, N., Rudenko, R.I., Usupbaeva, D.A., Kabaeva, Z., Imanov, B., Mirrakhimov, M.M., et al. (2005). Prevalence of cardiac beta-myosin heavy chain gene mutations in patients with hypertrophic cardiomyopathy. J. Mol. Med. 83, 468–477.

Pettersen, E.F., Goddard, T.D., Huang, C.C., Couch, G.S., Greenblatt, D.M., Meng, E.C., and Ferrin, T.E. (2004). UCSF Chimera--a visualization system for exploratory research and analysis. J Comput Chem 25, 1605–1612.

Phillips, G.N. (1986). Construction of an atomic model for tropomyosin and implications for interactions with actin. J. Mol. Biol. 192, 128–131.

Pintilie, G.D., Zhang, J., Goddard, T.D., Chiu, W., and Gossard, D.C. (2010). Quantitative analysis of cryo-EM density map segmentation by watershed and scale-space filtering, and fitting of structures by alignment to regions. Journal of Structural Biology 170, 427–438.

Pittenger, M.F., Kazzaz, J.A., and Helfman, D.M. (1994). Functional properties of non-muscle tropomyosin isoforms. Curr. Opin. Cell Biol. 6, 96–104.

Pollard, T.D. (1986). Rate constants for the reactions of ATP- and ADP-actin with the ends of actin filaments. J. Cell Biol. 103, 2747–2754.

Poole, K.J.V., Lorenz, M., Evans, G., Rosenbaum, G., Pirani, A., Craig, R., Tobacman, L.S., Lehman, W., and Holmes, K.C. (2006). A comparison of muscle thin filament models obtained from electron microscopy reconstructions and low-angle X-ray fibre diagrams from non-overlap muscle. Journal of Structural Biology 155, 273–284.

Porter, K.R., Claude, A., and Fullam, E.F. (1945). A study of tissue culture cells by electron microscopy methods and preliminary observations. J. Exp. Med. 81, 233–246.

Preller, M., and Manstein, D.J. (2013). Myosin structure, allostery, and mechano-chemistry. Structure 21, 1911–1922.

Radon, J. (1917). Über die Bestimmung von Funktionen durch ihre Integralwerte längs gewisser Mannigfaltigkeiten. Berichte Über Die Verhandlungen Der Königlich-Sächsischen Gesellschaft Der Wissenschaften Zu Leipzig 69, 262–277.

Ramachandran, G.N., Ramakrishnan, C., and Sasisekharan, V. (1963). Stereochemistry of polypeptide chain configurations. J. Mol. Biol. 7, 95–99.

Rao, J.N., Rivera-Santiago, R., Li, X.E., Lehman, W., and Dominguez, R. (2012). Structural analysis of smooth muscle tropomyosin α and β isoforms. J. Biol. Chem. 287, 3165–3174.

Rayment, I., Holden, H.M., Whittaker, M., Yohn, C.B., Lorenz, M., Holmes, K.C., and Milligan, R.A. (1993a). Structure of the actin-myosin complex and its implications for muscle contraction. Science 261, 58–65.

Rayment, I., Rypniewski, W.R., Schmidt-Bäse, K., Smith, R., Tomchick, D.R., Benning, M.M., Winkelmann, D.A., Wesenberg, G., and Holden, H.M. (1993b). Three-dimensional structure of myosin subfragment-1: a molecular motor. Science 261, 50–58.

Reimer, L., and Kohl, H. (2008). Transmission Electron Microscopy (New York: Springer).

Reimer, L. (2013). Transmission Electron Microscopy (Berlin, Heidelberg: Springer).

Resetar, A.M., Stephens, J.M., and Chalovich, J.M. (2002). Troponin-tropomyosin: an allosteric switch or a steric blocker? Biophys. J. 83, 1039–1049.

Rhodes, G. (2010). Crystallography Made Crystal Clear (Academic Press).

Richard, P., Charron, P., Carrier, L., Ledeuil, C., Cheav, T., Pichereau, C., Benaiche, A., Isnard, R., Dubourg, O., Burban, M., et al. (2003). Hypertrophic cardiomyopathy: distribution of disease genes, spectrum of mutations, and implications for a molecular diagnosis strategy. Circulation 107, 2227–2232.

Richards, T.A., and Cavalier-Smith, T. (2005). Myosin domain evolution and the primary divergence of eukaryotes. Nature 436, 1113–1118.

Robenek, H., M, A., Gieseler, R., Breiter-Hahn, J., Knebel, W., Eins, S., Reichelt, R., Engelhardt, J., Stiller, K.J., Gerlach, D., et al. (1995). Mikroskopie in Forschung und Praxis (Darmstadt: GIT Verlag GmbH).

Robinson, A.L. (1986). Electron Microscope Inventors Share Nobel Physics Prize: Ernst Ruska built the first electron microscope in 1931; Gerd Binnig and Heinrich Rohrer developed the scanning tunneling microscope 50 years later. Science 234, 821–822.

Rohou, A., and Grigorieff, N. (2014). Frealix: model-based refinement of helical filament structures from electron micrographs. Journal of Structural Biology.

Rohou, A., and Grigorieff, N. (2015). CTFFIND4: Fast and accurate defocus estimation from electron micrographs. Journal of Structural Biology 192, 216–221.

Rubinstein, J.L., and Brubaker, M.A. (2015). Alignment of cryo-EM movies of individual particles by optimization of image translations. Journal of Structural Biology 192, 188–195.

Ruska, E. (1987a). Das Entstehen des Elektronenmikroskops und der Elektronenmikroskopie (Nobel-Vortrag). Angewandte Chemie 99, 611–621.

Ruska, E. (1987b). The development of the electron microscope and of electron microscopy. Reviews of Modern Physics 59, 627–638.

Ruskin, R.S., Yu, Z., and Grigorieff, N. (2013). Quantitative characterization of electron detectors for transmission electron microscopy. Journal of Structural Biology 184, 385–393.

Rynkiewicz, M.J., Schott, V., Orzechowski, M., Lehman, W., and Fischer, S. (2015). Electrostatic interaction map reveals a new binding position for tropomyosin on F-actin. J. Muscle Res. Cell. Motil. 36, 525–533.

Sablin, E. (2001). Nucleotide switches in molecular motors: structural analysis of kinesins and myosins. Current Opinion in Structural Biology 11, 716–724.

Sali, A., and Blundell, T.L. (1993). Comparative protein modelling by satisfaction of spatial restraints. J. Mol. Biol. 234, 779–815.

Sasaki, N., Asukagawa, H., Yasuda, R., Hiratsuka, T., and Sutoh, K. (1999). Deletion of the myopathy loop of Dictyostelium myosin II and its impact on motor functions. J. Biol. Chem. 274, 37840–37844.

Sasaki, N., Ohkura, R., and Sutoh, K. (2000). Insertion or deletion of a single residue in the strut sequence of Dictyostelium myosin II abolishes strong binding to actin. J. Biol. Chem. 275, 38705–38709.

Scheres, S.H.W. (2010). Classification of structural heterogeneity by maximum-likelihood methods. Methods in Enzymology 482, 295–320.

Scheres, S.H.W. (2012). RELION: implementation of a Bayesian approach to cryo-EM structure determination. Journal of Structural Biology 180, 519–530.

Scheres, S.H.W., and Chen, S. (2012). Prevention of overfitting in cryo-EM structure determination. Nature Methods 9, 853–854.

Scheres, S.H.W., Núñez-Ramírez, R., Sorzano, C.O.S., Carazo, J.M., and Marabini, R. (2008). Image processing for electron microscopy single-particle analysis using XMIPP. Nature Protocols 3, 977–990.

Scheres, S.H.W., Valle, M., and Carazo, J.M. (2005). Fast maximum-likelihood refinement of electron microscopy images. Bioinformatics 21 Suppl 2, ii243–ii244.

Scheres, S.H.W., Valle, M., Grob, P., Nogales, E., and Carazo, J.M. (2009). Maximum likelihood refinement of electron microscopy data with normalization errors. Journal of Structural Biology 166, 234–240.

Scheres, S.H. (2014). Beam-induced motion correction for sub-megadalton cryo-EM particles. Elife 3, e03665.

Schmidt, W.M., Lehman, W., and Moore, J.R. (2015). Direct observation of tropomyosin binding to actin filaments. Cytoskeleton (Hoboken) n/a–n/a.

Schroer, M.A., Paulus, M., Jeworrek, C., Krywka, C., Schmacke, S., Zhai, Y., Wieland, D.C.F., Sahle, C.J., Chimenti, M., Royer, C.A., et al. (2010). High-pressure SAXS study of folded and unfolded ensembles of proteins. Biophys. J. 99, 3430–3437.

Schröder, R.R., Manstein, D.J., Jahn, W., Holden, H., Rayment, I., Holmes, K.C., and Spudich, J.A. (1993). Three-dimensional atomic model of F-actin decorated with Dictyostelium myosin S1. Nature 364, 171–174.

Schröder, R.R. (2015). Advances in electron microscopy: A qualitative view of instrumentation development for macromolecular imaging and tomography. Archives of Biochemistry and Biophysics 581, 25–38.

Schur, F.K.M., Hagen, W.J.H., Rumlová, M., Ruml, T., Müller, B., Kräusslich, H.-G., and Briggs, J.A.G. (2015). Structure of the immature HIV-1 capsid in intact virus particles at 8.8 Å resolution. Nature 517, 505–508.

Schutt, C.E., Myslik, J.C., Rozycki, M.D., Goonesekere, N.C., and Lindberg, U. (1993). The structure of crystalline profilin-beta-actin. Nature 365, 810–816.

Seraydarian, K., Briskey, E.J., and Mommaerts, W.F. (1967). The modification of actomyosin by alpha- actinin. I. A survey of experimental conditions. Biochimica Et Biophysica Acta 133, 399–411.

Shaikh, T.R., Gao, H., Baxter, W.T., Asturias, F.J., Boisset, N., Leith, A., and Frank, J. (2008). SPIDER image processing for single-particle reconstruction of biological macromolecules from electron micrographs. Nature Protocols 3, 1941–1974.

Shi, D., Nannenga, B.L., Iadanza, M.G., and Gonen, T. (2013). Three-dimensional electron crystallography of protein microcrystals. Elife 2, e01345.

Shi, D., Nannenga, B.L., la Cruz, de, M.J., Liu, J., Sawtelle, S., Calero, G., Reyes, F.E., Hattne, J., and Gonen, T. (2016). The collection of MicroED data for macromolecular crystallography. Nature Protocols 11, 895–904.

Sievers, F., Wilm, A., Dineen, D., Gibson, T.J., Karplus, K., Li, W., Lopez, R., McWilliam, H., Remmert, M., Söding, J., et al. (2011). Fast, scalable generation of high-quality protein multiple sequence alignments using Clustal Omega. Mol. Syst. Biol. 7, 539–539.

Sigworth, F.J. (1998). A maximum-likelihood approach to single-particle image refinement. Journal of Structural Biology 122, 328–339.

Sigworth, F.J., Doerschuk, P.C., Carazo, J.M., and Scheres, S.H.W. (2010). An introduction to maximum-likelihood methods in cryo-EM. Methods in Enzymology 482, 263–294.

Smith, C.A., and Rayment, I. (1996). Active site comparisons highlight structural similarities between myosin and other P-loop proteins. Biophys. J. 70, 1590–1602.

Sousa, D.R., Stagg, S.M., and Stroupe, M.E. (2013). Cryo-EM structures of the actin:tropomyosin filament reveal the mechanism for the transition from C- to M-state. J. Mol. Biol. 425, 4544–4555.

Sparrow, J.C., Nowak, K.J., Durling, H.J., Beggs, A.H., Wallgren-Pettersson, C., Romero, N., Nonaka, I., and Laing, N.G. (2003). Muscle disease caused by mutations in the skeletal muscle alpha-actin gene (ACTA1). Neuromuscul Disord 13, 519–531.

Spudich, J.A. (2014). Hypertrophic and dilated cardiomyopathy: four decades of basic research on muscle lead to potential therapeutic approaches to these devastating genetic diseases. Biophys. J. 106, 1236–1249.

Squire, J.M. (1997). Architecture and function in the muscle sarcomere. Current Opinion in Structural Biology 7, 247–257.

Stenson, P.D., Mort, M., Ball, E.V., Shaw, K., Phillips, A., and Cooper, D.N. (2014). The Human Gene Mutation Database: building a comprehensive mutation repository for clinical and molecular genetics, diagnostic testing and personalized genomic medicine. Hum. Genet. 133, 1–9.

Stenzel, W., Prokop, S., Kress, W., Huppmann, S., Loui, A., Sarioglu, N.M.E., Laing, N.G., Sparrow, J.C., Heppner, F.L., and Goebel, H.H. (2010). Fetal akinesia caused by a novel actin filament aggregate myopathy skeletal muscle actin gene (ACTA1) mutation. Neuromuscul Disord 20, 531–533.

Steyernagel, R. (2013). Bewegungsunschärfe - Stadtmarathon in Leibzig. download on 27.07.2016 and personal communication on 18.08.2016, http://www.fotoclub-berggut.de/wp-content/uploads/2013/05/Rolf_Steyernagel _unscharf_009.jpg.

Strzelecka-Gołaszewska, H., Mossakowska, M., Woźniak, A., Moraczewska, J., and Nakayama, H. (1995). Long-range conformational effects of proteolytic removal of the last three residues of actin. The Biochemical Journal 307 (Pt 2), 527–534.

Subramaniam, S., Kühlbrandt, W., and Henderson, R. (2016). CryoEM at IUCrJ: a new era. IUCrJ 3, 3–7.

Sudo, A., Hayashi, Y., Sano, H., Kawamura, N., Nishino, I., and Nonaka, I. (2013). [Sibling cases of severe infantile form of nemaline myopathy with ACTA1-gene mutation]. No to Hattatsu 45, 452–456.

Sun, Y.B., Lou, F., and Irving, M. (2009). Calcium- and myosin-dependent changes in troponin structure during activation of heart muscle. The Journal of Physiology 587, 155–163.

Sutoh, K., Ando, M., and Toyoshima, Y.Y. (1991). Site-directed mutations of Dictyostelium actin: disruption of a negative charge cluster at the N terminus. Proc. Natl. Acad. Sci. U.S.a. 88, 7711–7714.

Sweeney, H.L., and Houdusse, A. (2004). The motor mechanism of myosin V: insights for muscle contraction. Philosophical Transactions of the Royal Society of London. Series B, Biological Sciences 359, 1829–1841.

Sweeney, H.L., and Houdusse, A. (2010a). Structural and functional insights into the Myosin motor mechanism. Annual Review of Biophysics 39, 539–557.

Sweeney, H.L., and Houdusse, A. (2010b). Myosin VI rewrites the rules for myosin motors. Cell 141, 573–582.

Syamaladevi, D.P., Spudich, J.A., and Sowdhamini, R. (2012). Structural and functional insights on the Myosin superfamily. Bioinformatics and Biology Insights 6, 11–21.

Szent-Györgyi, A. (1948). Thermodynamic theory of the contraction of actomyosin. Biol. Bull. 95, 285.

Tan, Y.Z., Cheng, A., Potter, C.S., and Carragher, B. (2016). Automated data collection in single particle electron microscopy. Microscopy (Oxf) 65, 43–56.

Tang, G., Peng, L., Baldwin, P.R., Mann, D.S., Jiang, W., Rees, I., and Ludtke, S.J. (2007). EMAN2: an extensible image processing suite for electron microscopy. Journal of Structural Biology 157, 38–46.

Terwilliger, T.C. (2010a). Rapid chain tracing of polypeptide backbones in electron-density maps. Acta Crystallogr. D Biol. Crystallogr. 66, 285–294.

Terwilliger, T.C. (2010b). Rapid model building of alpha-helices in electron-density maps. Acta Crystallogr. D Biol. Crystallogr. 66, 268–275.

Terwilliger, T.C. (2010c). Rapid model building of beta-sheets in electron-density maps. Acta Crystallogr. D Biol. Crystallogr. 66, 276–284.

Thon, F. (1971). Phase contrast transfer function. Electron Microscopy in Material Sciences 571–625.

Tirion, M.M., ben-Avraham, D., Lorenz, M., and Holmes, K.C. (1995). Normal modes as refinement parameters for the F-actin model. Biophys. J. 68, 5–12.

Tobacman, L.S., and Adelstein, R.S. (1986). Mechanism of regulation of cardiac actin-myosin subfragment 1 by troponin-tropomyosin. Biochemistry 25, 798–802.

Toydemir, R.M., Rutherford, A., Whitby, F.G., Jorde, L.B., Carey, J.C., and Bamshad, M.J. (2006). Mutations in embryonic myosin heavy chain (MYH3) cause Freeman-Sheldon syndrome and Sheldon-Hall syndrome. Nat. Genet. 38, 561–565.

UniProt Consortium (2015). UniProt: a hub for protein information. Nucleic Acids Research 43, D204–D212.

Unwin, N. (2005). Refined structure of the nicotinic acetylcholine receptor at 4A resolution. J. Mol. Biol. 346, 967–989.

Urnavicius, L., Zhang, K., Diamant, A.G., Motz, C., Schlager, M.A., Yu, M., Patel, N.A., Robinson, C.V., and Carter, A.P. (2015). The structure of the dynactin complex and its interaction with dynein. Science 347, 1441–1446.

Uyeda, T.Q., Ruppel, K.M., and Spudich, J.A. (1994). Enzymatic activities correlate with chimaeric substitutions at the actin-binding face of myosin. Nature 368, 567–569.

Vagin, A.A., Steiner, R.A., Lebedev, A.A., Potterton, L., McNicholas, S., Long, F., and Murshudov, G.N. (2004). REFMAC5 dictionary: organization of prior chemical knowledge and guidelines for its use. Acta Crystallogr. D Biol. Crystallogr. 60, 2184–2195.

Vale, R.D., and Milligan, R.A. (2000). The way things move: looking under the hood of molecular motor proteins. Science 288, 88–95.

Van Dijk, J., Furch, M., Lafont, C., Manstein, D.J., and Chaussepied, P. (1999). Functional characterization of the secondary actin binding site of myosin II. Biochemistry 38, 15078–15085.

Van Dijk, J., Knight, A.E., Molloy, J.E., and Chaussepied, P. (2002). Characterization of three regulatory states of the striated muscle thin filament. J. Mol. Biol. 323, 475–489.

Van Driest, S.L., Jaeger, M.A., Ommen, S.R., Will, M.L., Gersh, B.J., Tajik, A.J., and Ackerman, M.J. (2004). Comprehensive analysis of the beta-myosin heavy chain gene in 389 unrelated patients with hypertrophic cardiomyopathy. J. Am. Coll. Cardiol. 44, 602–610.

van Heel, M., and Schatz, M. (2005). Fourier shell correlation threshold criteria. Journal of Structural Biology 151, 250–262.

van Heel, M., Harauz, G., Orlova, E.V., Schmidt, R., and Schatz, M. (1996). A new generation of the IMAGIC image processing system. Journal of Structural Biology 116, 17–24.

van Wijk, E., Krieger, E., Kemperman, M.H., De Leenheer, E.M.R., Huygen, P.L.M., Cremers, C.W.R.J., Cremers, F.P.M., and Kremer, H. (2003). A mutation in the gamma actin 1 (ACTG1) gene causes autosomal dominant hearing loss (DFNA20/26). J. Med. Genet. 40, 879–884.

Várkuti, B.H., Yang, Z., and Malnasi-Csizmadia, A. (2015). Structural model of weak binding actomyosin in the prepowerstroke state. J. Biol. Chem. 290, 1679–1688.

Várkuti, B.H., Yang, Z., Kintses, B., Erdélyi, P., Bárdos-Nagy, I., Kovács, A.L., Hári, P., Kellermayer, M., Vellai, T., and Malnasi-Csizmadia, A. (2012). A novel actin binding site of myosin required for effective muscle contraction. Nat. Struct. Mol. Biol. 19, 299–306.

Vibert, P.J., Haselgrove, J.C., Lowy, J., and Poulsen, F.R. (1972). Structural changes in actin-containing filaments of muscle. J. Mol. Biol. 71, 757–767.

Vicente-Manzanares, M., Ma, X., Adelstein, R.S., and Horwitz, A.R. (2009). Non-muscle myosin II takes centre stage in cell adhesion and migration. Nature Reviews. Molecular Cell Biology 10, 778–790.

Villard, E., Duboscq-Bidot, L., Charron, P., Benaiche, A., Conraads, V., Sylvius, N., and Komajda, M. (2005). Mutation screening in dilated cardiomyopathy: prominent role of the beta myosin heavy chain gene. Eur. Heart J. 26, 794–803.

Volkmann, N., Hanein, D., Ouyang, G., Trybus, K.M., DeRosier, D.J., and Lowey, S. (2000). Evidence for cleft closure in actomyosin upon ADP release. Nature Structural Biology 7, 1147–1155.

Volkmann, N., Liu, H., Hazelwood, L., Krementsova, E.B., Lowey, S., Trybus, K.M., and Hanein, D. (2005). The structural basis of myosin V processive movement as revealed by electron cryomicroscopy. Mol. Cell 19, 595–605.

von der Ecken, J. (2013). Kryoelektronenmikroskopische Struktur eines humanen Aktin-Tropomyosin-Myosin-Komplexes. Master Thesis, Max Planck Institute of Molecular Physiology.

von der Ecken, J., Heissler, S.M., Pathan-Chhatbar, S., Manstein, D.J., and Raunser, S. (2016). Cryo-EM structure of a human cytoplasmic actomyosin complex at near-atomic resolution. Nature 534, 724–728.

von der Ecken, J., Müller, M., Lehman, W., Manstein, D.J., Penczek, P.A., and Raunser, S. (2015). Structure of the F-actin-tropomyosin complex. Nature 519, 114–117.

Vorobiev, S., Strokopytov, B., Drubin, D.G., Frieden, C., Ono, S., Condeelis, J., Rubenstein, P.A., and Almo, S.C. (2003). The structure of nonvertebrate actin: implications for the ATP hydrolytic mechanism. Proc. Natl. Acad. Sci. U.S.a. 100, 5760–5765.

Walklate, J., Ujfalusi, Z., and Geeves, M.A. (2016). Myosin isoforms and the mechanochemical cross-bridge cycle. J. Exp. Biol. 219, 168–174.

Wang, L., and Sigworth, F.J. (2006). Cryo-EM and single particles. Physiology (Bethesda) 21, 13–18.

Wang, R.Y.-R., Kudryashev, M., Li, X., Egelman, E.H., Basler, M., Cheng, Y., Baker, D., and DiMaio, F. (2015). De novo protein structure determination from near-atomic-resolution cryo-EM maps. Nature Methods 12, 335–338.

Wang, Z., and Schröder, G.F. (2012). Real-space refinement with DireX: from global fitting to side-chain improvements. Biopolymers 97, 687–697.

Whitby, F.G., and Phillips, G.N. (2000). Crystal structure of tropomyosin at 7 Angstroms resolution. Proteins 38, 49–59.

Whittaker, M., Wilson-Kubalek, E.M., Smith, J.E., Faust, L., Milligan, R.A., and Sweeney, H.L. (1995). A 35-A movement of smooth muscle myosin on ADP release. Nature 378, 748–751.

Winn, M.D., Ballard, C.C., Cowtan, K.D., Dodson, E.J., Emsley, P., Evans, P.R., Keegan, R.M., Krissinel, E.B., Leslie, A.G.W., McCoy, A., et al. (2011). Overview of the CCP4 suite and current developments. Acta Crystallogr. D Biol. Crystallogr. 67, 235–242.

Wolff, G., Hagen, C., Grünewald, K., and Kaufmann, R. (2016). Towards correlative super-resolution fluorescence and electron cryo-microscopy. Biol. Cell.

Woo, A., Rakowski, H., Liew, J.C., Zhao, M.-S., Liew, C.-C., Parker, T.G., Zeller, M., Wigle, E.D., and Sole, M.J. (2003). Mutations of the beta myosin heavy chain gene in hypertrophic cardiomyopathy: critical functional sites determine prognosis. Heart 89, 1179–1185.

Woodrum, D.T., Rich, S.A., and Pollard, T.D. (1975). Evidence for biased bidirectional polymerization of actin filaments using heavy meromyosin prepared by an improved method. J. Cell Biol. 67, 231–237.

Wu, B., Peisley, A., Tetrault, D., Li, Z., Egelman, E.H., Magor, K.E., Walz, T., Penczek, P.A., and Hur, S. (2014). Molecular imprinting as a signal-activation mechanism of the viral RNA sensor RIG-I. Mol. Cell 55, 511–523.

Wulf, S.F., Ropars, V., Fujita-Becker, S., Oster, M., Hofhaus, G., Trabuco, L.G., Pylypenko, O., Sweeney, H.L., Houdusse, A.M., and Schröder, R.R. (2016). Force-producing ADP state of myosin bound to actin. Proc. Natl. Acad. Sci. U.S.a. 113, E1844–E1852.

Wüthrich, K. (2001). The way to NMR structures of proteins. Nature Structural Biology 8, 923–925.

Yang, S., Barbu-Tudoran, L., Orzechowski, M., Craig, R., Trinick, J., White, H., and Lehman, W. (2014). Three-dimensional organization of troponin on cardiac muscle thin filaments in the relaxed state. Biophys. J. 106, 855–864.

Yang, Z., Fang, J., Chittuluru, J., Asturias, F.J., and Penczek, P.A. (2012). Iterative stable alignment and clustering of 2D transmission electron microscope images. Structure 20, 237–247.

Yao, X., Grade, S., Wriggers, W., and Rubenstein, P.A. (1999). His(73), often methylated, is an important structural determinant for actin. A mutagenic analysis of HIS(73) of yeast actin. J. Biol. Chem. 274, 37443–37449.

Yengo, C.M., and Sweeney, H.L. (2004). Functional role of loop 2 in myosin V. Biochemistry 43, 2605–2612.

Yildiz, A., Forkey, J.N., McKinney, S.A., Ha, T., Goldman, Y.E., and Selvin, P.R. (2003). Myosin V walks hand-over-hand: single fluorophore imaging with 1.5-nm localization. Science 300, 2061–2065.

Yin, Z., Zheng, Y., Doerschuk, P.C., Natarajan, P., and Johnson, J.E. (2003). A statistical approach to computer processing of cryo-electron microscope images: virion classification and 3-D reconstruction. Journal of Structural Biology 144, 24–50.

Yu, B., Sawyer, N.A., Caramins, M., Yuan, Z.G., Saunderson, R.B., Pamphlett, R., Richmond, D.R., Jeremy, R.W., and Trent, R.J. (2005). Denaturing high performance liquid chromatography: high throughput mutation screening in familial hypertrophic cardiomyopathy and SNP genotyping in motor neurone disease. J. Clin. Pathol. 58, 479–485.

Zhang, X., Settembre, E., Xu, C., Dormitzer, P.R., Bellamy, R., Harrison, S.C., and Grigorieff, N. (2008). Near-atomic resolution using electron cryomicroscopy and single-particle reconstruction. Proc. Natl. Acad. Sci. U.S.a. 105, 1867–1872.

Zhang, X., Jin, L., Fang, Q., Hui, W.H., and Zhou, Z.H. (2010). 3.3 A cryo-EM structure of a nonenveloped virus reveals a priming mechanism for cell entry. Cell 141, 472–482.

Zheng, W., Hitchcock-DeGregori, S.E., and Barua, B. (2016). Investigating the effects of tropomyosin mutations on its flexibility and interactions with filamentous actin using molecular dynamics simulation. J. Muscle Res. Cell. Motil. 1–17.

Zhou, Z.H. (2011). Atomic resolution cryo electron microscopy of macromolecular complexes. Adv Protein Chem Struct Biol 82, 1–35.

Zhou, Z.H., and Chiu, W. (2003). Determination of icosahedral virus structures by electron cryomicroscopy at subnanometer resolution. Adv. Protein Chem. 64, 93–124.

Zhu, H., and Zhu, P. (2015). No longer “blob-ology”: Cryo-EM is getting into molecular details. Sci China Life Sci 58, 1154–1156.

6 Appendix

Both sections of the appendix give tables and figures belonging to section 4.3 (Structure of a skeletal F-actin-tropomyosin complex) at first and afterwards tables and figures belonging to section 4.4 (Structure of a human cytoplasmic actomyosin complex).

6.1 Tables

Structure of a skeletal F-actin-tropomyosin complex

Chain A	A	B	C	D	E	Function	Mutations*
Arg37	Asp80, Asp81					D-Loop stabilization	
Arg39		Asp286		Glu270		F-Actin/D-Loop stabilization	D286G[1-3]; E270Q[4]
Asp51	Arg37, Lys84					D-Loop stabilization	
Tyr53	Lys61	Glu167				F-Actin/D-Loop stabilization	
Arg62		Asp288				F-Actin/D-Loop stabilization	D288N[4]
Tyr69	Arg183					D-Loop stabilization	
His173			Same as chain B with A	Ile267, Gly268	Same as chain D with A	F-Actin stabilization	G268R[1,2,5], G268D[6], G268C[2,3,6,7], G268S[8]
Glu195				Lys113		F-Actin stabilization	K113E[4]; E195D†[9]
Asp244		Arg290				F-Actin stabilization	
Gly42-Gly48		SD3				F-Actin/D-Loop stabilization	oxidized M44, M47V[10];
Pro38-Lys50		Tyr169					M44T, G46D, G46C, M47V[4]

* Mutations connected to nemaline myopathies if not labeled differently

† Mutation connected to neuromuscular disorders

Table A6.1: Filament stability of inter- and intrastand interactions.

Table of identified residues that are involved in intra- and intermolecular interactions and known mutations. Mutation data are from references: [1]Bathe et al., 20070; [2]Costa et al., 2004; [3]Nowak et al., 1999; [4]Laing et al., 2009; [5]Sparrow et al., 2003; [6]Ohlsson et al., 2004; [7]Ilkovski et al., 2004; [8]Graziano et al., 2004; [9]Nair et al., 2008; [10]Hung et al., 2011.

Chain A	A	Function	Mutations*
Tyr69	Arg183	Cleft stabilization	R183C[1-3]; R183G[1,4], R183L[5]; R183S[6]
His73	Asp179	Cleft stabilization	H73N[5]; H73L, H73R, D179N, D179H[6]; H73R[7]; D179G[8]
Asp157	Arg183	Cleft stabilization	R183C[1-3]; R183G[1,4], R183L[5]; R183S[6]
Asp187	Arg206	Cleft stabilization	
Asp207	Arg210	Cleft stabilization	E207D[9]
Asp211	Arg210	Cleft stabilization	
Lys213	Tyr306	Cleft stabilization	
Tyr337	Lys18, Lys336	Cleft stabilization	K336E†[10]; K336I[6]
Ser14, Gly15	ADP	ADP binding	G15R‡[1,2,11], G15D§[12]
Lys18	ADP	ADP binding	
Gln137	ADP	ADP binding	Q137H[13]
Gly156, Asp157	ADP	ADP binding	
Arg210	ADP	ADP binding	
Glu214	ADP	ADP binding	
Gly302	ADP	ADP binding	
Gln137	Ion	Ion coordination	Q137H[13]
Asp154	Ion	Ion coordination	
Gly156	Ion	Ion coordination	

* Mutations connected to nemaline myopathies if not labeled differently

† Mutation connected to nemaline myopathies and hypertrophic cardiomyopathies

‡ Mutation connected to actin myopathies

§ Mutation connected to fetal akinesia

Table A6.2: Intramolecular interactions.

Table of identified intramolecular interactions that result in a stabilization of the nucleotide binding cleft, coordination of ADP and a divalent cation. Mutation data are from references: [1]Costa et al., 2004; [2]Nowak et al., 1999; [3]Sudo et al., 2013; [4]Ilkovski et al., 2004; [5]Laing et al., 2009; [6]Sparrow et al., 2003; [7]Yao et al., 1999; [8]Agrawal et al., 2004; [9]Graziano et al., 2004; [10]D'Amico et al., 2006; [11]Bathe et al., 2007; [12]Stenzel et al., 2010; [13]Koy et al., 2007.

Actin	Mutations*
Arg147	R147K[1]
Lys215	
Lys291	
Asp311	
Lys326	K326N[1,2]
Lys328	

* Mutations connected to nemaline myopathies if not labeled differently

Table A6.3: Tropomyosin binding to F-actin in A-state.

Table showing putative residues of F-actin involved in tropomyosin binding and known mutations. Mutation data are from references [1]Laing et al., 2009 and [2]Jain et al., 2012.

Data collection			
	Magnification	x122,270	
	Defocus range (μm)	0.8-2.6	
	Voltage (kV)	300	
	Microscope	Titan Krios (Cs corrected)	
	Camera	Falcon 2 (4k DED)	
	Frame recording time (s)	0.085-0.475	
	Number of frames	7	
	Electron dose (e^{-}Å^{2})	15.4	
	Pixel size (Å)	1.12	
Particle statistics			
	Filaments*	7,854 (5,239)	
	Box size (px)	256	
	Boxing distance (px)	29	
	Rise (Å)	27.5	
	Azimuthal rotation (°)	166.4	
	Segments*	109,242 (74,228)	
	Asymmetric subunits*	~180,000 (~120,000)	
			
Model composition	**Chain ID**	**ABCDE**	**A**
	Non-hydrogen atoms	14,450	2,890
	Protein residues	1,835	367
	Ligand (ADP, Mg^{2+})	140	28
Refinement			
	Resolution used for refinement (Å)	95.2-3.7	
	Map sharpening *b* factor (Å^{2})	-50	
	Average B-factor (Å^{2})	55.40	53.40
	R factor†	0.277	
	Cross-Resolution function (FCR)‡	0.81	0.83
Rms deviations			
	Bonds (Å)	0.004	0.005
	Angles (°)	1.10	1.12
Validation			
	Clashscore, all atoms	19.99	18.32
	Poor rotamers (%)	1.23	1.29
Ramachandran plot			
	Favored (%)	87.20	87.40
	Outliers (%)	1.37	1.37

* Number in parentheses is count after sorting the dataset regarding micrograph quality

† R factor = $\Sigma|F_{obs}|-|F_{calc}| / \Sigma|F_{obs}|$, where F_{obs} describes the structure factors for all measured reflections and F_{calc} corresponds to the calculated structure factors from the final model

‡ FCR = $\Sigma(N_{shell} FSC_{shell}) / \Sigma N_{shell}$, with N_{shell} as number of structure factors in given shell and $FSC_{shell} = \Sigma(F_{calc} F_{EM}) / \sqrt{(\Sigma|F_{calc}|^2 \Sigma|F_{EM}|^2)}$, where F_{EM} describes the structure factors for the final cryo-EM density map

Table A6.4: Data collection and refinement statistics.

Refinement statistics are shown after the last step of the refinement of the F-actin pentamer. In addition, relevant values of the central chain A are shown. Rms, root mean square.

Structure of a human cytoplasmic actomyosin complex

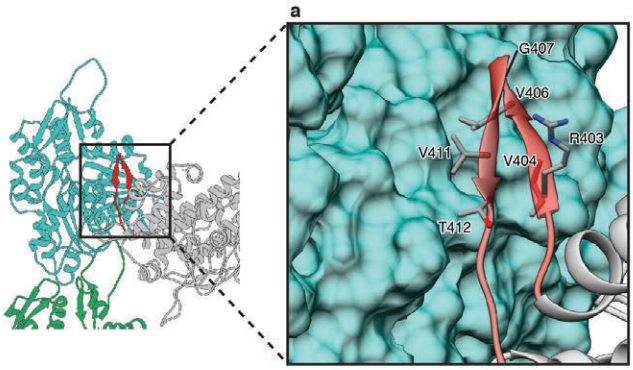

b

Cardiomyopathy loop mutations in β-cardiac myosin (MYH7)

CM-loop	Function	Mutation*
R403 (419)	Bridge with Y410	R403L[1,2], R403Q[2-12], R403W[1-3,13-16]
V404 (420)	F-actin interface	V404L[8], V404M[9]
V406 (422)	F-actin interface	V406M[17]
G407 (423)	F-actin interface	G407V[9]
V411 (427)	F-actin interface	V411I[3,8,14]
T412 (428)	F-actin interface	T412N†[18]

* Mutations connected to hypertrophic cardiomyopathies (HCM) if not labeled differently
† Mutation connected to dilated cardiomyopathy (DCM)

c

Mutations in human myosin isoforms at/near ATM interface

Mutation	Protein	Region	Function	Disease
G640S (659)	MYH1	Loop 2	F-actin interface	Myeloid leukaemia[19]
E375K (388)	MYH3	Loop 4	Inner loop	Freeman-Sheldon/Hall syndrome[20]
S532P (552)	MYH7	Helix-loop-helix	F-actin interface	Dilated cardiomyopathy (DCM)[21]
A550V (570)	MYH7	Helix-loop-helix	F-actin interface	Dilated cardiomyopathy (DCM)[18]
G571R (590)	MYH7	Loop 3	Inner loop	Hypertrophic cardiomyopathy (HCM)[10]
H576R (593)	MYH7	Loop 3	Inner loop	Hypertrophic cardiomyopathy (HCM)[13]
S642L (665)	MYH7	Loop 2 base	F-actin interface	Dilated cardiomyopathy (DCM)[22]
A636V (658)	MYH8	Loop 2	F-actin interface	natural variant[23]

Table A6.5: Cardiomyopathy loop and disease-causing mutations.

a, **b**, Mutations in β-cardiac myosin (MYH7) can lead to cardiomyopathies. Corresponding residues in β-cardiac myosin are illustrated with our rigor state model (**a**) and known mutations are listed (**b**) [1]Dausse et al., 1993; [2]Richard et al., 2003; [3]Yu et al., 2005; [4]Epstein et al., 1992; [5]Geisterfer-Lowrance et al., 1990; [6]Blanchard et al., 1999; [7]Cuda et al., 1993; [8]Woo et al., 2003; [9]Van Driest et al., 2004; [10]Mohiddin et al., 2003; [11]Marian et al., 1999; [12]Lankford et al., 1995; [13]Perrot et al., 2005; [14]Erdmann et al., 2003; [15]Moolman et al., 1993; [16]Moolman-Smook et al., 1999; [17]Greber-Platzer et al., 2001; [18]Villard et al., 2005. c, Table of known disease-causing mutations at the actomyosin interface. Numbers in parentheses give respective residue position in our published structure of NM-2C. Localization is described in parentheses. Mutation data are from references: [19]Ley et al., 2008; [20]Toydemir et al., 2006; [21]Kamisago et al., 2000; [22]Daehmlow et al., 2002; [23]UniProt Consortium, 2015.

Data collection			
	Magnification	x122,270	
	Defocus range (μm)	0.7-2.8	0.8-2.6
	Voltage (kV)	300	
	Microscope	Titan Krios	
	Camera	Falcon 2	
	Frame recording time (s)	0.085-0.475	
	Number of frames	7	
	Electron dose ($e^-/Å^2$)	16	
	Pixel size (Å)	1.1	
Particle statistics			
	Box size (px)	256	
	Boxing distance (px)	29	
	Rise* (Å)	27.5	
	Azimuthal rotation* (°)	166.9	
	Particles	118,000	91,000

Model composition		**F-actin-myosin**	**Bare F-actin**
	Non-hydrogen atoms	26,477	14,450
	Protein residues	3,354	1,845
	Ligand (ADP/Mg^{2+})	135/5	135/5
Refinement			
	Resolution (Å)	3.9	3.6
	Map sharpening *b* factor ($Å^2$)	-200	-200
	Average B-factor ($Å^2$)	180	98
	R factor	0.34	0.33
	Fourier Shell Correlation	0.84	0.83
Rms deviations			
	Bonds (Å)	0.015	0.013
	Angles (°)	1.83	1.74
Validation			
	Molprobity score	2.24	1.82
	Clashscore, all atoms	14.16	8.93
	Poor rotamers (%)	1.57	1.36
Ramachandran plot			
	Favored (%)	93.23	96.38
	Allowed (%)	5.14	3.07
	Outliers (%)	1.63	0.55

*Helical symmetry parameters were estimated after C1 refinement (see Methods for further details)

Table A6.6: Data collection and refinement statistics.

Refinement statistics are given after the last step of refinements of the actomyosin and bare F-actin data set. Rms, root mean square.

6.2 Figures

Structure of a skeletal F-actin-tropomyosin complex

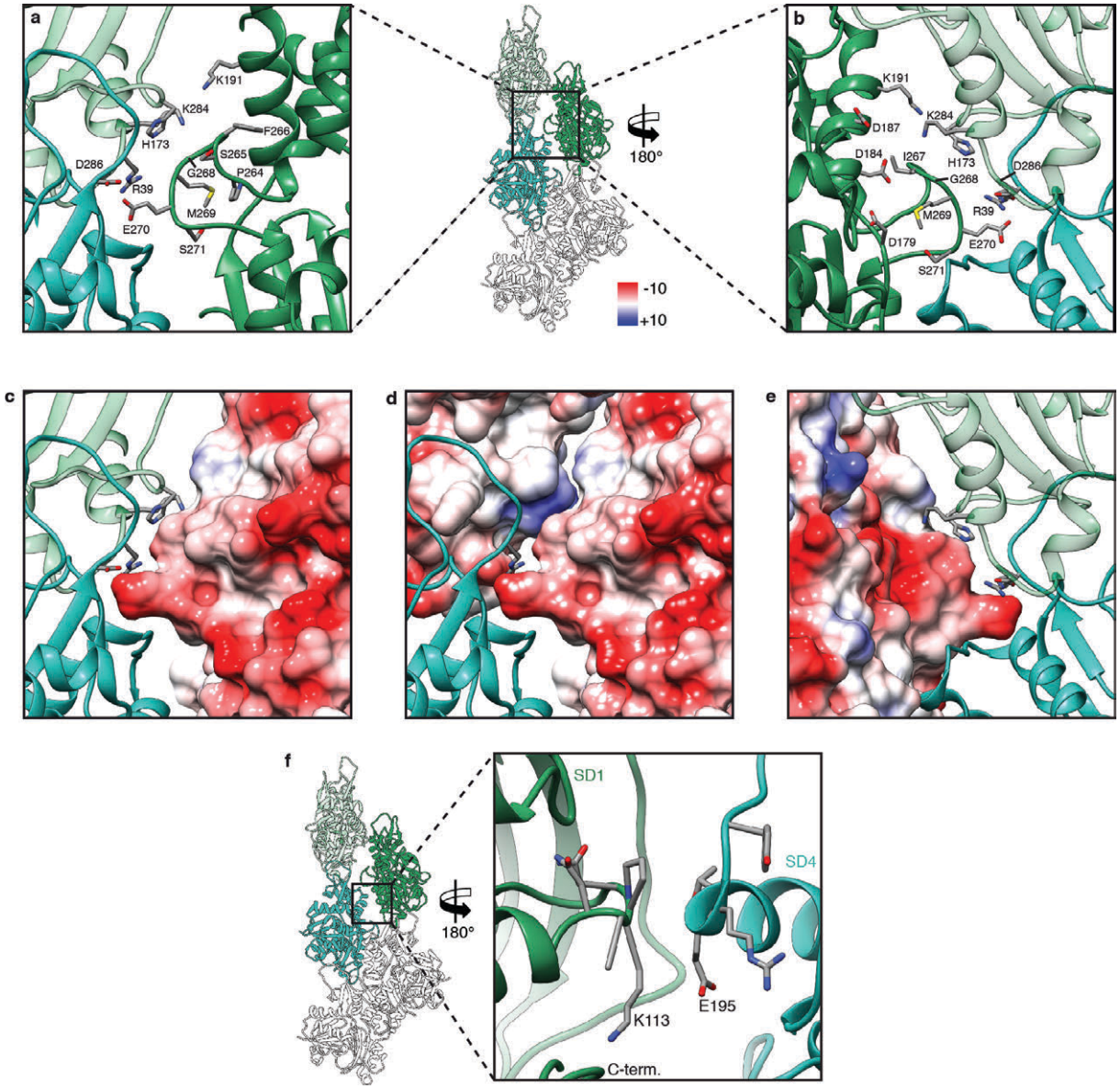

Figure A6.1: Inter- and intrastrand F-actin interactions.

a–**e**, The interface at the plug involves three residues (R39, E270, D286) that form salt bridges and mediate not only one interstrand contact but also one intrastrand contact. In addition, the orientation of residues 264–269 result in a negatively charged patch that electrostatically interacts with positively charged residues on the opposing actin. **a**, **b**, Front and back view of the interface at the plug, respectively. **c**–**e**, Surface representations (front views in **c** and **d**, back view in **e**) depicting the Coulomb potential (ranging from 210 kcal mol^{-1} (red) to 110 kcal mol^{-1} (blue) at pH 7.5), indicating that the interaction of the upper region of the plug with adjacent inter- or intrastrand molecules is mediated by electrostatic interactions. **f**, Another interstrand contact is formed by residues 110–115 of SD1 and residues 191–199 of SD4 of the adjacent actin. However, no prominent electrostatic or hydrophobic interactions could be identified at this interface.

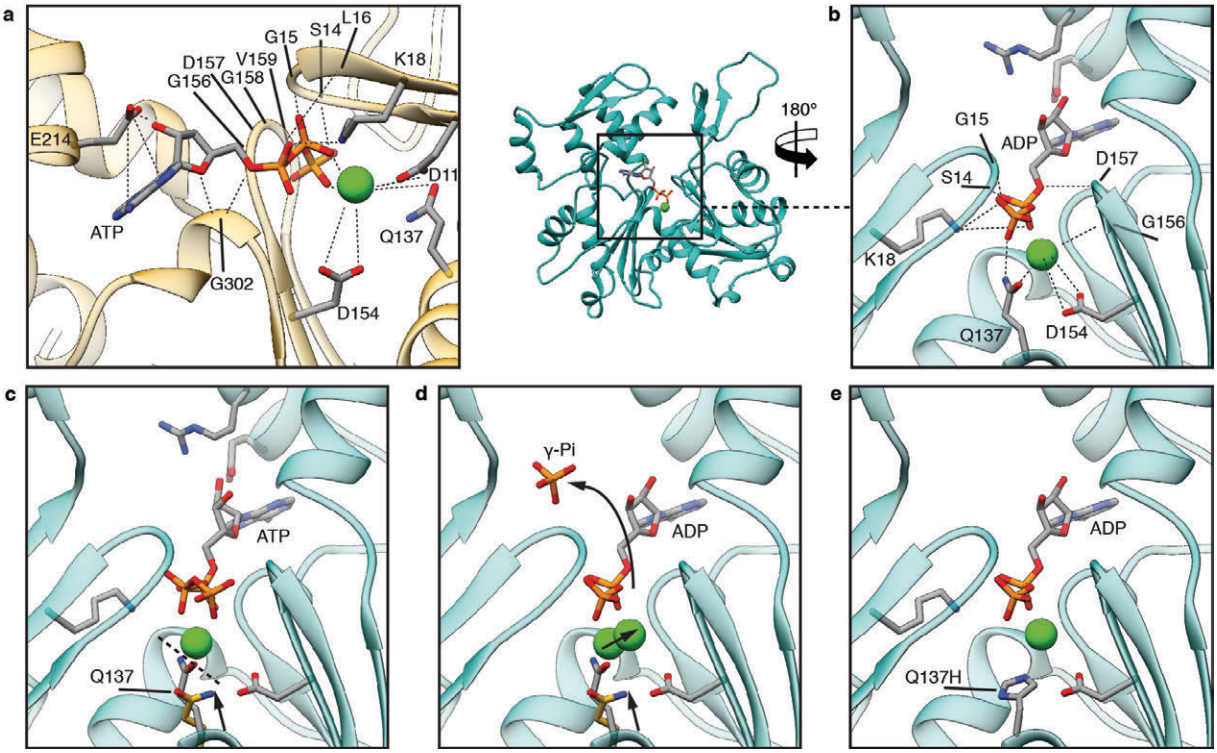

Figure A6.2: Nucleotide binding site.

a, Coordination of ADP and Ca^{2+} in the nucleotide binding cleft in G-actin (PDB accession code 3EL2). **b**–**c**, Back views of the nucleotide binding cleft of F-actin (cyan) with bound ADP–Mg^{2+} or ADP–Ca^{2+} (**b**), ATP–Ca^{2+} (**c**, relative position taken from PDB accession code 3EL2) and conformational changes between the G-actin-ATP and F-actin- ADP state (**d**). Glutamine 137 is moved closer to ADP, coordinating not only the cation (as in G-actin) but also the nucleotide b-phosphate (**b**). The presence of ATP instead of ADP in the nucleotide-binding site would be sterically unfavourable, suggesting that a different intermediate conformation exists for F-actin-ATP (**c**). The shorter distance of glutamine 137 to the c-phosphate probably induces ATP hydrolysis and then afterwards the cation takes the position of the c-phosphate in the ADP-state (**d**). For comparison the position of glutamine 137 in G-actin is shown in yellow and the transition from G-actin to F-actin is depicted by arrows. **e**, Mutation of glutamine 137 to histidine results in hampered coordination of the ion and the nucleotide and is connected to nemaline myopathies (Koy et al., 2007).

Structure of a human cytoplasmic actomyosin complex

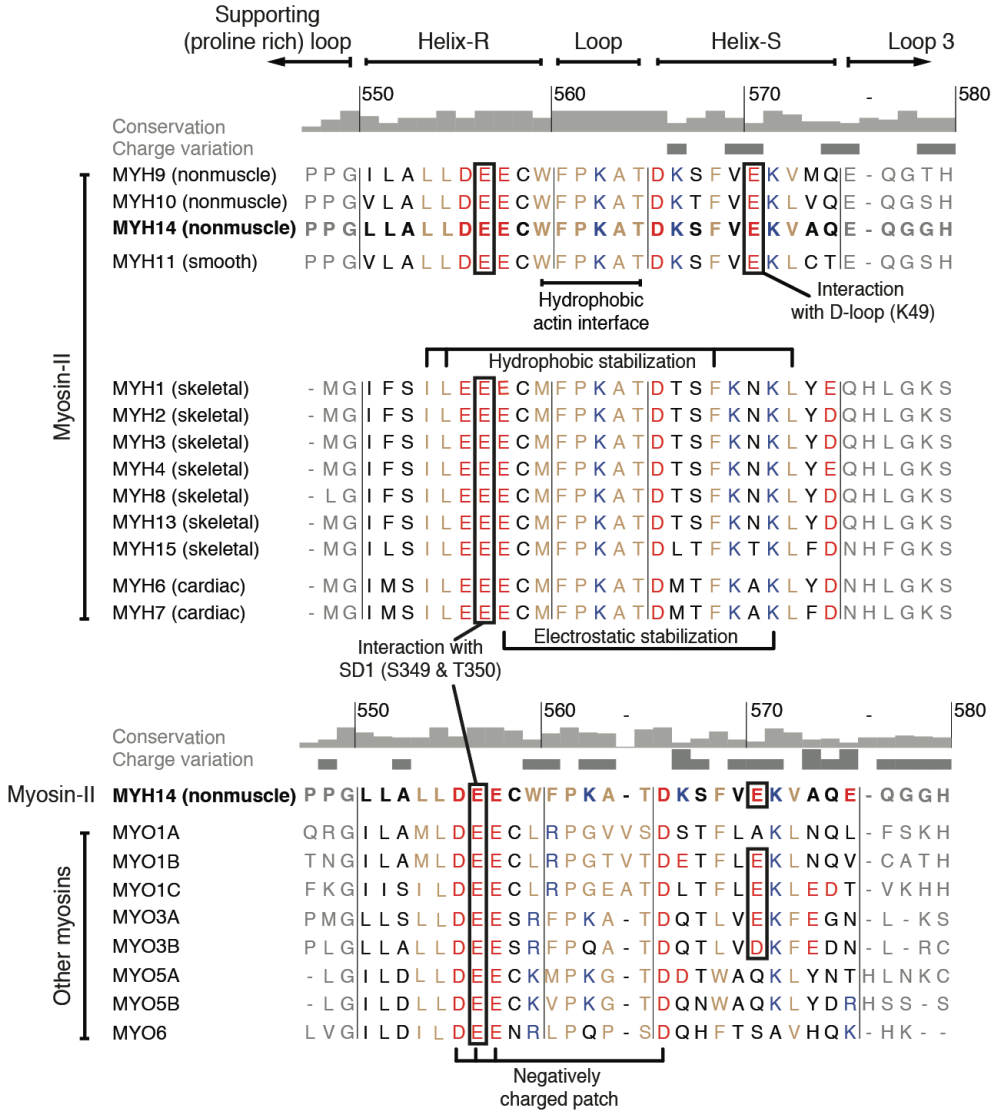

Figure A6.3: Sequence alignment of the HLH motif.

Sequence alignment of myosin (*H. sapiens* myosin-II, -I, -III, -V, -VI) in the region of the HLH (helix-R–loop–helix-S) motif. Important functions at the F-actin–myosin interface and roles in stabilizing these regions themselves are highlighted and labelled. Residue numbering refers to our published structure belonging to the sequence of NM-2C (depicted in bold type). Tissue localization of myosin-II is written in parentheses. We refer to the different myosin isoforms according to the nomenclature for the genes encoding the respective myosin heavy chains.

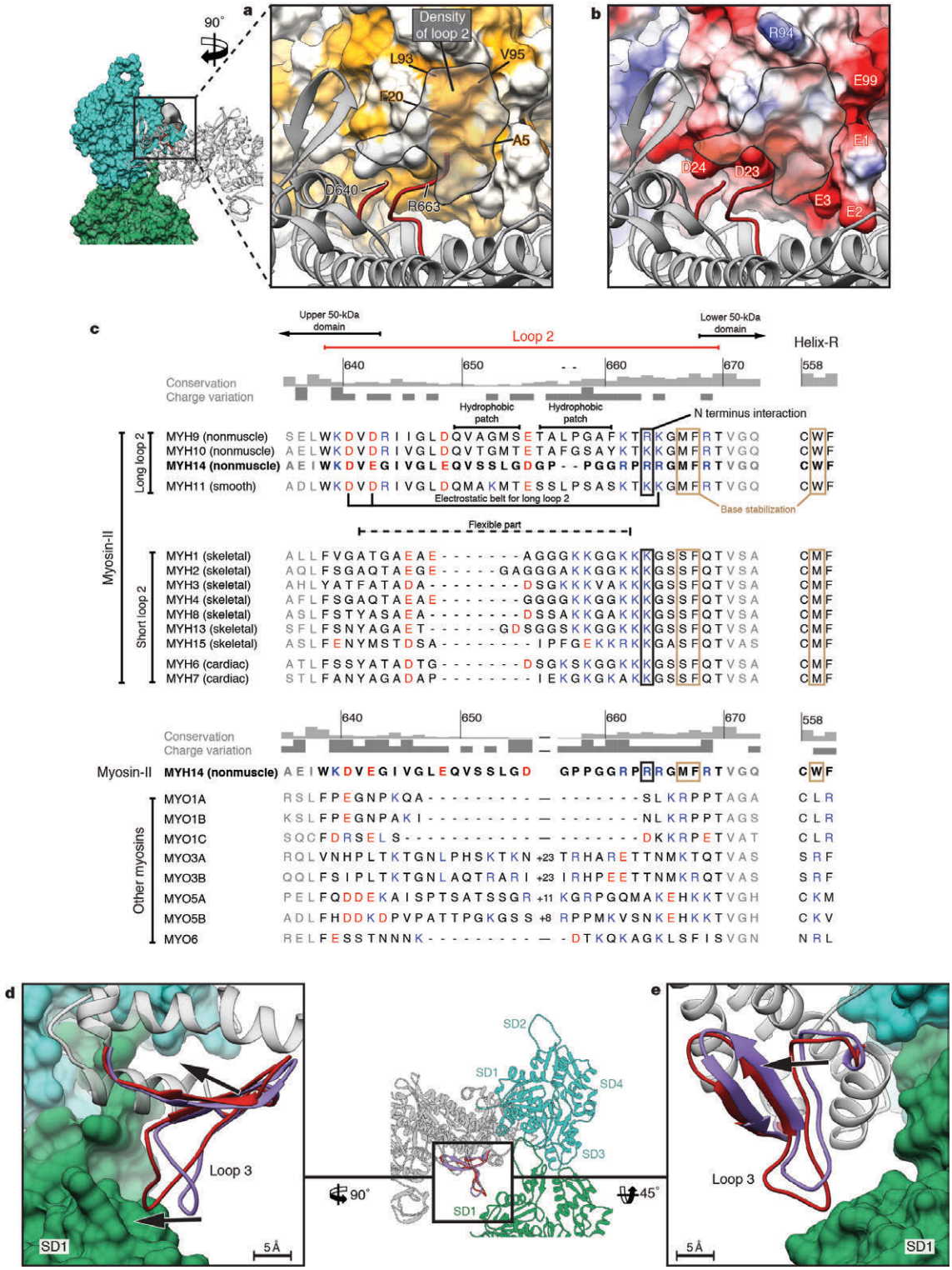

Figure A6.4: Loop 2 and loop 3 on F-actin.

a, **b**, Density map (grey) corresponding to the flexible part (residues 641–661) of loop 2 (red). F-actin is shown as surface model coloured from low (white) to high (yellow) hydrophobicity (**a**) or electrostatic Coulomb potential (**b**, -10 kcal mol^{-1} in red to +10 kcal mol^{-1} in blue). Residue labels belonging to F-actin are coloured as surface colours. **c**, Sequence alignment of myosin (*H. sapiens* myosin-II, -I, -III, -V, -VI) in the region of loop-2 and helix-R of the HLH region. Important functions at the F-actin–myosin interface and in stabilizing these regions are highlighted and labelled. Residue numbering refers to our published structure belonging to the sequence of NM-2C (depicted in bold). Tissue localization of myosin-II is written in parentheses. We refer to the different myosin isoforms according to the nomenclature for the genes encoding the respective myosin heavy chains. **d**, **e**, Changes between rigor (red) and PPS state (purple) in the loop 3 region relative to the rest of lower 50-kDa domain when bound to F-actin. Black arrows indicate movements and scale bars are given.

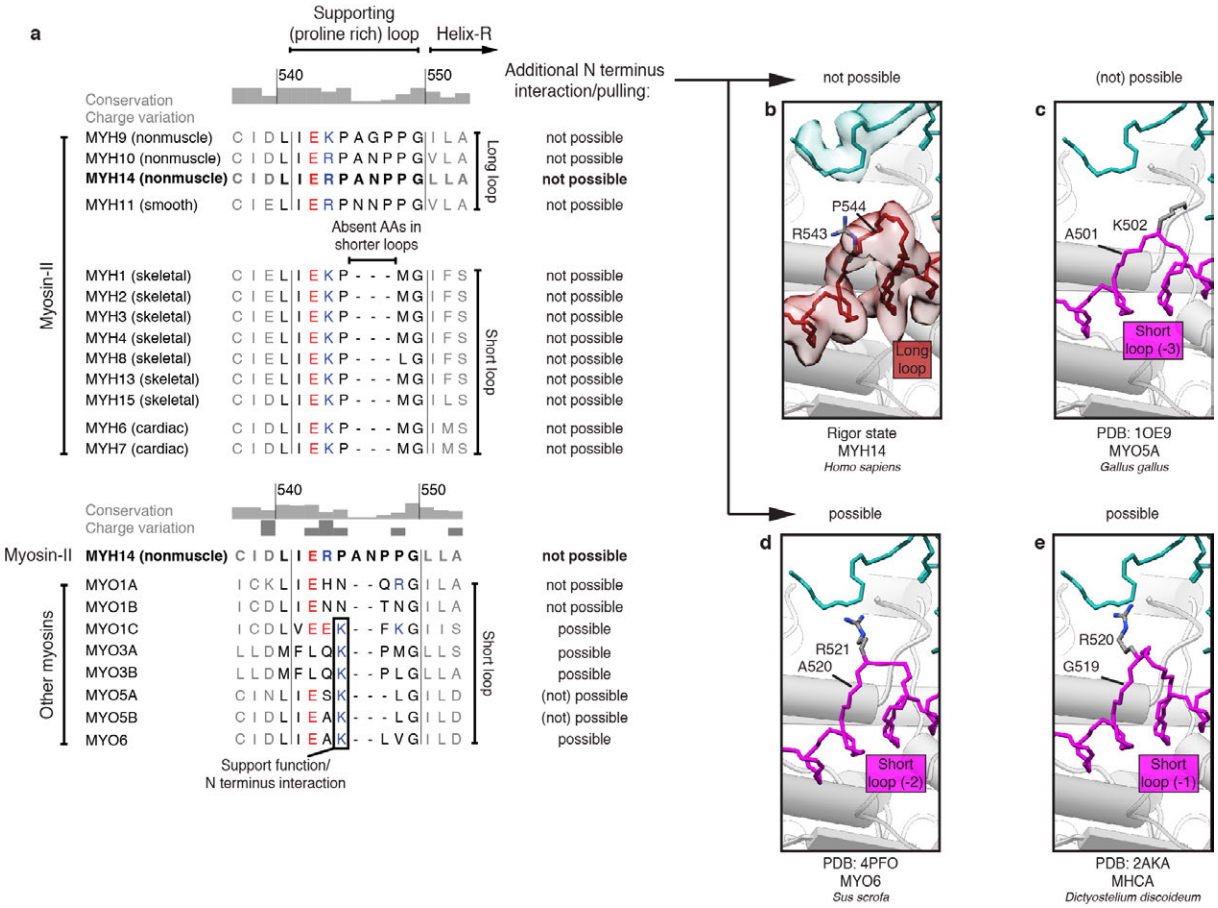

Figure A6.5: Sequence-dependent interaction of supporting loop with the N terminus of F-actin.

a, Sequence alignment of myosin (*H. sapiens* myosin-II, -I, -III, -V, -VI) in the region of the supporting loop. Different lengths of the loop and a possible supporting function are given in the last column. Residue numbering refers to our published structure belonging to the sequence of NM-2C (depicted in bold). Tissue localization of myosin-II is written in parentheses. We refer to the different myosin isoforms according to the nomenclature for the genes encoding the respective myosin heavy chains. **b**–**e**, Comparison of prominent properties in the supporting loop of different myosin classes (comparative models in purple) and their ability to undergo a direct interaction with the N terminus. Main differences are length of loop (numbers give absent amino acids relative to long loop) and position of the prominent positive-charged amino acid (R or K). Only an arginine or lysine sitting on the top would allow a direct interaction (**c**–**e**), while a sideward-oriented arginine (**b**) or a short loop (**c**) disables or reduces a possible interaction, respectively. In addition, respective densities (**b**) of the cryo-EM map are displayed.

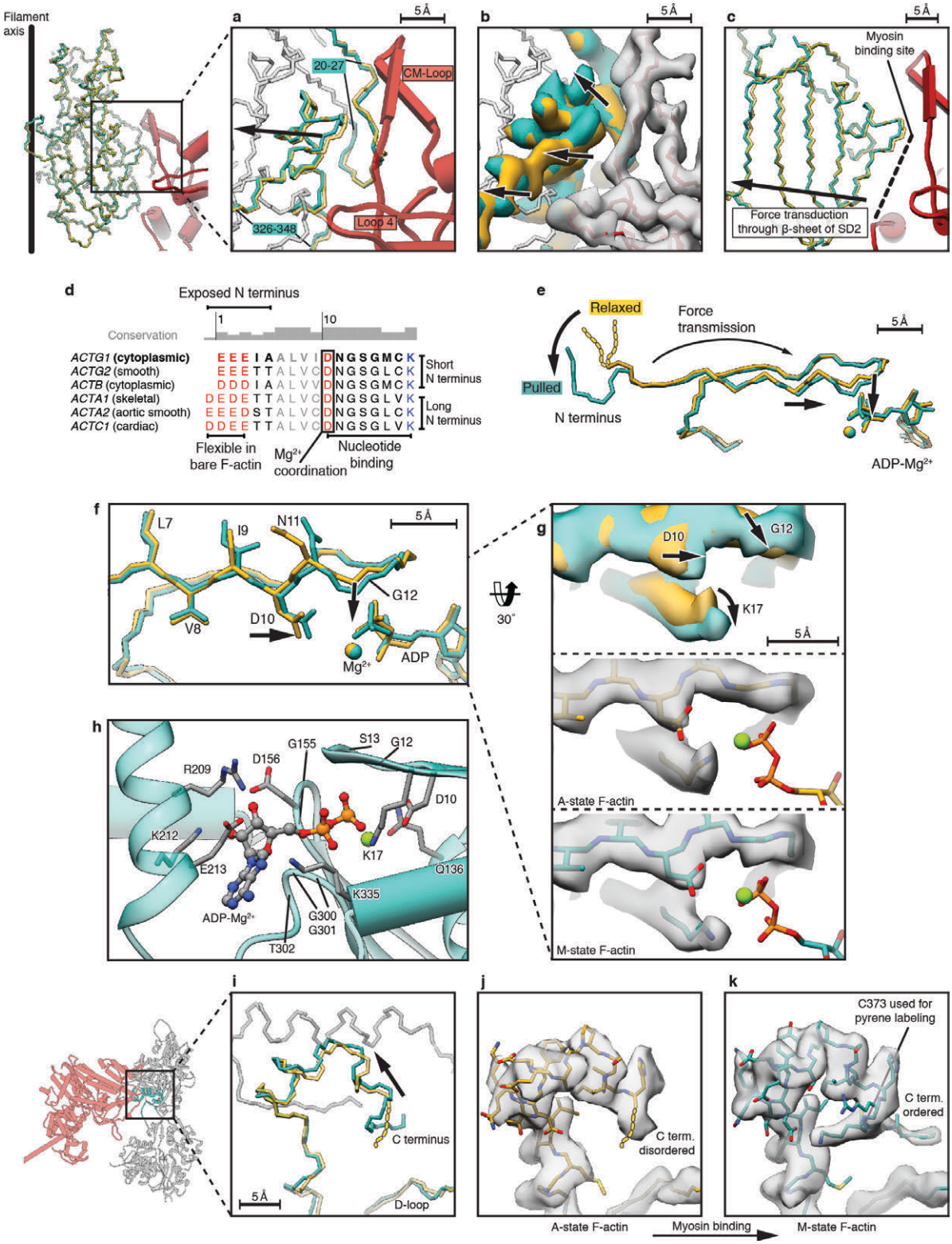

Figure A6.6: Myosin-induced conformational changes in F-actin.

a–**c**, Comparison of bare F-actin (A-state, yellow) with myosin- bound F-actin (M-state, cyan). Myosin is depicted in red. Either models (**a**) or representative parts of the electron density maps (**b**) illustrate conformational changes in F-actin (**c**). **d**, Sequence alignment of the N terminus region of human actin isoforms. Residue numbering refers to our published structure belonging to the sequence of non-muscular γ1-actin (*ACTG1*, depicted in bold type). To prevent confusion, the gene names instead of protein names are given. Localization is written in parentheses. **e**, N terminus and nucleotide binding region of F-actin undergo small changes (highlighted with arrows) through transmitted force of N terminus pulling. **f**, **g**, Close-ups of structural changes at the nucleotide binding site. **h**, Coordination of ADP and Mg^{2+} in the nucleotide binding cleft in M-state F-actin. **i**–**k**, Myosin binding induces a stabilization and shifting of the C terminus towards SD1 of F-actin. C373, which was used for pyrene labelling of F-actin, is part of the C-terminal region. Scale bars are given in the subfigures.

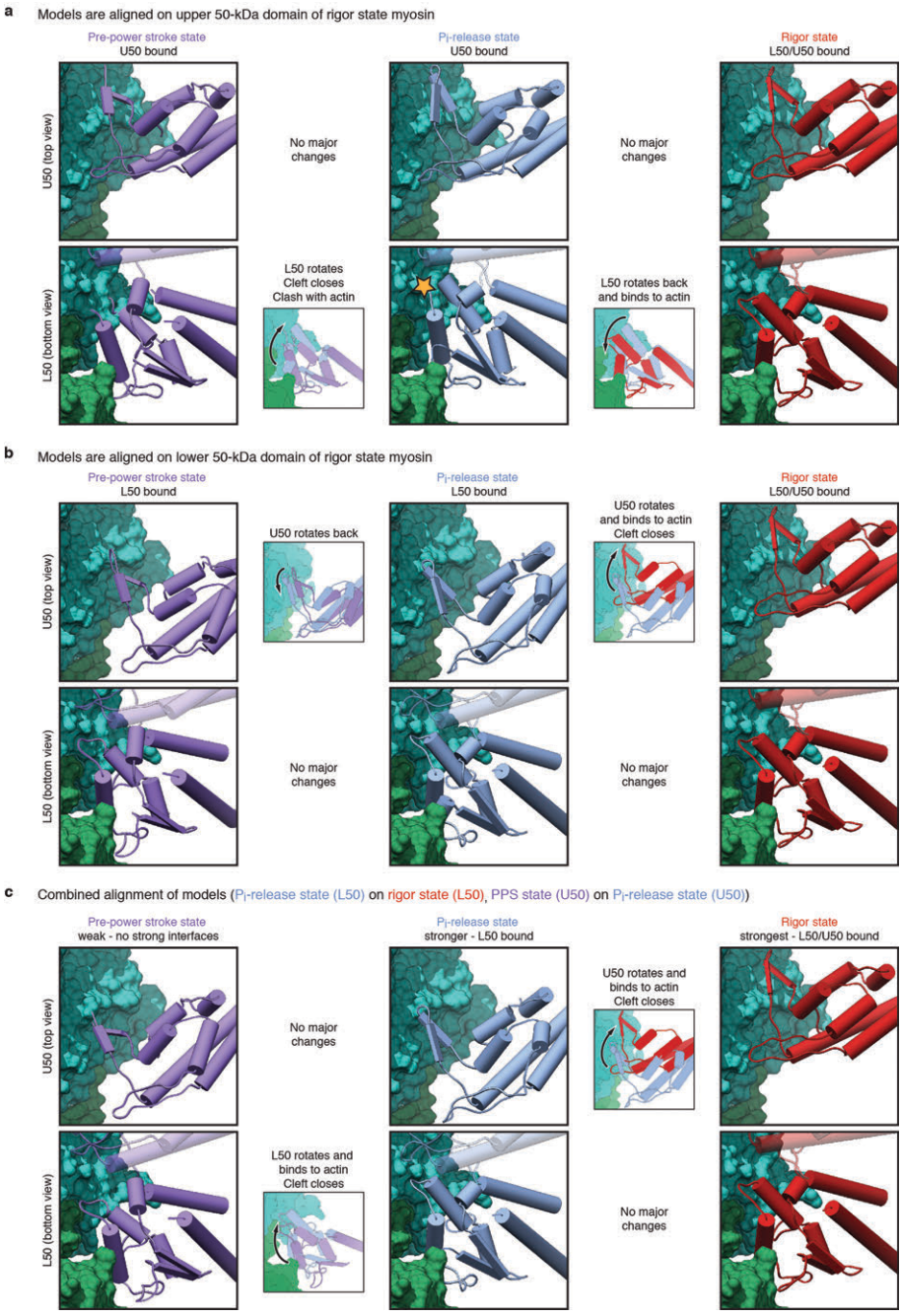

Figure A6.7: Different alignments of models for weak to strong binding of myosin.

a–**c**, Three possible alignments of myosin in the PPS (first column, purple, PDB accession number 5I4E), P_i-release (second column, blue) and rigor (third column, red) states are illustrated with respect to F-actin. For better visualization, differences in F-actin are not shown and F-actin is only depicted in the M-state (green, cyan). The P_i-release state represents a homology model of NM-2C based on a crystal structure of myosin in the P_i-release state (PBD accession number 4PFO). All models are either aligned to the U50 domain (**a**) or the L50 domain (**b**) of the rigor state. In **c**, the model of the P_i-release state was first aligned to the L50 domain of the rigor state. The PPS state was then aligned to the U50 domain of model of the P_i-release state. The first row in each subfigure shows changes in the U50 domain from the top (for a better visualization L50 was deleted). The second row shows the L50 domain from the bottom (U50 is transparent). Possible clashes are indicated by a yellow star (**a**).

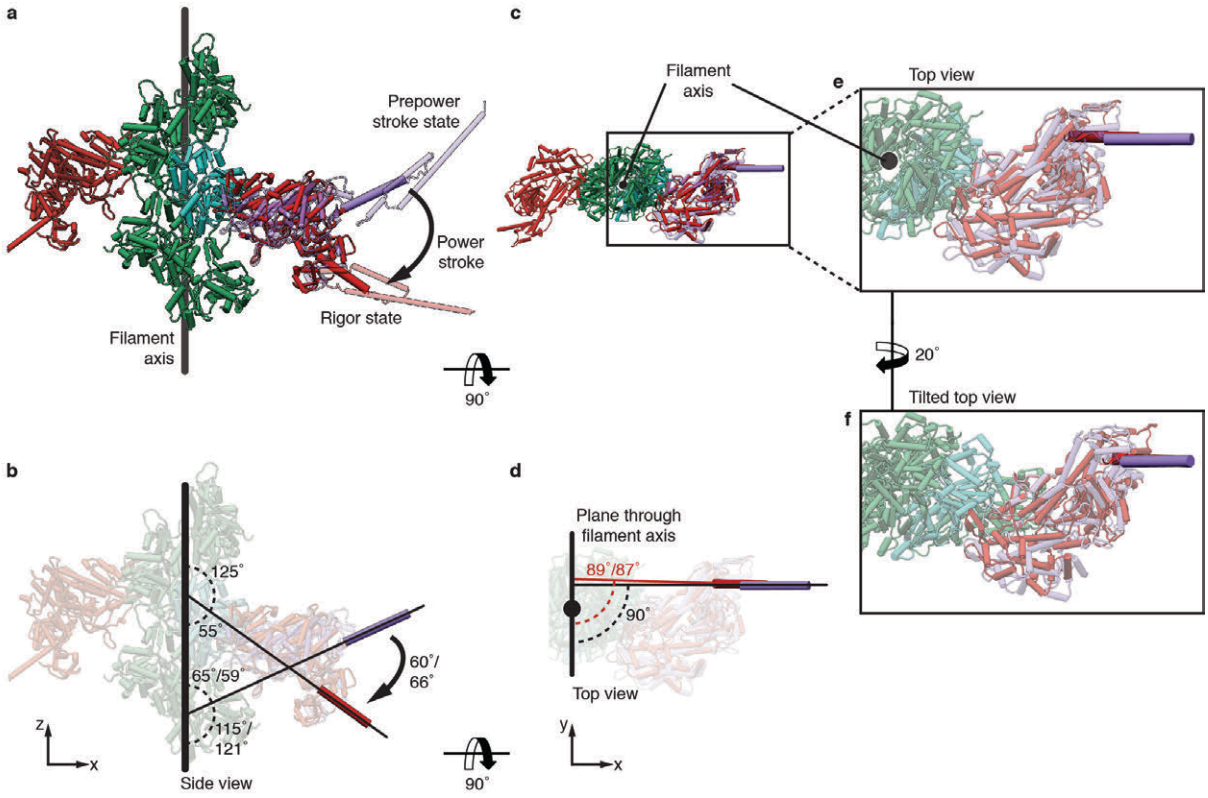

Figure A6.8: Lever arm movement between PPS and rigor state.

a-d, Superposition of myosin in PPS state (purple, PDB accession number 5I4E) and rigor state (red) on F-actin (green) in side (**a, b**) and top view (**c, d**). Angles are given between the first helix of the lever arm to the filament axis (**b**) and to a plane through the filament axis (**d**), respectively. First given angles were obtained based on an alignment on the L50 domain of the rigor state (Figure A6.7b). Second angles were obtained based on the combined alignment of the myosin models (Figure A6.7c). Orientation of models is adjusted such that the filament axis lays on the z-axis and the first helix of the lever arm in the PPS state is parallel to the x-axis. **e, f,** Close-up top view and a slightly tilted top view illustrating that the first helix of different lever arm positions in PPS state and rigor state share roughly a plane parallel to the filament axis resulting into an optimal force transfer on the lever arm.

Danksagungen

Als erstes möchte ich mich bei Herrn Prof. Raunser und Herrn Prof. Tolan bedanken, die gemeinsam es mir ermöglicht haben, meine Dissertation am Max-Planck-Institut anzufertigen.
Besonders ohne Herrn Raunsers kontinuierliche Unterstützung in den sehr „facettenreichen“ Phasen meiner Arbeit sowie ohne seine Hilfe bei schwierigen Entscheidungen wäre meine Promotionszeit nicht so erfolgreich verlaufen wie sie ist.
Aber auch ohne Herrn Tolans Offenheit für mein Anliegen auch meine Dissertation extern am MPI anzufertigen und sein interdisziplinäres Interesse wäre die Anfertigung meiner Arbeit in ihrer Form nicht möglich gewesen.

Auch danke ich Christos Gatsogiannis. Ich habe sehr von unseren sehr konstruktiven Gesprächen bei auftretenden Problemen profitiert und vieles gelernt. Zudem zeigte er mir bereits während meiner Masterarbeit die ersten Schritte des Prozessierens.

Weiter geht mein großer Dank an Oliver Hofnagel. Wie wäre meine Zeit verlaufen, ohne unsere gemeinsamen und extensiven Screening-Sessions am Mikroskop bei stets guter Laune.

Einen weiteren Dank möchte ich an Herrn Prof. Manstein sowie an seine Gruppe schicken, die mir auch für meine Promotion die biologischen Proben zur Verfügung gestellt haben sowie Herrn Prof. Penczek für unsere Zusammenarbeit und Austausch in der Softwareentwicklung.

Auch möchte ich mich bei Herrn Prof. Winter, Mimi Gao und Christopher Rosin für die früchtetragende Kollaboration bedanken, die eine tolle Abwechslung zu meiner eigentlichen Arbeit waren.

Das Schöne in einem Sechser- oder auch Siebenerbüro sind gerade nicht die produktiven Phasen mit den Kopfhörern auf den Ohren, sondern die freundschaftlichen Gespräche unter Freunden. Danke an euch!

Vielen Dank an die Korrekturleser um Dominic, Christos, Oliver, Sabrina und Felipe!

Und ganz besonders möchte ich mich natürlich bei meiner Frau bedanken. Danke für dein Verständnis und dass du immer für mich da bist.

Publikationen und Konferenzbeiträge

Publikationen

Rosin, C., Erlkamp, M., **von der Ecken, J.**, Raunser, S., and Winter, R. (2014). *Exploring the Stability Limits of Actin and Its Suprastructures. Biophys.* J. 107, 2973–2983.

von der Ecken J., Müller M., Lehman W., Manstein D.J., Penczek P.A., and Raunser S. (2015): *Structure of the F-actin--tropomyosin complex.* Nature 519, 114-117.

Gao, M., Berghaus, M., **von der Ecken, J.**, Raunser, S., and Winter, R. (2015). *Condensation agents determine the temperature-pressure stability of F-actin bundles.* Angew. Chem. Int. Ed. Engl. 54, 11088–11092.

von der Ecken J., Heissler S.M., Pathan-Chhatbar S., Manstein D.J., and Raunser S. (2016). *Cryo-EM structure of a human cytoplasmic actomyosin complex at near-atomic resolution.* Nature 534, 724-728

Konferenzbeiträge

Juni 2014 – Konferenzvortrag & Posterpräsentation
Gordon Research Conference (GRC) – Three Dimensional Electron Microscopy
Poster: Helicon - The Next Generation Approach for Processing Helical Structures
Vortrag: *F-actin at atomistic resolution*
Technical Advances for a Rising Star in Structural Biology
Girona, Spanien

September 2014 - Teilnehmervortrag
Vortrag: *Helical Image Processing in SPARX*
EMBO Practical Couse - Cryo-electron microscopy and 3D image processing
Heidelberg, Deutschland

Januar 2015 – Konferenzvortrag
50th Winter Seminar – Biophysical Chemistry
Vortrag: *Structure of the F-actin-tropomyosin complex - The resolution revolution in cryo-EM*
Molecular Biology and Cybernetics of Cell Functions
Klosters, Schweiz

Februar 2016 – Posterpräsentation
60th Annual Meeting – Biophysical Society Meeting
Poster: *Structure of the F-actin-tropomyosin Complex Revealed by Electron Cryomicroscopy.*
Los Angeles, USA

März 2016 – zwei Konferenzvorträge & Posterpräsentation
15th Alpbach Motors Workshop – Myosin and Muscle, and other Motors
Vortrag: *Structure of the F-actin-tropomyosin Complex Revealed by cryo-EM* (Kurzvortrag).
Vortrag: *Structure of the F-actin-tropomyosin Complex Revealed by cryo-EM* (Details und offene Diskussion).
Poster: *Structure of the F-actin-tropomyosin Complex Revealed by Electron Cryomicroscopy.*
Alpbach, Österreich

August 2016 – eingeladener Sprecher für Konferenzvortrag
EMC 2016 – The 16th European Microscopy Congress
Vortrag: *Our muscle at near-atomic resolution - Cryo-EM structures of F-actin-tropomyosin and Actomyosin.*
Lyon, Frankreich

Förderung

Studienstiftung des deutschen Volkes

Ich wurde von April 2014 bis einschließlich März 2016 in die Studienstiftung des deutschen Volkes als Promotionsstudent aufgenommen und finanziell gefördert. Ich möchte mich an dieser Stelle herzlichst dafür bedanken und hoffe, dass ich mich in der Zukunft weiterhin ehrenamtlich für die Studienstiftung in Bereich von Foren oder Auswahlgesprächen einbringen kann.